

**INVESTIGATIONS ON HOT CORROSION OF SOME
Fe-,Ni- AND Co-BASE SUPERALLOYS IN
Na₂SO₄-V₂O₅ ENVIRONMENT UNDER
CYCLIC CONDITIONS**

A THESIS

*submitted in fulfilment of the
requirements for the award of the degree*

of

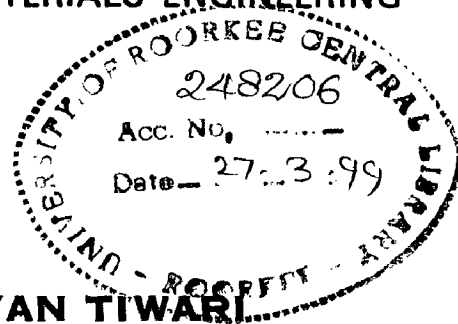
DOCTOR OF PHILOSOPHY

in

METALLURGICAL AND MATERIALS ENGINEERING

By

SHESH NARAYAN TIWARI



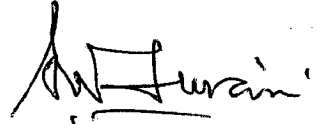
**DEPARTMENT OF METALLURGICAL AND MATERIALS ENGINEERING
UNIVERSITY OF ROORKEE
ROORKEE-247 667 (INDIA)**

JULY, 1997

CANDIDATE'S DECLARATION

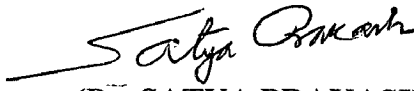
I hereby certify that the work which is being presented in the thesis entitled "INVESTIGATIONS ON HOT CORROSION OF SOME Fe-, Ni- AND Co-BASE SUPERALLOYS IN $\text{Na}_2\text{SO}_4\text{-V}_2\text{O}_5$ ENVIRONMENT UNDER CYCLIC CONDITIONS" in fulfilment of the requirement for the award of the degree of **Doctor of Philosophy** and submitted in the **Department of Metallurgical and Materials Engineering** of the University of Roorkee is an authentic record of my own work carried out during a period from Sept. 1994 to July 1997 under the supervision of **Dr. Satya Prakash**, Professor, Department of Metallurgical and Materials Engineering, University of Roorkee, Roorkee.

The matter presented in this thesis has not been submitted by me for the award of any other degree of this or any other university.


(SHESH NARAYAN TIWARI)
Signature of Candidate

This is to certify that the above statement made by the candidate is correct to the best of my knowledge.


Date : 23 / 7 / 1997


(Dr. SATYA PRAKASH)
Professor
Deptt. of Metallurgical & Materials Engg.
University of Roorkee, Roorkee

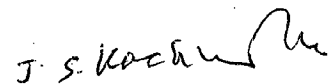
The Ph.D. Viva-voce examination of Shesh Narayan Tiwari, Research Scholar, has been held on 21/2/98.....



Signature of Supervisor(s)



Signature of H.O.D.



Signature of External Examiner

ACKNOWLEDGEMENTS

With pleasure, I express my deep gratitude to my supervisor **Dr. Satya Prakash**, Professor, Department of Metallurgical and Materials Engineering for his valuable guidance, wholehearted cooperation and encouragement during the period of this investigation. His suggestions, constructive criticism and painstaking efforts were instrumental in completing this thesis.

I take this opportunity to thank Dr. M.L. Kapoor and Dr. D.B. Goel, Ex-Heads of the Department and Dr. P.S. Mishra, the present Head of the Metallurgical and Materials Engg. Department for extending me the necessary facilities and providing a congenial research environment.

I am highly thankful to the Director, Defence Metallurgical Research Laboratory (DMRL), Hyderabad for extending me the EPMA facility. The help provided by Mr. K. Satya Prasad, Mr. V.V. RamaRao and Mr. T.V. Balasubramaniam, scientists, DMRL, Hyderabad in carrying out EPMA work is gratefully acknowledged.

My sincere thanks to Mr. J.B. Gnanamoorthy, Head, Metallurgy Division, Dr. V. S. Raghunathan, Head, Physical Metallurgy and Mrs. M. Vijayalakshmi, Scientist, Indira Gandhi Centre for Atomic Research, Kalpakkam (Tamilnadu) for extending me help in carrying out SEM and EDAX work in their laboratory.

My sincere thanks to Mr. K.K. Sharma, DGM, Research and Control Laboratory and Mr. A.G. Shembekar, DGM, Power Plant II of Bhilai Steel Plant (B.S.P.), Bhilai (M.P.) for extending me help in carrying out a series of corrosion tests at B.S.P.

I am highly thankful to Dr. K.B. Mishra, AGM, R & D, SAIL, Ranchi for extending me help in carrying out EDAX work in their laboratory.

My sincere thanks to Chief Managing Director and General Manager (Mktg. Deptt.), Mishra Dhatu Nigam Ltd., Hyderabad (A.P.) for providing the required superalloys for my research work.

I am highly thankful to Prof. R.A. Rapp, Prof. R.L. Jones, Prof. P. Hancock, Prof. M.G. Hocking for sending me the reprints of their valuable papers which were very useful for my research work.

I am thankful to my wife Mrs. Pushpa Tiwari and my children who took keen interest in the progress of my research work and provided valuable help during the period of this research work.

My sincere thanks to Dr. R. N. Sharma, Dr. Devendra Puri and Dr. Mukesh Kumar for their help in my research work.

A special word of thanks to:

- Mr. Madhu Singh, Mr. Rajendra Sharma, Mr. V.K. Tyagi, Mr. T.K. Sharma, Mr. Vidya Prakash for their valuable help during the experimental work.
- The help rendered by Mr. R.P. Singh, Mr. S.S. Saini, Mr. S.K. Sharma, Mr. R.C. Tyagi, Mr. S.S. Gupta, Mr. S.P. Anand and Mr. M.H. Sabari is gratefully acknowledged.
- Mr. S.K. Seth for preparing the photographs needed in this thesis.
- Mr. Anil Saini, Mrs. Rekha Sharma and Dr. T.K. Ghosh, USIC, University of Roorkee for carrying out XRD analysis, SEM and EPMA work respectively.
- Mr. Sandeep Jain for composing this thesis.

ABSTRACT

In many engineering systems like gas turbines, steam generators etc. materials come in direct contact with corrosive condensed phases which cause hot corrosion. The sources of these phases are the fuel and air necessary for combustion. When residual fuel oils are used, due to the presence of Na, V and S, the occurrence and damage by hot corrosion is likely to increase where more aggressive environments have to be encountered. Superalloys have been developed for such applications in gas turbines and steam boilers. Superfer 800H (alloy A) is an Fe-base alloy containing high Ni and Cr content. Superni 75 (alloy B), Superni 600 (alloy C) and Superni 718 (alloy D) are Ni-base alloys containing high Cr content with some other alloying elements. Superco 605 (alloy E) is a Co-base alloy containing high Fe, W, Cr and some Ni. All these alloys contain Cr in the range between 15.5 to 21.0%. They have wide applications in steam boilers, gas turbines, heat exchangers, furnace equipments, pump bodies, nuclear parts and pipe lines in chemical/petrochemical industries. The increasing demand of alloys in aggressive environments has stimulated interest in the hot corrosion studies.

In the present investigation, hot corrosion studies were carried out on above mentioned Fe-, Ni- and Co- base superalloys in different salt/salt-mixture environments. These alloys were studied in air and in c.g environments. The details of these alloys are given in Table 4.1 and those of environments employed in Table 4.2. For convenience these alloys are marked as A, B, C, D and E as shown in Table 4.1. The alloys were cut into specimens of 15 x 20 mm size for hot corrosion studies in laboratory and in actual industrial atmosphere. After polishing the specimens to a mirror finish, coating of Na_2SO_4 , Na_2SO_4 -15% V_2O_5 and Na_2SO_4 -60% V_2O_5 was applied by aqueous spray or by hair brush. Hot corrosion studies in air were carried out in laboratory for 24 cycles (cycle of 1 hr heating and 20 min. cooling) at 700, 800 and 900°C while the studies in c.g. were made in an industry for 6 cycles (cycle of 24 h heating and 1 h cooling) at 1100°C. The effect of MgO addition to the salt mixture (Na_2SO_4 -60% V_2O_5) on the hot corrosion of these alloys was studied for 24 cycles at 900°C in air in laboratory. After hot corrosion,

the specimens were studied thermogravimetrically to understand corrosion kinetics and by visual observation to characterize the nature of scales. Investigation of the scales included X-ray Diffractometry (XRD), Scanning Electron Microscopy (SEM), Energy Dispersive X-ray Analysis (EDAX) and Electron Microprobe Analysis (EPMA) to characterize the corrosion products and make an attempt to understand the mechanism of corrosion.

The wt. gain values for alloys A, B, C, D and E increased with increase in temperature. The wt. gain occurred in these alloys at a rapid rate during the first two cycles and then the rate of wt. gain decreased. The wt. gain values for these alloys were lower in pure Na_2SO_4 than in Na_2SO_4 -15% V_2O_5 . Maximum wt. gain values were obtained in Na_2SO_4 -60% V_2O_5 . Alloy A was comparatively corroded slightly more than the other alloys in pure Na_2SO_4 at all temperatures. Alloy D behaved in a very different manner at 900°C in Na_2SO_4 -15% V_2O_5 in which finally wt. loss of 6.8 mg/cm² was observed after an initial increase in wt. gain during the first two cycles. Alloy A also behaved in a different way in Na_2SO_4 -60% V_2O_5 at 900°C in which total wt. loss of 23.2 mg/cm² was observed. The wt. gain plots for all the alloys after exposure in combustion gas at 1100°C show that they obey parabolic rate law. The wt. gain values obtained with MgO addition to Na_2SO_4 -60% V_2O_5 are lower than those obtained without its addition. This suggests that MgO addition is very beneficial in reducing corrosion rates obtained by Na_2SO_4 -60% V_2O_5 . All the alloys have shown good corrosion resistance at all temperatures in pure Na_2SO_4 , Na_2SO_4 -15% V_2O_5 (except for alloy D at 900°C) and at 700 and 800°C in Na_2SO_4 -60% V_2O_5 .

The average thickness values of the scales, measured with the help of BSE images of the alloys at the cross-section, was lower with pure Na_2SO_4 than those with Na_2SO_4 -15% V_2O_5 while maximum values were obtained with Na_2SO_4 -60% V_2O_5 coating. The thickness measurement supported the observed wt. gain values to confirm that moderate to severe corrosion was induced by Na_2SO_4 -60% V_2O_5 and further MgO addition to this salt mixture reduced its corrosiveness.

EDAX and XRD analysis of the corrosion products formed on the alloys under different salt environments indicated the prominent phases on alloy A to be of α - Fe_2O_3 , Cr_2O_3 , Al_2O_3 , TiO_2 , NiO , FeV_2O_4 and $(\text{Cr,Fe})_2\text{O}_3$. The scales of alloys B, C and D also

contained these phases with an additional phase of $\text{Ni}(\text{VO}_3)_2$. The scale of alloy E mainly composed of $\alpha\text{-Fe}_2\text{O}_3$, Cr_2O_3 , NiO , FeV_2O_4 , $(\text{Cr,Fe})_2\text{O}_3$, Co_3O_4 , Co_2O_3 , CoO , NiCr_2O_4 , WO_3 and FeWO_4 . $\text{Mg}_3\text{V}_2\text{O}_8$ was present in the scales of the alloys after exposure for 24 cycles at 900°C in $\text{Na}_2\text{SO}_4\text{-60\%V}_2\text{O}_5 + \text{MgO}$.

X-ray mappings of elements such as Fe, Cr, Ni, Co, Na, S, O, V, W, Mo were also taken. The elemental maps for alloy A revealed Cr depleted zone in the substrate just below the oxide layer and internal oxidation of Ni was observed at 900°C with $\text{Na}_2\text{SO}_4\text{-15\%V}_2\text{O}_5$ and $\text{Na}_2\text{SO}_4\text{-60\%V}_2\text{O}_5$ coatings in air, while Al_2O_3 and TiO_2 were observed at the grain boundaries of the substrate with $\text{Na}_2\text{SO}_4\text{-60\%V}_2\text{O}_5$ coating in combustion gas. Sulphur penetration was observed with $\text{Na}_2\text{SO}_4\text{-60\%V}_2\text{O}_5 + \text{MgO}$ environment at 900°C at the grain boundaries in the substrates.

In alloy B continuous layer of Cr_2O_3 scale was formed with different salt coatings. Little internal oxidation of Cr was observed only at 900°C with $\text{Na}_2\text{SO}_4\text{-60\%V}_2\text{O}_5 + \text{MgO}$ coating. This alloy showed very good corrosion resistance in nearly all the environments. In alloy C internal oxidation of Al was observed only with $\text{Na}_2\text{SO}_4\text{-15\%V}_2\text{O}_5$ coating while continuous layer of Cr_2O_3 was observed with other coatings.

The alloy D showed good corrosion resistance in pure Na_2SO_4 due to the formation of a thick continuous Cr_2O_3 layer. It was corroded more in $\text{Na}_2\text{SO}_4\text{-15\%V}_2\text{O}_5$ which was observed by the irregular surface of the alloy revealed by the BSE image. Al_2O_3 and TiO_2 formation at the grain boundaries in the substrate was also observed. With $\text{Na}_2\text{SO}_4\text{-60\%V}_2\text{O}_5$ coating in c.g. at 1100°C and with $\text{Na}_2\text{SO}_4\text{-60\%V}_2\text{O}_5 + \text{MgO}$ coating at 900°C , it has shown good corrosion resistance as no internal oxidation or sulphidation was observed.

The alloy E formed a thin continuous layer of Cr_2O_3 in pure $\text{Na}_2\text{SO}_4\text{-15\%V}_2\text{O}_5$ while with $\text{Na}_2\text{SO}_4\text{-60\%V}_2\text{O}_5$ it formed a thick scale of oxides. In actual industrial atmosphere with $\text{Na}_2\text{SO}_4\text{-60\%V}_2\text{O}_5$ coating it showed good corrosion resistance. With $\text{Na}_2\text{SO}_4\text{-60\%V}_2\text{O}_5 + \text{MgO}$ coating it has shown some corrosion resistance but the presence of internal sulphidation of Ni was also observed in the substrate.

These alloys have shown good corrosion resistance against the aggressive environment at 700, 800, 900 and 1100°C under cyclic conditions in laboratory as well as

in industrial hot corrosion tests, except with Na_2SO_4 -60% V_2O_5 at 900°C , due to the formation of a protective continuous layer of Cr_2O_3 on the alloy surface.

An attempt has been made to suggest probable corrosion mechanisms, wherever possible with the help of schematic diagrams (Fig. 6.1-6.6) which are mostly supported by the existing literature or is based on the X-ray elemental maps of the cross-section of the corroded specimens. The schematic diagrams drawn for corrosion induced by pure Na_2SO_4 , Na_2SO_4 -15% V_2O_5 and Na_2SO_4 -60% V_2O_5 in air and in combustion gas as well as for Na_2SO_4 -60% V_2O_5 + MgO in air, are presented in Fig. 6.1-6.6. They also indicate the direction of diffusion of anions and cations through the scale.

CONTENTS

	Page No.
CERTIFICATE	(i)
ACKNOWLEDGEMENTS	(ii)
ABSTRACT	(iv)
PREFACE	(xiii)
LIST OF RESEARCH PAPERS	(ix)
ABBREVIATIONS	(x)
LIST OF TABLES	(xi)
LIST OF FIGURES	(xiv)
CHAPTER 1 INTRODUCTION	1
CHAPTER 2 LITERATURE REVIEW	5
2.1 HOT CORROSION OF METALS AND ALLOYS	5
2.1.1 Na ₂ SO ₄ -INDUCED CORROSION	5
2.1.2 FUEL OIL ASH CORROSION	6
2.1.3 HOT CORROSION MECHANISMS	6
2.1.3.1 TYPE I HOT CORROSION	8
2.1.3.2 TYPE II HOT CORROSION	9
2.1.4 FACTORS AFFECTING HOT CORROSION	9
2.1.5 TECHNIQUES OF HOT CORROSION TESTS	11
2.1.5.1 BURNER RIG TESTS	11
2.1.5.2 TESTS IN INDUSTRIAL ATMOSPHERE	11
2.1.5.3 LABORATORY TUBE FURNACE TESTS	11
2.1.5.4 CRUCIBLE TEST	12
2.1.5.5 ELECTROCHEMICAL TESTS	12
2.1.5.6 ACCELERATED OXIDATION TESTS	13

2.2	HOT CORROSION OF IRON AND IRON-BASE ALLOYS	13
2.2.1	HOT CORROSION OF IRON	13
2.2.2	HOT CORROSION OF IRON-BASE ALLOYS	14
2.3	HOT CORROSION OF NICKEL AND NICKEL-BASE ALLOYS	19
2.3.1	HOT CORROSION OF PURE NICKEL	19
2.3.2	HOT CORROSION OF NICKEL-BASE ALLOYS	20
	2.3.2.1 HOT CORROSION IN Na_2SO_4	20
	2.3.2.2 HOT CORROSION IN $\text{Na}_2\text{SO}_4\text{-V}_2\text{O}_5$	25
2.4	HOT CORROSION OF COBALT-BASE ALLOYS	30
2.4.1	HOT CORROSION IN Na_2SO_4	30
2.4.2	HOT CORROSION IN $\text{Na}_2\text{SO}_4\text{-V}_2\text{O}_5$	31
2.5	EFFECT OF MgO ON HOT CORROSION OF ALLOYS	32
2.5.1	INHIBITION OF HOT CORROSION BY MgO ADDITION IN THE ABSENCE OF Na_2SO_4	33
2.5.2	INHIBITION OF HOT CORROSION BY MgO ADDITION IN THE PRESENCE OF Na_2SO_4	34
CHAPTER 3	FORMULATION OF THE PROBLEM	37
3.1	SCOPE	37
3.2	AIM	38
CHAPTER 4	EXPERIMENTAL TECHNIQUES AND PROCEDURE	41
4.1	MATERIALS	41
4.2	SPECIMEN PREPARATION AND COATING	41
	4.2.1 PREPARATION OF MATERIALS	41
	4.2.2 COATING OF SPECIMENS WITH SALTS	42
4.3	HOT CORROSION STUDIES	42
	4.3.1 IN LABORATORY TUBE FURNACE	42
	4.3.2 IN ACTUAL INDUSTRIAL ENVIRONMENT	42

- 4.4 INVESTIGATION OF CORROSION PRODUCT
 - 4.4.1 THERMOGRAVIMETRIC STUDIES
 - 4.4.2 VISUAL OBSERVATION
 - 4.4.3 MEASUREMENT OF SCALE THICKNESS
 - 4.4.4 X-RAY DIFFRACTOMETRY
 - 4.4.5 OPTICAL MICROSCOPY
 - 4.4.6 SCANNING ELECTRON MICROSCOPY AND EDAX ANALYSIS
 - 4.4.7 ELECTRON MICROPROBE ANALYSIS

CHAPTER 5 RESULTS

- 5.1 HOT CORROSION STUDIES IN PURE Na_2SO_4
 - 5.1.1 KINETIC DATA
 - 5.1.2 VISUAL OBSERVATION
 - 5.1.3 MEASUREMENT OF SCALE THICKNESS
 - 5.1.4 X-RAY DIFFRACTION ANALYSIS
 - 5.1.5 SEM-EDAX AND EPMA RESULTS
- 5.2 HOT CORROSION STUDIES IN Na_2SO_4 -15% V_2O_5
 - 5.2.1 KINETIC DATA
 - 5.2.2 VISUAL OBSERVATION
 - 5.2.3 MEASUREMENT OF SCALE THICKNESS
 - 5.2.4 X-RAY DIFFRACTION ANALYSIS
 - 5.2.5 SEM-EDAX AND EPMA RESULTS
- 5.3 HOT CORROSION STUDIES IN Na_2SO_4 -60% V_2O_5
 - 5.3.1 KINETIC DATA
 - 5.3.2 VISUAL OBSERVATION
 - 5.3.3 MEASUREMENT OF SCALE THICKNESS
 - 5.3.4 X-RAY DIFFRACTION ANALYSIS
 - 5.3.5 SEM-EDAX AND EPMA RESULTS

5.4	HOT CORROSION STUDIES IN COMBUSTION GASES	54
5.4.1	KINETIC DATA	55
5.4.2	VISUAL OBSERVATION	55
5.4.3	MEASUREMENT OF SCALE THICKNESS	56
5.4.4	X-RAY DIFFRACTION ANALYSIS	56
5.4.5	SEM-EDAX AND EPMA RESULTS	56
5.5	HOT CORROSION STUDIES IN Na_2SO_4 -60% V_2O_5 + MgO	58
5.5.1	KINETIC DATA	58
5.5.2	VISUAL OBSERVATION	59
5.5.3	MEASUREMENT OF SCALE THICKNESS	59
5.5.4	X-RAY DIFFRACTION ANALYSIS	60
5.5.5	SEM-EDAX AND EPMA RESULTS	60
CHAPTER 6	DISCUSSION	63
6.1	HOT CORROSION STUDIES IN PURE Na_2SO_4	63
6.2	HOT CORROSION STUDIES IN Na_2SO_4 -15% V_2O_5	68
6.3	HOT CORROSION STUDIES IN Na_2SO_4 -60% V_2O_5	74
6.4	HOT CORROSION STUDIES IN COMBUSTION GASES	81
6.4.1	HOT CORROSION STUDIES OF SUPERFER 800H IN COMBUSTION GASES	81
6.4.2	HOT CORROSION STUDIES OF SUPERNI 75 IN COMBUSTION GASES	83
6.4.3	HOT CORROSION STUDIES OF SUPERNI 600 IN COMBUSTION GASES	85
6.4.4	HOT CORROSION STUDIES OF SUPERNI 718 IN COMBUSTION GASES	86
6.4.5	HOT CORROSION STUDIES OF SUPERCO 605 IN COMBUSTION GASES	87

6.5	HOT CORROSION STUDIES IN Na_2SO_4 -60% V_2O_5 + MgO	89
6.5.1	EFFECT OF MgO ADDITION ON HOT CORROSION OF SUPERFER 800H	89
6.5.2	EFFECT OF MgO ADDITION ON HOT CORROSION OF SUPERNI 75	91
6.5.3	EFFECT OF MgO ADDITION ON HOT CORROSION OF SUPERNI 600	92
6.5.4	EFFECT OF MgO ADDITION ON HOT CORROSION OF SUPERNI 718	93
6.5.5	EFFECT OF MgO ADDITION ON HOT CORROSION OF SUPERCO 605	94
6.6	COMPREHENSIVE DISCUSSION	96
CHAPTER 7 CONCLUSIONS		101
SUGGESTIONS FOR FUTURE WORK		105
REFERENCES		107
TABLES		
FIGURES		

PREFACE

The entire thesis has been divided into following seven chapters.

The first chapter deals with the general introduction of hot corrosion of metals and alloys highlighting its relevance and importance.

Chapter two contains a critical review of the hot corrosion studies on iron-, nickel- and cobalt-base alloys by various investigators and some basic principles and information as relevant to the topic. Studies on effect of inhibitors specially magnesium oxide addition to the salt mixture on hot corrosion behaviour of alloys have also been mentioned.

How the selected information from literature led to the formulation of the present investigation is the matter of discussion of chapter three.

Chapter four gives the details of the experimental techniques and procedures employed in the present investigation.

In chapter five, the findings of hot corrosion studies in air and in combustion gas on superalloys: Superfer 800H, Superni 75, Superni 600, Superni 718 and Superco 605 have been presented. The results include gravimetric studies, visual observation, Scanning Electron Microscopy (SEM), Energy Dispersive X-ray Analysis (EDAX), X-ray Diffractometry (XRD) and Electron Microprobe Analysis (EPMA) of the scale formed on the alloy surfaces.

Chapter six consists of the discussion of the results of hot corrosion studies on the above alloys in laboratory and in industrial environment in the present investigation. The results of studies of MgO addition to the salt mixture on hot corrosion resistance of alloys have also been discussed, Schematic diagrams of probable modes of corrosion have also been included wherever possible. A comprehensive discussion for comparison of hot corrosion behaviour of the alloys has also been presented.

Chapter seven summarizes the conclusions drawn on the basis of the findings of the present investigation.

LIST OF RESEARCH PAPERS

On the basis of critical literature review and results of the present investigations the following papers were presented/communicated for publication in international journals.

1. A review paper on "Fire Side Corrosion in Boilers", Presented in National Conference on "Boiler Corrosion" at National Metallurgical Laboratory, Jamshedpur held on 11-12 April 1995.
2. "Hot Corrosion Behaviour of an Iron Base Superalloy in Salt Environment at Elevated Temperatures", Presented in National Symposium of Research Scholars on "Metals and Materials Research" at IIT Madras held on 4-5 July 1996.
3. "Thermochemistry Involved in Hot Corrosion of Superalloys in Sodium Sulphate-Vanadium Pentoxide", Presented in International Conference on "Advanced Thermochemistry and Ferrous Metallurgy" at Banaras Hindu University, Varanasi held on 14-16 October, 1996.
4. "Studies on the Hot Corrosion Behaviour of Some Superalloys in $\text{Na}_2\text{SO}_4\text{-V}_2\text{O}_5$ ", Presented in National Conference on "Localised Corrosion and Environmental Cracking" at Indira Gandhi Centre for Atomic Research Centre, Kalpakkam held on 22-24 Jan. 1997.
5. "The Corrosion of an Incoloy 800H in $\text{Na}_2\text{SO}_4\text{-V}_2\text{O}_5$ Systems in the Temperature Range 700-800°C", Communicated to the International Journal Material Science and Technology for Publication.
6. "A Review on the Role of Magnesium Oxide as an Inhibitor of Hot Oil Ash Corrosion" Accepted for publication in the international journal Material Science and Technology.
7. A review paper "Vanadic Corrosion of Metals and Alloys", Communicated to the Int. Jnl. Corrosion NACE for publication.
8. "Study of Hot Corrosion Behaviour of Superni 600 in $\text{Na}_2\text{SO}_4\text{-V}_2\text{O}_5$ Environments", Accepted for publication in Int. Conf. on Corrosion by NACE at IIT Bombay, to be held in Dec 1997.
9. "Hot Corrosion Behaviour of Superni 718 in $\text{Na}_2\text{SO}_4\text{-V}_2\text{O}_5$ Environment and its prevention with MgO Addition", Accepted for Publication in National Symposium by NCCI, Karnikudi, Hyderabad, to be held in Sept 1997.
10. "The role of Inhibitors on Hot Corrosion Behaviour of Superni 75 in $\text{Na}_2\text{SO}_4\text{-V}_2\text{O}_5$ Environments Under Cyclic Conditions", Accepted for Publication in National Seminar on "Surface Engineering" at the Institution of Engineers (Jaipur) to be held on 5-6 Sept. 1997.

ABBREVIATIONS

%	Weight percent
Wt.	Weight
SEM	Scanning Electron Microscopy
EDAX	Energy Dispersive X-ray Analysis
EPMA	Electron Microprobe Analysis
BSEI	Back Scattered Electron Image
c.s.	Cross Section
c.g.	Combustion Gas
Kp	Parabolic Rate Constant
m.p.	Melting Point
LTHC	Low Temperature Hot Corrosion
HTHC	High Temperature Hot Corrosion
Alloy A	Superfer 800H (Incoloy 800H)
Alloy B	Superni 75 (Nimonic 75)
Alloy C	Superni 600 (Inconel 600)
Alloy D	Superni 718 (Inconel 718)
Alloy E	Superco 605 (Incoloy 605)

LIST OF TABLES

TABLE NO.	PARTICULARS
4.1	Nominal Composition of the alloys used.
4.2	Environmental Conditions of Hot Corrosion Tests
5.1	Weight change (mg/cm^2) for alloys A,B,C,D and E in different salts and temperatures.
5.2	Parabolic rate constants ($\text{gm}^2 \text{cm}^{-4} \text{sec}^{-1}$) for alloys A,B,C,D and E in combustion gas at 1100°C .
5.3	Average scale thickness of alloys A,B,C,D and E after exposure in salt environments at 900°C .
5.4	XRD analysis of Alloy A (Superfer 800H) after hot corrosion for 24 cycles at 700, 800 and 900°C in pure Na_2SO_4 .
5.5	XRD analysis of Alloy B (Superni 75) after hot corrosion for 24 cycles at 700, 800 and 900°C in pure Na_2SO_4 .
5.6	XRD analysis of Alloy C (Superni 600) after hot corrosion for 24 cycles at 700, 800 and 900°C in pure Na_2SO_4 .
5.7	XRD analysis of Alloy D (Superni 718) after hot corrosion for 24 cycles at 700, 800 and 900°C in pure Na_2SO_4 .
5.8	XRD analysis of Alloy E (Superco 605) after hot corrosion for 24 cycles at 700, 800 and 900°C in pure Na_2SO_4 .
5.9	XRD analysis of Alloy A (Superfer 800H) after hot corrosion for 24 cycles at 700, 800 and 900°C in Na_2SO_4 -15% V_2O_5 .
5.10	XRD analysis of Alloy B (Superni 75) after hot corrosion for 24 cycles at 700, 800 and 900°C in Na_2SO_4 -15% V_2O_5 .
5.11	XRD analysis of Alloy C (Superni 600) after hot corrosion for 24 cycles at 700, 800 and 900°C in Na_2SO_4 -15% V_2O_5 .
5.12	XRD analysis of Alloy D (Superni 718) after hot corrosion for 24 cycles at 700, 800 and 900°C in Na_2SO_4 -15% V_2O_5 .

- 5.13 XRD analysis of Alloy E (Superco 605) after hot corrosion for 24 cycles at 700, 800 and 900°C in Na_2SO_4 -15% V_2O_5 .
- 5.14 XRD analysis of Alloy A (Superfer 800H) after hot corrosion for 24 cycles at 700, 800 and 900°C in Na_2SO_4 -60% V_2O_5 .
- 5.15 XRD analysis of Alloy B (Superni 75) after hot corrosion for 24 cycles at 700, 800 and 900°C in Na_2SO_4 -60% V_2O_5 .
- 5.16 XRD analysis of Alloy C (Superni 600) after hot corrosion for 24 cycles at 700, 800 and 900°C in Na_2SO_4 -60% V_2O_5 .
- 5.17 XRD analysis of Alloy D (Superni 718) after hot corrosion for 24 cycles at 700, 800 and 900°C in Na_2SO_4 -60% V_2O_5 .
- 5.18 XRD analysis of Alloy E (Superco 605) after hot corrosion for 24 cycles at 700, 800 and 900°C in Na_2SO_4 -60% V_2O_5 .
- 5.19 XRD analysis of Alloy A (Superfer 800H) after hot corrosion for 6 cycles in industrial atmosphere at 1100°C with different salt coating.
- 5.20 XRD analysis of Alloy B (Superni 75) after hot corrosion for 6 cycles in industrial atmosphere at 1100°C with different salt coating.
- 5.21 XRD analysis of Alloy C (Superni 600) after hot corrosion for 6 cycles in industrial atmosphere at 1100°C with different salt coating.
- 5.22 XRD analysis of Alloy D (Superni 718) after hot corrosion for 6 cycles in industrial atmosphere at 1100°C with different salt coating.
- 5.23 XRD analysis of Alloy E (Superco 605) after hot corrosion for 6 cycles in industrial atmosphere at 1100°C with different salt coating.
- 5.24 XRD analysis of Alloy A (Superfer 800H) after hot corrosion for 24 cycles at 900°C in Na_2SO_4 -60% V_2O_5 + MgO.

- 5.25 XRD analysis of Alloy B (Superni 75) after hot corrosion for 24 cycles at 900°C in Na_2SO_4 -60% V_2O_5 + MgO.
- 5.26 XRD analysis of Alloy C (Superni 600) after hot corrosion for 24 cycles at 900°C in Na_2SO_4 -60% V_2O_5 + MgO.
- 5.27 XRD analysis of Alloy D (Superni 718) after hot corrosion for 24 cycles at 900°C in Na_2SO_4 -60% V_2O_5 + MgO.
- 5.28 XRD analysis of Alloy E (Superco 605) after hot corrosion for 24 cycles at 900°C in Na_2SO_4 -60% V_2O_5 + MgO.
- 5.29 EDAX analysis of Alloy A (Superfer 800H) after cyclic hot corrosion under different salts and temperatures.
- 5.30 EDAX analysis of Alloy B (Superni 75) after cyclic hot corrosion under different salts and temperatures.
- 5.31 EDAX analysis of Alloy C (Superni 600) after cyclic hot corrosion under different salts and temperatures.
- 5.32 EDAX analysis of Alloy D (Superni 718) after cyclic hot corrosion under different salts and temperatures.
- 5.33 EDAX analysis of Alloy E (Superco 605) after cyclic hot corrosion under different salts and temperatures.

LIST OF FIGURES

- Fig. 2.1 Phase stability diagram for Na-V-S-O system at $900^{\circ}\text{C}^{(17)}$.
- Fig. 2.2(a) Schematic diagram for fluxing.
- Fig. 2.2(b) Precipitation of a porous MO oxide supported by the solubility gradient in a fused salt film⁽⁴⁾.
- Fig. 2.3 Cathodic reduction of SO_3 (as $\text{S}_2\text{O}_7^{2-}$) or molecular oxygen for
 (a) a high permeability of SO_3 or O_2 in the salt film
 (b) high concentration and diffusivities of M^{2+} and M^{3+} or electronic conduction in the salt film.
- Fig. 2.4 Sequential steps in the vanadic corrosion of metals
- Fig. 2.5 Schematic illustration of the growth of chromia scales in
 (i) the absence of oxygen active element and with predominant outward transport of chromium through the scale, and
 (ii) the presence of oxygen active elements and with predominant inward transport of oxygen
- Fig. 2.6 Phase diagram of the $\text{Na}_2\text{O}-\text{V}_2\text{O}_5-\text{SO}_3$ system.
 (1) $\text{Na}_3\text{VO}_2(\text{SO}_4)_2$, (2) $\text{NaVO}(\text{SO}_4)_2$
- Fig. 2.7 Equilibrium diagram $\text{V}_2\text{O}_5-\text{Na}_2\text{SO}_4$ mixture
- Fig. 2.8 Effect of adding various oxides on melting point of a typical crude oil ash.
- Fig. 2.9 Phase diagram for $\text{MgO}-\text{V}_2\text{O}_5$ system
- Fig. 5.1 Weight change plots for the Alloy A (Superfer 800H) in pure Na_2SO_4 .
- Fig. 5.2 Weight change plots for the Alloy B (Superni 75) in pure Na_2SO_4 .
- Fig. 5.3 Weight change plots for the Alloy C (Superni 600) in pure Na_2SO_4 .
- Fig. 5.4 Weight change plots for the Alloy D (Superni 718) in pure Na_2SO_4 .
- Fig. 5.5 Weight change plots for the Alloy E (Superco 605) in pure Na_2SO_4 .
- Fig. 5.6 Weight change plots for the Alloy A (Superfer 800H) in $\text{Na}_2\text{SO}_4-15\% \text{V}_2\text{O}_5$.

- Fig. 5.7 Weight change plots for the Alloy B (Superni 75) in Na_2SO_4 -15% V_2O_5 .
- Fig. 5.8 Weight change plots for the Alloy C (Superni 600) in Na_2SO_4 -15% V_2O_5 .
- Fig. 5.9 Weight change plots for the Alloy D (Superni 718) in Na_2SO_4 -15% V_2O_5 .
- Fig. 5.10 Weight change plots for the Alloy E (Superco 605) in Na_2SO_4 -15% V_2O_5 .
- Fig. 5.11 Weight change plots for the Alloy A (Superfer 800H) in Na_2SO_4 -60% V_2O_5 .
- Fig. 5.12 Weight change plots for the Alloy B (Superni 75) in Na_2SO_4 -60% V_2O_5 .
- Fig. 5.13 Weight change plots for the Alloy C (Superni 600) in Na_2SO_4 -60% V_2O_5 .
- Fig. 5.14 Weight change plots for the Alloy D (Superni 718) in Na_2SO_4 -60% V_2O_5 .
- Fig. 5.15 Weight change plots for the Alloy E (Superco 605) in Na_2SO_4 -60% V_2O_5 .
- Fig. 5.16 Weight change plots for the Alloy A (Superfer 800H) in combustion gas at 1100°C.
- Fig. 5.17 Weight change plots for the Alloy B (Superni 75) in combustion gas at 1100°C.
- Fig. 5.18 Weight change plots for the Alloy C (Superni 600) in combustion gas at 1100°C.
- Fig. 5.19 Weight change plots for the Alloy D (Superni 718) in combustion gas at 1100°C.
- Fig. 5.20 Weight change plots for the Alloy E (Superco 605) in combustion gas at 1100°C.
- Fig. 5.21 Weight change plots for the Alloy A (Superfer 800H) in Na_2SO_4 -60% V_2O_5 + MgO.
- Fig. 5.22 Weight change plots for the Alloy B (Superni 75) in Na_2SO_4 -60% V_2O_5 + MgO.
- Fig. 5.23 Weight change plots for the Alloy C (Superni 600) in Na_2SO_4 -60% V_2O_5 + MgO.
- Fig. 5.24 Weight change plots for the Alloy D (Superni 718) in Na_2SO_4 -60% V_2O_5 + MgO.
- Fig. 5.25 Weight change plots for the Alloy E (Superco 605) in Na_2SO_4 -60% V_2O_5 + MgO.

- Fig. 5.26 Macrographs of Alloy A (Superfer 800H) after cyclic hot corrosion under different salts and temperatures.
- Fig. 5.27 Macrographs of Alloy B (Superni 75) after cyclic hot corrosion under different salts and temperatures.
- Fig. 5.28 Macrographs of Alloy C (Superni 600) after cyclic hot corrosion under different salts and temperatures.
- Fig. 5.29 Macrographs of Alloy D (Superni 718) after cyclic hot corrosion under different salts and temperatures.
- Fig. 5.30 Macrographs of Alloy E (Superco 605) after cyclic hot corrosion under different salts and temperatures.
- Fig. 5.31 X-ray diffraction profile for Alloy A (Superfer 800H) after cyclic hot corrosion at 700, 800 and 900°C in pure Na₂SO₄.
- Fig. 5.32 X-ray diffraction profile for Alloy B (Superni 75) after cyclic hot corrosion at 700, 800 and 900°C in pure Na₂SO₄.
- Fig. 5.33 X-ray diffraction profile for Alloy C (Superni 600) after cyclic hot corrosion at 700, 800 and 900°C in pure Na₂SO₄.
- Fig. 5.34 X-ray diffraction profile for Alloy D (Superni 718) after cyclic hot corrosion at 700, 800 and 900°C in pure Na₂SO₄.
- Fig. 5.35 X-ray diffraction profile for Alloy E (Superco 605) after cyclic hot corrosion at 700, 800 and 900°C in pure Na₂SO₄.
- Fig. 5.36 X-ray diffraction profile for Alloy A (Superfer 800H) after cyclic hot corrosion at 700, 800 and 900°C in Na₂SO₄-15% V₂O₅.
- Fig. 5.37 X-ray diffraction profile for Alloy B (Superni 75) after cyclic hot corrosion at 700, 800 and 900°C in Na₂SO₄-15% V₂O₅.
- Fig. 5.38 X-ray diffraction profile for Alloy C (Superni 600) after cyclic hot corrosion at 700, 800 and 900°C in Na₂SO₄-15% V₂O₅.
- Fig. 5.39 X-ray diffraction profile for Alloy D (Superni 718) after cyclic hot corrosion at 700, 800 and 900°C in Na₂SO₄-15% V₂O₅.
- Fig. 5.40 X-ray diffraction profile for Alloy E (Superco 605) after cyclic hot corrosion at 700, 800 and 900°C in Na₂SO₄-15% V₂O₅.

- Fig. 5.41 X-ray diffraction profile for Alloy A (Superfer 800H) after cyclic hot corrosion at 700, 800 and 900°C in Na₂SO₄-60% V₂O₅.
- Fig. 5.42 X-ray diffraction profile for Alloy B (Superni 75) after cyclic hot corrosion at 700, 800 and 900°C in Na₂SO₄-60% V₂O₅.
- Fig. 5.43 X-ray diffraction profile for Alloy C (Superni 600) after cyclic hot corrosion at 700, 800 and 900°C in Na₂SO₄-60% V₂O₅.
- Fig. 5.44 X-ray diffraction profile for Alloy D (Superni 718) after cyclic hot corrosion at 700, 800 and 900°C in Na₂SO₄-60% V₂O₅.
- Fig. 5.45 X-ray diffraction profile for Alloy E (Superco 605) after cyclic hot corrosion at 700, 800 and 900°C in Na₂SO₄-60% V₂O₅.
- Fig. 5.46 X-ray diffraction profile for Alloy A (Superfer 800H) after cyclic hot corrosion at 1100°C in industrial atmosphere.
- Fig. 5.47 X-ray diffraction profile for Alloy B (Superni 75) after cyclic hot corrosion at 1100°C in industrial atmosphere.
- Fig. 5.48 X-ray diffraction profile for Alloy C (Superni 600) after cyclic hot corrosion at 1100°C in industrial atmosphere.
- Fig. 5.49 X-ray diffraction profile for Alloy D (Superni 718) after cyclic hot corrosion at 1100°C in industrial atmosphere.
- Fig. 5.50 X-ray diffraction profile for Alloy E (Superco 605) after cyclic hot corrosion at 1100°C in industrial atmosphere.
- Fig. 5.51 X-ray diffraction profile for Alloy A (Superfer 800H) after cyclic hot corrosion at 900°C in Na₂SO₄-60% V₂O₅ + MgO.
- Fig. 5.52 X-ray diffraction profile for Alloy B (Superni 75) after cyclic hot corrosion at 900°C in Na₂SO₄-60% V₂O₅ + MgO.
- Fig. 5.53 X-ray diffraction profile for Alloy C (Superni 600) after cyclic hot corrosion at 900°C in Na₂SO₄-60% V₂O₅ + MgO.
- Fig. 5.54 X-ray diffraction profile for Alloy D (Superni 718) after cyclic hot corrosion at 900°C in Na₂SO₄-60% V₂O₅ + MgO.
- Fig. 5.55 X-ray diffraction profile for Alloy E (Superco 605) after cyclic hot corrosion at 900°C in Na₂SO₄-60% V₂O₅ + MgO.

- Fig. 5.56 Scanning electron micrographs of Alloy A (Superfer 800H) after cyclic hot corrosion at 700, 800 and 900°C in pure Na₂SO₄ (X640).
- Fig. 5.57 Scanning electron micrographs of Alloy A (Superfer 800H) after cyclic hot corrosion at 700, 800 and 900°C in Na₂SO₄-15%V₂O₅ (X640).
- Fig. 5.58 Scanning electron micrographs of Alloy B (Superni 75) after cyclic hot corrosion at 700, 800 and 900°C in pure Na₂SO₄ (X640).
- Fig. 5.59 Scanning electron micrographs of Alloy B (Superni 75) after cyclic hot corrosion at 700, 800 and 900°C in Na₂SO₄-15%V₂O₅ (X640).
- Fig. 5.60 Scanning electron micrographs of Alloy C (Superni 600) after cyclic hot corrosion at 700, 800 and 900°C in pure Na₂SO₄ (X640).
- Fig. 5.61 Scanning electron micrographs of Alloy C (Superni 600) after cyclic hot corrosion at 700, 800 and 900°C in Na₂SO₄-15% V₂O₅ (X640).
- Fig. 5.62 Scanning electron micrographs of Alloy D (Superni 718) after cyclic hot corrosion at 700, 800 and 900°C in pure Na₂SO₄ (X640).
- Fig. 5.63 Scanning electron micrographs of Alloy D (Superni 718) after cyclic hot corrosion at 700, 800 and 900°C in Na₂SO₄-15% V₂O₅ (X640).
- Fig. 5.64 Scanning electron micrographs of Alloy E (Superco 605) after cyclic hot corrosion at 700, 800 and 900°C in pure Na₂SO₄ (X640).
- Fig. 5.65 Scanning electron micrographs of Alloy E (Superco 605) after cyclic hot corrosion at 700, 800 and 900°C in Na₂SO₄-15% V₂O₅ (X640).
- Fig. 5.66 Scanning electron micrographs of Alloy A (Superfer 800H) after cyclic hot corrosion at 700, 800 and 900°C in Na₂SO₄-60% V₂O₅ (X640).
- Fig. 5.67 Scanning electron micrographs of Alloy A (Superfer 800H) after cyclic hot corrosion at 1100°C with pure Na₂SO₄, Na₂SO₄-15% V₂O₅ and Na₂SO₄-60% V₂O₅ in c.g. (X640).
- Fig. 5.68 Scanning electron micrographs of Alloy B (Superni 75) after cyclic hot corrosion at 700, 800 and 900°C in Na₂SO₄-60% V₂O₅ (X640).

- Fig. 5.69 Scanning electron micrographs of Alloy B (Superni 75) after cyclic hot corrosion at 1100°C with pure Na₂SO₄, Na₂SO₄-15% V₂O₅ and Na₂SO₄-60% V₂O₅ in c.g. (X640).
- Fig. 5.70 Scanning electron micrographs of Alloy C (Superni 600) after cyclic hot corrosion at 700, 800 and 900°C in Na₂SO₄-60% V₂O₅ (X640).
- Fig. 5.71 Scanning electron micrographs of Alloy C (Superni 600) after cyclic hot corrosion at 1100°C with pure Na₂SO₄, Na₂SO₄-15% V₂O₅ and Na₂SO₄-60% V₂O₅ in c.g. (X640).
- Fig. 5.72 Scanning electron micrographs of Alloy D (Superni 718) after cyclic hot corrosion at 700, 800 and 900°C in Na₂SO₄-60% V₂O₅ (X640).
- Fig. 5.73 Scanning electron micrographs of Alloy D (Superni 718) after cyclic hot corrosion at 1100°C with pure Na₂SO₄, Na₂SO₄-15% V₂O₅, Na₂SO₄-60% V₂O₅ in c.g. (X640).
- Fig. 5.74 Scanning electron micrographs of Alloy E (Superco 605) after cyclic hot corrosion at 700, 800 and 900°C in Na₂SO₄-60% V₂O₅ (X640).
- Fig. 5.75 Scanning electron micrographs of Alloy E (Superco 605) after cyclic hot corrosion at 1100°C with pure Na₂SO₄, Na₂SO₄-15%V₂O₅, Na₂SO₄-60% V₂O₅ in c.g. (X640).
- Fig. 5.76 Scanning electron micrographs of Alloy A (Superfer 800H) after cyclic hot corrosion at 900°C in Na₂SO₄-60% V₂O₅ + MgO (X640).
- Fig. 5.77 Scanning electron micrographs of Alloy B (Superni 75) after cyclic hot corrosion at 900°C in Na₂SO₄-60% V₂O₅ + MgO (X640).
- Fig. 5.78 Scanning electron micrographs of Alloy C (Superni 600) after cyclic hot corrosion at 900°C in Na₂SO₄-60% V₂O₅ + MgO (X640).
- Fig. 5.79 Scanning electron micrographs of Alloy D (Superni 718) after cyclic hot corrosion at 900°C in Na₂SO₄-60% V₂O₅ + MgO (X640).
- Fig. 5.80 Scanning electron micrographs of Alloy E (Superco 605) after cyclic hot corrosion at 900°C in Na₂SO₄-60% V₂O₅ + MgO (X640).

Fig. 5.81 BSEI and X-ray mappings of the cross-section of Alloy A (Superfer 800H) after cyclic hot corrosion at 900°C in pure Na₂SO₄ (X1000).

(a) Composition image (BSEI)

(b) Cr K_α x-ray image

(c) Ni K_α x-ray image

(d) Fe K_α x-ray image

(e) O K_α x-ray image

Fig. 5.82 BSEI and X-ray mappings of the cross-section of Alloy B (Superni 75) after cyclic hot corrosion at 900°C in pure Na₂SO₄ (X1000).

(a) Composition image (BSEI)

(b) Cr K_α x-ray image

(c) Ni K_α x-ray image

(d) O K_α x-ray image

Fig. 5.83 BSEI and X-ray mappings of the cross-section of Alloy C (Superni 600) after cyclic hot corrosion at 900°C in pure Na₂SO₄ (X1000).

(a) Composition image (BSEI)

(b) Cr K_α x-ray image

(c) Ni K_α x-ray image

(d) Fe K_α x-ray image

(e) O K_α x-ray image

Fig. 5.84 BSEI and X-ray mappings of the cross-section of Alloy D (Superni 718) after cyclic hot corrosion at 900°C in pure Na₂SO₄ (X1000).

(a) Composition image (BSEI)

(b) Cr K_α x-ray image

(c) Ni K_α x-ray image

(d) Fe K_α x-ray image

(e) Ti K_α x-ray image

(f) O K_α x-ray image

Fig. 5.85 BSEI and X-ray mappings of the cross-section of Alloy E (Superco 605) after cyclic hot corrosion at 900°C in pure Na₂SO₄ (X1000).

(a) Composition image (BSEI)

(b) Cr K_α x-ray image

(c) Ni K_α x-ray image

(d) Fe K_α x-ray image

(e) Co K_α x-ray image

(f) W K_α x-ray image

(g) O K_α x-ray image

Fig. 5.86 BSEI and X-ray mappings of the cross-section of Alloy A (Superfer 800H) after cyclic hot corrosion at 900°C in Na₂SO₄-15% V₂O₅ (X1000).

(a) Composition image (BSEI)

(b) Cr K_α x-ray image

(c) Ni K_α x-ray image

(d) Fe K_α x-ray image

(e) O K_α x-ray image

Fig. 5.87 BSEI and X-ray mappings of the cross-section of Alloy B (Superni 75) after cyclic hot corrosion at 900°C in Na₂SO₄-15% V₂O₅ (X300).

(a) Composition image (BSEI)

(b) Cr K_α x-ray image

(c) Ni K_α x-ray image

(d) O K_α x-ray image

Fig. 5.88 BSEI and X-ray mappings of the cross-section of Alloy C (Superni 600) after cyclic hot corrosion at 900°C in Na₂SO₄-15% V₂O₅ (X400).

(a) Composition image (BSEI)

(b) Cr K_α x-ray image

(c) Ni K_α x-ray image

- (d) Fe K_{α} x-ray image
- (e) Al K_{α} x-ray image
- (f) V K_{α} x-ray image
- (g) O K_{α} x-ray image

Fig. 5.89 BSEI and X-ray mappings of the cross-section of Alloy D (Superni 718) after cyclic hot corrosion at 900°C in Na₂SO₄-15% V₂O₅ (X1000).

- (a) Composition image (BSEI)
- (b) Cr K_{α} x-ray image
- (c) Ni K_{α} x-ray image
- (d) Fe K_{α} x-ray image
- (e) Al K_{α} x-ray image
- (f) Ti K_{α} x-ray image
- (g) O K_{α} x-ray image

Fig. 5.90 BSEI and X-ray mappings of the cross-section of Alloy E (Superco 605) after cyclic hot corrosion at 900°C in Na₂SO₄-15% V₂O₅ (X500).

- (a) Composition image (BSEI)
- (b) Cr K_{α} x-ray image
- (c) Ni K_{α} x-ray image
- (d) Fe K_{α} x-ray image
- (e) Co K_{α} x-ray image
- (f) W K_{α} x-ray image
- (g) O K_{α} x-ray image

Fig. 5.91 BSEI and X-ray mappings of the cross-section of Alloy A (Superfer 800H) after cyclic hot corrosion at 900°C in Na₂SO₄-60% V₂O₅ (X400).

- (a) Composition image (BSEI)
- (b) Cr K_{α} x-ray image
- (c) Ni K_{α} x-ray image

(d) Fe K_{α} x-ray image

(e) O K_{α} x-ray image

Fig. 5.92 BSEI and X-ray mappings of the cross-section of Alloy B (Superni 75) after cyclic hot corrosion at 900°C in Na₂SO₄-60% V₂O₅ (X600).

(a) Composition image (BSEI)

(b) Cr K_{α} x-ray image

(c) Ni K_{α} x-ray image

(d) Fe K_{α} x-ray image

(e) V K_{α} x-ray image

(f) O K_{α} x-ray image

Fig. 5.93 BSEI and X-ray mappings of the cross-section of Alloy C (Superni 600) after cyclic hot corrosion at 900°C in Na₂SO₄-60% V₂O₅ (X400).

(a) Composition image (BSEI)

(b) Cr K_{α} x-ray image

(c) Ni K_{α} x-ray image

(d) Fe K_{α} x-ray image

(e) Na K_{α} x-ray image

(f) V K_{α} x-ray image

(g) O K_{α} x-ray image

Fig. 5.94 BSEI and X-ray mappings of the cross-section of Alloy D (Superni 718) after cyclic hot corrosion at 900°C in Na₂SO₄-60% V₂O₅ (X400).

(a) Composition image (BSEI)

(b) Cr K_{α} x-ray image

(c) Ni K_{α} x-ray image

(d) Fe K_{α} x-ray image

(e) V K_{α} x-ray image

(f) O K_{α} x-ray image

Fig. 5.95 BSEI and X-ray mappings of the cross-section of Alloy E (Superco 605) after cyclic hot corrosion at 900°C in Na₂SO₄-60% V₂O₅ (X300).

(a) Composition image (BSEI)

(b) Cr K_α x-ray image

(c) Ni K_α x-ray image

(d) Fe K_α x-ray image

(e) Co K_α x-ray image

(f) W K_α x-ray image

(g) V K_α x-ray image

(h) O K_α x-ray image

Fig. 5.96 BSEI and X-ray mappings of the cross-section of Alloy A (Superfer 800H) after cyclic hot corrosion at 1100°C in industrial atmosphere (X1000).

(a) Composition image (BSEI)

(b) Cr K_α x-ray image

(c) Ni K_α x-ray image

(d) Fe K_α x-ray image

(e) Al K_α x-ray image

(f) Ti K_α x-ray image

(g) O K_α x-ray image

Fig. 5.97 BSEI and X-ray mappings of the cross-section of Alloy B (Superni 75) after cyclic hot corrosion at 1100°C in industrial atmosphere (X600).

(a) Composition image (BSEI)

(b) Cr K_α x-ray image

(c) Ni K_α x-ray image

(d) Fe K_α x-ray image

(e) V K_α x-ray image

(f) O K_α x-ray image

Fig. 5.98 BSEI and X-ray mappings of the cross-section of Alloy C (Superni 600) after cyclic hot corrosion at 1100°C in industrial atmosphere (X600).

- (a) Composition image (BSEI)
- (b) Cr K_{α} x-ray image
- (c) Ni K_{α} x-ray image
- (d) Fe K_{α} x-ray image
- (e) O K_{α} x-ray image

Fig. 5.99 BSEI and X-ray mappings of the cross-section of Alloy D (Superni 718) after cyclic hot corrosion at 1100°C in industrial atmosphere (X600).

- (a) Composition image (BSEI)
- (b) Cr K_{α} x-ray image
- (c) Ni K_{α} x-ray image
- (d) Fe K_{α} x-ray image
- (e) O K_{α} x-ray image

Fig. 5.100 BSEI and X-ray mappings of the cross-section of Alloy E (Superco 605) after cyclic hot corrosion at 1100°C in industrial atmosphere (X400).

- (a) Composition image (BSEI)
- (b) Cr K_{α} x-ray image
- (c) Ni K_{α} x-ray image
- (d) Fe K_{α} x-ray image
- (e) Co K_{α} x-ray image
- (f) W K_{α} x-ray image
- (g) V K_{α} x-ray image
- (h) O K_{α} x-ray image

Fig. 5.101 BSEI and X-ray mappings of the cross-section of Alloy A (Superfer 800H) after cyclic hot corrosion at 900°C in Na₂SO₄-60%V₂O₅ + MgO (X600).

- (a) Composition image (BSEI)
- (b) Cr K_α x-ray image
- (c) Ni K_α x-ray image
- (d) Fe K_α x-ray image
- (e) V K_α x-ray image
- (f) Mg K_α x-ray image
- (g) S K_α x-ray image
- (h) O K_α x-ray image

Fig. 5.102 BSEI and X-ray mappings of the cross-section of Alloy B (Superni 75) after cyclic hot corrosion at 900°C in Na₂SO₄-60%V₂O₅ + MgO (X500).

- (a) Composition image (BSEI)
- (b) Cr K_α x-ray image
- (c) Ni K_α x-ray image
- (d) Fe K_α x-ray image
- (e) V K_α x-ray image
- (f) Mg K_α x-ray image
- (g) O K_α x-ray image

Fig. 5.103 BSEI and X-ray mappings of the cross-section of Alloy C (Superni 600) after cyclic hot corrosion at 900°C in Na₂SO₄-60%V₂O₅ + MgO (X600).

- (a) Composition image (BSEI)
- (b) Cr K_α x-ray image
- (c) Ni K_α x-ray image
- (d) Fe K_α x-ray image
- (e) V K_α x-ray image

(f) Mg K_{α} x-ray image

(g) O K_{α} x-ray image

Fig. 5.104 BSEI and X-ray mappings of the cross-section of Alloy D (Superni 718) after cyclic hot corrosion at 900°C in Na_2SO_4 -60% V_2O_5 + MgO (X300).

(a) Composition image (BSEI)

(b) Cr K_{α} x-ray image

(c) Ni K_{α} x-ray image

(d) Fe K_{α} x-ray image

(e) V K_{α} x-ray image

(f) Mg K_{α} x-ray image

(g) O K_{α} x-ray image

Fig. 5.105 BSEI and X-ray mappings of the cross-section of Alloy E (Supperco 605) after cyclic hot corrosion at 900°C in Na_2SO_4 -60% V_2O_5 + MgO (X400).

(a) Composition image (BSEI)

(b) Cr K_{α} x-ray image

(c) Ni K_{α} x-ray image

(d) Fe K_{α} x-ray image

(e) Co K_{α} x-ray image

(f) W K_{α} x-ray image

(g) V K_{α} x-ray image

(h) S K_{α} x-ray image

(i) O K_{α} x-ray image

Fig. 6.1 Schematic diagram showing probable mechanism of hot corrosion of Alloy A (Superfer 800H), Alloy D (Superni 718) and Alloy E (Supperco 605) in pure Na_2SO_4 at 900°C.

Fig. 6.2 Schematic diagram showing probable hot corrosion mechanism of Alloy A (Superfer 800H) in Na_2SO_4 -15% V_2O_5 at 900°C.

- Fig. 6.3 Schematic diagram showing probable hot corrosion mechanism of Alloy D (Superni 718) and Alloy E (Superco 605) in Na_2SO_4 -15% V_2O_5 at 900°C .
- Fig. 6.4 Schematic diagram showing probable hot corrosion mechanism of (a) Alloy A (Superfer 800H), (b) Alloy B (Superni 75) and (c) Alloy E (Superco 605) in Na_2SO_4 -60% V_2O_5 at 900°C .
- Fig. 6.5 Schematic diagram showing probable hot corrosion mechanism of Alloy A (Superfer 800H) with Na_2SO_4 -60% V_2O_5 in c.g. at 1100°C .
- Fig. 6.6 Schematic diagram showing internal oxidation and sulphidation during hot corrosion of (a) Alloy A (b) Alloy D and (c) Alloy E in Na_2SO_4 -60% V_2O_5 + MgO at 900°C .

INTRODUCTION

Hot corrosion is a serious problem in engineering systems such as steam boilers, gas turbines, waste incinerators, internal combustion engines, aircrafts and chemical process systems, where low grade fossil fuels are used⁽¹⁾. This problem is still severe when residual fuel oils are used. Vanadium, sulphur and sodium are common impurities present in low grade petroleum fuels. Molten sulphate-vanadate deposits resulting from the condensation of combustion products of such fuels are extremely corrosive to high temperature materials used in the combustion systems⁽²⁾. Depending on the impurity concentration in the fuel and intake air, various vanadium compounds e.g. V_2O_5 , $NaVO_3$ and Na_3VO_4 , with decreasing acidity, may form in the corrosive deposits.

The hot corrosion of materials by sulphates, vanadates or sulphate-vanadate solutions depends strongly on the compositions of the salt deposits and the gas atmosphere. Seiersten and Kofstad⁽³⁾ studied the hot corrosion of MCrAlY coatings on Inconel 600 by $NaVO_3$ - V_2O_5 mixtures in O_2 at 650 to 800°C and found that the corrosion rates increased with increasing V_2O_5 content. Vanadium is a transition element that may exist in various oxidation states, with the +5 and +4 valencies usually the most stable⁽²⁾. Rapp and Goto⁽⁴⁾ have suggested that the presence of such multivalent transition metal ions in a fused salt deposit could greatly accelerate the hot corrosion rate by counter diffusion of the multivalent cations through the salt film.

Iron-, nickel- and cobalt-base superalloys are the commercial alloys commonly used for the manufacture of components used in aggressive environments of gas turbines, steam boilers etc. Chromium is the most important element in developing resistance to hot corrosion. This element forms a protective oxide layer on the metal surface and inhibits the onset of attack regardless of the hot corrosion mechanism⁽⁵⁾.

Refractory metal concentration is also an important composition variable. It is necessary to keep the concentration low. However, higher concentrations of these elements can be used if the chromium concentration is also increased. The molten salt deposits dissolve the protective oxide layer of either chromium or aluminium at the working temperature. This phenomenon is known as *fluxing*. The resistance to hot corrosion attack depends upon the amount and type of fluxing, acidic or basic. A knowledge of the solubilities of metal oxides in molten salts is important in evaluating corrosion resistance property of alloys. The solubilities of NiO, Co₃O₄, iron oxides, Al₂O₃, Cr₂O₃, Y₂O₃ and CeO₂ in pure fused Na₂SO₄, as well as the solubilities of Y₂O₃, HfO₂ and CeO₂ in a fused Na₂SO₄-30%NaVO₃ salt solution have been reported⁽²⁾. In the sulphate-vanadate melt, the conversion of the metavanadate to the orthovanadate solute drastically increased the acidic solubility for CeO₂ compared to that in pure Na₂SO₄. This mechanism and the resulting increase in acidic solubility is expected to be valid generally for all oxides in vanadate solutions⁽²⁾.

Bornstein and DeCrescente proposed a hot corrosion mechanism based on the basic dissolution of the protective oxide scale by a reaction involving Na₂O, the basic minority component of the fused salt⁽⁵⁾. Goebel and Pettit⁽⁶⁾ at the same time, also interpreted the hot corrosion of pure nickel in terms of a basic dissolution and reprecipitation of NiO in the fused salt film. Goebel and Pettit⁽⁶⁾ extended the mechanism to include acidic fluxing and oxide reprecipitation to account for the catastrophic oxidation caused by pure Na₂SO₄ for alloys containing strong acid components such as V or Mo.

Numerous factors affect the time at which the hot corrosion process moves from the initiation stage into the propagation stage. The factors, which have been found to be important are the alloy composition, deposit composition and its physical state, amount of deposit on the superalloy, temperature etc.⁽⁷⁾. Alloy composition can be a critical factor in the initiation of attack. It is necessary to specify the conditions causing the attack since the alloy may behave differently under other conditions. The gross composition of the salt deposit is also an important variable. The presence of chlorine or V in a predominantly alkali sulphate deposit can drastically increase corrosion rate. The composition of the salt

deposit and the rate at which it accumulates on the surface of the alloys affects not only the time required to initiate hot corrosion but also the type of propagation mode that is followed. Temperature has a wide range of effects on hot corrosion processes.

Investigations have been carried out on the hot corrosion of stainless steels, iron, nickel and Fe-, Ni-, Co-base superalloys in various environments (solid, liquid, gaseous) at different temperatures (300-1200°C) for various time periods in isothermal and cyclic conditions without or under loads⁽⁸⁾. For troublefree and continuous long service of power plants running at high temperatures, suitable materials should be selected after complete hot corrosion studies of alloys.

The performance of the protective coatings were also studied by several investigators⁽⁹⁾. Aluminide coatings, overlay coating of CoCrAlY and Y-implanted CoCrAl were used to extend the life of gas turbine components and were successful in decreasing the corrosion rate and protecting superalloys from coming in direct contact with environment, but on the contrary they increased the material cost⁽¹⁰⁾.

By controlling the various process parameters (air/fuel ratio, temperature, pressure etc.) of the boilers and gas turbines were also useful to some extent in combating the fuel oil ash corrosion. Inhibitors and fuel additives have been used with varying success to prevent oil ash corrosion. There are numerous inhibitors commercially available that are intended to reduce the severity of oil ash corrosion such as MgO, MgSO₄, CaO, MnO, Ca₂O₃, ZrO₂, Y₂O₃, In₂O₃, SnO₂, Al₂O₃, ZnO, BaO, PbO, SiO₂ etc.⁽¹¹⁾. Some oil soluble Ni, Fe and Al and other compounds have also been tried with some success. Because of its effectiveness and relatively low cost the most common fuel additives are based on MgO⁽¹¹⁾. Mg reacts with vanadium in the fuel oil and produces compounds with melting point above most metal surface temperatures. Magnesium oxide was able to reduce the rate of corrosion without forming a detectable coating. Thus hot corrosion problem of metals and alloys may be minimized to a great extent by designing a suitable industrial alloy and selecting a proper composition of protective coating, process parameters and the inhibitor as per the requirement in a given environment.

LITERATURE REVIEW

2.1 HOT CORROSION OF METALS AND ALLOYS

Hot corrosion is defined by Rapp and Zhang⁽⁵⁾ as the accelerated oxidation of materials at elevated temperatures induced by a thin film of fused salt deposit. Because of its high thermodynamic stability in the natural presence of sodium and sulphur impurities in an oxidising gas, Na_2SO_4 is often found to be dominant salt in the deposit. The source of this salt may be (1) the direct ingestion of sea salt in a marine environment, (2) the formation of Na_2SO_4 during the combustion of fuels containing sulphur and (3) the formation of Na_2SO_4 during combustion from sodium contaminated air borne dust and sulphur in the fuel. This form of attack is particularly severe in the temperature range 760-1000°C⁽⁵⁾.

Deposit modified corrosion is observed in boilers, incinerators, diesel engines, mufflers of internal combustion engines, aircraft engines, marine and industrial gas turbines⁽¹⁾.

2.1.1 Na_2SO_4 - Induced Corrosion

As pure Na_2SO_4 is often the dominant corrosive salt in the deposit, particular attention has been given to its chemistry and phase stability^(5,103). A Pourbaix-type phase stability diagram for the Na-V-S-O system at 1173 K is shown in Fig. 2.1⁽¹⁷⁾. Liquid Na_2SO_4 is stable over a wide range of the two environmental parameters by p_{O_2} and $\log a_{\text{Na}_2\text{O}}$ (or $\log p_{\text{SO}_3}$). The dotted lines superimposed on the field of Na_2SO_4 stability indicate the regimes of dominance for the minority solute species under the assumption of unit activity coefficients for these solutes.

For a melt of pure Na_2SO_4 (m.p. 884°C), there exists the equilibrium⁽¹¹¹⁾.



$$\text{with } \log a_{\text{Na}_2\text{O}} + \log p_{\text{SO}_3} = \frac{\Delta G^\circ(I)}{2.303 RT} = -16.7 (\text{at } 1200 \text{ K}) \quad (\text{ii})$$

The parameter $-\log a_{\text{Na}_2\text{O}}$ can be defined as the melt basicity, and $\log p_{\text{SO}_3}$ is referred to as the melt acidity. These parameters and the oxygen activity are more important in understanding oxide fluxing and electrochemical reactions. Fortunately, the values of melt basicity and oxygen activity can be measured by the use of high temperature electrochemical reference electrodes.

2.1.2 Fuel Oil Ash Corrosion

The accumulation of mineral ashes from residual fuel oil combustion on surfaces of various metals and alloys causes fouling and corrosion resulting from the formation of low melting aggressive compounds by the reaction between vanadium pentoxides and sodium sulphates in steam boilers and gas turbines^(12,98,117). The high temperature of the metal parts allows the oil ash to become molten, causing rapid corrosion. Corrosion occurs when the protective oxide layers (Fe_2O_3 , Cr_2O_3 , Al_2O_3) which normally form on hot metal surfaces during operation are dissolved by molten vanadate compounds, which are good oxidation catalysts and allow oxygen and other gases in the combustion atmosphere to diffuse rapidly to the metal surface^(13,116). The use of residual fuel oil in boilers and gas turbines is limited by the severe degradation of materials.

2.1.3 Hot Corrosion Mechanisms

Hot corrosion can occur by one or more of the following mechanisms as suggested by Luthra et. al.⁽⁸⁴⁾.

- (i) sulphidation - oxidation.
- (ii) formation of volatile compounds beneath the oxide film, and
- (iii) fluxing.

The initial concept of basic fluxing was first proposed by Bornstein and DeCrescente^(85,86) based on dissolution of the protective oxide scale by Na_2O , the basic minority component of pure Na_2SO_4 . Goebel and Pettit⁽⁶⁾ extended this idea to include

acidic fluxing to account for the role of certain alloying elements. According to these authors^(6,14,15), high concentrations of base resulted when the alloy reacted with Na₂SO₄ and thereby removed sulphur from the melt. Acidic conditions were produced when certain oxides (e.g. MoO₃) were introduced into the melt.

In these models rapid degradation was proposed to result from acidic or basic dissolution of protective oxide films on the surface which for most industrial alloys and coatings consist of Cr₂O₃ and/or Al₂O₃.

The next important step in the development of the fluxing model was taken by Rapp and Goto⁽⁴⁾ who proposed that, if the gradient in solubility of the protective oxide with distance into the salt layer was negative at the oxide/salt interface, accelerated attack could be sustained. This provided a quantitative expression of the earlier concepts of solubility gradients and oxide precipitation, that is, when

$$\frac{d[\text{solubility of oxide}]}{dx} \Big|_{x=0} < 0 \quad (i)$$

Oxide can dissolve at the oxide/salt interface, migrate down a concentration gradient away from that side of a region of low solubility and precipitate. At steady state, oxide dissolves and is transformed away from the oxide/salt interface, just as fast as the oxide layer grows (Fig. 2.2a,b)⁽⁴⁾. They recognized that such a gradient can be established across a thin salt film and that it need not be a consequence of the removal of sulphur from Na₂SO₄ or the introduction of acidic ions from the corrosion products as required by the Goebel and Pettit model. When Rapp-Goto criterion for the oxide solubility is satisfied, fluxing is expected.

The solubility of an oxide depends on the acidity or basicity of the melt and in some cases on p_{O_2} as well. In basic fluxing the solubility decreases with increasing p_{SO_3} (decreasing activity of O²⁻). In acidic fluxing the solubility increases with increasing p_{SO_3} (decreasing activity of O²⁻).

Rapp and Goto⁽⁴⁾ suggested that the electrochemical reduction reaction should generally be expected to create a condition of locally high basicity, because reduction reactions may generate oxide ions as reaction products. The electrochemical model for the

hot corrosion attack of a pure passivated metal is shown in Fig. 2.3⁽⁴⁾. If the salt film contains only a low concentration of transition metal ions, then the reduction of the oxidant species dissolved in the salt film must occur at the oxide/salt interface, where electrons are supplied directly from the metal oxidation reaction (Fig. 2.3a). In that case, the oxide/salt interface should be the most basic location in the salt film. Either acidic or basic solutes would be formed there, depending on the oxide solubility plot.

In Fig. 2.3b, the site for reduction of the oxidant species has been shifted to the salt/gas interface because the electronic charge is carried through the salt either by the counter diffusion of two differently charged transition metal ions or as electronic conduction in the film resulting from electron hopping between transition metal species. In this case the most basic site in the salt film should be the salt/gas interface. Thus the gradient in basicity across the salt film could be decided dominantly by the location of electrochemical reduction reaction, a generalization equally valid for the corrosion of multicomponent alloys and their impure salt films.

2.1.3.1 Type I Hot Corrosion

Stringer⁽¹⁷⁾ discussed the temperature dependence for the occurrence of hot corrosion and the corresponding corrosion morphologies and kinetics. "High Temperature Hot Corrosion" (HTHC) is normally observed in the temperature range of about 825-950°C when the condensed salt film is clearly liquid (melting point of pure Na₂SO₄ is 884°C). The typical microstructure for HTHC shows the formation of sulphides and a corresponding depletion of the reactive component in the alloy substrate. The external corrosion products frequently comprised of oxide precipitates dispersed in the salt film. The presence of a pore, crevice or crack across a protective oxide film can lead to sulphidation in the alloy substrate. This results in a significant shift in the basicity of the salt film. Once the fused salt contacts the alloy substrate, the rate and duration of the rapid corrosion kinetics is decided by the magnitude and gradient of the salt basicity relative to the local solubilities for the oxide scale phases.

2.1.3.2 Type II Hot Corrosion

The "Low Temperature Hot Corrosion" (LTHC) occurs well below the melting point of pure Na_2SO_4 . The reaction product morphology is characterized by a non-uniform attack in the form of pits, with only little sulphide formation close to the alloy/scale interface and little depletion of chromium or aluminium in the alloy substrate. Luthra and Shores⁽¹⁸⁾ studied Co-30Cr and Ni-30Cr alloys coated with pure Na_2SO_4 in $\text{O}_2/\text{SO}_2/\text{SO}_3$ gas environments. A maximum corrosion rate for Co-30Cr was found at 650-700°C with about 90% CaSO_4 in a binary CoSO_4 - Na_2SO_4 liquid phase in O_2 - 0.15% ($\text{SO}_2 + \text{SO}_3$) gas. The maximum kinetics for Ni-30Cr occurred at 700-750°C with the formation of NiSO_4 - Na_2SO_4 melt of about 45% NiSO_4 in an O_2 - 1.0 % ($\text{SO}_2 + \text{SO}_3$) gas.

Luthra and Wood⁽¹⁹⁾ have shown that binary Co-Cr coating with more than 37.5% Cr and a small reactive element addition provide excellent LTHC resistance. Similarly a diffusion coating with about 50% Cr at its outermost surface provided excellent protection for iron⁽²⁰⁾.

2.1.4 Factors Affecting Hot Corrosion

The hot corrosion degradation sequence (initiation stage to propagation stage) is not always clearly evident and the time for which protective reaction products are stable beneath the salt layer is influenced by a number of factors. Important factors are⁽²¹⁾,

- 1) Alloy Composition
- 2) Fabrication condition
- 3) Gas Composition and Velocity
- 4) Salt Composition
- 5) Salt deposition rate
- 6) Condition of salt
- 7) Temperature
- 8) Temperature cycles
- 9) Erosion
- 10) Specimen geometry

No alloy is immune to hot corrosion attack indefinitely, although there are some alloy compositions that require extremely long initiation times before the propagation stage is evident⁽²²⁾. The composition of the deposit and the rate at which it accumulates on the surfaces of alloys affects not only the time required to initiate hot corrosion attack but also the type of propagation mode that is followed. The propagation modes of hot corrosion are intimately related to the reactions between the molten deposits or moving gases and the alloys.

At low temperatures, where the salt deposit is solid, some internal sulphides may be formed but the oxide scale is compact and the rate of attack is relatively slow. The temperature of the onset of the catastrophic attack, the "threshold temperature" generally occurs near the melting point of the salt or salt mixture⁽²³⁾. The initiation of the hot corrosion attack frequently occurs at compositional inhomogeneities in alloys. Fabrication condition, extent of erosion, salt conditions and thermal stresses also affect the hot corrosion behaviour of alloys to a considerable extent.

Sulphur and vanadium affect in a significant manner. Vanadium concentration in the ppm range has been shown to increase the propensity of oxide scales on alloys to crack and spall⁽¹²⁾.

Some elements may produce deleterious effects for one propagation mode and beneficial effects for another⁽²²⁾. Cr has been shown to inhibit basic fluxing. It has also been shown to lengthen the time before alloy-induced acid fluxing is observed. Mo, W, and V inhibit basic fluxing, but their oxides are responsible for alloy-induced acid fluxing⁽²⁴⁾. Ta and Ti have been reported to produce beneficial effects on hot corrosion⁽²²⁾.

Bornstein and DeCrescente⁽²³⁾ have shown that Na_2SO_4 was consumed rapidly during the first few minutes of accelerated oxidation of B1900. After approximately 10 minutes, less than 30% of the initial Na_2SO_4 remained, after 100 min only approximately 12% was left. However, the sample continued to oxidize rapidly (wt.gain) at an undiminished rate for several hundred minutes.

2.1.5 Techniques of Hot Corrosion Tests

To study hot corrosion in the laboratory and to evaluate candidate alloys several accelerated corrosion tests have been devised⁽²³⁾. As the test more closely duplicates conditions in a turbine, the cost, complexity and exposure time are necessarily increased. In return the reliability of the data is improved.

2.1.5.1 Burner Rig Tests

The apparatus consists of a burner for liquid or gas fuels, attendant air and fuel supplies, a combustion chamber, and a specimen chamber in which the specimens may be rotated or kept stationary. Specimen shapes are often cylindrical but other configurations have also been used. A contaminant, such as sea water, may be injected into the combustion chamber or it may be mixed with the fuel.

The extent of corrosion may be assessed by several different kind of measurements, but the two frequently used are wt. loss after descaling and penetration depth of the reaction products. Burner rig conditions are usually much more severe than service exposure. The burner rig tests are adequate for ranking alloys and their value for predicting lives in specific applications⁽²¹⁾.

2.1.5.2 Tests in Industrial Atmosphere

The pressurized burner rig provides the closest simulation of turbine operating conditions by allowing control of gas pressures and velocity as well as gas composition and temperature⁽²³⁾.

2.1.5.3 Laboratory Tube Furnace Tests

There are a variety of tube furnace tests that have been used to study hot corrosion. The simplest is to coat the specimen with the desired deposit and then to expose it to a controlled gas mixture or air at a specific temperature⁽²¹⁾. Deposits are applied by spraying warm (~100°C) test coupons with solutions containing the compound of interest. Continuous weight change vs time measurements can be recorded to attempt to define the

hot corrosion kinetics. Detailed metallographic analyses of the exposed specimens are usually necessary.

In some such tests the specimens are removed periodically from the hot zone of the furnace in an attempt to induce cracking and spalling of the the oxide scales. However, substantially different results can be obtained for the hot corrosion of alloy even where the only variable is the thickness of the molten deposit covering their surfaces⁽²¹⁾.

2.1.5.4 Crucible Test

In the crucible test a specimen is completely or partially submerged in a container of fused salt, such as Na_2SO_4 , NaCl , $\text{Na}_2\text{SO}_4\text{-V}_2\text{O}_5$ mixtures at an elevated temperature. Gases may be bubbled through the melt or passed over it to provide oxidizing or reducing environments. Further variations may include alternatively dipping and removing the specimens from the melt. Because of its simplicity and rapid attack, the crucible test has found use for screening a series of candidate alloys or for assessing the effectiveness of corrosion inhibitors⁽²³⁾.

2.1.5.5 Electrochemical Tests

In electrochemical tests, samples are exposed to an environment similar to that of the crucible test. The experimental arrangement involves an electrochemical cell comprised of a fused salt as the electrolyte, a reference electrode, a working electrode and perhaps auxiliary electrodes. The purpose of the experiment may be either to investigate the properties of the salt mixture or to determine the corrosion resistance of the specimen. In this measurement, a reliable reference electrode is essential. For the temperature of preliminary screening of a series of candidate alloys, a useful empirical correlation may be established between cell voltage and the resistance to corrosion. Polarization techniques are being used for the study of the hot corrosion resistance of superalloys⁽²³⁾.

2.1.5.6 Accelerated Oxidation (Wt. Change) Tests

In this test a thin sheet specimen is sprayed with an aqueous salt solution, dried and then suspended in a resistance heated furnace in flowing air or oxygen. The weight gain or loss of the specimen is monitored for times ranging from several hours to a few hundred hours. For alloys susceptible to hot corrosion, the initial weight of salt and the rate of increase is much greater than for simple oxidation⁽²³⁾.

2.2 HOT CORROSION OF IRON AND IRON-BASE ALLOYS

2.2.1 Hot Corrosion of Iron

Gesmundo and Viani⁽²⁵⁾ studied the mechanism of LTHC of pure iron in simulated combustion gases containing SO_3 at 600-800°C. The accelerated reaction has been attributed to the formation of a liquid salt solution with the production of duplex scales composed of a mixture of metal oxide and sulphide. The sulphide formation was limited to the inner scale. This has been ascribed to a relatively small difference between the diffusivities of the metal in its oxide and in the corresponding sulphide.

The accelerated oxidation of pure iron beneath Na_2SO_4 deposits in O_2 -rich atmospheres containing SO_2 - SO_3 at 650-750°C was believed by Shi et. al.⁽²⁶⁾ to be induced by the formation of eutectic melt of Na_2SO_4 -iron sulphate. The direct growth of oxide was reported to predominate although fluxing contributed a little to the corrosion.

The Na_2SO_4 -induced corrosion of pure iron has been studied by Buscaglia et. al.⁽²⁷⁾ between 600 and 800°C in SO_3 - SO_2 - O_2 mixed atmospheres. Accelerated phenomenon observed has been attributed to the formation of a liquid sulphate phase from the initial solid Na_2SO_4 deposit. First, a liquid phase was believed to be formed from pure solid Na_2SO_4 layer, then accelerated oxidation continued by inward diffusion of SO_3 and outward diffusion of iron through the molten salt. At the beginning, the oxidising species in the gas phase diffused through the solid salt layer and reached the metal surface where the formation of solid scale took place. At the same time, the formation of FeSO_4 in solution with Na_2SO_4 occurred. The salt mixture, which was initially solid, became liquid when the iron sulphate concentration reached a critical value. Once the salt layer was completely liquid, SO_3 migrated inward from the gas/salt interface.

Trafford and Whittle⁽⁸²⁾ observed that pure iron did not undergo accelerated oxidation in the presence of Na_2SO_4 at 1 atmosphere of oxygen at 900°C . This was attributed to the thickening of the scale too rapidly for sulphur to penetrate the oxide and interact directly with the metal.

2.2.2 Hot Corrosion of Iron-base Alloys

The corrosion in combustion gases of two commercial ferritic steels designated A213-T22 and H7-91 having respectively the composition (wt. %): Cr 2.09, Mo:0.93, Mn:0.57, Si:0.135, C:0.135, Fe:balance and Cr:11.35, Mo:1.07, Ni:0.68, Mn:0.57, Si:0.48, C:0.204, Fe:balance used in the construction of parts of industrial boilers had been studied by Gesmundo and Nanni⁽²⁸⁾ at $600\text{-}800^\circ\text{C}$ in the presence of deposits of pure Na_2SO_4 . It was concluded that the presence of liquid layer produced metal sulphides in the inner-scale region and partial scale dissolution in the salt. Precipitation of solid particles in the liquid formed a porous non protective scale. A maximum reaction rate was observed at 750°C . At least 10% Cr was required to reduce the reaction rate above 750°C .

Ferritic steels containing Cr, Al and Ti have been studied by Coze et. al.⁽²⁹⁾ in a fused salt mixture containing Na_2SO_4 at 527°C and gas mixture containing CO , CO_2 , CH_4 , H_2 , H_2O and H_2S at 600°C . The presence of Ti with 12% Cr and 3% Al was believed to increase the proportion of Fe which diffused to the outer layer of the scale. Consequently, the concentrations of the protective elements were raised in the inner oxide. The excellent behaviour of these steels above 600°C was explained by the increase of Al diffusion coefficient with temperature. A protective barrier of alumina, whose properties were improved by the presence of Ti, can thus form more readily.

As observed by Gesmundo et. al.⁽²⁸⁾, the presence of ferritic steels accelerated the corrosion rate in combustion gas at 800°C . This effect is related to the formation of a liquid layer by dissolution of metal sulphates in Na_2SO_4 , which would otherwise be solid if pure. The presence of the liquid layer led to the formation of metal sulphides in the inner-scale region and partial scale dissolution in the salt. Precipitation of solid particles in the liquid results in a porous non protective scale.

Paul and Seeley⁽³⁰⁾ reviewed oil ash corrosion of utility boilers and concluded that fuel chemistry, boiler operation and boiler design influenced oil ash corrosion. V in fuels reacted with Na, S and Cl during combustion to produce low melting point ash compositions, which accelerated tube wastage. Ferritic materials were more resistant to oil ash corrosion than Ni-containing austenitic materials for tubing purposes. High Cr coatings were suggested to resist oil ash corrosion.

Na_2SO_4 deposits greatly accelerated the oxidation of Fe-Al alloys in oxygen-rich atmospheres containing SO_2 - SO_3 at 650 to 700⁰C. It is reported by Shi et. al.⁽²⁶⁾ that fluxing proceeded at a considerable rate in the early stages due to the low oxygen pressure at the oxide/melt interface. Reaction of SO_3 released SO_2 which caused the formation of sulphides in the scale. Sulphides were supposed to contribute considerably to the acceleration due to their high defect concentration.

Malik et. al.⁽³¹⁾ studied the high temperature oxidation behaviour of 18:8 austenitic steel in the presence of Na_2SO_4 , NiSO_4 , CoSO_4 , $\text{Cr}_2(\text{SO}_4)_3$ in the temperature range of 923 - 1273K in air. They have concluded that the higher oxidation rates for this salt mixture coated steel at 923K in comparison with the corresponding Na_2SO_4 coated steel have been attributed to the formation of low temperature eutectics. The presence of Na_2WO_4 , $(\text{NH}_4)_2\text{MoO}_4$ or NaVO_3 was always detrimental to the oxidation resistance of steel specially in the temperature range 1123 - 1273K which has been attributed to the decomposition of these salts into volatile compounds. Austenitic Fe-based alloys AISI310 and alloy 800H formed protective Cr_2O_3 oxide scales when oxidised in air.⁽³²⁾

The corrosion of commercial steels SS 110, AISI 303 and 18 Cr - 8 Ni has been studied by Malik et. al.⁽³³⁾ in the temperature range of 650 - 1000⁰C in the presence of ash residues obtained from coals of Indian origin. The ash was non-aggressive at low temperatures of 650 and 850⁰C due to their inability to form alkali trisulphates. At temperatures of 900 and 1000⁰C the coal ash showed corrosivity as a result of combined sulphidation and molten alkali sulphate attack. The high ash with higher SiO_2 content was invariably more aggressive than the low ash, which contained more silicate.

The hot corrosion test of AISI 304 has been carried out by Misbahul Amin⁽³⁴⁾ to examine the influence of eutectic and solid phases present in the $\text{Na}_2\text{SO}_4 + \text{Fe}(\text{SO}_4)_3$

systems. The inner layers of the scales contained Cr_2S_3 followed by a thick but discontinuous layer of FeS . The middle layer forming bulk of the scale seemed to contain Na_2CrO_4 , NaFeO_4 and NaNiO_4 while the outer layer composed of Fe_2O_3 . The cracking of the scale has been attributed to these fluxing products and to the evolution of gases.

Grabke et. al.⁽³⁵⁾ carried out studies on the oxidation of a low alloy steel at 500°C and high alloy steel at 600 and 700°C in which fly ash was deposited on the scale of the steels after 24h of preoxidation. The chlorides reacted with the scale forming $\text{FeCl}_2(\text{s})$ at the scale/metal interface, evaporation of $\text{FeCl}_2(\text{g})$ and its oxidation to Fe_2O_3 at the scale surface, chlorine partially returning to the scale. This according to them resulted in porous unprotective scale and active oxidation.

Rapp⁽⁹⁶⁾ has studied about the chemistry and electrochemistry of the hot corrosion of metals under Na_2SO_4 and suggested that for a given application a suitable alloy be chosen so that it readily forms a simple protective scale having a low solubility in the salt environment and the protective scale should involve a minimum number of components. It was concluded that basic salts like MgO can be introduced as an inhibiting component if liquid salt condensates.

Pettit and Meier⁽⁹⁹⁾ studied Fe-, Ni- and Co-base superalloys with combustion gases and Na_2SO_4 . They observed that Mo delayed the initiation of hot corrosion attack because the formation of MoO_3 inhibited the formation of oxide ions in the melt. Ta did not produce deleterious effect, due to the formation of high melting sodium tantalate by avoiding sodium molybdate formation. Nb adversely affected hot corrosion resistance but enough data is not available for its reasoning. W, Mo and V are also harmful as their oxides induced acidic fluxing. Carbon is undesirable as carbide phases were sites for initiation of hot corrosion. Mn, Si, B and Zr increase superalloy corrosion resistance. Cr and Al produced beneficial effects by formation of protective oxides on alloy surfaces.

Rapp et. al.⁽¹⁰¹⁾ have also reviewed the high temperature corrosion in energy systems. It has been found that S forms Na_2SO_4 vapours which condense on superheater tubes and reheater tubes in the boiler. Corrosion is attributed to fluxing action of the molten deposits on the oxide scales. They have suggested the need to establish the corrosion rates of alloys over a wide range of gaseous environment, to determine the

reaction mechanisms and to characterize completely the reaction products using the wide range of modern analytical techniques now available. Stroosnijder and Quadackers⁽¹⁰²⁾ in their review of high temperature corrosion on Fe-, Ni- and Co- base alloys in SO₂, SO₃, O₂ atmospheres have also recommended the use of thermodynamic stability diagram to determine which reaction product is stable if equilibrium has been established. The lowest sulphur pressure required to form FeS is $p_{S_2} = 2.25 \times 10^{-11}$ atmosphere whereas oxygen pressure $p_{O_2} = 4.49 \times 10^{-13}$ atmosphere. The condition for S diffusion across the oxide layer is $p_{S_2}(\text{gas/MO}) > p_{S_2}(\text{MO/M})$. S transport through oxide may result in sulphide formation at the scale/metal interface or within the oxide.

Fairman⁽¹⁰⁵⁾ has studied some metal specimens in an ash mixture (V₂O₅ + 10% Na₂SO₄) environment in air. He has observed that attack was greatest where the concentration of O₂ and V₂O₅ were greatest suggesting the transfer of oxygen atoms or ions by the pentoxide to the metal surface. Accelerated oxidation is a diffusion controlled process of the incorporation of defects into the oxide scale. Slagging action of low melting point oxides constantly exposed fresh metal to the atmosphere⁽¹¹²⁾. If this mechanism is valid, V₂O₅ has no effect when ash is molten. The mechanism of accelerated attack is most satisfactorily explained by the catalytic action of V₂O₅ operating with an increase in the defect concentration of the scale, Kerby and Wilson⁽¹⁰⁶⁾ have suggested that liquid vanadates have shown to increase the corrosion rate of metals by fluxing or adhering the normally protective oxide layers present on the surface of the alloys and by providing a source of oxide ion for the corrosion reaction. The electrical conductivity increased with increase in temperature and with decreasing oxygen pressure. Incorporation of sodium into the V₂O₅ lattice structure caused a reduction in the valency of the vanadium atoms from V⁵⁺ to V⁴⁺ due to donation of the alkali metal valence electron to a vanadium atom.

AISI 446 stainless steel when studied by Dooley et. al. under V₂O₅, Na₂ 0.6 V₂O₅ environment in the temperature range 700-900⁰C in air, it was found that the oxide scale was mainly Cr₂O₃ with some vanadium oxide and were moderate barrier to corrosion. Above 850⁰C, breakaway corrosion reaction occurred. No Cr₂O₃ oxide barrier was there but it was a continuous oxide of Cr₂O₃, Fe₂O₃, V₂O₅ at the metal/oxide interface. The

addition of Na_2O to V_2O_5 increased the oxide ion (O^{2-}) content of the melt and made it more aggressive to acidic oxides such as Cr_2O_3 .

Sachs ⁽¹¹⁰⁾ studied accelerated high temperature corrosion of steels and stainless steels in V_2O_5 environment. They reported that oxidation of pure Cr in V_2O_5 occurs with a very rapid diffusion rate and so only the initial stages of the curve were proposed to be more important. Later slowing down of the oxidation rate was attributed mainly to the effect of scale thickening. Loose and spongy appearance of the scale was observed. At the beginning of the process V_2O_5 was present in excess and dissolved the products of oxidation. According to them at some point the liquid was saturated with the oxide and which would get precipitated. The presence of various phases in a thin layer of scale would impose such severe strain on the film that cracking and exfoliation could be expected. This would permit liquid phase to reach the metal surface again and the conditions to form a spongy scale were seen to prevail. This mechanism would apply only to iron alloys which are susceptible to catastrophic corrosion.

Thilkan et. al. ⁽¹¹⁴⁾ studied hot corrosion of nickel free stainless steel, Cr-Ni stainless steel with Na_2SO_4 - V_2O_5 salt mixture environment. It is stated that saturated solution was used as the liquid medium because of its low gas solubility, vapour pressure and viscosity. Threshold is found to lie between 700 - 800°C . Above the threshold temperature the extent of attack initially increased but with increasing temperature either it became constant or decreased. Increasing amount of Na_2SO_4 in mixtures with V_2O_5 first increased and then decreased the amount of oxidation at the temperature of 820 - 870°C . At 950°C all Na_2SO_4 additions decreased the corrosive effect of V_2O_5 . Fluidity of slag was important in allowing diffusion. Increase in fluidity might have a marked effect in increasing the attack. Short term tests were carried out to get an idea of the comparative behaviour of different alloys specially during the initial stages of corrosion. CaO and MgO additives were found to give best results in improving corrosion resistance. Nickel free stainless steel offered a better corrosion resistance. However, Tiwari et. al. ⁽¹⁰⁰⁾ have shown that 32% of Ni containing Fe-base superalloy offered good corrosion resistance in Na_2SO_4 , Na_2SO_4 -15% V_2O_5 at 700 - 900°C .

The scaling behaviour of Fe-25Cr, Co-25Cr and Ni-25Cr were investigated by Upadhyaya and Strafford⁽¹¹³⁾ under $O_2:SO_2 = 4 : 1$ atmosphere at $700^\circ C$ at 1 atmosphere pressure and concluded that Fe-25Cr alloy exhibited superior corrosion properties over the extended exposure periods upto 200 hrs over Co-25Cr and Ni-25Cr. This was attributed to the inhibition of internal sulphide formation by the more rapid and earlier growth of a protective Cr-rich oxide scale on this alloy. This alloy appeared to be the best coating material, especially at lower temperatures $< 750^\circ C$.

2.3 HOT CORROSION OF NICKEL AND NICKEL-BASE ALLOYS

2.3.1 Hot Corrosion of Pure Nickel

Corrosion behaviour of pure nickel has been investigated by Motihara et. al.⁽³⁶⁾ in molten Na_2SO_4 at $900^\circ C$ under $SO_3 + SO_2 + O_2$ gas mixture as well as impure SO_2 and O_2 atmospheres. The corrosion loss in mixed atmosphere containing SO_3 is reported to be larger than those observed in pure SO_2 and O_2 atmospheres. The corrosion loss was found to correspond to the thickness of the oxide layers. High corrosion losses have been attributed to the fact that SO_3 strongly acts as an oxidizing agent for the corrosion process.

Goebel and Pettit⁽³⁷⁾ studied the hot corrosion of pure nickel with Na_2SO_4 coating. Sulphur reportedly penetrated through the oxide from the Na_2SO_4 forming nickel sulphide immediately below the oxide. It is contemplated that the removal of sulphur has the effect of displacing the stoichiometry of the sulphate to the Na_2O -rich side (it becomes basic) and the oxide ion activity rises. Eventually, it rose high enough to oxidize the NiO to nickelate, NiO_2^{2-} , which was soluble in the salt and migrated to the salt/air interface where the salt was more nearly stoichiometric and the oxygen ion activity was lower. Further, NiO reprecipitated forming a porous non protective oxide layer.

Arbab and Shatynski⁽³⁸⁾ have studied the hot corrosion of pure nickel in Na_2SO_4 - $CaSO_4$ salt mixtures at $900^\circ C$ in purified oxygen. For salt mixtures containing 80% or more of $CaSO_4$, the sulphide layer was found to be virtually absent and sulphide particles were dispersed in the oxide layer. The authors concluded that the sulphur diffusing through the initial oxide was totally consumed by nickel sulphide (Ni_3S_2) formation within the oxide layer and did not reach the Ni-NiO interface. Giggins and Pettit⁽¹¹⁸⁾ have

pointed out that the initial formation of Ni_3S_2 in the oxide layer, probably created an easy path for sulphur diffusion. Fast attack was observed for pure Na_2SO_4 and for Na_2SO_4 -50% CaSO_4 wherein the deposit or a portion of it melted.

Mishra⁽¹¹⁹⁾ studied the corrosion of Ni at 750°C in the presence of sulphate mixtures (Na_2SO_4 - Li_2SO_4 and Na_2SO_4 - CaSO_4) in an atmosphere of $\text{O}_2 + 0.12\%\text{SO}_2$. The corrosion product consisted of a thick layer of metal oxide and metal sulphide.

Hot corrosion studies on pure Ni was made by Sidky and Hocking⁽³⁹⁾ in melts of Na_2SO_4 , NaVO_3 and mixture thereof at temperatures ranging from 680 to 900°C by electrochemical measurements using X-ray diffractometer. Potentiodynamic polarization plots in Na_2SO_4 , NaVO_3 , Na_2SO_4 -5% NaVO_3 melt at 900°C was drawn and they concluded that Ni behaved relatively better than the Ni-Cr alloy due to its neutral or beneficial characteristics.

The effects of chromate and vanadate anions on the hot corrosion of Ni by a thin fused Na_2SO_4 film in an SO_2 - O_2 gas atmosphere at 900°C were investigated by Otsuka and Rapp⁽⁴⁰⁾. Their results show that the inhibition of sulphidation may result from the precipitation of solid Cr_2O_3 from the melt and thereby partially sealing/plugging the crack defects and grain boundaries of the original protective oxide layer. It is proposed that vanadate anions enhanced the onset of the hot corrosion and sulphidation probably via rapid dissolution of the protective oxide scale at cracks/defects or grain boundaries.

2.3.2 Hot Corrosion of Nickel-base Alloys

2.3.2.1 Hot Corrosion in Na_2SO_4

Investigations have been made to study the effect of NiSO_4 - Na_2SO_4 ⁽⁴¹⁾ on hot corrosion of Nickel-200, Rene-80 and CoCrAlY coating at 750°C. Little corrosion was reported when solid solution mixed sulphates formed on the metal surface, but severe corrosion occurred when molten sulphates were formed. In nickel-200, corrosion was found to proceed by liquid Ni_3S_2 -Ni formation below the surface oxide. No discernible sulphide was produced with Rene-80 and CoCrAlY which gave the characteristic LTHC morphology.

The aluminide and Cr-Al diffusion coatings on Ni and Ni-base alloy EI 867 have been studied by Godlewski et. al.⁽⁴²⁾ in the presence of pure Na₂SO₄. It is observed that the low alloyed aluminide and Cr-Al coatings showed very poor resistance to oxidation. After 24 hrs, these had been almost completely removed. Modification of highly alloyed aluminide coatings with Cr resulted in uniform and relatively slow degradation of the coating. Cr enriched zone is supposed to act as a barrier to the oxidation of refractory metals such as Mo, W and V thus preventing the onset of catastrophic corrosion.

Levy and Pettit⁽⁴³⁾ studied cyclic hot corrosion of Ni-base superalloys at 704 and 900°C beneath Na₂SO₄ in air. Alloys contained Cr, Co, W, Ta, Ti, Al and Mo. The alloys showed high wt. loss at 900°C. Thick corrosion products formed on the alloys were stated to be composed of oxides near the gas interface and of sulphides adjacent to the unaffected substrate. The hot corrosion microstructures typical of those observed on structural alloys under Na₂SO₄-induced attack have been reported. At 704°C more severe attack was reported when 45 mole% MgSO₄ was added to Na₂SO₄. Addition of SO₃ to gas mixture containing oxygen at 704°C caused severe corrosion of many alloys. It is stated that in the case of hot corrosion resistant coatings, the composition of the gas is critical, and SO₃ is required for the attack to occur. In the case of Ni-base superalloys the presence of refractory metal oxides must be a sufficient condition to cause severe attack even in the absence of SO₃.

The hot corrosion resistance of two directionally solidified alloys Ni-23.1 Nb-4.4Al and Ni-19.7Nb-6.0Cr-2.5Al has been studied by Johnson et. al.⁽⁴⁴⁾ using Na₂SO₄ coating and Dean rig test in which the salt was evaporated into the gas stream and allowed to condense continuously on the specimen. These alloys were reported to be generally quite resistant to Na₂SO₄-induced corrosion at 900°C. Below the outer layer, mainly of NiNb₂O₆, high proportion of Al₂O₃ is believed to be present. Internal oxidation of the metal producing Al₂O₃ and Cr₂O₃ is believed to occur before the development of external Al₂O₃ layer. In some isolated regions the alloy was found to be much more severely attacked. The pit contained NiNb₂O₆, NbCrO₄ and Ni. At higher temperatures more uniform corrosion is reported. At 1100°C the outer layer was mainly NiCr₂O₄, while beneath it a layer of Cr₂O₃ containing particles of NbCrO₄ was observed. Internal oxides

were largely Al_2O_3 and there were massive sulphides ahead of the oxidation front. The large sulphides near the oxidation front appeared to be Ni-rich. In the Dean rig test it was shown that NaCl addition greatly increased the severity of attack.

Fryburg et. al.⁽⁴⁵⁾ conducted a detailed study of the initiation of hot corrosion on two preoxidised Al_2O_3 forming Ni-base superalloys, B-1900 and NASA-TRW IVA. The tests were carried out at 900°C in pure O_2 with Na_2SO_4 salt deposit. After an induction period of little corrosion, local basic fluxing attack of the $\text{Cr}_2\text{O}_3/\text{Al}_2\text{O}_3$ scale spreaded to cover the surface and generated catastrophic linear kinetics. It is proposed that at the initiation stage, a decrease in sulphate ions correlated to increase in the H_2O -soluble Cr and Al solutes. During the catastrophic attack of B-1900, the sulphate ions reacted to release SO_2 and formed sulphides in the alloy and the salt was converted to Na_2MoO_4 . The self sustaining feature was a consequence of the cyclic nature of the acidic fluxing.

Fryburg et. al.⁽⁴⁶⁾ conducted a similar study of hot corrosion for the preoxidised $\text{Cr}_2\text{O}_3 + \text{TiO}_2$ forming alloy IN738 at 975°C in oxygen also. During an induction period of 55 hrs first Cr_2O_3 and then TiO_2 were dissolved as basic solutes in Na_2SO_4 . Thereafter the oxidation of Mo and W formed liquid $\text{Na}_2(\text{MoO}_4, \text{WO}_4)$, which served as a flux for the acidic dissolution of Cr_2O_3 and Al_2O_3 . The beneficial effect of Ta with respect to hot corrosion attack is explained by them⁽⁴⁷⁾ on the basis of the ability of the Ta_2O_5 to tie up the Na_2O and prevent the formation of a molten Na_2MoO_4 phase as the ΔG for the formation of NaTaO_3 is more negative than the formation of Na_2MoO_4 .

Shores and Luthra⁽⁵⁴⁾ have studied the Na_2SO_4 induced corrosion by accelerated oxidation tests on Ni-base alloys in the temperature range of $700\text{-}850^\circ\text{C}$ in varying concentrations of SO_3 . Rapid degradation was reported to result from the formation of low melting sulphate mixtures on the surface.

Addition of 1% PbO to Na_2SO_4 resulted in large increase in the rate of hot corrosion of Ni-Cr alloys at 900°C . This effect observed by Chatterji et. al.⁽⁴⁸⁾ was ascribed to the formation of PbCrO_4 which was soluble in molten Na_2SO_4 and became more significant with increasing Cr content in the alloy. Catastrophic corrosion resulted with alloys containing 10-15% Cr. The Na_2SO_4 induced hot corrosion of Ni-30Al was

also enhanced by the addition of PbO to the salt. This is attributed to the formation of a soluble complex $\text{PbO} \cdot \text{Al}_2\text{O}_3$.

Hot corrosion behaviour of some Ni base alloys has been studied by Malik et. al. ^(49,50) in the presence of Na_2SO_4 and have concluded that Na_2SO_4 -induced corrosion proceeded by fluxing and sulphidation reactions. Lower oxidation rates observed upto 800°C has been attributed to a scale morphology consisting of inner scale of Cr_2O_3 acting as a protective oxide film. External scales of $\text{NiO} \cdot \text{Cr}_2\text{O}_3$, CoO or NiO present at the scale surface formed a protective oxide layer at lower temperature (800°C), whereas mixed oxide layer $\text{Cr}_2\text{O}_3 \cdot \text{NiO}$ or $\text{CoO} \cdot \text{NiO}$ formed at higher temperature (1000°C).

Alloys with high concentration of Cr have good resistance to hot corrosion attack by Na_2SO_4 resulting from the formation of a protective Cr_2O_3 scale in oxidizing atmospheres at high temperatures was observed by Zhang ⁽⁵¹⁾. The Cr_2O_3 scale, however, had been observed to react with Na_2SO_4 and water soluble chromium was detected in the hot corrosion products of Cr bearing alloys. He had also measured the solubilities of Cr_2O_3 in fused Na_2SO_4 as a function of the melt basicity and had observed that Cr_2O_3 was stable in Na_2SO_4 .

Hot corrosion studies were carried out by Sidky and Hocking ^(52,53) on IN 738 superalloy, Ni-20Cr, Ni-20Cr-3Al and Ni-20Cr-4Mo in SO_2 / O_2 atmosphere at 700 and 900°C . They have concluded that Al improved the corrosion resistance at 700°C . Mo had a detrimental effect on the corrosion rate due to the volatile MoO_3 . At 900°C IN 738 and at 700°C Ni-20Cr-3Al proved to be the best. They proposed a stage-by-stage mechanism of corrosion. In the first stage, initial oxide layer was built up immediately, in the second stage external oxide layers and sulphide areas were built up whereas in the third stage, internal sulphide structure was developed.

Na_2SO_4 -induced hot corrosion of B-1900 was studied by Bornstein and DeCrescente ^(14,15). Based on their observations they concluded that Na_2SO_4 interacts with the alloy to form sodium and sulphur compounds. Rapid removal of sulphur from the Na_2SO_4 by unretarded diffusion of sulphur and precipitation of Cr-rich sulphide phases promoted the formation of Na_2O . In any case, the catastrophic oxidation observed during sulphidation was due to interactions between Na_2O and the substrate.

The kinetics of Na_2SO_4 -induced corrosion were measured by Shores and Luthra^(18,54) by accelerated oxidation tests on Ni-30Cr as a function of temperature between 600-900°C. The rapid rate of attack is explained on the basis of sulfation of the transient surface oxides (Ni or Co oxides) and the dissolution of these transition metal sulphates into Na_2SO_4 to yield a liquid phase. This retarded the formation of a protective Cr_2O_3 scale. Thermodynamic calculations showed that Na_2SO_4 - CoSO_4 and Na_2SO_4 - NiSO_4 liquids could be formed at moderate SO_3 levels in the gas.

The interactions of different metal oxides such as Co_3O_4 , NiO , Al_2O_3 , Cr_2O_3 , Fe_2O_3 and SiO_2 with Na_2SO_4 at a temperature of 1100 and 1200 K in flowing oxygen has been studied by Mobin et. al.⁽⁵⁵⁾. They have inferred from their results that the high temperature reaction products usually contained a three phase structure namely $\text{Na}_2\text{O} \cdot \text{M}_2\text{O}_2 \cdot \text{M}_2\text{O}_x$ and metal sulphide and/or metal sulphate. They proposed that the formation of $\text{Na}_2\text{O} \cdot \text{M}_2\text{O}_x$ depended upon the solid state solubility of metal oxide in the molten salt at high temperatures. Under limited solubility conditions $\text{Na}_2\text{O} \cdot \text{M}_2\text{O}_x$ was invariably formed, but as soon as this condition was relaxed the oxide M_2O_x precipitation occurred and formed a separate phase. From the wt. loss vs mole fraction of Na_2SO_4 plots they have inferred that a decrease in wt. loss value with increasing Na_2SO_4 concentration was because of the binding of sulphur in the form of metal sulphide or metal sulphate. Further increase in the wt. loss value with increasing concentration of Na_2SO_4 was because of the release of SO_2/SO_3 (g) and volatility of reaction products in certain cases.

Peters et. al.⁽⁹³⁾ have studied Nimonic 105 alloy with Na_2SO_4 coating for 24 hr at 900°C and have concluded that the greater the Cr content, the greater is the resistance to hot corrosion. For the complex alloys acid fluxing seemed to be a more probable process than basic fluxing although basic fluxing cannot be dismissed. The breakaway to catastrophic attack was clearly related to Mo content. MoO_3 was transferred to vapour phase. The role of sulphur in the breakdown process was probably only secondary, it entered the alloy only as a consequence of the breakdown. Above 3-4% Mo catastrophic attack was encountered.

Stewart and Shatynski⁽⁹⁵⁾ have studied B-1900 superalloy under 10% Na_2SO_4 -90% CaSO_4 mixture deposit at 900°C in air for 6, 12 and 24 h of exposure. It was

concluded that the addition of CaSO_4 was shown to reduce dramatically the magnitude of Na_2SO_4 -induced hot corrosion of the alloy at 900°C . Trace quantity of PbO impurity in coal caused catastrophic corrosion.

The aluminide and Cr-Al diffusion coatings on Ni and the nickel based alloy EI 867 (8.5 Cr, 4.2 Al, 4.3 W, 9 Mo, 4 Co, bal Ni) obtained by pack cementation technique were subjected to various corrosion tests consisting of oxidation under thermal cycling conditions as well as isothermal oxidation in the presence of fused Na_2SO_4 ⁽⁴²⁾. It was found by them that the oxide scale on the Cr-Al coating adhered well to the substrate whereas that on the aluminide coating spalled off. They observed that Cr had advantageous effect in the improvement of oxidation resistance of Ni based alloys in the presence of Na_2SO_4 .

2.3.2.2 Hot Corrosion in Na_2SO_4 - V_2O_5

Pantony and Vasu⁽¹²⁰⁾ have explained the process of the fire side corrosion of boilers and gas turbines in the presence of vanadium pentoxide with the help of a schematic diagram (Fig. 2.4)⁽¹²⁰⁾. They divided the process into six stages, any of which can be a rate-controlling. In the system, stages 1, 2 and 6 would be governed by the physical properties of the melt while stage 4 would be controlled by the physical nature and impurities of the metal surface. They mentioned that if any of the stages 1, 2, 3, 5 or 6 were rate-controlling the process was likely to be diffusion controlled with relatively low activation energy while if stage 4 was rate-controlling then the whole process would be activation controlled with a high activation energy. They⁽¹²¹⁾ further mentioned that the vanadic corrosion could be viewed as a two stage diffusion process, viz an inward diffusion of oxygen and an outward diffusion of the corrosion products away from the surface. Kofstad⁽¹²²⁾ has explained these diffusion processes with the help of neat sketches shown in Fig. 2.5⁽¹²²⁾ which illustrates the growth of chromia scales in the presence or absence of oxygen active elements.

A 50Cr-50Ni commercial alloy had been corroded in pure V_2O_5 and in vanadate melts containing sodium sulphate and chloride in the temperature range 750 to 950°C in a rotating disc apparatus by Dooley et. al.⁽¹²³⁾. They concluded that Cr_2O_3 scale formed on

the alloy which dissolved only slowly into the liquid melt and was thus observed as a barrier layer. They did not observe this layer in vanadates. A marked internal oxidation of the Cr-rich α -phase occurred in chloride containing melts throughout the temperature range 750-950°C.

A standard NiCrAlY and a silicon enriched alloys were studied by Lambert et. al.⁽⁵⁶⁾ to investigate the effects of Si addition on their oxidation and hot corrosion behaviour in $\text{Na}_2\text{SO}_4\text{-V}_2\text{O}_5$ environment. The chemical composition (wt%) of these alloys were Ni-17Cr-6Al-0.5Y and Ni-16Cr-5.7Al-0.47Y-5Si. They observed an outer layer of NiO developed on the surface of the standard alloy whereas a thin Al_2O_3 scale formed on the Si enriched alloy. Hot corrosion testing was carried out at 700°C on specimens that were plasma spray coated with a corrosive mixture of Na_2SO_4 -10 wt% V_2O_5 . According to them, the development of protective oxide barrier was considerably affected by the corrosive coating, particularly in the Si enriched alloy. Ni, Cr, Al oxides were detected in the inner layer.

Phase equilibria in the $\text{Na}_2\text{O-V}_2\text{O}_5\text{-SO}_3$ system (Fig. 2.6)⁽⁵⁷⁾ has been studied by Krasilnikov et. al.⁽⁵⁷⁾ using XRD and they inferred that the mixture of sodium sulphates with V_2O_5 have considerably higher melting points with lower thermal stability and they lose SO_3 . Spontaneous reduction of V_2O_5 on heating occurs leading to the formation of sodium vanadate.

Otero et. al.⁽⁵⁸⁾ studied the morphological characteristics and chemical composition of corrosion products produced on IN657 (46.5 Cr, 1.32 Nb, bal-Ni) alloy when operated in oxidizing atmosphere together with molten phases formed of 60:40 V_2O_5 : Na_2SO_4 (mol%) mixture at 908 K using $\text{Na}_2\text{SO}_4\text{-V}_2\text{O}_5$ phase diagram (Fig. 2.7)⁽⁵⁸⁾. It was observed that the oxidation products were basically formed of chromium oxides. The corrosion products had three structures,

- (i) Radial growth of sulphur rich particles dispersed into matrix.
- (ii) The acicular shaped vanadium rich phase, and
- (iii) Idiomorphic Cr rich crystals which were formed from Cr of surface metal.

They concluded that the substrate is depleted of Cr near to surface of alloy

and with the increase in exposure time from 6 to 48 hrs there was a tendency of particles to take rounded shapes.

Using polarization resistance method Otero et. al. ⁽⁵⁹⁾ studied hot corrosion behaviour of IN657 in 60%V₂O₅-40% Na₂SO₄. They observed that for duration less than 100h the corrosion kinetics increased with temperature when the temperature was less than 1000K. For temperatures > 1000K, a decrease in corrosion rate was observed. Increase in corrosion rate was related to the higher fluidity of the molten salt mixture. Once the appropriate fluidity was achieved, corrosion rate decreased due to the decrease in the oxygen solubility in the molten salt and oxygen being one of the oxidizing agents. They⁽⁶⁰⁾ compared the gravimetric method with electrochemical data also and confirmed that the hot corrosion in molten salts is an electrochemical process.

Laser glazing of gas flame sprayed NiCrAl, FeNiCrAl and NiCr alloys had a new surface composition and morphology. Hot corrosion tests by Longa et. al.⁽⁶¹⁾ in a mixed salt of 15% Na₂SO₄-V₂O₅ at 900°C have shown that the modified coating offered excellent corrosion resistance compared to the as sprayed coating because after laser modification the coatings achieved a more dense and homogenous structure without pores which supported the formation of continuous layers of Cr₂O₃ and Al₂O₃.

Luthra and Spacil⁽⁶²⁾ carried out a thermochemical analysis of impurity deposits in gas turbines for liquid fuels containing Na and V. They observed that the predominant species containing these elements were Na₂SO₄ and V₂O₅ in the condensed phase. The minimum concentrations of Na and vanadium in the fuel above which deposition could occur were found to be 2.5.10⁻⁴ - 0.2 ppm and 3.5 - 259 ppm respectively.

Hwang and Rapp⁽²⁾ have studied the solubilities of Al₂O₃, Cr₂O₃, CeO₂ and Y₂O₃ in the mixed sodium sulphate-vanadate solution containing 30 mole % vanadate. They concluded that the basicity of the melt and oxygen partial pressure and the proportion of V⁵⁺ and V⁴⁺ states of vanadate in the sulphate-vanadate solution decided the solubilities of oxides.

Jones^(63,64) developed hot corrosion resistant stabilizers for zirconia coating used against sulphur and vanadium contaminants contained in the low quality fuel. These were CeO₂ (Ceria), Sc₂O₃ (Scandia), In₂O₃ (India). He has also recommended SnO₂⁽⁶⁵⁾ to be

potentially useful as a material for protection against molten vanadate-sulphate hot corrosion below 800°C as it is inert to this atmosphere.

The mechanisms of hot corrosion by molten sulphate-vanadate deposits were investigated by Sidky and Hocking⁽³⁹⁾ by studying the corrosion of Ni-10Cr, Ni-30Cr, Ni-20Cr-3Al, Ni-21Cr-0.3Si, Ni-20Cr-5V and IN738 superalloy. The effect of adding Cr to Ni was found by them to be beneficial in the Na₂SO₄ melt, however, on increasing the VO₃⁻ concentration in the melt, this effect diminished, becoming harmful in pure NaVO₃ due to the formation of the non protective CrVO₄. Al alloying element was found to be harmful in Na₂SO₄-NaVO₃ melts. Cr depletion was observed in rich VO₃⁻ melts but internal corrosion was more obvious in the SO₄²⁻ rich melts. Corrosion in rich VO₃⁻ melts was aggressive due to the fluxing action of the salt which takes place along internally sulphidised areas. According to their study, IN738 suffered tremendous internal attack due to its γ' precipitates which became sulphidation prone areas, which in turn were fluxed by the VO₃⁻ melt.

The kinetics of the reactions between Na₂SO₄(x) and V₂O₅ (y) have been studied by Kolta et. al.⁽⁶⁶⁾. It has been shown that the rate of reaction depends both on the temperature (600-1300°C) and the molar ratios X:Y. During the first 30 minutes and at a mole ratio 1:1, the reaction obeyed the second order. Under such conditions, the activation energy was found to be 54.8 kcal/mole⁻¹.

Swaminathan et. al.⁽⁸⁾ studied the hot corrosion attack of Ni-base superalloy samples of Nimonic 80A, Hastelloy C276 and Superni 600 coated with different amount of V₂O₅ by the wt. change measurement for a period of 100 hrs at 923, 973 and 1073 K in air. Their results have shown that the hot corrosion kinetics obeyed a parabolic law with two regions at 973 and 1023 K, the corrosion rate falling with the formation of a solid Ni₃V₂O₈ layer. The rapid increase in weight at the initial hours was attributed to the ease in diffusion of nickel and oxygen ions in the molten V₂O₅. Once the compact solid vanadate layer was formed, the short circuit diffusion paths were blocked and diffusion became difficult for the oxygen ions to move towards the metal surface.

Thermogravimetric studies by simultaneous sulphate/vanadate induced corrosion at 650 to 800°C have been performed by Sciersten and Kofstad⁽³⁾. NiCrAlY coatings with

potassium sodium vanadyl vanadate deposits and the deposit alone have been exposed to oxygen containing 4% sulphur dioxide at 650-800°C. The solubility of SO₂ in fused Na-vanadate was observed to be higher than that expected from the literature values. The corrosion mechanism is found to change from initial vanadate induced to essentially sulphate induced hot corrosion as and when the SO₃ pressure was high enough. The phases Na₂SO₄, NiS, nickel oxides, nickel sulphate and nickel vanadates were identified.

The corrosion caused by sodium sulphate sodium vanadate mixtures has a complex mechanism as observed by Hideaki et. al.⁽⁶⁷⁾. Nickel oxide in the oxide layer adjacent to the metal dissolved in the sulphate and precipitated as vanadate near the surface.

Na₂SO₄ must be present in the condensed state for sulphidation to occur as has been inferred by Bornstein et. al.⁽⁶⁸⁾. According to them, the adhesion of molten salt increased with decreasing amount of liquid V₂O₅. Liquid V₂O₅ was both an excellent flux and an easy path for oxygen diffusion.

Iyer et. al.⁽⁹⁷⁾ have studied hot corrosion cracking behaviour of Nimonic 80A in flue gas atmosphere containing Na, S, V at 600-700°C under tensile stress. Hot corrosion mechanism was explained by them on the basis that S forms CrS which decomposes into CrO and SO₂ and then SO₂ escapes into atmosphere. With V, large quantities of oxides NiO, Cr₂O₃, Ni(VO₃)₂, NiO.Cr₂O₃ were formed. Fusion of these compounds had taken place and the scale was spongy. Cr₂O₃ formed a non-protective sodium chromate (yellow stains) and hence further oxidation of Ni took place and the scale spalled off.

Kerby and Wilson⁽¹⁰⁸⁾ have studied hot corrosion behavior of Fe, Ni and alloys containing Fe, Ni, Cr and Inconel 600 by static and dynamic accelerated corrosion tests. They concluded that the presence of Fe and Na in the vanadate melts did not alter the rate controlling process of oxygen diffusion and oxygen sorption but they increased the non stoichiometry and hence increased the oxygen diffusion. The rate of corrosion was affected by temperature, oxygen partial pressure, rotational speed, volume of liquid vanadate, composition of the metal, composition of the liquid vanadates. According to them, Inconel showed better corrosion resistance than stainless steels.

Iyer et. al.⁽¹¹⁵⁾ have studied hot corrosion behaviour of Nimonic 80A under tension using combustion gases environment at 600-700°C and have shown that the oxide

morphology had become irregular. Their X-ray examination indicated the presence of NiO, Cr₂O₃, Ni(VO₃)₂ and NiO.Cr₂O₃. Oxidation appeared to be very heavy and the scales were spongy. They have observed that the lowest melting liquid was formed even at 550°C. They proposed that presence of stress enhanced the damage due to scale spalling off and allowing fresh surface to be exposed to hot corrosion. V was supposed to get participated in forming vanadates and increasing V concentration would not be very aggressive. The critical level has been observed to be around 20 ppm V. Also at high temperature the stability of V₂O₅ would decrease resulting in critical level of V for the worst corrosion attack.

The corrosion behaviour of Ni₃Al containing small additions of Ti, Zr and B in combustion gases with Na₂SO₄ deposits at 600-800°C has been studied for 4 days by Gesmundo et. al.⁽⁹²⁾. They observed that the presence of salt deposits considerably increased the corrosion rate especially at 600 and 800°C. The corrosion rate of Ni₃Al in the SO₂-O₂ mixture was found to be quite low at 600°C but increased significantly at 700 and 800°C due to the presence of nickel oxide and of metal sulphides and TiO₂. S was not detected in the scales but was able to penetrate them and could reach the alloy-scale interface, dissolving in the alloy to form internal precipitates of TiS as observed by them at 700 and 800°C.

2.4 HOT CORROSION OF COBALT-BASE ALLOYS

2.4.1 Hot Corrosion in Na₂SO₄

The morphology of the reaction product was observed to be dependent on the temperature and p_{SO_2} by Luthra⁽⁶⁹⁾. Under all conditions a thin sulphur-rich band containing sulphides was observed by him at the alloy/scale interface and he proposed that cobalt dissolved near the interface and formed Co₃O₄ and/or CoSO₄ (s) in different regions of the reaction product. The degradation of Co-base alloys and coatings has also been observed by him⁽⁷⁰⁾ at temperatures below the melting point of Na₂SO₄. According to Luthra and Leblanc⁽¹⁶⁾, corrosion was believed to be caused by the formation of Na₂SO₄-CoSO₄ eutectic (melting point 575°C) on binary Co-Cr alloys containing about 37.5 wt % Cr. However, the presence of Al possibly interfered with the formation of

CoCr₂O₄ and Cr₂O₃. Addition of small amount of reactive element such as Y or Hf to Co-37.5 to 50 wt% Cr alloy had been shown to promote scale adhesion.

The presence of MgSO₄ in Na₂SO₄ affected the chemistry of corrosion behaviour of the sulphate melt in relation to the LTHC of CoCrAlY alloy as observed by Jones et. al.⁽⁷¹⁾. The corrosion initially observed was found to be controlled by sulphidation/dissolution of cobalt oxide from CoCrAlY surface. At a later stage, the corrosion rate was believed to be controlled by involving S rich phases at the corrosion front.

Luthra^(70,72) elaborated on type II corrosion of Co-Cr, Co-Al and Co-Cr-Al alloys. After the low temperature CoSO₄/Na₂SO₄ liquid phase was formed, the acidic dissolution of CoO or at the oxide/salt interface supported the precipitation of either Co₃O₄ or solid CoSO₄ near the salt/gas interface. The detailed mechanism being dependent on p_{SO_3} pressure maintained at the salt/gas interface.

Santaro⁽⁹⁴⁾ has studied Co-base alloys HA 188 and S-57 under cyclic condition with sea salt + Na₂SO₄ at 900-1000°C for 100h by burner rig test. An outer porous scale of CoO and Cr₂O₃ was observed by them on alloy S-57 and the thickness was more at 1000°C than that at 900°C. Most of the outer scale spalled upon thermal cycling. Beneath the porous scale was a dense scale consisting of spinels probably CoCr₂O₄.25CoAl₂O₄. The internal corrosion zone was reported to be consisting of Al and S.

Luthra⁽¹⁰⁴⁾ has studied hot corrosion behaviour of Co-base alloy in liquid salt with SO₂, SO₃ and O₂ gas environment and had concluded that at $p_{O_2} = 1$ atm. Co₃O₄ was more stable than CoO at temperature below 947°C. SO₃ levels below which a liquid cannot form on Co₃O₄ at $p_{O_2} = 1$ atm. have been referred to as low SO₃ level and those which can form CoSO₄ from Co₃O₄ are termed as high SO₃ levels.

2.4.2 Hot Corrosion in Na₂SO₄-V₂O₅

The mechanisms of hot corrosion by molten sulphate-vanadate deposits were investigated by Jones et. al.⁽⁷³⁾ by studying the corrosion of CoCrAlY gas turbine blade coating alloy by Na₃VO₄, NaVO₃, V₂O₅ and Na₂SO₄ or combinations thereof, in air or in controlled SO₃-air environments at 700°C. They proposed that mixtures of 50% V₂O₅-

Na_2SO_4 might produce greater corrosion than the pure vanadate product (NaVO_3) because of SO_3 liberated in the reaction $\text{Na}_2\text{SO}_4 + \text{V}_2\text{O}_5 = \text{NaVO}_3 + \text{SO}_3$. The mechanisms of $\text{Co}_2\text{V}_2\text{O}_7$ formation had been elucidated in depth with surface layers of $\text{Co}_2\text{V}_2\text{O}_7$ being shown to reduce the corrosion rate by acting as a barrier against SO_2 or O_2 inward diffusion and also possibly by reducing V_2O_5 activity within the corrosion phase.

Tiwari et. al.⁽¹⁰⁷⁾ studied the hot corrosion behaviour of Co-base superalloy with $\text{Na}_2\text{SO}_4\text{-V}_2\text{O}_5$ environment in air and in combustion gas at 700-1100°C and have shown its good corrosion resistance due to the formation of a continuous Cr_2O_3 scale which did not allow oxide ion diffusion towards the alloy surface. No oxidation and sulphidation into the substrate was observed in X-ray mappings of the cross section taken by EPMA.

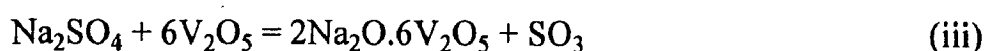
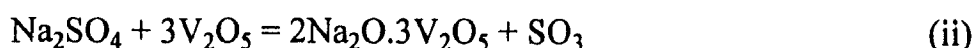
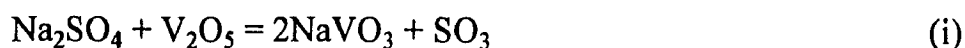
2.5 EFFECT OF MgO ON HOT CORROSION OF ALLOYS

As suggested by Niles and Sanders⁽⁷⁴⁾, high temperature corrosion problem in oil fired steam boilers and gas turbines have been attacked with success in recent years by fuel additives and inhibitors. Protection of metals and alloys by fuel additives and inhibitors is therefore an important field of research. There are number of inhibitors commercially available that are intended to reduce the severity of oil ash corrosion such as MgO ^(11,83,111,112), MgSO_4 ⁽⁸³⁾, CaO ⁽¹¹²⁾, CaSO_4 , MnO , Cr_2O_3 , ZrO_2 ⁽⁶³⁾, Y_2O_3 ⁽⁷⁵⁾, In_2O_3 ⁽⁷⁶⁾, SnO_2 ⁽⁶⁵⁾, TiO_2 , Al_2O_3 , ZnO ⁽⁷⁷⁾, BaO , Ba(OH)_2 , PbO ⁽⁴⁸⁾, Ca(OH)_2 , CaCO_3 , SiO_2 , Ta_2O_5 etc. Some oil soluble compounds of Fe, Ni, Al etc. have also been tried with some success⁽¹⁹⁾. Mn based additives are effective due to reaction of Mn with sodium in the fuel and thereby preventing it from reacting with vanadium to produce corrosive sodium vanadate. These inhibitors reduced the rate of hot corrosion but apparently acted by forming deposits on the metal⁽¹⁹⁾.

Because of its effectiveness and relatively low cost the most common fuel additives are based on MgO . Magnesium reacts with vanadium present in the fuel oil and produces compounds with a melting point above most metal surface temperatures. MgO was able to reduce the rate of corrosion without forming a detectable coating as observed by Rhys-Jones et. al.⁽⁷⁸⁾.

The treatment level with magnesium recommended by additive suppliers is based more on an art than a science. The form of magnesium whether organometallic or inorganic is another criterion. Economics dictate that the additive be applied in the problem areas directly and in active, fine form. Alkaline additives such as MgO have been shown to be effective as observed by Sinha⁽⁷⁹⁾.

Vanadic attack has been studied by several investigators^(77,74,80) with the help of the phase diagram for Na₂SO₄-V₂O₅ (Fig. 2.7)⁽⁵⁸⁾. They have shown that NaVO₃, Na₂O.3V₂O₅ and Na₂O.6V₂O₅ are the possible compounds formed as follows:



X-ray diffraction also identified the presence of Na₂O.V₂O₄.5V₂O₅ at ambient temperature. It was generally accepted that when Na₂O.6V₂O₅ was cooled to freezing point, one atom of oxygen is evolved to give Na₂O.V₂O₄.5V₂O₅ at all temperatures. The results of Niles and Sanders⁽⁷⁴⁾ confirmed the presence of only three vanadates formed by reactions (i)-(iii). Na/V ratio plays an important role in deciding the reactions and their products.

2.5.1 Inhibition of Hot Corrosion by MgO Addition in the Absence of Na₂SO₄

Fichera et. al.⁽⁸¹⁾ have evaluated the effectiveness of magnesium oxide as an additive of fuel oil. The increase in melting point of fuel ash after addition of MgO is shown in Fig. 2.8⁽⁸¹⁾. MgO directly reacts with V₂O₅ (Fig. 2.9)⁽¹¹⁾ giving 2MgO.V₂O₅, magnesium pyrovanadate (m.p. 835°C) and 3MgO.V₂O₅, magnesium orthovanadate (m.p. 1190°C) as



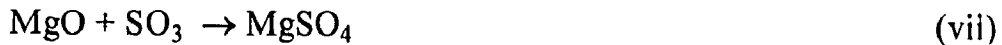
The increasing of melting points of the fuel ash constituents was supposed to greatly increase its viscosity and reduce the diffusion of oxygen upto an order.

2.5.2 Inhibition of Hot Corrosion by MgO Addition in the Presence of Na₂SO₄

It is necessary to assume that where V and Na are the major metal contaminants in a fuel, deposits will be composed principally of compounds of these two metals and likewise, if an additive is used, it too will be a principal deposit component. The compound formed will depend upon the ratio of Na/V as recommended by Niles and Sanders⁽⁷⁴⁾



When sufficient SO₃ is present the MgO can be sulphated as MgSO₄⁽⁷⁸⁾



Rhys-Jones et. al.⁽⁷⁸⁾ studied the effect of various levels of V₂O₅ and V₂O₅ + MgO upon the high temperature corrosion of Nimonic 90 and X-40 alloys in the absence and presence of SO₂/SO₃ at the temperature 850°C. They have suggested that 3MgO:1 V₂O₅ reduces the metal loss to a maximum extent.

To express the effectiveness with which MgO inhibits vanadic corrosion, a term “inhibitor efficiency” has been proposed by Rhys-Jones et. al.⁽⁷⁸⁾

$$I = \frac{\text{Corr. I} - \text{Corr. II}}{\text{Corr. I}} \times 100$$

where I = Inhibitor efficiency, in %.

Corr. I = Corrosion in the system, alloy + V₂O₅ + air (mm 100h⁻¹)

Corr. II = Corrosion in the system, alloy + V₂O₅ + 3MgO + air (mm 100h⁻¹)

One hundred percent inhibitor efficiency will be achieved when Corr_{II} = 0, i.e. when all the corrosion due to the presence of V₂O₅ is stopped by the MgO, i.e. when the measured corrosion rate is equal to that obtained in air oxidation⁽⁷⁸⁾.

Barbooti et. al.⁽⁸³⁾ studied the effect of magnesium sulphate addition in depressing hot ash corrosion on stainless steel 304 by carrying out weight loss experiment. They have shown that MgSO₄ is stable upto 892°C, above which it decomposes into MgO and SO₃ at increasing rate. It has been observed by them that in presence of V₂O₅, there was no influence of MgSO₄ in the temperature range 630-690°C. They finally concluded that the

optimum MgSO_4 ash ratio was 1:1, where the scale analysis showed Cr:Fe values of 0.12 corresponded to a range of 77-82% inhibition efficiency in the temperature range 600-800°C.

Rhys-Jones et. al. ⁽⁷⁸⁾ have concluded from their studies on Nimonic 90 and X-40 alloys that the effectiveness of MgO as an inhibitor of vanadic corrosion depended upon the SO_2/SO_3 ratio. Their results showed that efficiencies of 80-95% could be realized in the SO_2 free system.

FORMULATION OF THE PROBLEM

3.1 SCOPE

Hot corrosion is a serious problem in power generation equipments, in gas turbines for ships and aircrafts and in other energy conversion and chemical process systems. Hot corrosion is the accelerated oxidation of materials at elevated temperatures induced by a thin film of fused salt deposit. Corrosion has been attributed to the fluxing action of the molten salt deposits on the oxide scales formed on the tubes, leading to rapid localized corrosion, accompanied by some sulphidation also. Hot corrosion first became known to engineers and researchers with the failure of boiler tube and later with the severe attack of gas turbine component materials.

Although the operating systems and end products of coal combustion and coal conversion are quite different, many of the potential corrosion problems have features in common and stem from the impurities in the coal.

Due to depletion of high grade fuels and for economic reason use of residual fuel oil in these systems is well known. Residual fuel oil contains sodium, vanadium and sulphur as impurities. Sodium and sulphur form Na_2SO_4 (m.p. 884°C) by reactions in the combustion system. Vanadium is usually present as a porphyrin or other organometallic complexes but inorganic compounds of vanadium have also been reported. During combustion of the fuel, vanadium reacts with oxygen to form an oxide V_2O_5 (m.p. 670°C). Thus V_2O_5 is a liquid at gas turbine operating temperature. These compounds (known as ash) deposit on the surface of the materials and induce accelerated oxidation (hot corrosion). The corrosion problem is more acute when the vanadium pentoxide ash-deposits on the metal surface is molten as it acts as a catalyst. These molten ash-deposits dissolve the protective oxide scale thus fluxing it.

During early work from 1950, through 1965, the details of oil ash-induced corrosion mechanisms and possible solutions were largely studied. Operating conditions of the plant affect the corrosion rate. Thus by decreasing the metal temperature, flue gas temperature, lowering excess air used in fuel oil combustion can lower wastage rate of the component material.

Superalloys are used to resist oil ash corrosion and success is achieved to considerable extent. There appears to be an advantage in using high chromium alloys. Thermal barrier coatings of alloys and ceramics are used for studies on resistance to oil ash corrosion and they were found effective. Inhibitors and fuel additives have been used with varying success to combat oil ash corrosion. Because of its effectiveness and relatively low cost, the most common fuel additives are based on MgO.

Some investigations were carried out on the hot corrosion of stainless steels, Fe-, Ni- and Co-base superalloys by V_2O_5 , Na_2SO_4 , $Na_2SO_4-V_2O_5$, $Na_2SO_4-NaVO_3$ mixtures. Most of the studies have been made in isothermal conditions. Relatively fewer studies are reported under cyclic conditions which actually simulate the working condition of boilers and gas turbines. In cyclic condition, high thermal stresses are developed. During cooling the scale cracking takes place and fresh areas are exposed to corrosion. Cyclic hot corrosion studies have been made either with the help of a burner rig test or by using laboratory tube furnaces usually in the temperature range 600-1000°C. Levy et. al.⁽⁴³⁾ have concluded from their hot corrosion studies on Ni-base alloys that tube furnace tests can be used in place of burner rig tests to rank alloys provided the tests are accompanied by detailed metallographic examination of the exposed specimen.

3.2 AIM

In view of the fact that further investigations on the hot corrosion of superalloys are needed, it was proposed to study the hot corrosion behaviour of some Fe-, Ni- and Co-base superalloys containing high chromium (15.5-21%) in an aggressive environment of oil fired boilers and gas turbines ($Na_2SO_4-V_2O_5$) under cyclic conditions (similar to actual working condition of the plant) in the temperature range (700-900°C) where corrosion

problem is very acute using a laboratory tube furnace in air and in an actual boiler combustion gas environment.

It is learnt from literature that the oil ash corrosion occurs at a rapid rate in the initial hours of the test and then the rate decreases. Hence the corrosion of alloys in vanadic environment is of particular interest in the initial period. Therefore 24 cycles (Cycle of 1 h heating and 20 min. cooling) for laboratory tests and 6 cycles (cycle of 24 h heating and 1 h cooling) for tests in industrial environment were selected for hot corrosion studies. It is recommended in literature that $1 \text{ mg/cm}^2 \text{ Na}_2\text{SO}_4$ is more than sufficient to undergo severe attack, therefore $4.0\text{-}5.0 \text{ mg/cm}^2$ of salt mixture deposit was chosen in the form of thin film to create an aggressive environment. The literature also indicates that MgO addition in fuel oil increases melting point of the deposits considerably and inhibit the formation of molten sodium vanadate. Therefore it was proposed to study this effect in laboratory for these alloys under cyclic conditions. It was also proposed to measure weight change to study the corrosion kinetics and to use X-ray diffractometer (XRD), Scanning Electron Microscope (SEM), Energy Dispersive X-ray Analysis (EDAX) and Electron Microprobe Analyser (EPMA) to characterize the corrosion products and to make an attempt to understand the mechanism of corrosion.

EXPERIMENTAL TECHNIQUES AND PROCEDURE

4.1 MATERIALS

High chromium (15.5-21.0%) containing Fe-, Ni- and Co-base superalloys namely Superfer 800H, Superni 75, Superni 600, Superni 718 and Superco 605 were procured from Mishra Dhatu Nigam Ltd. (MIDHANI), Hyderabad (India) for the present investigation. The alloys were in the rolled condition with varying thickness (1.4 - 4.0 mm). For convenience these alloys are marked as A, B, C, D and E. Their chemical composition and other details are shown in Table 4.1.

4.2 SPECIMEN PREPARATION AND COATING

4.2.1 Preparation of Materials

The alloy sheets were cut into rectangular (15 mm × 20 mm) specimens. Some specimens used for hot corrosion studies in industrial environment had a hole of 3 mm diameter to hang them using stainless steel wire (2 mm dia). The specimens were polished using silicon carbide papers up to 1200 grit and finally wheel polished with 1 μm alumina powder to a mirror finish. They were then washed with distilled water and cleaned with acetone. Their surface areas were determined and weights were measured with an electronic balance to an accuracy of 0.01 mg.

4.2.2 Coating of Specimens with Salts

The uniform coating of saturated solution of Na₂SO₄ was given on warm (~170°C) polished specimen by spraying with a spray gun. The salt mixtures of Na₂SO₄ - 15% V₂O₅, Na₂SO₄-60% V₂O₅ and Na₂SO₄-60% V₂O₅ + MgO were coated on warm polished specimens with a camel hair brush. The amounts of salt coating ranged from 4.0 to 5.0

mg/cm². The coated specimens were then dried (~110°C), cooled in a desiccator and then weighed.

4.3 HOT CORROSION STUDIES

4.3.1 In Laboratory Tube Furnace

The coated specimens were kept in alumina boats and then transferred into the hot zone of a Silicon Carbide Horizontal Tube Furnace closed at both ends. A constant temperature was maintained. Studies were made at 700, 800 and 900°C with an accuracy of $\pm 5^\circ\text{C}$ in air under cyclic conditions for 24 cycles (cycle of 1h heating and 20 min. cooling). After each cycle the weight of the specimen was measured to obtain the wt. change value.

4.3.2 In Actual Industrial Environment

The alloys A, B, C, D and E were studied in actual industrial environment also at the superheater zone of Boiler-3 of Power Plant II of Bhilai Steel Plant (India). The salt coated specimens were hanged inside the boiler with the help of stainless steel wire and a rigid support of stainless steel rod. The rod was inserted inside the boiler through the trip hole and was rigidly held. The composition of the flue gas inside the boiler is given in Table 4.2. The specimens were exposed in combustion gas for 6 cycles (cycle of 24 h heating and 1h cooling) at 1100°C. After each cycle the weight of the specimen was measured so as to obtain the wt. change value. The flue gas flow rate was about 56 m³/sec and its static pressure 250 mm. W.C.

4.4 INVESTIGATION OF CORROSION PRODUCT

4.4.1 Thermogravimetric Studies

The wt. change values of the specimens were plotted with respect to the time (no. of cycles) and are shown in Fig. 5.1-5.25. The plots show the effect of temperature, time and the salt mixture on the corrosion rate. The nature of the curves also shows that in most of the cases a rapid rate of corrosion occurred during the first two cycles and then the rate decreased. The total wt. gain values of the specimens observed after completion

of the exposure are shown in Table 5.1. The specimens exposed in industrial environment have shown to obey parabolic law hence their parabolic rate constants were determined and are shown in Table 5.2.

4.4.2 Visual Observation

Visual examination of the exposed specimens was made after each cycle for their colour, lustre, adherence, spalling tendency etc. After 24 cycles in laboratory studies and after 6 cycles studies in industrial environment, the specimens were finally carefully observed and then their macrographs were taken, which are shown in Fig. 5.26-5.30.

4.4.3 Measurement of Scale Thickness

The average scale thickness values of the specimens after exposure at 900 and 1100°C, whose X-ray mappings were taken, have been measured and these values are shown in Table 5.3.

4.4.4 X-ray Diffractometry

X-ray diffractometry of the exposed specimens was carried out for the phase identification of the corrosion products. Scale surfaces were examined by X-ray diffractometer PW 1140/90 Phillips employing copper target and nickel filter at a voltage of 35 kV and a current of 15 mA. The specimens were scanned from 20-100°. In most of the instances the scanning speed was kept at 1kcs (kilo cycles per second). Diffractograms were analysed by adopting the following procedure :

- (i) 'd' values were calculated for all the discernible peaks in the usual manner.
- (ii) Assuming the height of the most prominent peak as 100%, the relative intensities of all peaks were determined.
- (iii) The data thus obtained was compared with ASTM data cards following the standard procedure for search and identification was carried out.

The XRD profiles of the specimens were drawn and are shown in Fig. 5.31-5.55 while their 'd' values and phases are shown in Table 5.4-5.28.

4.4.5 Optical Microscopy

Optical microscopy was mainly used at the preliminary stage of sample preparation. The microstructure of the unreacted and exposed specimens were compared with Reichert Metavert - 368 Microscope.

4.4.6 Scanning Electron Microscopy and EDAX Analysis

Surfaces of the exposed specimens were examined by SEM. The surfaces of the hot corroded specimens were first coated with gold and then their micrographs were taken. The SEM studies were carried out mainly on Phillips SEM 501. Photographs were taken mostly at 160 and 640 X and are shown in Fig. 5.56-5.80.

The point analysis were also obtained simultaneously with an EDAX attached to the SEM of the selected areas of interest present in the scale formed on the alloy surface. Only those specimens were selected in which higher corrosion rates were observed. EDAX analysis of the scales of alloys A, B, C, D and E are shown in Table 5.29-5.33.

4.4.7 Electron Microprobe Analysis

EPMA was used to take the micrographs of the cross sections known as the Back Scattered Electron (BSE) image and the X-ray maps showing the distribution of the elements (e.g. Fe, Ni, Cr, Co, S, V, Na, O etc.). The EPMA model Cameca - Micro Bax was employed using accelerated voltage of 20 kV.

The line scan technique was also used in a very limited extent as the porosity in the scale created a hinderance. To carry out such an analysis, the electron beam was kept stationary while moving the specimen along the desired direction. This also provided the distribution of selected elements in the scale, substrate and at the interface. X-ray maps have been taken for only those specimens in which in which higher corrosion rates were observed. The BSE images and X-ray maps of alloy A, B, C, D and E are shown in Fig. 5.81-5.105.

RESULTS

The results of the present investigation on hot corrosion studies in pure Na_2SO_4 , Na_2SO_4 -15% V_2O_5 and Na_2SO_4 -60% V_2O_5 coatings for 24 cycles in air at 700, 800 and 900°C and also with coatings of Na_2SO_4 -60% V_2O_5 + MgO at 900°C for 24 cycles in air in laboratory while with Na_2SO_4 , Na_2SO_4 -15% V_2O_5 , Na_2SO_4 -60% V_2O_5 coatings in actual industrial environment for alloys A, B, C, D and E are described in this chapter.

5.1 HOT CORROSION STUDIES IN PURE Na_2SO_4

5.1.1 Kinetic Data

Fig 5.1 to 5.5 shows the plots drawn between wt. gain (expressed in mg/cm^2) and time (expressed in number of cycles) for the specimens of alloys A, B, C, D and E after exposure for 24 cycles (cycle of 1 h heating and 20 min. cooling) with pure Na_2SO_4 coating at 700, 800 and 900°C in air. The plots for alloy A at all temperatures of study (Fig 5.1) show a rapid increase in wt. gain during the first two cycles, then it remains constant and after 10 cycles there is a decrease in the wt. gain value. It shows a significant effect of temperature on corrosion. Similar trend of wt. change is observed in the plots of alloys B, C, D and E also. An increase in wt. gain value with increase in temperature (700, 800 and 900°C) is also observed in all cases. The total wt. gain value is minimum ($0.27 \text{ mg}/\text{cm}^2$) for alloy B at 700°C and is maximum ($0.53 \text{ mg}/\text{cm}^2$) at 900°C for alloy A. Wt. gain values are very nominal for all alloys suggesting that the alloys have good corrosion resistance against pure Na_2SO_4 at all the test temperatures.

5.1.2 Visual Observation

Fig 5.26 to 5.30 shows the macrographs of corroded specimens of alloys A, B, C, D and E after exposure for 24 cycles at 700, 800 and 900°C with Na_2SO_4 coating. The

scale of alloy A was grey and yellow coloured adherent mass at 700 and 800°C, but at 900°C it was slightly porous. The oxide scales of alloy B was grey and yellow coloured at 700°C, dark grey with some unreacted Na₂SO₄ particles at 800°C, while it was grey and yellow coloured, lusturous and adherent at 900°C. The alloy C after similar exposure formed similar type of scale as that of alloy B. The alloy D also formed similar scales with some unreacted salt particles sticking on the surface at 700°C and 800°C while at 900°C, grey coloured adherent scale with dull appearance was observed after similar exposure. The scale on the surface of alloy E was of dark grey colour and adherent with some unreacted salt particles at 700 and 800°C while at 900°C dark grey coloured scale, adherent in nature, was observed..

5.1.3 Measurement of Scale Thickness

The average thickness values for scales of these alloys were measured by EPMA after exposure in pure Na₂SO₄ at 900°C and these values are 17.0, 7.5, 9.0, 10.0 and 8.0 microns for alloys A, B, C, D and E respectively.

5.1.4 X-Ray Diffraction Analysis

The X-ray diffraction results (Tab. 5.4 - 5.8, Fig. 5.31-5.35) of the corroded specimens of alloys A, B, C, D and E, in general, indicated similar phases at 700, 800 and 900°C. The phases identified on the corroded specimens of alloy A in pure Na₂SO₄ at 700, 800 and 900°C for 24 cycles are compiled in Table 5.4 and their X-ray diffraction profiles are shown in Fig. 5.31. The prominent phases identified in the scales of alloy A were α -Fe₂O₃, Cr₂O₃ and NiCr₂O₄. The scales on alloy B after similar exposure also consisted of these phases at all temperatures. In the scales of alloy C in addition to these phases CrS was also identified. In the scales of alloy D, additional phases CrS and TiO₂ were identified as the prominent ones. The phases identified on the surface of alloy E were mainly Cr₂O₃, α -Fe₂O₃, Co₃O₄, WO₃ and NiCr₂O₄.

5.1.5 SEM - EDAX and EPMA Results

Fig. 5.56-5.65 presents SEM micrographs of specimens of alloys A, B, C, D and E with pure Na_2SO_4 coating exposed at 700, 800 and 900°C for 24 cycles in air. The micrographs show typical features observed after hot corrosion. Fine particles are observed on the scale surface of alloy A at 700°C, while irregular coarse crystals of various size are observed at 800 and 900°C. The EDAX shows the surface to be rich in Cr and Fe at areas 1 and 2 (Tab. 5.29, Fig. 5.56a) in specimens exposed at 900°C. After similar exposure SEM micrographs of alloy B (Fig. 5.58) shows a cracked scale of fine grain size at 700°C, while at 800 and 900°C coarse grained structure is revealed. The surface is rich in Cr and Ni at areas 1-3 as indicated by EDAX (Tab. 5.30, Fig. 5.58a). The SEM micrographs of alloy C (Fig. 5.60) reveals fine grained structure at 700°C, a cracked scale with coarse grains on the surface and fine grained structure is revealed in the interior part of the scale at 800°C, while at 900°C coarse grained structure with a very big particle is revealed. The surface is rich in Cr with lower Ni, Fe and S content at area 1-3 as indicated by EDAX (Tab. 5.31, Fig. 5.60c). Similarly SEM micrographs of alloy D (Fig. 5.62) after similar exposure reveals irregular scale surface with fine grains at 700°C, while at 800°C big particles of rounded shape in various sizes are revealed. At 900°C coarse grained particles with some big particles were revealed. The EDAX analysis (Tab. 5.32, Fig. 5.62a) at areas 1-3 indicates the presence of Cr, Ti, Fe and Ni on the scale surface. Also the SEM micrographs of alloy E (Fig. 5.64) reveals fine grained structure at 700°C and 800°C, while at 900°C some coarse grained structure with uniform distribution on the surface is revealed. At areas 1-2 the EDAX (Tab. 5.33, Fig. 5.64a) shows that the scale is rich in Co and Ni but little amounts of Fe and Cr are also present.

Due to the observed high rate of wt. gain at 900°C for these alloys with pure Na_2SO_4 coating, EDAX and EPMA analysis have been carried out for those specimens only.

The BSEI and X-Ray maps of elements of alloy A after exposure at 900°C in pure Na_2SO_4 are shown in Fig. 5.81. The specimen surface is irregular indicating more corrosion at 900°C. The outer scale consists of oxides of Fe and Cr below which a continuous Cr_2O_3 layer is observed on the alloy surface. Cr depletion is also observed in

the alloy substrate. The BSEI and X-ray maps of elements in alloy B after similar exposure are shown in Fig. 5.82. The outer and inner layer of scale is predominantly rich in oxides of Cr. Similarly the BSEI and X-ray maps of alloy C after similar exposure are shown in Fig. 5.83. The outer layer consists of oxides of Ni, Cr and Fe while the inner layer is mainly Cr₂O₃. The BSEI and X-ray maps for alloy D after similar exposure are shown in Fig. 5.84. The scale consists mainly of oxides of Cr and Ti. Cr depletion is also observed in the alloy substrate. Similarly the BSEI and X-ray maps of alloy E after similar exposure are shown in Fig. 5.85. The outer layer consists of oxides of Cr, Fe, Co and W. While the inner layer is mainly Cr₂O₃. In general, Cr depletion was observed in the substrate of all the alloys.

5.2 HOT CORROSION STUDIES IN Na₂SO₄-15% V₂O₅

The superalloys marked A, B, C, D and E were coated with Na₂SO₄-15% V₂O₅ salt mixture and then subjected to hot corrosion in the laboratory tube furnace under static air at 700, 800 and 900°C for 24 cycles. Their results are presented in this section.

5.2.1 Kinetic Data

The wt. gain - time plots for the alloys A, B, C, D and E are shown in Fig. 5.6-5.10. It can be observed from the plots that these alloys show good resistance to hot corrosion at 700, 800 and 900°C except for the alloy D at 900°C, where comparatively more corrosion was observed. These plots, in general, show a linear rate of corrosion in the initial period, afterwards the rate decreases. The plot for alloy A (Fig. 5.6) shows a rapid rate of wt. gain during the first two cycles and then it remains constant at 700, 800 and 900°C. The plots of alloy B and C (Fig. 5.6, 5.7) also follow similar trend at 700 and 800°C but at 900°C the wt. gain value slowly increases. Wt. change plot for alloy E (Fig. 5.10) shows that after rapid increase in the initial period, the wt. gain values remain constant. The wt. change plots for alloy D (Fig. 5.9) shows that at 700 and 800°C its behaviour is very similar to other alloys, while at 900°C the wt. gain value changes in a peculiar way. There is a rapid rate of wt. gain during the first 6 cycles. Then the value

starts decreasing which leads to the wt. loss of 6.8 mg/cm^2 after 12 cycles. Then finally, the wt. loss (6.8 mg/cm^2) remains constant during 12 to 24 cycles..

5.2.2 Visual Observation

Visual observation of the scales formed on alloy A after hot corrosion at 700, 800 and 900°C shows that they were crystalline, grey coloured, adherent and had a shining lustre (Fig. 5.26). The scales formed on alloy B were also grey coloured, adherent but had a dull appearance (Fig. 5.27). Some unreacted salt was also observed. The oxide scales of alloy C had a dark grey colour, dull appearance and were adherent at all temperatures (Fig. 5.28). The scales of alloy D at 700 and 800°C were grey coloured with shining lustre and were adherent (Fig. 5.29). At 900°C it was uneven, black and porous. Spalling was observed during experiment. The scales of alloy E were grey coloured with shining lustre and adherent at 700 and 800°C but at 900°C , it was dark grey and yellow coloured with dull appearance and was adherent (Fig. 5.30).

5.2.3 Measurement of Scale Thickness

The average thickness values for scales of these alloys were measured by EPMA, after exposure in $\text{Na}_2\text{SO}_4\text{-15\%V}_2\text{O}_5$ at 900°C and these values are 40.3, 43.3, 42.5, 47.0 and 40.0 microns for alloys A, B, C, D and E respectively.

5.2.4 X-Ray Diffraction Analysis

X-ray diffraction results of hot corroded specimens of alloys A, B, C, D and E at 700, 800 and 900°C for 24 cycles are compiled in Tab. 5.9-5.13 and plotted in Fig. 5.36-5.40. The main peaks in most of these diffractograms were mainly of $\alpha\text{-Fe}_2\text{O}_3$ or Cr_2O_3 , while the peaks of low intensity were of NiO, FeV_2O_4 , $\text{Ni}(\text{VO}_3)_2$ and $(\text{Cr, Fe})_2\text{O}_3$. The prominent phases identified in the scales of alloy A were $\alpha\text{-Fe}_2\text{O}_3$, Cr_2O_3 , FeV_2O_4 and NiCr_2O_4 at 700, 800 and 900°C . In the scales of alloy B after similar exposure NiO, Cr_2O_3 and NiCr_2O_4 were identified at these temperatures. In the scales formed on the surface of alloy C, NiO, NiCr_2O_4 , FeV_2O_4 , $\text{Ni}(\text{VO}_3)_2$ and $(\text{Cr, Fe})_2\text{O}_3$ were identified as the main phases at these temperatures. The scales of alloy D consisted mainly of Fe_3O_4 , NiO, Cr_2O_3 , Al_2O_3 , TiO_2 , $\text{Ni}(\text{VO}_3)_2$ and NiCr_2O_4 . The phases identified in the scales formed on

the surface of alloy E were mainly Cr_2O_3 , NiO , CoO , FeWO_4 and NiCr_2O_4 at these temperatures.

5.2.5 SEM - EDAX and EPMA Results

Fig. 5.57-5.65 presents SEM micrographs of alloys A, B, C, D and E with Na_2SO_4 -15% V_2O_5 coating after exposure at 700, 800 and 900°C for 24 cycles in air. The micrographs show typical features observed. Fig. 5.57 of alloy A shows big particles of irregular shape with some cavities at 700°C, the mixed type of granular structure ranging from fine to coarse is observed at 800°C, while at 900°C, thin plate like structure is revealed. The EDAX shows the surface to be rich in Cr and Fe at areas 3-4 (Tab. 5.29, Fig. 5.57a) in specimens exposed at 900°C. Fig. 5.59 presents SEM micrographs of specimens of alloy B after similar exposure, fine grained particles are observed after exposure at 700°C, while thin plate like structure with uniform distribution are revealed at 800°C. Crystals of various sizes with rounded edge are revealed at 900°C. At areas 4-5 (Tab. 5.30, Fig. 5.59a) Ni rich scale is observed in which some Cr and Al are also present. Fig. 5.61 presents SEM micrographs of specimens of alloy C after similar exposure. Fine grained compact structure is observed at 700°C, while crystals of fine size with different shapes are observed at 800°C. At 900°C crystalline structure with rounded edge is observed. The EDAX shows the surface to be rich in Cr, Ni and Fe at areas 4-6 (Tab. 5.31, Fig. 5.61a) in specimens exposed at at 900°C. The SEM micrographs of alloy D (Fig. 5.63) after similar exposure shows fine to coarse grained structure at 700°C, while at 800°C also similar structure is observed with some cavities in between. At 900°C a mixed structure with fine to coarse grains of different shapes is revealed. The scale is rich in Cr, Ni and Fe at areas 4-5 (Tab. 5.32, Fig. 5.63a) as revealed by EDAX. Fig. 5.65 presents SEM micrographs of specimens of alloy E after similar exposure. At 700°C the scale shows a uniform distribution of fine grains with some coarse particles, while it reveals a compact scale with some voids at 800°C. At 900°C the scale shows a coarse grained continuous structure with rounded particles. The scale surface is rich in Co and Ni while small amounts of W, Fe and Cr are also present at areas 3-4 (Tab. 5.33, Fig. 5.65a) as indicated by EDAX.

248206.



Due to the observed high rate of wt. gain at 900°C for these alloys with Na₂SO₄-15%V₂O₅ coating, EDAX and EPMA analysis have been carried out for those specimens only.

The BSEI and X-Ray maps of alloy A coated with Na₂SO₄-15%V₂O₅ and exposed at 900°C in static air are shown in Fig. 5.86. The specimen surface is irregular indicating higher corrosion at 900°C. The outer layer of scale contains oxides of Fe, Ni and Cr, while the inner layer is mainly Cr₂O₃. Cr depletion in the substrate has also been observed. The BSEI and X-ray maps of alloy B after similar exposure are shown in Fig. 5.87. The outer scale is rich in oxides of Ni and Cr while the inner layer is mainly Cr₂O₃. The BSEI and X-ray maps of alloy C after similar exposure are shown in Fig. 5.88. The outer scale is rich in oxides of Ni, Cr, Al and Fe while near the alloy surface Cr, Al and V elements are present in their oxide form. Al₂O₃ is present at the grain boundaries in the alloy substrate also. The BSEI and X-ray maps for alloy D are shown in Fig. 5.89. Top layer of scale consists of α-Fe₂O₃, NiO and TiO₂ below this is the layer of Cr₂O₃. Al is present in the substrate at the grain boundaries in its oxide form. The BSEI and X-ray maps of alloy E are shown in Fig. 5.90. The top layer consists of oxides of Cr, W, Ni, Co and Fe below which is the layer of Cr₂O₃ only.

5.3 HOT CORROSION STUDIES IN Na₂SO₄ - 60% V₂O₅

5.3.1 Kinetic Data

Fig 5.11 to 5.15 show the plots drawn between wt. change and number of cycles (time) for the specimens of alloys A, B, C, D and E after exposure for 24 cycles with Na₂SO₄ - 60% V₂O₅ (eutectic mixture) coating in air at 700, 800 and 900°C. The plot for alloy A (Fig 5.11) shows a rapid increase in wt. gain during the first two cycles and then the rate of wt. gain decreases at 700 and 800°C. At 900°C after an initial increase in wt. gain there is a continuous decrease in the wt. of the specimen leading ultimately to a wt. loss of 23.2 mg/cm². It suggests that the alloy is severely corroded. The plot for alloy B (Fig. 5.12) shows a rapid increase in wt. gain during the first two cycles, after which the rate of wt. gain is very slow at 700°C whereas there is a little increase in the rate of weight gain at 800 and 900°C. In case of alloy C (Fig. 5.13) the plot shows a rapid increase in wt.

gain during initial first cycle and then the wt. gain value remains constant at 700 and 800°C, while at 900°C there is a gradual increase in the wt. gain value. For alloy D the Fig. 5.14 shows a rapid increase in wt. gain during first four cycles, later there is a little decrease in wt. gain value at 700°C, while a gradual increase in wt. gain occurs at 800 and 900°C. The plot for alloy E (Fig. 5.15) also shows a rapid increase in wt. gain during the first two cycles and then the rate of wt. gain decreases at 700 and 800°C. At 900°C there is a continuous increase in wt. gain upto 16 cycles of exposure, afterwards the wt. gain value remains constant upto the last cycle of the test. It has been observed, in general, that wt. gain value increases with increase in temperature.

5.3.2 Visual Observation

Fig 5.26 to 5.30 shows the macrographs of the specimens of alloys A, B, C, D and E after exposure for 24 cycles at 700, 800 and 900°C with Na₂SO₄ - 60%V₂O₅ coating. The scales on alloy A were of grey colour, non adherent, porous and shining mass at 700, 800 and 900°C. The oxide scales of alloy B after similar exposure were steel grey, adherent, compact and dull in appearance at 700 and 800°C but it was porous at 900°C. The alloy C after identical exposure also formed scale similar to alloy B. The scales formed on alloy D were grey coloured, compact and dull in appearance at 700 and 800°C but it was shining at 900°C. Alloy E after similar exposure formed grey coloured shining and adherent scales on its surface at 700 and 800°C but it was porous at 900°C.

5.3.3 Measurement of Scale Thickness

The average thickness values for scales of these alloys were measured by EPMA after exposure in Na₂SO₄-60%V₂O₅ at 900°C and these values are 62.5, 45.0, 75.0, 67.5 and 96.6 microns for alloys A, B, C, D and E respectively.

5.3.4 X-Ray Diffraction Analysis

The XRD results of the corroded samples of alloys A, B, C, D and E at 700, 800 and 900°C are compiled in Table. 5.14 to 5.18 and X-Ray diffraction profiles are shown in Fig. 5.41 to 5.45. The prominent phases identified on the corroded specimens of alloy

A at these temperatures were α -Fe₂O₃, Cr₂O₃, NiO, (Cr, Fe)₂O₃ and FeV₂O₄. In the scales of alloy B, after similar exposure, Cr₂O₃, NiO, (Cr, Fe)₂O₃, FeV₂O₄, Ni(VO)₂ and NiCr₂O₄ were the main phases identified. The scales of alloy C contain the oxides Cr₂O₃, NiO and the spinels (Cr, Fe)₂O₃, FeV₂O₄, Ni(VO₃)₂ and NiCr₂O₄ as the main phases. The prominent phases identified in the scales of alloy D were NiO, Ni(VO₃)₂, FeV₂O₄ and NiCr₂O₄. The phases identified in the scales of alloy E were mainly Cr₂O₃, Co₂O₃, WO₃, Co₃V₂O₈, CoV₃ and NiCr₂O₄. The XRD results of these alloys show the presence of some common phases in the scales of these alloys.

5.3.5 SEM-EDAX and EPMA Results

Fig. 5.66 to 5.74 presents SEM micrographs showing typical features on the scale surfaces of alloys A, B, C, D and E after hot corrosion with Na₂SO₄ - 60% V₂O₅ coating at 700, 800 and 900°C for 24 cycles in air. At 700°C the micrograph of alloy A (Fig. 5.66) shows a cracked scale with fine grained structure, while at 800°C the scale has a fine to coarse particles mixed together. At 900°C the scale consists of coarse particles with some cavities. The scale is rich in Fe, Ni and Cr at areas 5-6 (Tab 5.29, Fig. 5.66) as indicated by EDAX in the specimen exposed at 900°C. Fig. 5.68 shows the SEM micrograph of alloy B after similar exposure. At 700°C, it reveals a broken scale with fine grained structure, while at 800°C the scale is having coarse crystalline structure of porous nature. At 900°C the scale has fragmented structure consisting of fine grains. The EDAX shows the surface to be rich in Ni, Cr and V at areas 6-7 (Tab. 5.30, Fig. 5.68a) in specimens exposed at 900°C.

Fig. 5.70 shows the micrographs of alloy C after similar exposure. At 700°C the scale has a thin plate like structure with cavities in between, while at 800 and 900°C the surface of the corrosion product appears as crystals of rounded shape. The EDAX shows the surface to be rich in Ni and Cr with small concentrations of V and Fe at areas 7-8 (Tab. 5.31, Fig. 5.70a) in specimens exposed to 900°C. The SEM micrograph (Fig. 5.72) of alloy D after similar exposure shows a fragmented structure of fine grains at 700°C while at 800°C it reveals a continuous coarse grained structure with some voids. At 900°C the scale surface consists of crystals of different size with rounded edges. Cavities are also

visible in between them. The scale surface is rich in Fe, Ni, Cr and V at areas 6-7 (Tab 5.32, Fig. 5.72a).

The SEM micrographs of alloy E (Fig. 5.74) after similar exposure, shows a fragmented structure of fine grains at 700°C, while at 800°C it reveals fine grained structure distributed uniformly. At 900°C the scale consists of coarse grains of irregular shapes. Voids are also visible at certain areas. The scale is rich in Co and Cr but small amounts of V, Fe and Ni are also present as indicated by EDAX at areas 5-6 (Tab. 5.33, Fig. 5.74a).

The BSE image and X-Ray maps of alloy A coated with Na₂SO₄ - 60% V₂O₅ after exposure for 24 cycles at 900°C in air are shown in Fig. 5.91. The specimen surface is irregular indicating severe corrosion at 900°C. The top layer of scale consists of oxides of Fe and Ni while the inner layer is mainly Cr₂O₃ and some NiO. No internal oxidation has been observed. The BSE image and X-Ray maps of alloy B are shown in Fig. 5.92. The outer layer of scale consists of oxides of Fe, Ni and V while the inner layer is mainly Cr₂O₃ with some vanadium oxide. No internal oxidation/ sulphidation has been observed. The BSE image and X-Ray maps of alloy C are shown in Fig. 5.93. The top layer of the scale consists of oxides of Na, Cr, Fe and Ni and the inner layer consists mainly of Cr₂O₃ and some vanadium oxide. Cr depletion is also observed in the alloy substrate. The BSEI and X-Ray maps of alloy D are shown in Fig. 5.94. The outer scale is rich in the oxides of V, Cr, Fe and Ni whereas the inner layer is mainly Cr₂O₃. The BSEI and X-Ray maps of alloy E are shown in Fig. 5.95. The outer layer is rich in the oxides of Cr, Ni, Co, Fe and W and the inner layer is mainly Cr₂O₃ and some vanadium oxide.

5.4 HOT CORROSION STUDIES IN COMBUSTION GASES

The specimens of alloys A, B, C, D and E with pure Na₂SO₄, Na₂SO₄-15%V₂O₅ and Na₂SO₄-60%V₂O₅ coatings were studied in the actual industrial environment at the superheater zone of a boiler of power plant of the Bhilai Steel Plant, Bhilai (India). Their results are presented in this section.

5.4.1 Kinetic Data

Fig 5.16-5.20 show the plots drawn between wt. gain and time (no. of cycles), for the salt mixtures (pure Na_2SO_4 , Na_2SO_4 -15% V_2O_5 , Na_2SO_4 -60% V_2O_5) coated specimens of alloys A, B, C, D and E after exposure at 1100°C for 6 cycles (cycle of 24h heating and 1h cooling) in combustion gas whose composition is shown in Table 4.2. The plot for alloy A (Fig. 5.16) shows a rapid increase in wt. gain during the first cycle, afterwards the rate of wt. gain decreases. The wt. gain values are higher for Na_2SO_4 -60% V_2O_5 coated specimen than those for Na_2SO_4 -15% V_2O_5 and Na_2SO_4 coated specimens. It can be inferred that the increase in V_2O_5 content in the salt mixture increases the corrosion rate. The plots for alloy B (Fig. 5.17) also show a rapid increase in wt. gain during the first cycle, afterwards the rate of wt. gain slows down for Na_2SO_4 and Na_2SO_4 -15% V_2O_5 coated specimens. But for the specimen coated with Na_2SO_4 -60% V_2O_5 , the rate of wt. gain is higher. For alloy C, D and E (Fig. 5.18-5.20) also similar trend of wt. change was observed. For these alloys the wt. gain values, in general, are minimum with pure Na_2SO_4 coated specimens which increase with increase in V_2O_5 concentration.

All these alloys obey parabolic rate law during their hot corrosion in the present studies. Parabolic rate constants for these alloys were calculated from the (wt. gain)²-time plots and the values are shown in Table 5.2. The rate constant values increase with increase in V_2O_5 content. This again confirms that corrosiveness of the environment increases with increase in V_2O_5 concentration.

5.4.2 Visual Observation

Fig. 5.26-5.30 shows the macrographs of the specimens of alloys A, B, C, D and E after exposure at 1100°C for 6 cycles in c.g. environment. Pure Na_2SO_4 and Na_2SO_4 -15% V_2O_5 coated specimens of these alloys revealed grey coloured, adherent scale on their surfaces. Some dust and dirt particles of the furnace atmosphere were also sticking to it. Na_2SO_4 -60% V_2O_5 coated specimens of these alloys revealed dark grey coloured, adherent scale with some dust particles on their surfaces. The general appearance of these alloys after exposure was dull.

5.4.3 Measurement of Scale Thickness

The average thickness for scales of these alloys were measured by EPMA after exposure in Na_2SO_4 -60% V_2O_5 in c.g. at 900°C and these values are 18.0, 33.0, 31.6, 2.0 and 37.0 microns for alloys A, B, C, D and E respectively.

5.4.4 X-ray Diffraction Analysis

The X-ray diffraction results of the corroded specimens of alloys A, B, C, D and E after exposure in c.g. at 1100°C are shown in Tab. 5.19-5.23 and XRD profiles are shown in Fig. 5.46-5.50. The phases identified on the corroded specimen of alloy A with Na_2SO_4 coating were α - Fe_2O_3 , Cr_2O_3 , NiO, TiO_2 and Al_2O_3 and with Na_2SO_4 -15% V_2O_5 coating in addition to these oxides, FeV_2O_4 was also present, while with Na_2SO_4 -60% V_2O_5 coating an additional phase NiCr_2O_4 was identified. NiO, Cr_2O_3 , TiO_2 and NiCr_2O_4 were identified with Na_2SO_4 specimens, whereas in addition to these FeV_2O_4 was also identified with Na_2SO_4 -15% V_2O_5 and Na_2SO_4 -60% V_2O_5 coated specimens of alloy B. In alloy C the phases identified were α - Fe_2O_3 , Cr_2O_3 , NiO, CrS with pure Na_2SO_4 coating, α - Fe_2O_3 , NiO, Cr_2O_3 , $\text{Ni}(\text{VO}_3)_2$ and FeV_2O_4 with Na_2SO_4 -15% V_2O_5 coating and α - Fe_2O_3 , Cr_2O_3 and NiO with Na_2SO_4 -60% V_2O_5 coating.

The XRD indicated α - Fe_2O_3 , Cr_2O_3 , NiO, TiO_2 and CrS as the prominent phases with Na_2SO_4 coated specimen, Cr_2O_3 , α - Fe_2O_3 , NiO, TiO_2 , Al_2O_3 and $\text{Ni}(\text{VO}_3)_2$ with Na_2SO_4 -15% V_2O_5 coated specimen and α - Fe_2O_3 , Cr_2O_3 , NiO and TiO_2 with Na_2SO_4 -60% V_2O_5 coated specimen of alloy D. The phases identified on the corroded specimens of alloy E with Na_2SO_4 coating were α - Fe_2O_3 , Cr_2O_3 and Co_3O_4 , with Na_2SO_4 -15% V_2O_5 coating were α - Fe_2O_3 , Cr_2O_3 , NiO, CoO, $\text{Co}_3\text{V}_2\text{O}_8$ and FeV_2O_4 whereas α - Fe_2O_3 , Cr_2O_3 , CoO, $\text{Co}_3\text{V}_2\text{O}_8$ and NiCr_2O_4 were identified as the prominent phases with Na_2SO_4 -60% V_2O_5 coated specimen.

5.4.5 SEM-EDAX AND EPMA RESULTS

The SEM micrographs for alloy A specimens (Fig. 5.67) after hot corrosion at 1100°C with coatings of pure Na_2SO_4 , Na_2SO_4 -15% V_2O_5 and Na_2SO_4 -60% V_2O_5 in c.g. for 6 cycles shows a compact surface containing some voids with pure Na_2SO_4 coating,

while with $\text{Na}_2\text{SO}_4\text{-15\%V}_2\text{O}_5$ it reveals fine grains but are fragmented. With $\text{Na}_2\text{SO}_4\text{-60\%V}_2\text{O}_5$ coating the scale surface has fragments consisting of fine particles. The scale surface is rich in Cr and Ni with small amounts of Fe, V and Ti at bright and dark areas 7-8 (Tab. 5.29, Fig. 5.67a) as indicated by EDAX. Fig. 5.69 shows the SEM micrographs of alloy B specimens after similar exposure. With pure Na_2SO_4 coated specimen it reveals a mixed structure of fine to coarse grains with some cavities, while with $\text{Na}_2\text{SO}_4\text{-15\%V}_2\text{O}_5$ coating, the scale surface consists of fine grains with rounded shape. With $\text{Na}_2\text{SO}_4\text{-60\%V}_2\text{O}_5$ coated specimen the micrograph reveals again a mixture of fine and coarse particles and is rich in Ni and Cr at bright and dark areas 8-9 (Tab. 5.30, Fig. 5.69a), as indicated by EDAX.

Fig. 5.71 shows the SEM micrographs of alloy C after similar exposure. With pure Na_2SO_4 coating it reveals a network of rounded particles with some cavities, while with $\text{Na}_2\text{SO}_4\text{-15\%V}_2\text{O}_5$ coating it reveals a mixed structure consisting of fine and coarse size particles of rounded shape and are present in various fragments. With $\text{Na}_2\text{SO}_4\text{-60\%V}_2\text{O}_5$ coating the scale structure consists of a heterogeneous mixture of fine to large grains and is rich in Cr and Ni while small amounts of Fe, V, Ti and Al are also present at bright and dark areas 8-9 (Tab. 5.33, Fig. 5.71a) as indicated by EDAX. Fig. 5.73 shows the SEM micrograph of alloy D after similar exposure. With pure Na_2SO_4 and $\text{Na}_2\text{SO}_4\text{-15\%V}_2\text{O}_5$ it reveals a mixture of fine and coarse particles of rounded shape, while with $\text{Na}_2\text{SO}_4\text{-60\%V}_2\text{O}_5$ coating it reveals a structure of two fragments consisting of fine grains. The scale surface of $\text{Na}_2\text{SO}_4\text{-60\%V}_2\text{O}_5$ coated specimen is rich in Cr, Ni, Fe, Si, Ti and Al at bright and dark areas 7-8 (Tab. 5.32, Fig. 5.73a) as revealed by EDAX.

The SEM micrograph of alloy E after similar exposure are shown in Fig. 5.75. With pure Na_2SO_4 coated specimen it reveals a mixture of particles of various sizes and shapes. Some big particles are also observed. With $\text{Na}_2\text{SO}_4\text{-15\%V}_2\text{O}_5$ coated specimen it reveals fragmented structure of black and white regions, while with $\text{Na}_2\text{SO}_4\text{-60\%V}_2\text{O}_5$ coating it reveals again a fragmented structure with some cavities in between which is rich in Co, Cr, Ni, Fe and Al at dark and bright areas 7-8 (Tab. 5.33, Fig. 5.75a) based on EDAX analysis.

The BSEI and X-ray maps of alloy A coated with $\text{Na}_2\text{SO}_4\text{-60\%V}_2\text{O}_5$ after hot corrosion in c.g. for 6 cycles at 1100°C are shown in Fig. 5.96. The top layer of scale consists of oxides of Fe, Al and Cr, while the inner layer is mainly Cr_2O_3 with some Al_2O_3 and TiO_2 at the grain boundaries in the substrate. The X-ray maps of alloy B are shown in Fig. 5.97. The top layer consists of oxides of Fe, Ni, Cr and V, whereas the inner layer is of Cr_2O_3 and some $\alpha\text{-Fe}_2\text{O}_3$. The BSE image and X-ray maps of alloy C are shown in Fig. 5.98. The outer layer is mainly $\alpha\text{-Fe}_2\text{O}_3$ while the inner layer is mostly Cr_2O_3 . The X-ray maps of alloy D are shown in Fig. 5.99. The outer layer is of $\alpha\text{-Fe}_2\text{O}_3$ and Cr_2O_3 , while the inner layer is mainly Cr_2O_3 . Oxygen has penetrated into the substrate so as to cause internal oxidation and is present at the grain boundaries. The BSEI and X-ray maps of the alloy E are shown in Fig. 5.100. The top scale is rich in the oxides of Fe, Ni, Co and V and the thin inner layer is mainly of Cr_2O_3 .

5.5 HOT CORROSION STUDIES IN $\text{Na}_2\text{SO}_4\text{-60\% V}_2\text{O}_5 + \text{MgO}$

From the wt. gain values obtained in the present studies for alloys A, B, C, D and E in various environments, it was observed that the wt. gain values were maximum at 900°C in $\text{Na}_2\text{SO}_4\text{-60\%V}_2\text{O}_5$. Thus moderate to severe corrosion of these alloys has been observed in $\text{Na}_2\text{SO}_4\text{-60\%V}_2\text{O}_5$ at 900°C . To minimize the aggressiveness of the environment, hot corrosion studies for these alloys were made by MgO addition to the salt mixture $\text{Na}_2\text{SO}_4\text{-60\%V}_2\text{O}_5$ at 900°C for 24 cycles in air. MgO was used in the ratio of 3MgO:1 V_2O_5 . Their results are presented in this section.

5.5.1 Kinetic Data

Fig 5.21 - 5.25 show the plots drawn between wt. change and time (no. of cycles) for the alloys A, B, C, D and E after exposure in $\text{Na}_2\text{SO}_4 - 60\% \text{V}_2\text{O}_5 + \text{MgO}$ at 900°C for 24 cycles. Fig 5.21 for alloy A shows that there is a rapid increase in wt. gain during the first two cycles and then there is a gradual decrease in wt. gain. In this figure a comparison is shown between the wt. gain values obtained for alloy A in $\text{Na}_2\text{SO}_4 - 60\% \text{V}_2\text{O}_5$ at 900°C with and without MgO addition. The total wt. gain value obtained without MgO addition (23.2 mg/cm^2 wt. loss) changed to 2.2 mg/cm^2 with MgO addition. Figure

5.22 for alloy B shows that a rapid increase in wt. gain occurs during the first two cycles, then there is a slower rate of decrease in wt. gain. The wt. gain values obtained with MgO addition are much lower than the values obtained with only Na_2SO_4 -60% V_2O_5 environment only under similar condition. The total wt. gain value for alloy B decreased from 6.75 to 5.0 mg/cm^2 . Fig 5.23 for alloy C also shows similar trend of rapid increase in the wt. gain value during the first two cycles and then a continuous decrease in wt. gain. The wt. gain values are much lower with MgO addition than those obtained without its addition. The total wt. gain value decreases from 11.55 to 6.3 mg/cm^2 with MgO addition. Fig 5.24 shows the wt. change plot for alloy D. Again there is a rapid increase in wt. gain during the first two cycles and then the rate of wt. gain decreases. The wt. gain values with MgO addition are lower than that for Na_2SO_4 -60% V_2O_5 coated specimens. The total wt. gain value decreases from 12.0 to 8.05 mg/cm^2 with MgO addition. Fig 5.25 for alloy E also shows a rapid increase in wt. gain during the first two cycles and then the rate of wt. gain decreases. The total wt. gain value decreases from 35.75 to 5.20 mg/cm^2 with MgO addition. From these observations it can be inferred that MgO addition has a beneficial effect in resisting corrosion of these alloys in Na_2SO_4 -60% V_2O_5 environment.

5.5.2 Visual Observation

Fig 5.26 - 5.30 shows the macrographs of the corroded specimens of alloys A, B, C, D and E after exposure for 24 cycles at 900°C with Na_2SO_4 - 60% V_2O_5 + MgO coating in air. The scale on alloy A showed a brown and yellow coloured mass adherent in nature. The scale of alloy B also revealed similar scale to that of alloy A. The scale of alloy C showed a dark grey and yellow coloured mass on the surface. The scale of alloy D revealed dark grey, yellow and brown coloured mass. The scale of alloy E showed grey, yellow and green coloured lustrous mass of adherent nature. Some spalling of the scale was also observed.

5.5.3 Measurement of Scale Thickness

The beneficial effect of MgO addition is also confirmed by the observed scale thickness values. The thickness values obtained with Na_2SO_4 -60% V_2O_5 coating were

62.5, 45.0, 75.0, 67.5 and 96.6 micron for these alloys decreased to 33.3, 43.0, 62.0, 62.7 and 55.0 microns respectively for alloys A, B, C, D and E.

5.5.4 X-Ray Diffraction Analysis

The results of XRD analysis of the corroded specimens of alloys A, B, C, D and E with Na₂SO₄-60% V₂O₅ + MgO coating after exposure for 24 cycles at 900°C in air are compiled in Table 5.24-5.28 and their XRD profiles are shown in Fig. 5.5-5.55. The prominent phases identified in the scale of alloy A were α -Fe₂O₃, Cr₂O₃, FeS, FeV₂O₄, Mg₃V₂O₈ and NiCr₂O₄, whereas Cr₂O₃, NiO, Ni(VO₃)₂ and Mg₃V₂O₈ were identified as the main phases in the scale of alloy B. The prominent phases identified in the scale of alloy C were NiO, Cr₂O₃, FeV₂O₄, Mg₃V₂O₈ and NiCr₂O₄. The presence of α -Fe₂O₃, Cr₂O₃, FeV₂O₄, Mg₃V₂O₈ and NiCr₂O₄ as main phases was indicated in the scale of alloy D. The prominent phases identified in the scale of alloy E were Cr₂O₃, WO₃, FeV₂O₄, Co₃V₂O₈ and NiCr₂O₄.

5.5.5 SEM-EDAX AND EPMA RESULTS

Fig 5.76-5.80 presents SEM micrographs of alloys A, B, C, D and E with Na₂SO₄ - 60% V₂O₅ + MgO coating after exposure at 900°C in air for 24 cycles. The micrographs show typical features observed after hot corrosion. The micrograph of the scale on alloy A (Fig. 5.76) reveals an irregular structure consisting of various sized crystals having rounded corners and is rich in Cr, Fe, Mg and V with little amounts of Ti and Mn at areas 9-12 (Tab. 5.29, Fig 5.76) as indicated by EDAX. The micrograph of alloy B (Fig 5.77) shows an irregular structure of coarse grains. There are big cavities between them. Based on EDAX the scale surface is rich in Ni, Cr, V and Mg at areas 10 and 11 (Tab. 5.30, Fig. 5.77).

The micrograph of alloy C (Fig 5.78) shows a heterogeneous structure consisting of rounded particles. Some very big particles are also observed. Cavities in between them also exist. Based on EDAX, the scale surface is found to be rich in Ni, Cr, Fe, V and Mg at areas 11-13 (Tab 5.31, Fig 5.78). The micrograph of alloy D (Fig 5.79) shows a compact structure of scale with some voids in them. Some rounded particles are also

observed. Based on the EDAX, the scale surface is found to be rich in Cr, Ni and Fe with small amounts of V, Ti and Al at areas 10-12 (Tab 5.32, Fig 5.79).

The micrograph of alloy E (Fig 5.80) shows a structure of fine grains uniformly distributed throughout. Some small cavities are also visible. Based on the EDAX, the scale surface is rich in Co and Cr with small amounts of Fe, Ni, V, Mn and Mg at areas 9-10 (Tab 5.33, Fig 5.80).

The BSEI and X-ray maps of alloy A with $\text{Na}_2\text{SO}_4\text{-60\%V}_2\text{O}_5 + \text{MgO}$ coating after exposure for 24 cycles at 900°C in air are shown in Fig 5.101. The BSEI reveals a duplex scale. The outer layer is rich in oxides of V, Mg, Cr, S and Fe while the inner layer is mainly Cr_2O_3 with some sulphur. Internal sulphidation has also been observed. The X-ray maps of alloy B are shown in Fig 5.102. The top scale is rich in oxides of Cr, V, Ni, and Fe whereas the inner layer is rich in Cr_2O_3 . Internal oxidation has occurred at the grain boundaries. The X-ray maps of alloy C (Fig 5.103) reveal an outer layer consisting of oxides of Mg, Fe, V, Cr and Ni and the inner layer consisting mainly of Cr_2O_3 . The X-ray maps of alloy D (Fig 5.104) show that the top scale is rich in the oxides of Mg, Ni and V while the inner scale consists of Cr_2O_3 and some oxides of Fe, V and Ni. The X-ray maps of alloy E are shown in Fig 5.105. The top layer of the scale is rich in the oxides of Cr, W, Ni, Co and V, while the inner scale consists of Cr_2O_3 and some oxides of W and V also, Cr depletion in the substrate has also been observed. Sulphur has penetrated into the substrate and the formation of NiS has been observed.

DISCUSSION

In this chapter, the results of hot corrosion studies on super alloys Superfer 800H(A), Superni 75(B), Superni 600(C), Superni 718(D) and Superco 605(E) in various salt mixture environments like pure Na_2SO_4 , Na_2SO_4 -15% V_2O_5 , Na_2SO_4 -60% V_2O_5 and Na_2SO_4 -60% V_2O_5 + MgO under cyclic conditions at 700, 800, 900 and 1100°C are discussed.

6.1 Hot Corrosion Studies in Pure Na_2SO_4

The influence of pure Na_2SO_4 coating on alloys A, B, C, D and E was not very marked at 700, 800 and 900°C. The wt. change - time plots for alloys A, B, C, D and E (Fig. 5.1-5.5) show that the temperature of corrosion has significant effect on the wt. gain values. The weight gain value (0.29 mg/cm²) for alloy A after exposure for 24 cycles at 700°C increases with temperature to 1.2 times at 800°C and 1.79 times at 900°C. Similarly for alloy B under similar exposure, the wt. gain value 0.15 mg/cm² at 700°C increases 1.66 and 1.8 times at 800 and 900°C respectively. For alloy C the value of weight gain (0.21 mg/cm²) at 700°C increases 1.52 and 2.23 times at 800 and 900°C respectively. For alloy D the wt. gain value increases from 0.22 mg/cm² at 700°C to 1.59 and 1.68 times more at 800 and 900°C respectively. For alloy E the wt. gain value increases from 0.24 mg/cm² at 700°C to 1.2 and 1.75 times at 800 and 900°C respectively. The overall ranking for all the alloys studied on the basis of wt. change, the extent of corrosion follows the sequence (in order of decreasing rate)

$$900^\circ\text{C} > 800^\circ\text{C} > 700^\circ\text{C}$$

The nature of the wt. change vs time plots for alloys A, B, C and D are nearly similar, hence it may be inferred that these alloys might have behaved very similarly at

700, 800 and 900°C. For these alloys, there is a rapid increase in wt. gain during the first two cycles and then the wt. gain rate of specimens decreases. But the wt. gain vs time plot for alloy E shows that after the rapid wt. gain during the first two cycles, it remains constant. As the wt. gain values observed for all the alloys after exposure for 24 cycles at 700, 800 and 900°C are very nominal, it can be inferred that all these alloys studied have good corrosion resistance against pure Na₂SO₄ attack. The average scale thickness values measured by EPMA are also very nominal to the extent of 17.0, 7.5, 9.0, 10.0 and 8.0 micron for alloys A, B, C, D and E respectively for exposure at 900°C. This further confirms the good corrosion resistance of these alloys against 4.0-5.0 mg/cm² Na₂SO₄ salt coating environment. This may be due to the high concentrations of Cr in these alloys (15.5 - 21.0%)⁽⁵¹⁾.

As Fe, Ni and Cr are the predominant elements present in the Fe-, Ni- and Co-base superalloys studied in the present investigation, the oxides of these elements are present in high concentrations in the scales of these alloys. Generally Cr₂O₃ is present at the alloy/scale interface. Other oxides are present in the outer layer of the scale as clearly revealed by the X-ray maps (Fig. 5.81-5.85). XRD also identified the presence of α-Fe₂O₃, Cr₂O₃, NiO phases as shown in the X-ray diffraction profile (Fig. 5.31-5.55). CrS was identified in the scales of alloys C and D by XRD, although X-ray maps did not detect the presence of sulphur. TiO₂ is also present in the scale formed on the surface of alloy D after exposure for 24 cycles at 900°C as detected by XRD and X-ray maps (Fig. 5.84e). In the scale of alloy E the presence of additional phases Co₃O₄ and WO₃ were also detected by XRD and EPMA (Fig. 5.85 e and f). These oxides later formed spinels such as NiCr₂O₄, (Cr, Fe)₂O₃ and are present in the outer part of the scales as revealed by X-ray maps (Fig. 5.81-5.85). Oxygen or sulphur penetration into the alloys has not been observed by EPMA which suggests that the chromia layer was quite continuous and compact. The X-ray maps of A, B, C, D and E (Fig. 5.81-5.85) reveal the thick, compact layer of Cr₂O₃ at the scale/alloy interface. It has been observed that the chemical nature of the compounds formed normally does not change with temperature as observed by XRD results. It can be inferred that the corrosion mechanism is almost similar at 700, 800 and 900°C. The maximum corrosion rate observed at 900°C in all the alloys may be attributed

to the molten state of the Na₂SO₄ (m.p. 884⁰C) during the test as suggested by Shores and Luthra⁽⁵⁴⁾ that the presence of a liquid phase is regarded as necessary for hot corrosion to occur. It was observed during the test at 900⁰C for these alloys that the attack normally occurred on the bottom half of the specimen due to slumping of the liquid Na₂SO₄. Shores and Luthra⁽⁵⁴⁾ also have observed similar phenomena in their test in pure Na₂SO₄.

The possible mechanism of corrosion induced by pure Na₂SO₄ on alloy A during exposure for 24 cycles at 700, 800 and 900⁰C can be explained as follows:

First of all Cr might have formed Cr₂O₃, due to its high affinity for oxygen and its higher stability as compared to that of other oxides⁽⁸⁵⁾.

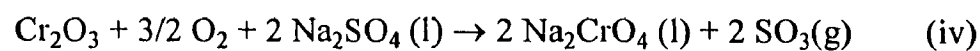


Chromium might have developed a continuous film of stable Cr₂O₃ at the alloy/scale interface. Cr₂O₃ formation at the initial stage of the corrosion reaction may be the reason for rapid increase in wt. gain during the first two cycles of the test⁽⁸⁵⁾. And the development of continuous film might have reduced the corrosion rate (wt. gain rate) after 2 cycles as the oxidation now proceeds by diffusion of oxygen to the metal/oxide interface through the oxide layer. Similar reporting has been made by Luthra⁽⁷²⁾ in his studies on Co-Cr alloys in Na₂SO₄.

Fe and Ni present in the alloy A in high concentrations also might have reacted to form their respective oxides as



Similar sequence of reactions have been reported by Malik et. al⁽³¹⁾, Fryburg et. al⁽⁴⁶⁾ and Luthra⁽⁷²⁾. Cr₂O₃ scale then might have been basically fluxed with Na₂SO₄ to form Na₂CrO₄ as



Later Na₂CrO₄ evaporated⁽⁴⁶⁾



Due to reaction (v) the Cr₂O₃ layer no longer remains protective and further degradation of the alloy A takes place after 10 cycles up to the end (Fig. 5.1). Malik et.

al⁽³¹⁾ have also suggested the reaction (v) in their studies on 18:8 Cr:Ni stainless steel in Na₂SO₄.

The oxides Fe₂O₃, Cr₂O₃ and NiO are present in the outer part of the scale. The initially built layer of oxides moved away from the matrix and made it the outer most oxide layer as mentioned by Saxena⁽⁸⁵⁾.

Similar mechanism, as explained for Fe-base alloy A (superfer 800H), can be extended to Ni-base alloys B, C and D due to the reason that the nature of the wt. change-time plots of these alloys are similar to that of alloy A. Also in alloys B and C the prominent elements are Fe, Ni and Cr only which are predominantly present in alloy A. These alloys might have behaved similarly against pure Na₂SO₄ attack during 24 cycle exposure at 700, 800 and 900⁰C. In alloy B, the Cr content is more (19.5%) than that present in alloy C (15.5%), hence the alloy B probably resisted pure Na₂SO₄ attack to higher extent than alloy C as lower wt. gain values were observed at 700, 800 and 900⁰C. (Fig. 5.2 - 5.3).

Due to the formation of oxides by reactions (i) - (iii), the reduction in O²⁻ activities might have occurred which resulted in an increase in sulphur activity and would be sufficient to form CrS as observed in the scales of alloys C and D as shown by XRD profile (Fig. 5.33-5.34). Similar reporting has been made by Malik et. al.⁽⁴⁹⁾ in their studies on Ni-base alloys with pure Na₂SO₄ coating. The presence of TiO₂ in the scale of alloy D is observed (Fig. 5.84 e). Ti also might have reacted in the similar manner to Fe, Ni, Cr (reactions i - iii) with oxygen to form TiO₂⁽⁴⁶⁾.

Similar mechanism, as explained for Fe- and Ni-base alloys may be extended to Co-base alloy E as well, as similar nature of wt. gain plots is observed and XRD also detected similar phases. The additional phases CoO₃ and WO₃ observed in the scale of alloy E might be due to the oxidation of elements Co and W present in high concentrations in the alloy by similar reactions (i) to (iii). The oxygen was available from pure Na₂SO₄. Fryburg et. al.⁽⁴⁶⁾ have also suggested similar reactions for Co and W oxidation in illustrating the corrosion mechanism of Ni-base alloys in pure Na₂SO₄. Luthra⁽⁷²⁾ and Shores⁽⁵⁴⁾ after hot corrosion studies on Ni-30Cr and Co-30Cr alloys by pure Na₂SO₄, have mentioned that the rapid attack of oxygen at the beginning of

oxidation would be accompanied by the formation of nuclei of cobalt and chromium oxides.

The morphology of scales formed on the surfaces of alloys A, B, C, D and E is, in general, duplex in nature as observed by X-ray maps of these alloys. The morphology observed in this investigation is similar to that observed by Malik et. al.⁽⁴⁹⁾ in their studies on Nimonic alloys at 1000⁰C and also resembles to that reported by Sharma⁽⁸⁶⁾ in his hot corrosion studies on Fe- and Ni-base alloys in pure Na₂SO₄ at 950⁰C. Some unreacted particles of the salt were also visually observed on the surface of the scale formed on these alloys after exposure for 24 cycles at 700 and 800⁰C. Na₂SO₄ was identified in the scale of alloy A by XRD (Fig. 5.31), while Na and S were not detected by EPMA X-ray maps (Fig. 5.81). This may be due to the solid state of pure Na₂SO₄ (m.p 884⁰C) at these temperatures⁽⁸⁶⁾.

With a thin deposit (4.0-5.0 mg/cm²) of pure Na₂SO₄ used in the present studies , the hot corrosion rates follow the sequence :

700⁰C → alloy A > alloy E > alloy D > alloy C > alloy B

800⁰C → alloy E > alloy A > alloy D > alloy C > alloy B

900⁰C → alloy A > alloy C > alloy E > alloy D > alloy B

No internal oxidation or sulphidation was observed in the substrate of any of the alloys, this indicates that Cr₂O₃ protective layer was dense and compact (Fig. 5.81-5.85). Mo and Ta are present in a markable concentration in alloy D but their presence in the scale has not been detected either by EDAX or by EPMA analysis. Hence it can not be said in what way they have behaved during the corrosion. However, Fryburg et. al.⁽⁴⁷⁾ have concluded from their studies on Ni-base alloys B1900 and IN738 with Na₂SO₄ coating that Ta has beneficial effect while Mo is deleterious. Ta₂O₅ has the ability to tie up with Na₂SO₄ and prevent the formation of a molten Na₂MoO₄. Thus Ta minimises the deleterious effect of Mo. Spinel formation has also been observed in the scales of all the alloys by the combination of oxides. The combination of oxides occurs in the outer layer of the scale and their presence is detected by XRD (Fig . 5.31-5.35) and further confirmed by EPMA X-ray maps (Fig. 5.85). Peters et. al.⁽⁹³⁾ have also observed the presence of spinels in their studies on Ni-base alloys in pure Na₂SO₄. The EPMA X-ray maps reveal

regular surfaces of the alloys after exposure at 900°C for 24 cycles suggesting that these alloys have good corrosion resistance against pure Na₂SO₄. The wt. gain and scale thickness values both are low and hence confirm their high corrosion resistance. The probable corrosion mechanism has been explained with schematic diagrams for alloy A, D and E (Fig. 6.1).

6.2 HOT CORROSION STUDIES IN Na₂SO₄ - 15% V₂O₅

The effect of 15% V₂O₅ addition in Na₂SO₄ on the hot corrosion behaviour of alloys A, B, C, D and E after exposure for 24 cycles at 700, 800 and 900°C in air in laboratory tube furnace was investigated and their results are discussed in this section.

The influence of Na₂SO₄ - 15% V₂O₅ salt mixture coating on alloys A, B, C, D and E was not very marked at 700 and 800°C as the observed wt. gain values for these alloys at 700 and 800°C were quite low. At 900°C the total wt. gain values were moderate (3.0-3.75 mg/cm²) for alloys A, B, C and E while it was high (6.8mg/cm² wt. loss) for alloy D. The wt. change-time plots for these alloys show that the temperature of corrosion has significant effect on the total wt. gain values. The wt. gain value for alloy A after 24 cycle exposure at 700°C is 2.2 mg/cm² which increases 1.25 times at 800°C and 1.34 times at 900°C. Similarly for alloy B, under similar exposure, the wt. gain value at 700°C (0.60 mg/cm²) increases 2.0 times at 800°C and 6.26 times at 900°C. The wt. gain value 0.50 mg/cm² at 700°C for alloy C increases 1.3 times at 800°C and 7.8 times at 900°C. For alloy D the wt. gain value at 700°C (0.60 mg/cm²) after 24 cycle exposure increases 2.33 times at 800°C and 11.33 times at 900°C. The wt. gain value for alloy E after 24 cycle exposure at 700°C (1.05 mg/cm²) increases 2.09 times at 800°C and 3.0 times at 900°C. The overall ranking for all the alloys studied on the basis of wt. change, the extent of corrosion follows the sequence :

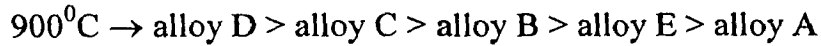
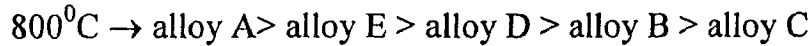
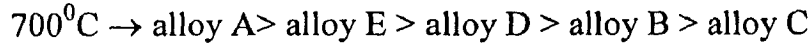
$$900^{\circ}\text{C} > 800^{\circ}\text{C} > 700^{\circ}\text{C}$$

The wt. gain values after exposure for 24 cycles at 700, 800 and 900°C in Na₂SO₄-15% V₂O₅ environment for alloy A are 7.5, 7.8 and 5.67 times higher than their corresponding values at 700, 800 and 900°C respectively in pure Na₂SO₄. For alloy B, under similar exposure condition, the wt. gain values are 4, 4.8 and 13.92 times higher

than their corresponding values at 700, 800 and 900⁰C respectively in pure Na₂SO₄. The wt. gain values for alloy C, after exposure under similar condition, are 2.5, 2.0 and 8.0 times higher than their corresponding values at 700, 800 and 900⁰C respectively in pure Na₂SO₄. For alloy D, the wt. change values, after exposure under similar conditions, increase 3.0, 4.0 and 18.0 times their corresponding values in Na₂SO₄ at 700, 800 and 900⁰C respectively. The wt. gain values of alloy E are 4, 7.6 and 8.5 times higher than their corresponding values in Na₂SO₄ at 700, 800 and 900⁰C respectively. On comparison of the values of wt. gain observed for these alloys in Na₂SO₄ and Na₂SO₄ - 15% V₂O₅ environments, it can be clearly inferred that 15% V₂O₅ addition increases the corrosion rate and thus it makes the environment more severe than that of pure Na₂SO₄.

The nature of the wt. change vs time plots for alloys A, B, C, D and E are nearly similar i.e. a rapid increase in corrosion rate during the first two cycles and then the reduction in rate of wt. gain during the remaining period at 700 and 800⁰C. Hence it can be inferred that these alloys behaved very similarly at 700 and 800⁰C during the corrosion process. At 900⁰C, the nature of curve differs from alloy to alloy. For alloy A after the linear increase during first two cycles the rate of wt. gain value decreases slowly, while for alloy E there is an increase in wt. gain up to 8 cycles and then the wt. gain value remains constant. For alloys B and C there is a rapid rate of wt. gain during first two cycles and then the corrosion rate decreases although the rate of wt. gain gradually increases up to the last cycle of the test. But the nature of wt. change vs time plot for alloy D is quite irregular. There is a rapid rate of corrosion during the first 6 cycles then the wt. gain value starts decreasing and after about 9 cycles it becomes zero. Later, there is a further decrease in weight of the corroded specimen leading to wt. loss which continues up to 12 cycles. After 12 cycles the wt. loss value remains constant. It is observed that the difference in nature of the wt. gain-time plots for alloys A, B, C and E is insignificant and hence their mechanism of corrosion must be very similar at 900⁰C also during exposure for 24 cycles. The mechanism of corrosion for alloy D seems to be a complex one. The total weight gain values for alloys A, B, C and E after exposure for 24 cycles at 900⁰C lie between 2.9 to 3.75 mg/cm² which is a very moderate value. It can be inferred that alloys A, B, C and E have good corrosion resistance against Na₂SO₄ - 15% V₂O₅ at 700, 800 and

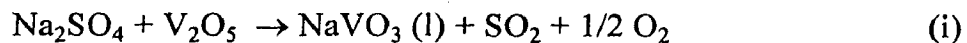
900⁰C while alloy D behaves well at 700 and 800⁰C only. For alloy D the wt. loss of 6.8 mg/cm² was observed. It is suggested that with a thin deposit of Na₂SO₄ - 15% V₂O₅, the hot corrosion rates follow the sequence :



The average scale thickness values (40.0-47.0 μm) measured by EPMA, X-ray maps for alloys A, B, C, D and E are also comparable. These values are nearly 5 times for alloys B, C, D and E while it is only 2.4 times for alloy A of their values in Na₂SO₄. This observation further confirms that V₂O₅ addition to pure Na₂SO₄ makes the environment more corrosive which ultimately leads to the formation of thicker scales. The alloys A, B, C and E at 700, 800 and 900⁰C and alloy D only at 700 and 800⁰C have good corrosion resistance which may be due to the presence of high Cr content in these alloys⁽⁵¹⁾.

The possible mechanism for the corrosion of alloy A against Na₂SO₄ -15% V₂O₅ coating at 700, 800 and 900⁰C for 24 cycle exposure can be explained as follows :

Na₂SO₄ and V₂O₅ salt mixture coated specimens of these alloys when heated they might have reacted together to form a liquid phase of NaVO₃ as observed by Kolta et. al.⁽⁶⁶⁾.



The oxygen available from reaction (i) then might react with Cr to form Cr₂O₃ because Cr₂O₃ is much more thermodynamically stable compound than NiO and FeO over the temperature range of the present studies⁽⁸⁵⁾.



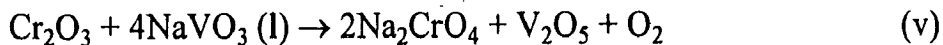
Thus, Cr₂O₃ would form in the earliest stages of corrosion⁽⁸⁵⁾. The rapid increase in corrosion rate during the first two cycles may be attributed to the Cr₂O₃ formation. The molten NaVO₃ (m.p. 610⁰C) at the test temperatures (700, 800 and 900⁰C) causes higher extent of corrosion in these alloys than that observed in pure Na₂SO₄ at 700, 800 and 900⁰C⁽⁵⁴⁾. NaVO₃ might have acted as a catalyst for oxidation and served as a oxygen carrier to the alloy⁽⁶⁶⁾. In alloy A the concentration of Fe being the base metal and Ni are very high hence they might have reacted to form their respective oxides as⁽⁴⁶⁾.



The presence of oxides of Fe, Ni and Cr is revealed by the X-ray maps (Fig. '5.86-5.90) in the outer layer of the scale, whereas Cr_2O_3 is present at the alloy/scale interface. XRD also detected the presence of these oxides as the prominent phases. (Tab. 5.9-5.13, Fig. 5.36-5.40).

Once the compact and adherent layer of Cr_2O_3 is formed (Fig. 5.86-5.90), it acts as a barrier for the oxidising species and the diffusion becomes difficult for oxygen or sulphur ions towards the alloy surface. The decreasing rate of wt. gain after two cycles may be due to the formation of protective Cr_2O_3 scale⁽⁸⁶⁾.

Fluxing of Cr_2O_3 with NaVO_3 might have followed the mechanism recommended by Seiersten and Kofstad⁽³⁾ that simultaneous growth of oxide scales and their dissolution in molten salt occurs :



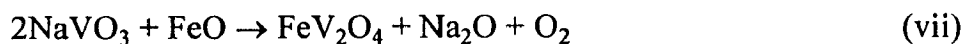
Similar reaction has been reported by Swaminathan et. al.⁽⁸⁷⁾ during their studies on Ni-base superalloy in NaVO_3 environment.

Later Na_2CrO_4 might have evaporated⁽⁴⁶⁾ as



Sodium element was indicated to be absent by the EPMA analysis.

After that, remaining NaVO_3 might have fluxed with Fe_2O_3 to form FeV_2O_4 as

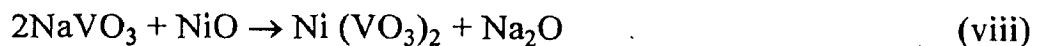


The presence of FeV_2O_4 has been identified by XRD (Fig. 5.36) and Malik et. al.⁽³¹⁾ have also observed the presence of this spinel in their studies on 18:8 stainless steel in Na_2SO_4 - NaVO_3 environment at 850 and 1000⁰C. After that it is expected that the oxides initially formed went away from the substrate⁽⁸⁵⁾ and they might have formed spinels NiCr_2O_4 and $(\text{Cr, Fe})_2\text{O}_3$. These compounds were identified by XRD (Fig. 5.36). The spinel formation and their occurrence in the scales have been reported by Malik et. al.⁽³¹⁾.

Nickel-base superalloys B, C and D might have behaved similarly as alloy A due to the presence of similar elements in high concentrations and also due to their similar nature of wt. change-time plots at 700 and 800⁰C. Hence the mechanism mentioned for

alloy A in this section can be used to explain the mechanism of corrosion for these alloys also during exposure in Na₂SO₄-15% V₂O₅ at 700 and 800⁰C. During first two cycles, the corrosion reaction continued with gradual increase in wt. gain value. This may be due to the formation of Cr₂O₃ film which was not fully protective. The X-ray mappings of alloy B (Fig. 5.87) shows the non protective nature of scale on alloy surface. XRD identified the presence of the Cr₂O₃, NiO and spinel NiCr₂O₄ (Tab. 5.10, Fig. 5.37). EDAX analysis has confirmed the presence of these elements in the scales of alloy B (Tab. 5.30). The heterogeneous mixture of these oxides and spinels can be seen in SEM micrograph (Fig. 5.59). Fe content is only 3% in alloy B hence it has not played an important role in the corrosion process. EPMA indicated that Fe to be absent in the scale.

In case of alloy C, at 900⁰C, the nature of the kinetic curve is of similar nature to that for alloy B. Hence the mechanism may perhaps be similar to that for alloy B. But Fe content in this alloy is 10%, which has oxidised and is present in the form of spinels (Cr,Fe)₂O₃ and FeV₂O₄. These are identified by XRD (Fig. 5.38). In addition to these the following reaction might also have taken place



Sidky and Hocking⁽⁸⁸⁾ have observed the occurrence of this reaction in their studies. The presence of Ni(VO₃)₂ phase has been identified by XRD (Fig. 5.38). Internal oxidation was also revealed by X-ray maps (Fig. 5.88) for alloy C.

In case of alloy D at 900⁰C the nature of the wt. change-time plot is shown to be dramatic. Similar nature of curve was observed by Hou and Stringer⁽⁸⁹⁾. Alloy D contains many number of alloying elements like Fe, Ni, Cr, Ti, Al, Ta and Mo. They might have oxidised and the presence of NiO, Cr₂O₃, Al₂O₃, TiO₂, Fe₃O₄ were identified by XRD as the prominent phases (Fig. 5.39). The MoO₃ might have been formed and then evaporated⁽⁸⁷⁾, hence Mo was indicated to be absent by EPMA in our studies. The very irregular shape of the alloy surface revealed by EPMA X-ray maps (Fig. 5.89) confirms the excessive reaction of the alloy at 900⁰C. It is also revealed by the X-ray map for Cr (Fig. 5.89b) that Cr does not form a uniform, compact and protective scale. The SEM micrograph (Fig. 5.63) for alloy D shows the coarse grained porous structure of the scale surface hence spalling might have taken place which caused the reduction in wt. gain

value. After 6 cycles the reduction in wt. gain value started and continued linearly upto 12 cycles so as to possess a wt. loss of 6.8 mg/cm^2 . As the time progresses the thickness of the oxide layer increased to such an extent that stresses developed in the oxide scale. Since the oxide is quite brittle, the scale cracks and causes fissures that act as channels from the oxide/salt interface to the metal/oxide interface⁽⁸⁴⁾. Thus fresh metal surface gets exposed to oxygen available from the molten salt mixture coating. As a result corrosion rate increases suddenly showing a linear behaviour. This is called breakaway corrosion⁽⁸⁴⁾. Spalling was actually observed during the experiment. The formation and volatilization of some compounds like Na_2CrO_4 , and MoO_3 during the period might also have contributed to the wt. loss of the specimen⁽⁴⁶⁾.

The process of continuous formation and dissolution of oxides continued⁽³⁾ and then as the time progresses the rate of oxide formation might be faster than its dissolution rate, so that Cr_2O_3 again formed a continuous protective layer. Therefore further corrosion became difficult and thus wt. loss remained constant during 12-24 cycles of the present test as shown in Fig. 5.9. Similar explanations have been reported by Hou and Stringer⁽⁸⁹⁾ in their cyclic oxidation test on Ni - 20 Cr alloy at 1100°C . Internal oxidation was also revealed by EPMA X-ray map (Fig. 5.89e-g) through the grain boundaries. Al_2O_3 and TiO_2 were present at the grain boundaries. The formation of $\text{Ni}(\text{VO}_3)_2$ can be assigned to reaction (viii).

The mechanism of corrosion of alloy E at 900°C is similar to that for alloys A, B, C. The mechanism of corrosion is not complex as that of alloy D. The nature of the wt. gain-time plot for alloy E (Fig. 5.10) shows that after rapid increase in corrosion rate during the first two cycles, the wt. gain value increases slowly up to 6 cycles and then it remains constant. The elements Co, Ni, Cr, Fe, W present in the alloy E oxidised during the corrosion process and later their spinel formation might have taken place to form FeWO_4 and NiCr_2O_4 . The phases NiO, Cr_2O_3 , CoO, FeWO_4 and NiCr_2O_4 were identified by XRD (Fig. 5.40). The scale is revealed as multilayered by EPMA X-ray maps (Fig. 5.90). X-ray maps also indicate the presence of NiCr_2O_4 and CoO in the outer layer, below which is the layer of FeWO_4 , CoO and Cr_2O_3 while the inner layer is mainly Cr_2O_3 . Once the compact layer of Cr_2O_3 was formed, further corrosion was not possible

hence the wt. gain-time plot shows constant wt. gain region after 12 cycles. Due to the nature of wt. change plot and the ultimate wt. gain value (3.25 mg/cm^2), the Co-base alloy E resisted $\text{Na}_2\text{SO}_4 - 15\% \text{ V}_2\text{O}_5$ attack even at 900°C during exposure for 24 cycles. The probable mechanism of corrosion is shown schematically in Fig. 6.2-6.3 for alloys A, D and E.

6.3 HOT CORROSION STUDIES IN Na_2SO_4 -60% V_2O_5

The effect of 40% Na_2SO_4 -60% V_2O_5 eutectic mixture coating on the hot corrosion behaviour of alloys A, B, C, D and E after exposure for 24 cycles at 700, 800 and 900°C in air in laboratory tube-furnace was investigated and their results are discussed in this section.

The influence of an eutectic mixture (60% $\text{V}_2\text{O}_5 - 40\% \text{Na}_2\text{SO}_4$) coating on alloys A, B, C, D and E was moderate (2.25 - 11.6 mg/cm^2) at 700 and 800°C but at 900°C the attack was moderate to severe (6.75 - 35.75 mg/cm^2). The attack on alloys A and E was more severe and it can be said rather catastrophic (23.2 mg/cm^2 wt. loss for alloy A and 35.75 mg/cm^2 wt. gain for alloy E)⁽⁴⁸⁾. The wt. change-time plots for these alloys show that the temperature of corrosion has a significant effect on the wt. gain values. The total wt. gain value for alloy A after 24 cycle exposure at 700°C (11.4 mg/cm^2) increases only to 11.6 mg/cm^2 at 800°C and about 2.03 times at 900°C . For alloy B, the total weight gain value at 700°C (2.55 mg/cm^2) increases 2.0 times at 800°C and 2.64 times at 900°C . The total wt. gain value (2.25 mg/cm^2) at 700°C for alloy C increases to 2.85 mg/cm^2 at 800°C while it increases 5.13 times at 900°C . The total wt. gain value for alloy D at 700°C (2.45 mg/cm^2) increases 2.5 times at 800°C whereas it increases 4.89 times at 900°C . The total wt. gain value for alloy E at 700°C (4.9 mg/cm^2) increases 1.67 times at 800°C , while it increases 7.29 times at 900°C after similar exposure. The overall ranking for these alloys on the basis of wt. change, the extent of corrosion follows the sequence :

$$900^\circ\text{C} > 800^\circ\text{C} > 700^\circ\text{C}$$

The total wt. gain values after exposure for 24 cycles at 700, 800 and 900°C in Na_2SO_4 -60% V_2O_5 environment for alloy A are 39.31, 33.14 and 44.6 times more than their corresponding values in Na_2SO_4 at 700, 800 and 900°C respectively. For alloy B, the

total wt. gain values under similar condition are higher by 17.0, 20.4 and 25.0 times of their corresponding values at 700, 800 and 900°C respectively in pure Na₂SO₄ environment. For alloy C, the total wt. gain values, obtained after similar exposure are higher by 10.71, 8.90 and 24.57 times of their corresponding values at 700, 800 and 900°C respectively in pure Na₂SO₄. The increase in total wt. gain values for alloy D in Na₂SO₄-60% V₂O₅ exposure are 11.13, 17.57 and 32.43 times of their corresponding values at 700, 800 and 900°C respectively in pure Na₂SO₄. For alloy E, the total wt. gain values increase 20.41, 28.27 and 85.11 times of their corresponding values at 700, 800 and 900°C respectively in pure Na₂SO₄. The total wt. change values for these alloys are much higher than their corresponding values in Na₂SO₄-15%V₂O₅ as well. On comparison of the observed wt. gain values for these alloys in pure Na₂SO₄, Na₂SO₄-15% V₂O₅ and Na₂SO₄-60% V₂O₅ environments, it can be inferred that the eutectic composition of the salt mixtures (60% V₂O₅-40% Na₂SO₄) is most corrosive of all the three environments. The hot corrosion rates follow the sequence :

700°C → alloy A > alloy E > alloy B > alloy D > alloy C

800°C → alloy A > alloy E > alloy D > alloy B > alloy C

900°C → alloy E > alloy A > alloy D > alloy C > alloy B

This may be attributed to the high fluidity of the molten salt mixture which allows intimate contact with the alloy surface.

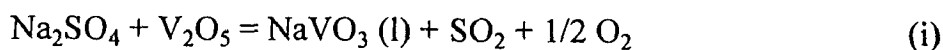
The nature of the wt. change vs time plots for alloys A, B, C, D and E obtained after exposure at 700 and 800°C are similar showing a rapid increase in the corrosion rate during the first two cycles and then marginal rate of wt. gain. This observation suggests that these alloys must have behaved similarly at 700 and 800°C. But the nature of curve differs greatly from alloy to alloy at 900°C. In case of alloy B after an increase in wt. gain values upto 4 cycles, the wt. gain value decreases slowly. For alloys C and D, the nature of the curve is nearly similar, i.e., after rapid increase during first two cycles there is a slower rate of increase in wt. gain values. The nature of the curve for alloy E at 900°C shows a rapid rate of increase in wt. gain values upto about fifteen cycles and then the corrosion process nearly stops and thus the wt. gain value remains constant during the remaining nine cycles.

The nature of the curve for alloy A at 900°C is dramatic. Similar nature of curve was observed by Hou and Stringer⁽⁸⁹⁾. There is an increase in the wt. gain values upto 6 cycles thereafter the wt. gain value continuously decreases. After about 14 cycle exposure, the wt. gain value becomes negligible and then for the remaining cycles, there is a rapid rate of wt. loss in the specimen. It is observed that the nature of curves for these alloys (Fig. 5.11-5.15) even at 900°C are similar in the early stages of corrosion (rapid rate) hence they must have behaved similarly in this period (two cycles). In the later stages the corrosion behaviour of these alloys differs a lot. The observed good corrosion resistance of alloys A, B, C, D and E at 700 and 800°C and of alloys B, C and D even at 900°C may be due to the formation of a thick and continuous protective Cr₂O₃ layer on the alloy surfaces as observed by X-ray maps for Cr in these alloys (Fig. 5.91-5.95)⁽⁵¹⁾.

The average scale thickness values measured by EPMA BSEI for alloys A, B, C, D, and E show that the maximum value 96.6 micron is for alloy E and minimum value 45.0 micron is for alloy B. The thickness values are 3.67, 6.0, 8.33, 6.75 and 12.07 times higher than their corresponding values in pure Na₂SO₄ environment for alloys A, B, C, D and E respectively. This observation further confirms that 60% V₂O₅ addition to Na₂SO₄ makes the environment extremely corrosive leading to the formation of thicker scales.

The possible mechanism for the corrosion of these alloys in Na₂SO₄-60% V₂O₅ at 700, 800 and 900°C for 24 cycle exposure in air can be explained as follows:

When salt mixture coated specimen of alloy A was heated for hot corrosion studies, then at about 500°C the salt mixture might have melted because of its eutectic temperature as shown in Na₂SO₄-V₂O₅ equilibrium diagram (Fig. 2.7)⁽⁵⁸⁾. The mixture has high fluidity at the test temperatures 700, 800 and 900°C leading to high reactivity. Then the salt mixtures might have reacted together to form a liquid NaVO₃ (m.p. 610°C) as observed by Kolta et. al.⁽⁶⁶⁾



This NaVO₃ formation might have created oxidising atmosphere so as to cause oxidation of Cr which has higher affinity for oxygen as compared to other elements and also Cr₂O₃ is much more thermodynamically stable⁽⁸⁵⁾.



For alloy A, the rapid rate of corrosion during the early stages (two cycles) at 700, 800 and 900°C may be due to the Cr₂O₃ formation which is facilitated by availability of more oxygen and better contact between highly fluid salt mixture and the alloy surface. The observed slower rate of increase in wt. gain values after two cycles at 700 and 800°C may be attributed to change in fluidity of salt mixture and its better coverage of the surface by Cr₂O₃ scale.

At 900°C the wt. gain values for alloy A started to decrease after 6 cycles and then even the wt. loss occurred as shown in wt. change -time plot for alloy A (Fig. 5.11). This may be attributed to the inability of Cr to form a continuous protective scale on alloy surface to resist oxide ion diffusion towards metal which is clearly revealed by X-ray map for Cr (Fig. 5.91b)⁽⁶⁸⁾. Kolta et. al.⁽⁶⁶⁾ have observed that NaVO₃ acted as a catalyst for oxidation and served as a oxygen carrier to the metal⁽⁶⁶⁾. Otero et. al.⁽⁵⁸⁾ have also reported similar observation after their studies on IN 657 in molten salts (60% V₂O₅-40% Na₂SO₄) and they have mentioned certain causes for the increase in corrosion attack, such as

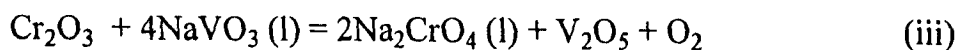
- (i) Molten salts act as the oxygen carriers. This process helped both diffusion and transport phenomena.
- (ii) Protective scale is destroyed and/or eliminated by molten salts, therefore metal surface is exposed to direct action of aggressive environment.
- (iii) Molten salts provide rapid diffusion paths for the reactant species.

Cracking of the scale, consisting of coarse grained heterogeneous mixture of oxides and spinels, has been observed as shown by the BSE image of EPMA (Fig. 5.91) and it extended even upto the alloy surface so that fresh alloy surface was exposed to the direct action of aggressive environment. Radhakrishnan et. al.⁽⁸⁴⁾ have also explained the high rate of oxidation that as the time progressed the thickness of the oxide layer increased to such an extent that stresses developed in the oxide scale. Since the oxide scale was quite brittle the scale cracked and caused fissures that acted as channels from the oxide/salt interface to the metal/oxide interface. Thus fresh metal got exposed to oxygen available from the molten salt mixture coating. As a result corrosion rate increased suddenly showing a linear behaviour. This they called breakaway corrosion⁽⁸⁴⁾.

Spalling was actually visually observed during experimentation. Spalling as well as formation and volatilization of certain compounds (such as Na_2CrO_4 , NaVO_3 , V_2O_5) might have caused the continuous reduction in wt. gain values leading to the total wt. loss of 23.2 mg/cm^2 .

Fe being the base metal and Ni are present in high concentrations in alloy A and they might have formed their respective oxides⁽⁹⁰⁾ according to reactions (iii) and (iv) of sec. 6.2. The presence of the oxides of Fe, Ni and Cr is revealed by the EPMA X ray maps (Fig. 5.91) in the outer layer of scale. Continuous dissolution of Cr_2O_3 in the NaVO_3 could not form a protective coating as revealed by the Cr distribution in X-ray maps (Fig. 5.91b) and therefore corrosion process continued up to the last.

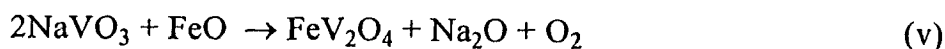
Fluxing of Cr_2O_3 with NaVO_3 might have followed the mechanism recommended by Seiersten and Kofstad⁽³⁾ that simultaneous growth of oxides and their dissolution in molten salt occurs as



Swaminathan et.al.⁽⁸⁷⁾ have also recommended this reaction. Later Na_2CrO_4 might have evaporated as pointed out by Fryburg et.al.⁽⁴⁶⁾ as :



Later FeO might also have been fluxed

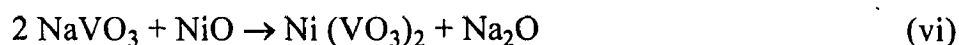


The presence of FeV_2O_4 has been identified by XRD (Fig. 5.41). The spinel formation might have taken place as mentioned in sec. 6.2. The presence of $(\text{Cr,Fe})_2\text{O}_3$ was also identified by XRD (Fig. 5.41). Similar phases were identified by Malik et. al.⁽³¹⁾ also in their studies on 18:8 stainless steel in Na_2SO_4 - NaVO_3 environment at 850 and 1000°C. The presence of these elements in the scale has been indicated by the EDAX analysis (Tab. 5.29) of the corroded specimen of alloy A. The coarse grained structure of the outer layer is quite visible in the SEM micrograph (Fig. 5.66). Some internal oxidation was also revealed by X-ray maps (Fig. 5.91) consisting of NiO at the grain boundaries of the substrate.

Nickel-base superalloys B,C and D might also have behaved similarly as alloy A in the eutectic mixture environment at 700 and 800°C due to the presence of similar

elements Fe, Ni and Cr in high concentrations. Hence the corrosion mechanism for alloy A can be extended for these alloys also. The nature of wt. change-time plots is also similar for these alloys (Fig. 5.11-5.14). For alloy B, after two cycles the wt. gain value decreases which may be attributed to the formation of a thick protective Cr₂O₃ scale on the alloy surface at 900°C. A duplex nature of the scale is revealed by BSEI (Fig. 5.92). The presence of coarse grained structure on the scale surface is observed by SEM (Fig. 5.68). XRD identified the presence of the oxides Cr₂O₃, NiO and the spinels Ni(VO₃)₂, (Cr,Fe)₂O₃ and NiCr₂O₄ as the prominent phases (Fig. 5.42). The EPMA X-ray maps (Fig. 5.92) revealed the presence of these phases in the outer scale, while the inner layer was mainly Cr₂O₃. The EDAX analysis indicates the presence of these elements in the scale of alloy B (Tab. 5.30). No internal oxidation or sulphidation was observed in X-ray maps by EPMA (Fig. 5.92).

The wt.gain-time plot for alloy C (Fig. 5.13) shows a very minor increase in wt.gain after two cycles which may be due to the protective scale formed on the surface of alloy as revealed by EPMA X-ray map for Cr (Fig. 5.93b). The SEM micrograph (Fig. 5.70) shows a crystalline structure at the surface of scale of alloy C. A thick protective inner layer of Cr₂O₃ is clearly visible in EPMA X-ray map for Cr of alloy C (Fig. 5.93b). The outer layer consists mainly of the mixture of oxides Cr₂O₃, NiO and the spinels NaVO₃, Ni(VO₃)₂, FeV₂O₄, NiCr₂O₄ and (Cr,Fe)₂O₃, as revealed by X-ray maps of alloy C for these elements (Fig. 5.93). The XRD (Fig. 5.43) identified the presence of these phases. The mechanism of formation of these phases are similar to that explained for alloy A in this section and in section 6.2. Similar phases were identified by Malik et.al.⁽⁴⁹⁾ and Swaminathan et.al.⁽⁸⁾ in their studies on Nickel -base alloys. Ni(VO₃)₂ formation might have taken place⁽⁸⁷⁾ as below



In case of alloy D, the nature of the plot for wt. gain vs time at 700 and 800°C shows that after two cycles the wt. gain value decreases at 700°C while it increases very slowly at 800°C. This may be attributed to the formation of a protective Cr₂O₃ layer leading to reduction of corrosion rate. But at 900°C, due to high fluidity of the salt mixture, the corrosion rate gradually increased till end of the test. The corrosion

mechanism must have followed as suggested by Seiersten and Kofstad⁽³⁾ that simultaneous growth of oxides and their dissolution in molten salts, as shown in reactions (iii), (v) and (vi) of this section, occurs. Cr did not form a dense and continuous scale as revealed by EPMA (Fig. 5.94) hence corrosion reactions continued and the wt. gain value increased upto the last cycle at 900°C. The main compounds formed on the alloy surface and their presence in the scale were identified by XRD (Fig. 5.44) as NiO, Ni(VO₃)₂, NiCr₂O₄ and FeV₂O₄. The elemental distribution in EPMA X-ray maps (Fig. 5.94) reveals the presence of these compounds. The presence of the elements are confirmed by the EDAX analysis (Tab. 5.32). Bornstein and DeCrescente⁽⁶⁸⁾ have also reported the formation of similar compounds in their studies on Ni-base alloys in V₂O₅ environment. No internal oxidation was observed by EPMA (Fig. 5.94).

In case of alloy E due to the formation of Cr₂O₃ the corrosion proceeded at a fast rate at 700, 800 and 900°C and as soon as the scale became protective the rate of reaction decreased and minor wt. gain rate was observed at 700 and 800°C. But at 900°C, the reaction proceeded at a faster rate upto 15 cycles (Fig. 5.15), which suggests that the high fluidity of the salt mixture might have caused rapid formation and dissolution of oxides in molten salt mixture⁽³⁾. The protective layer of scale could not be formed during this period due to higher rate of dissolution than its formation⁽³⁾. Later higher rate of chromia formation than the dissolution rate might have caused to form a protective layer due to which the corrosion process nearly stopped and wt. gain value remained constant upto the last cycle as shown in wt. change-time plot (Fig. 5.15). The XRD (Fig. 5.45) identified the oxides of the elements present in the Co-base alloy D such as Cr₂O₃, Co₂O₃, WO₃ and CoV₃ which later formed the spinels Co₃V₂O₈, (Cr,Fe)₂O₃ and NiCr₂O₄. These oxides and spinels are distributed throughout the scale which is clearly revealed by the BSEI and the X-ray maps (Fig. 5.95). The presence of the elements is confirmed by the EDAX analysis (Tab. 5.33) also. The formation of thicker scale on the alloy surface is revealed by the EPMA (Fig. 5.95) suggesting that excessive corrosion of the alloy has occurred. The probable corrosion mechanism of alloy A, D and E is explained with the help of a schematic diagram (Fig. 6.4a-c).

6.4 HOT CORROSION STUDIES IN COMBUSTION GASES

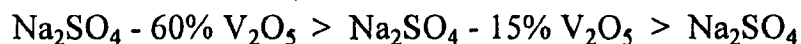
The alloys A, B, C, D and E were coated with pure Na_2SO_4 , Na_2SO_4 -15% V_2O_5 and Na_2SO_4 -60% V_2O_5 to the extent of 4.0-5.0 mg/cm^2 and then were subjected to hot corrosion in combustion gas environment of a boiler of Power Plant of Bhilai Steel Plant (India) for 6 cycles (cycle of 24h heating and 1h cooling) at 1100°C. The results of these hot corrosion tests are discussed in this section.

The hot corrosion studies in the actual boiler environment were very tedious as the samples had to be hanged at a height of 24 metres from the ground floor. This might have led to some change in coating thickness. Flyash deposit was also observed on the coated exposed specimens which was to be removed periodically. The role of high velocity combustion gas striking the exposed specimen has to be considered.

From the visual observations made on corroded specimens of alloy A, B, C, D and E after exposure for 6 cycles at 1100°C in combustion gas, it is evident that these alloys did not suffer severe corrosion. Lot of claye flyash deposits was observed on the surfaces of specimens during exposure which was removed very carefully with the help of a camel hair brush after each cycle before weighing. Precaution was taken that the scale should not be detached with flyash. The scales were, in general, dark grey in colour and adherent as shown by the macrographs of the corroded specimens (Fig. 5.26-5.30).

6.4.1 Hot Corrosion Studies of Alloy A (Superfer 800H) in Combustion Gases

The total wt. gain values shown for alloy A after exposure for 6 cycles in the combustion gas with coatings of pure Na_2SO_4 , Na_2SO_4 -15% V_2O_5 , Na_2SO_4 -60% V_2O_5 are 1.25, 2.9 and 4.5 mg/cm^2 respectively. It is observed that the wt. gain values increase significantly with increase in V_2O_5 content. The corrosion rate follows the sequence (with decreasing rate):



Similar observation were made in the laboratory tests as well. From the weight gain values it is quite obvious that the extent of corrosion even in the aggressive environment is moderate, which suggests that the alloy A is highly corrosion resistant in c.g. environment as well. The wt. change plots for alloy A (Fig 5.16) shows that the time

of exposure has a significant effect on the corrosion reaction. The alloy obeys a parabolic rate law. The parabolic plots for the alloy A in Na_2SO_4 , Na_2SO_4 -15% V_2O_5 and Na_2SO_4 -60% V_2O_5 show clearly two linear regions: an initial region of higher parabolic rate constant and a second region with a lower parabolic rate constant. Such a change occurs when the contributing factors get altered with time⁽⁸⁾. The parabolic rate constants are given in Table 5.2.

The rapid rate of weight gain value during the first cycle is followed by a slower rate of wt. gain during the remaining cycles of test. The rapid rate of wt. gain may be due to the formation of a chromia scale on the surface of the alloy in the initial stage and when the scale becomes thicker, it acts as a barrier to the diffusion of corrosive species towards the alloy surface leading to the decreasing rate of corrosion as already explained in sec 6.1-6.3.

Visual examination of the exposed samples showed the presence of liquid on the surface as the salt mixture was in molten state at 1100°C. The grey coloured scale indicated the presence of iron oxide in the top scale. The SEM micrograph of the scale surface (Fig 5.67) obtained after 6 cycle exposure at 1100°C, with pure Na_2SO_4 , Na_2SO_4 -15% V_2O_5 and Na_2SO_4 -60% V_2O_5 coatings reveals the presence of a porous structure containing white and dark phases. The EDAX analysis at the areas 7 and 8 on SEM micrograph are indicated in Table 5.29. The bright region (7) is rich in Cr and Ni, whereas the dark area (8) is rich in Fe, Cr, Ni and Ti as indicated by EDAX (Tab 5.29, Fig 5.67a).

The corrosion products identified by XRD analysis (Table 5.19, Fig 5.46) on the scale surface of alloy A with Na_2SO_4 coating are the oxides of Cr, Fe, Ti, Ni and Al, whereas with Na_2SO_4 -15% V_2O_5 and Na_2SO_4 -60% V_2O_5 coatings in addition to these oxides, spinels NiCr_2O_4 and FeV_2O_4 are also identified as the main phases. Formation of these compounds might have occurred in accordance with the commonly accepted fluxing mechanism for vanadic attack⁽⁹¹⁾ as already explained in section 6.1-6.3. EDAX analysis (Table 5.29) indicates the presence of these elements. The molten salt/ salt mixture acts as a short circuit diffusion path⁽⁸⁾ for Fe, Cr, Ni, Ti, Al and V ions ensuring accelerated oxidation attack reflected in the form of a rapid wt. gain in the initial hours. When solid

vanadates of Fe forms, the corrosion rate decreases because it acts as a diffusion barrier⁽⁸⁾ blocking the short circuit paths for the diffusing Fe, Ni and Cr ions. Further as the melt becomes concentrated with Ni, Cr, Fe ions, diffusion of oxygen ions gets affected and consequently the rate of corrosion falls with time hence the wt. gain gets slowed down with time⁽⁸⁾. The attack of $\text{Na}_2\text{SO}_4\text{-V}_2\text{O}_5$ is more important in the initial hours and as the grains coarsen the short circuit path area available at the grain boundaries decreases⁽⁹¹⁾.

The BSEI and X-ray maps (Fig 5.96) reveals the duplex nature of the scale. The average thickness value of the scale was 18.5 micron. The top layer consists mainly of Fe_2O_3 in which some Al_2O_3 , TiO_2 and NiO have also been incorporated. The inner layer is rich in Cr_2O_3 but some oxides of Al and Ti are also evident (Fig 5.96). Cr_2O_3 layer may not be completely protective due to the presence of some other phases hence oxygen ions have penetrated into the alloy substrate through the grain boundaries so as to cause internal oxidation of Al and Ti (Fig 5.96). The dissolution of the scale in the liquid salt may contribute to maintain high reaction rates by keeping the thickness of the inner layer relatively thin and producing a porous external scale⁽²⁸⁾. Precipitation of the solid particles in the liquid forms a porous nonprotective outer scale⁽²⁸⁾. As alloy A has shown good corrosion resistance against $\text{Na}_2\text{SO}_4\text{-60}\%\text{V}_2\text{O}_5$ coating its probable mechanism of corrosion has been shown schematically (Fig 6.5a).

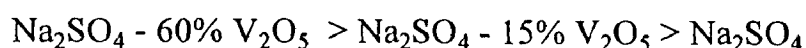
6.4.2 Hot Corrosion Studies of Alloy B (Superni 75) in Combustion Gases

From the visual observations made on the corroded specimens of Ni-base superalloy B after exposure for 6 cycles at 1100°C with Na_2SO_4 , $\text{Na}_2\text{SO}_4 - 15\% \text{V}_2\text{O}_5$ and $\text{Na}_2\text{SO}_4 - 60\% \text{V}_2\text{O}_5$ coatings in c.g. atmosphere, it is evident that this alloy also did not suffer severe corrosion. The scale was grey coloured and adherent as shown in visual photographs (Fig 5.27) which indicates the presence of various oxides. The nature of the wt. gain-time plots for alloy B with Na_2SO_4 , $\text{Na}_2\text{SO}_4 - 15\% \text{V}_2\text{O}_5$ and $\text{Na}_2\text{SO}_4 - 60\% \text{V}_2\text{O}_5$ coatings are similar which suggests that the corrosion mechanism of this alloy with these coatings must also be similar. The wt. change plots show that the time of exposure has significant effect on the corrosion rate. There is a rapid rate of reaction during the first two cycles and then the wt. gain rate decreases. The effect of V_2O_5 addition to Na_2SO_4 is

the spinel formation might have occurred as described in sec. 6.1-6.3 by fluxing mechanism and hence the phases $\text{Ni}(\text{VO}_3)_2$ and FeV_2O_4 were also detected. Similar fluxing mechanism of corrosion has also been reported by Germundo et. al.⁽⁹²⁾ in their studies on Ni_3Al compound with Na_2SO_4 - NaCl coating in c.g. environment at 600-800°C and they concluded that the molten NaVO_3 formed was mainly responsible for the hot corrosion. No spinel formation was observed in the Na_2SO_4 and Na_2SO_4 -60% V_2O_5 coated specimens. Some internal oxidation along the grain boundaries was also observed by EPMA X-ray maps (Fig 5.98e). The X-ray maps of alloy C (Fig 5.98) reveal that the thick top layer is mainly of Fe_2O_3 and the inner layer is mainly that of Cr_2O_3 . Other elements are incorporated in traces in both layers. The Cr_2O_3 layer is not uniform and dense as revealed by X ray map Fig 5.98b. The plane surface of the alloy revealed by X ray maps (Fig 5.98) suggests that the extent of corrosion was very less.

6.4.4 Hot Corrosion Studies of Alloy D (Superni 718) in Combustion Gases

Visual observation of the exposed specimen of Ni-base superalloy D with Na_2SO_4 , Na_2SO_4 -15% V_2O_5 and Na_2SO_4 - 60% V_2O_5 coatings for 6 cycles in c.g. environment of a boiler shows that this alloy also did not suffer severe corrosion. The colour of the scale was greyish black with some flyash particles sticking to it even after careful cleaning with a camel hair brush. The nature of the wt. gain-time plots (Fig. 5.19) for Na_2SO_4 , Na_2SO_4 -15% V_2O_5 and Na_2SO_4 -60% V_2O_5 coated specimens of alloy D is similar, suggesting that the behaviour of this alloy against these coatings might be similar. The wt. change plots (Fig 5.19) also show that the time of exposure has also a significant effect on the corrosion behaviour of the alloy. There is a rapid rate of corrosion during the first two cycles and then the rate decreases. The effect of V_2O_5 addition to Na_2SO_4 is also clearly visible in these plots (Fig 5.19) from the wt. gain values. The total wt. gain value 1.25 mg/cm^2 for Na_2SO_4 coated specimen is 2.24 and 4.32 times higher for Na_2SO_4 - 15% V_2O_5 and Na_2SO_4 - 60% V_2O_5 coated specimens respectively. This observation again confirms that the corrosion rate for this alloy follows the sequence :



This observation is similar to that observed for other alloys in industrial environment as well as in laboratory tests.

The rapid rate of corrosion during the first two cycles may be due to the Cr_2O_3 formation and the reduced rate of corrosion during the later cycles may be attributed to the protective nature of the Cr_2O_3 sub-scale. The mechanism of corrosion reactions observed during laboratory tests for these coatings may be extended for the industrial conditions due to the presence of similar compounds in the scale⁽⁹²⁾.

The SEM micrographs (Fig 5.73) of specimens of alloy D with different coatings of salt mixture after exposure for 6 cycles at 1100°C in c.g. show that the scale consists of a homogeneous mixture of coarse and fine grains. The XRD analysis (Tab 5.22, Fig 5.49) identified the presence of Fe_2O_3 , Cr_2O_3 , NiO , TiO_2 and CrS as the main phases in the scale of Na_2SO_4 coated specimen. Cr_2O_3 , $\alpha\text{-Fe}_2\text{O}_3$, NiO , TiO_2 , Al_2O_3 and $\text{Ni}(\text{VO}_3)_2$ were detected in the scale of $\text{Na}_2\text{SO}_4\text{-}15\%\text{V}_2\text{O}_5$ coated specimens, while Cr_2O_3 , NiO , $\alpha\text{-Fe}_2\text{O}_3$ and TiO_2 were identified in the scale of $\text{Na}_2\text{SO}_4\text{-}60\%\text{V}_2\text{O}_5$ coated specimens. The mechanism of formation of the oxides and the spinels has already been mentioned in sec. 6.1-6.3 of this chapter. Deep internal oxidation at the grain boundaries is clearly revealed by the EPMA X-ray maps (Fig 5.99). These X-ray maps reveal a plain and regular alloy surface after exposure which suggests that the alloy has good corrosion resistance against the $\text{Na}_2\text{SO}_4\text{-V}_2\text{O}_5$ in c.g. environment which may be attributed to the formation of a thick, uniform compact protective layer of Cr_2O_3 (Fig 5.99).

6.4.5 Hot Corrosion Studies of Alloy E (Superco 605) in Combustion Gases

Visual observation of the exposed specimens of Co-base superalloy E with Na_2SO_4 , $\text{Na}_2\text{SO}_4\text{-}15\%\text{V}_2\text{O}_5$ and $\text{Na}_2\text{SO}_4\text{-}60\%\text{V}_2\text{O}_5$ coatings in c.g. for 6 cycles at 1100°C shows that the alloy did not suffer severe corrosion and thus has a good corrosion resistance against the corrosion test environment. The colour of the scale was greyish and some flyash particles were also sticking to the alloy surface. The nature of the wt. gain-time plots (Fig 5.20) for Na_2SO_4 , $\text{Na}_2\text{SO}_4\text{-}15\%\text{V}_2\text{O}_5$ and $\text{Na}_2\text{SO}_4\text{-}60\%\text{V}_2\text{O}_5$ coated specimens of alloy E is similar which suggests that the alloy has behaved very similarly in these environments. The kinetic plots also show that the time of exposure has a significant effect on the corrosion rate. There is a rapid rate of corrosion during the first two cycles and the rate then decreases. The effect of V_2O_5 addition to Na_2SO_4 is clearly visible in

these plots (Fig 5.20) and can be quantitatively indicated by the total wt. gain values obtained after exposure for 6 cycles. The total wt. gain value 1.15 mg/cm^2 for Na_2SO_4 coated specimen is higher by 2.39 and 4.13 times for Na_2SO_4 -15% V_2O_5 and Na_2SO_4 - 60% V_2O_5 coated specimens respectively. This observation again confirms the corrosion rate for this alloy taking place in the order :



The rapid rate of corrosion during the first two cycles may be due to the Cr_2O_3 formation and the reduced rate of corrosion during the remaining cycles may be attributed to Cr_2O_3 layer becoming compact, thus protecting the alloy surface from interacting with corrosive environment. The mechanism of corrosion reactions, occurring by common fluxing of the oxide scale into the molten salt, has already been discussed in sec 6.1-6.3. SEM micrographs of the scales of alloy E (Fig 5.75) shows that it consists of coarse grained porous structure on their surfaces, while fine particles are also embedded in the structure. The scale consists of oxides of Cr, Fe, Co and W with Na_2SO_4 coating as identified by XRD analysis (Tab 5.23, Fig 5.50). XRD identified, in addition to these oxides, the presence of spinels $\text{Co}_3\text{V}_2\text{O}_8$ and NiCr_2O_4 with Na_2SO_4 -15% V_2O_5 and Na_2SO_4 -60% V_2O_5 coated specimens. No oxidation/ sulphidation was observed by EPMA (Fig 5.100). The EPMA X ray maps (Fig 5.100) with Na_2SO_4 -60% V_2O_5 coating reveal the presence and distribution of these elements in the scale and the substrate. The inner thin and uniform layer is of Cr_2O_3 while the outer layer consists mainly of Fe_2O_3 in which some oxides of Co, Ni and V are also incorporated. Spinels NiCr_2O_4 and $\text{Co}_3\text{V}_2\text{O}_8$ are also present in the outer scale. The presence of the elements forming oxides and spinels is confirmed by the EDAX analysis (Tab 5.33) at areas 7 and 8.

Although the weight gains values of these alloys are comparable, the ranking of the alloy A, B, C, D and E on the basis of weight gain under different salt/ salt mixture, in c.g. is as follows :

- (1) $\text{Na}_2\text{SO}_4 \rightarrow$ alloy A > Alloy D > alloy C > alloy B > alloy E
- (2) $\text{Na}_2\text{SO}_4 \rightarrow 15\% \text{V}_2\text{O}_5$ alloy A > Alloy D > alloy E > alloy C > alloy B
- (3) $\text{Na}_2\text{SO}_4 \rightarrow 60\% \text{V}_2\text{O}_5$ - alloy D > alloy C > alloy B > alloy E > alloy A

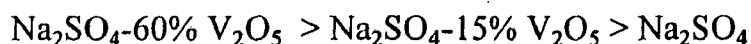
vanadates of Fe forms, the corrosion rate decreases because it acts as a diffusion barrier⁽⁸⁾ blocking the short circuit paths for the diffusing Fe, Ni and Cr ions. Further as the melt becomes concentrated with Ni, Cr, Fe ions, diffusion of oxygen ions gets affected and consequently the rate of corrosion falls with time hence the wt. gain gets slowed down with time⁽⁸⁾. The attack of $\text{Na}_2\text{SO}_4\text{-V}_2\text{O}_5$ is more important in the initial hours and as the grains coarsen the short circuit path area available at the grain boundaries decreases⁽⁹¹⁾.

The BSEI and X-ray maps (Fig 5.96) reveals the duplex nature of the scale. The average thickness value of the scale was 18.5 micron. The top layer consists mainly of Fe_2O_3 in which some Al_2O_3 , TiO_2 and NiO have also been incorporated. The inner layer is rich in Cr_2O_3 but some oxides of Al and Ti are also evident (Fig 5.96). Cr_2O_3 layer may not be completely protective due to the presence of some other phases hence oxygen ions have penetrated into the alloy substrate through the grain boundaries so as to cause internal oxidation of Al and Ti (Fig 5.96). The dissolution of the scale in the liquid salt may contribute to maintain high reaction rates by keeping the thickness of the inner layer relatively thin and producing a porous external scale⁽²⁸⁾. Precipitation of the solid particles in the liquid forms a porous nonprotective outer scale⁽²⁸⁾. As alloy A has shown good corrosion resistance against $\text{Na}_2\text{SO}_4\text{-60}\%\text{V}_2\text{O}_5$ coating its probable mechanism of corrosion has been shown schematically (Fig 6.5a).

6.4.2 Hot Corrosion Studies of Alloy B (Superni 75) in Combustion Gases

From the visual observations made on the corroded specimens of Ni-base superalloy B after exposure for 6 cycles at 1100°C with Na_2SO_4 , $\text{Na}_2\text{SO}_4 - 15\% \text{V}_2\text{O}_5$ and $\text{Na}_2\text{SO}_4 - 60\% \text{V}_2\text{O}_5$ coatings in c.g. atmosphere, it is evident that this alloy also did not suffer severe corrosion. The scale was grey coloured and adherent as shown in visual photographs (Fig 5.27) which indicates the presence of various oxides. The nature of the wt. gain-time plots for alloy B with Na_2SO_4 , $\text{Na}_2\text{SO}_4 - 15\% \text{V}_2\text{O}_5$ and $\text{Na}_2\text{SO}_4 - 60\% \text{V}_2\text{O}_5$ coatings are similar which suggests that the corrosion mechanism of this alloy with these coatings must also be similar. The wt. change plots show that the time of exposure has significant effect on the corrosion rate. There is a rapid rate of reaction during the first two cycles and then the wt. gain rate decreases. The effect of V_2O_5 addition to Na_2SO_4 is

clearly visible from the wt. change plots (Fig 5.17) and can be quantitatively understood by the total wt. gain values obtained after exposure of 6 cycles. The wt. gain value 0.9 mg/cm^2 with Na_2SO_4 coating is higher by 2.55 and 5.66 times in $\text{Na}_2\text{SO}_4 - 15\% \text{V}_2\text{O}_5$ and $\text{Na}_2\text{SO}_4 - 60\% \text{V}_2\text{O}_5$ respectively. This observation suggests that the corrosion rate follows the sequence :

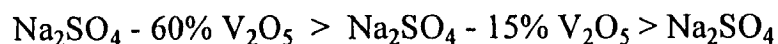


Same sequence was observed during the laboratory tests also. The rapid rate of corrosion during the first two cycles might be due to Cr_2O_3 scale formation and the reduction in wt. gain after two cycles may be due to the protective nature of the Cr_2O_3 layer on the alloy surface. The mechanism of corrosion reactions has already been dealt in sec 6.1-6.3 of this chapter by which the oxides of the elements are formed.

The SEM micrograph of the scale of alloy B (Fig 5.69) shows a mixture of fine to coarse particles whose chemical composition by EDAX for the bright and the dark phases (areas 8 and 9) are shown in Table 5.30, XRD analysis (Tab. 5.20, Fig 5.47) identified the presence of Cr_2O_3 , NiO , TiO_2 and NiCr_2O_4 in the scale of Na_2SO_4 coated specimen, while additional phase of $\text{Fe}_2\text{V}_2\text{O}_4$ was also identified in the scale of $\text{Na}_2\text{SO}_4 - 15\% \text{V}_2\text{O}_5$ and $\text{Na}_2\text{SO}_4 - 60\% \text{V}_2\text{O}_5$ coated specimens. The formation of spinels might have occurred in the similar way as already mentioned in sec 6.1-6.3. The EPMA X-ray maps (Fig 5.97) reveal the presence of FeV_2O_4 and NiCr_2O_4 in the top scale, while Cr_2O_3 and Fe_2O_3 are indicated in the lower portion. The BSEI (Fig. 5.97) of the alloy B reveals the alloy surface to be regular, which suggests that the lesser extent of corrosion of the alloy B in $\text{Na}_2\text{SO}_4 - 60\% \text{V}_2\text{O}_5$, (the most aggressive environment) after 6 cycle exposure has occurred. Little internal oxidation has also been indicated by EPMA (Fig. 5.97). This alloy has shown good corrosion resistance in the most aggressive environment ($\text{Na}_2\text{SO}_4 - 60\% \text{V}_2\text{O}_5$ in c.g. of the furnace at 1100°C) which may be due to the formation of a thin compact and continuous protective scale on the alloy surface as revealed by X ray map (Fig 5.97b). The probable mechanism of corrosion for alloy B in $\text{Na}_2\text{SO}_4\text{-60\%V}_2\text{O}_5$ is shown in schematic diagram Fig. 6.5b.

6.4.3 Hot Corrosion Studies of Alloy C (Superni 600) in Combustion Gases

The visual observations of the corroded specimens of Ni-base superalloy C, after exposure for 6 cycles at 1100°C with Na₂SO₄, Na₂SO₄ - 15% V₂O₅ and Na₂SO₄ - 60% V₂O₅ coatings in c.g. environment of a boiler, shows that this alloy also did not suffer severe corrosion. It can be inferred that the alloy has good corrosion resistance against these environments. The colour of the scale was greyish black (Fig 5.28) with some flyash particles sticking to it even after careful cleaning it with hair brush. The nature of the wt. gain-time plots (Fig. 5.18) for Na₂SO₄, Na₂SO₄-15%V₂O₅ and Na₂SO₄-60%V₂O₅ coated specimens of alloy C is similar which suggests that the corrosion behaviour of the alloy with these coatings must also be similar. The wt. gain-time plots (Fig 5.18) also show that the time of exposure has a significant effect on the corrosion rate. There is a rapid rate of corrosion during the first two cycles and then the reaction rate decreases. Similar observation has already been made in sec 6.1-6.3. The effect of V₂O₅ addition to Na₂SO₄ is quite visible in these plots also that the total wt. gain value obtained after exposure for 6 cycles is 1.05 mg/cm² for Na₂SO₄ coated specimen which is 2.42 and 4.8 times higher for Na₂SO₄-15%V₂O₅ and Na₂SO₄-60%V₂O₅ coated specimens respectively. This observation again confirms that the extent of corrosion for this alloy follows the sequence:

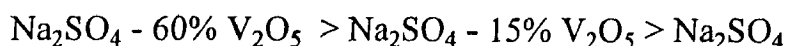


The rapid rate of corrosion during the first two cycles might be due to Cr₂O₃ and Fe₂O₃ formation and the reduced rate of corrosion in later cycles may be due to the formation of compact, adherent and protective nature of Cr₂O₃ scale with acts as a barrier for inward diffusion of corroding species towards alloy surface. The mechanism of corrosion reactions, occurring by common fluxing mechanism has already been dealt in sec. 6.1-6.3. SEM micrographs (Fig 5.71(a-c)) show a scale consisting of a mixture of coarse and fine grains of various shapes. The scale consists of oxides as detected by XRD analysis (Tab 5.21, Fig 5.48). Cr₂O₃, Fe₂O₃, NiO and CrS were identified as main phases with Na₂SO₄ coated specimen. The formation of CrS may be due to the lowering of oxygen activity⁽³¹⁾. Sharma⁽⁸⁶⁾ has also identified similar phases in his studies on Ni-base superalloys with Na₂SO₄ coating in c.g. environment. But with Na₂SO₄-15%V₂O₅ coating

the spinel formation might have occurred as described in sec. 6.1-6.3 by fluxing mechanism and hence the phases $\text{Ni}(\text{VO}_3)_2$ and FeV_2O_4 were also detected. Similar fluxing mechanism of corrosion has also been reported by Germundo et. al.⁽⁹²⁾ in their studies on Ni_3Al compound with Na_2SO_4 - NaCl coating in c.g. environment at 600-800°C and they concluded that the molten NaVO_3 formed was mainly responsible for the hot corrosion. No spinel formation was observed in the Na_2SO_4 and Na_2SO_4 -60% V_2O_5 coated specimens. Some internal oxidation along the grain boundaries was also observed by EPMA X-ray maps (Fig 5.98e). The X-ray maps of alloy C (Fig 5.98) reveal that the thick top layer is mainly of Fe_2O_3 and the inner layer is mainly that of Cr_2O_3 . Other elements are incorporated in traces in both layers. The Cr_2O_3 layer is not uniform and dense as revealed by X ray map Fig 5.98b. The plane surface of the alloy revealed by X ray maps (Fig 5.98) suggests that the extent of corrosion was very less.

6.4.4 Hot Corrosion Studies of Alloy D (Superni 718) in Combustion Gases

Visual observation of the exposed specimen of Ni-base superalloy D with Na_2SO_4 , Na_2SO_4 -15% V_2O_5 and Na_2SO_4 - 60% V_2O_5 coatings for 6 cycles in c.g. environment of a boiler shows that this alloy also did not suffer severe corrosion. The colour of the scale was greyish black with some flyash particles sticking to it even after careful cleaning with a camel hair brush. The nature of the wt. gain-time plots (Fig. 5.19) for Na_2SO_4 , Na_2SO_4 -15% V_2O_5 and Na_2SO_4 -60% V_2O_5 coated specimens of alloy D is similar, suggesting that the behaviour of this alloy against these coatings might be similar. The wt. change plots (Fig 5.19) also show that the time of exposure has also a significant effect on the corrosion behaviour of the alloy. There is a rapid rate of corrosion during the first two cycles and then the rate decreases. The effect of V_2O_5 addition to Na_2SO_4 is also clearly visible in these plots (Fig 5.19) from the wt. gain values. The total wt. gain value 1.25 mg/cm^2 for Na_2SO_4 coated specimen is 2.24 and 4.32 times higher for Na_2SO_4 - 15% V_2O_5 and Na_2SO_4 - 60% V_2O_5 coated specimens respectively. This observation again confirms that the corrosion rate for this alloy follows the sequence :



This observation is similar to that observed for other alloys in industrial environment as well as in laboratory tests.

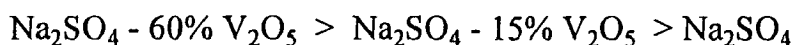
The rapid rate of corrosion during the first two cycles may be due to the Cr_2O_3 formation and the reduced rate of corrosion during the later cycles may be attributed to the protective nature of the Cr_2O_3 sub-scale. The mechanism of corrosion reactions observed during laboratory tests for these coatings may be extended for the industrial conditions due to the presence of similar compounds in the scale⁽⁹²⁾.

The SEM micrographs (Fig 5.73) of specimens of alloy D with different coatings of salt mixture after exposure for 6 cycles at 1100°C in c.g. show that the scale consists of a homogeneous mixture of coarse and fine grains. The XRD analysis (Tab 5.22, Fig 5.49) identified the presence of Fe_2O_3 , Cr_2O_3 , NiO , TiO_2 and CrS as the main phases in the scale of Na_2SO_4 coated specimen. Cr_2O_3 , $\alpha\text{-Fe}_2\text{O}_3$, NiO , TiO_2 , Al_2O_3 and $\text{Ni}(\text{VO}_3)_2$ were detected in the scale of $\text{Na}_2\text{SO}_4\text{-}15\%\text{V}_2\text{O}_5$ coated specimens, while Cr_2O_3 , NiO , $\alpha\text{-Fe}_2\text{O}_3$ and TiO_2 were identified in the scale of $\text{Na}_2\text{SO}_4\text{-}60\%\text{V}_2\text{O}_5$ coated specimens. The mechanism of formation of the oxides and the spinels has already been mentioned in sec. 6.1-6.3 of this chapter. Deep internal oxidation at the grain boundaries is clearly revealed by the EPMA X-ray maps (Fig 5.99). These X-ray maps reveal a plain and regular alloy surface after exposure which suggests that the alloy has good corrosion resistance against the $\text{Na}_2\text{SO}_4\text{-V}_2\text{O}_5$ in c.g. environment which may be attributed to the formation of a thick, uniform compact protective layer of Cr_2O_3 (Fig 5.99).

6.4.5 Hot Corrosion Studies of Alloy E (Superalloy 605) in Combustion Gases

Visual observation of the exposed specimens of Co-base superalloy E with Na_2SO_4 , $\text{Na}_2\text{SO}_4\text{-}15\%\text{V}_2\text{O}_5$ and $\text{Na}_2\text{SO}_4\text{-}60\%\text{V}_2\text{O}_5$ coatings in c.g. for 6 cycles at 1100°C shows that the alloy did not suffer severe corrosion and thus has a good corrosion resistance against the corrosion test environment. The colour of the scale was greyish and some flyash particles were also sticking to the alloy surface. The nature of the wt. gain-time plots (Fig 5.20) for Na_2SO_4 , $\text{Na}_2\text{SO}_4\text{-}15\%\text{V}_2\text{O}_5$ and $\text{Na}_2\text{SO}_4\text{-}60\%\text{V}_2\text{O}_5$ coated specimens of alloy E is similar which suggests that the alloy has behaved very similarly in these environments. The kinetic plots also show that the time of exposure has a significant effect on the corrosion rate. There is a rapid rate of corrosion during the first two cycles and the rate then decreases. The effect of V_2O_5 addition to Na_2SO_4 is clearly visible in

these plots (Fig 5.20) and can be quantitatively indicated by the total wt. gain values obtained after exposure for 6 cycles. The total wt. gain value 1.15 mg/cm^2 for Na_2SO_4 coated specimen is higher by 2.39 and 4.13 times for Na_2SO_4 -15% V_2O_5 and Na_2SO_4 - 60% V_2O_5 coated specimens respectively. This observation again confirms the corrosion rate for this alloy taking place in the order :



The rapid rate of corrosion during the first two cycles may be due to the Cr_2O_3 formation and the reduced rate of corrosion during the remaining cycles may be attributed to Cr_2O_3 layer becoming compact, thus protecting the alloy surface from interacting with corrosive environment. The mechanism of corrosion reactions, occurring by common fluxing of the oxide scale into the molten salt, has already been discussed in sec 6.1-6.3. SEM micrographs of the scales of alloy E (Fig 5.75) shows that it consists of coarse grained porous structure on their surfaces, while fine particles are also embedded in the structure. The scale consists of oxides of Cr, Fe, Co and W with Na_2SO_4 coating as identified by XRD analysis (Tab 5.23, Fig 5.50). XRD identified, in addition to these oxides, the presence of spinels $\text{Co}_3\text{V}_2\text{O}_8$ and NiCr_2O_4 with Na_2SO_4 -15% V_2O_5 and Na_2SO_4 -60% V_2O_5 coated specimens. No oxidation/ sulphidation was observed by EPMA (Fig 5.100). The EPMA X ray maps (Fig 5.100) with Na_2SO_4 -60% V_2O_5 coating reveal the presence and distribution of these elements in the scale and the substrate. The inner thin and uniform layer is of Cr_2O_3 while the outer layer consists mainly of Fe_2O_3 in which some oxides of Co, Ni and V are also incorporated. Spinels NiCr_2O_4 and $\text{Co}_3\text{V}_2\text{O}_8$ are also present in the outer scale. The presence of the elements forming oxides and spinels is confirmed by the EDAX analysis (Tab 5.33) at areas 7 and 8.

Although the weight gains values of these alloys are comparable, the ranking of the alloy A, B, C, D and E on the basis of weight gain under different salt/ salt mixture, in c.g. is as follows :

- (1) $\text{Na}_2\text{SO}_4 \rightarrow$ alloy A > Alloy D > alloy C > alloy B > alloy E
- (2) $\text{Na}_2\text{SO}_4 \rightarrow 15\% \text{V}_2\text{O}_5$ alloy A > Alloy D > alloy E > alloy C > alloy B
- (3) $\text{Na}_2\text{SO}_4 \rightarrow 60\% \text{V}_2\text{O}_5$ - alloy D > alloy C > alloy B > alloy E > alloy A

The probable hot corrosion mechanism of alloy A has been shown schematically in Fig. 6.5.

6.5 HOT CORROSION STUDIES IN Na_2SO_4 - 60% V_2O_5 + MgO

From the available literature on fuel additives, MgO was supposed to be quite effective and the cheapest additive to minimise corrosion of metals and alloys in vanadic environments. Hence some hot corrosion tests were also carried out on alloys A, B, C, D and E as a part of the present investigations, to investigate the effect of MgO addition on the most severe salt environment of Na_2SO_4 -60% V_2O_5 at 900°C for 24 cycles. The amount of MgO addition was in the ratio of 3 MgO : 1 V_2O_5 . The results of this investigation are discussed in this section.

6.5.1 Effect of MgO Addition on Hot Corrosion of Alloy A (Superfer 800H)

The wt. change plots for alloy A (Fig 5.21) after exposure for 24 cycles at 900°C with Na_2SO_4 - 60% V_2O_5 + MgO coating shows a rapid rate of wt. gain during the first two cycles and then a reduction in wt. gain rate. The rapid rate of corrosion in the early stage obeys a linear law which allows the formation of a thin, thermodynamically stable Cr_2O_3 layer of scale. When Cr_2O_3 layer becomes compact and protective, the direct interaction between metal and the salt mixture becomes difficult and hence the corrosion rate decreases. When a comparison is made between the total wt. gain values obtained with and without MgO addition, it was observed after 24 cycles that it decreased from 23.2 to 2.2 mg/cm^2 with MgO addition. The thickness value of the scale also reduced from 62.5 to 33.3 micron with MgO addition. Thus it can be inferred that MgO addition has very beneficial effect in reducing the aggressiveness of the environment.

The possible mechanism of corrosion with MgO addition can be explained as follows:

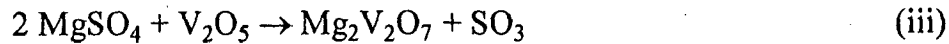
As suggested by Hancock et. al.⁽⁷⁷⁾ when the coated specimen was heated to 900°C, Na_2SO_4 dissociation into Na_2O and SO_3 might have occurred:



When sufficient SO₃ is generated by above equation MgO can be sulphated as MgSO₄ as suggested by Rhys - Jones⁽⁷⁸⁾ et. al.,



V₂O₅ does not react with Na₂SO₄ to form molten sodium vanadate, instead it has higher affinity for MgO and formed magnesium pyrovanadate, Mg₂V₂O₇ (m.p. 835°C). The molten Mg pyrovanadate deposits on the turbine blades⁽⁷⁸⁾



If $p_{\text{SO}_3} \leq p_{\text{SO}_3}$ (equilibrium), then magnesium orthovanadate and MgO are more stable⁽⁷⁸⁾.

Mg₃V₂O₈ (m.p. 1190°C) is produced when MgO is added in the ratio 3MgO: 1V₂O₅



Mg₃V₂O₈ is in the solid form, hence only solid state reaction was possible during the corrosion test. Mass transfer in solids is slower than in liquids due to difference in densities. The corrosion process is a dynamic one in which true equilibrium is not achieved⁽⁷⁷⁾. The formation of oxides of various elements present in the alloy and then their spinel formation has already been discussed in sec 6.3 of this chapter.

The visual observation shows the presence of brown coloured particles of the unreacted salt on the surface of the scale (Fig 5.26). The coarse crystalline structure of Mg₃V₂O₈ is revealed in the SEM micrograph (Fig 5.76).

The XRD analysis identified the presence of Cr₂O₃, Fe₂O₃, FeS, NiCr₂O₄, FeV₂O₄ and Mg₃V₂O₈ (Tab 5.24, Fig 5.51). The EDAX analysis at areas 10-12 (Tab 5.29) indicates the presence of Fe, Ni, Cr, V, S and Mg so as to confirm the presence of compounds identified by XRD. The EPMA X ray maps (Fig 5.101) show a thin layer of chromia scale formed on the alloy surface which may be attributed for the reduced corrosion rate after two cycles. Mg and V are present throughout the scale in high concentration. Formation of oxides and sulphide both has occurred and are homogeneously distributed (Fig 5.101).

Major portion of the Cr present in the alloy might have formed Cr₂O₃, hence Cr depletion is observed in the substrate near the alloy surface (Fig 101). As the oxygen ion concentration might have reduced, sulphur reacted to form sulphides⁽⁸⁵⁾ which are present in the scale as well as into the substrate at the grain boundaries Ni has not taken much part

in the corrosion reaction hence it is present in the negligible amount in the scale as revealed by X-ray map (Fig 5.101c). Very little amount of iron has also been incorporated in the scale (Fig 5.101d). Probable hot corrosion mechanism for alloy A under Na₂SO₄-60% V₂O₅ + MgO has been shown schematically in Fig 6.6.

6.5.2 Effect of MgO Addition on Hot Corrosion of Alloy B (Superni 75)

Wt. gain-time plot for Ni-base superalloy B after exposure for 24 cycles at 900°C with Na₂SO₄ - 60% V₂O₅ + MgO coating also shows similar trend of wt. change as observed with alloy A. Cr₂O₃ formation took place due to its high thermo dynamic stability during the initial stages and as soon as it became sufficient thick and protective the corrosion rate decreased. When the total wt. gain values, obtained with and without MgO addition to the salt mixture, were compared, it was observed that MgO addition decreased it from 6.75 to 5.0 mg/cm². The thickness value of the scale also decreased from 45.0 to 43.0 micron. Thus it can be inferred from these observations that the MgO addition has a beneficial effect in reducing corrosion, although to a lower extent. This may be due to the inherent corrosion resistance property of the alloy B towards vanadic corrosion by the formation of thick protective Cr₂O₃ scale on its surface as observed in sec. 6.3 of this chapter.

Some unreacted salt mixture was visually observed which may be due to the incomplete consumption of the salt mixture during exposure. Due to the higher affinity of V₂O₅ for MgO as compared to Na₂SO₄, it formed Mg₃V₂O₈ (m.p. 1190°C) which remained solid during studies. The amount of Mg₃V₂O₈ formation depends upon the Mg/MgO + V₂O₅ as shown in V₂O₅ - MgO phase diagram (Fig 2.9). 3 MgO : 1 V₂O₅ addition provides the maximum efficiency⁽⁷⁸⁾. The reaction for Mg₃V₂O₈ formation is shown in reaction (iv) of sec. 6.5.1. The mechanism of corrosion reactions might be similar to that described for alloy A in sec 6.5.1 of this chapter. SEM micrograph (Fig 5.77) reveals the irregular coarse grained structure of the scale with big cavities between them and is porous in nature. The XRD analysis (Tab 5.25, Fig 5.52) identified Cr₂O₃, NiO, Ni(VO₃)₂ and Mg₃V₂O₈ as the prominent phases. The strong peaks are of Cr₂O₃, NiO and Mg₃V₂O₈ while other peaks are weak. The EDAX analysis at areas 10 and 11 (Tab 5.30,

The SEM micrograph (Fig 5.79) shows the bright and dark particles 10-12 whose EDAX analysis (Tab 5.32) indicates the presence of Fe, Ni, Cr, V, Ti, Al and Mg. The XRD analysis (Tab 5.27, Fig 5.54) identified the phases Cr_2O_3 , Fe_2O_3 , NiO, $\text{Ni}(\text{VO}_3)_2$, $\text{Mg}_3\text{V}_2\text{O}_8$ and NiCr_2O_4 as the prominent ones.

The strong peaks were of $\text{Mg}_3\text{V}_2\text{O}_8$, Cr_2O_3 and NiO, while other peaks were weak. The BSEI and X-ray maps (Fig 5.104 a-g) of alloy D specimen shows two distinct layers of the scale. The top layer consists of magnesium vanadate and NiO in high concentration, while the scale beneath it consists of a homogeneous mixture of oxides of Fe, Ni, Cr, Mg and V. The scale near the surface of alloy is rich oxides of vanadium and chromium. Cr depletion in the substrate is also observed. The concentration of oxygen ion was high enough to diffuse even into the substrate to cause internal oxidation at the grain boundaries to a little extent. The probable corrosion mechanism for alloy D has been shown schematically in Fig 6.6a-c.

6.5.5 Effect of MgO addition on Hot Corrosion of Alloy E (Superco 605)

When MgO was added in the ratio of $3\text{MgO}:1\text{V}_2\text{O}_5$ in the $\text{Na}_2\text{SO}_4 - 60\% \text{V}_2\text{O}_5$ salt mixture as recommended by Rhys-Jones et. al. (78) and then exposed for hot corrosion for 24 cycles at 900°C , it was observed that the extent of corrosiveness of the environment reduced considerably. The wt. change vs time plots (Fig 5.25) show that there is a rapid rate of reaction during the first two cycles, then the wt. gain rate decreases upto 10 cycles of exposure. Later the wt. gain value decreases with a high rate upto the last cycle.

By the comparison of the total wt. gain values, obtained with and without MgO addition to $\text{Na}_2\text{SO}_4 - 60\% \text{V}_2\text{O}_5$, it was observed that the total wt. gain value decreased from 35.75 to 5.2 mg/cm^2 after exposure for 24 cycles. The thickness value of the scale formed on the alloy surface decreased from 96.6 to 55.0 micron after exposure for 24 cycles at 900°C with MgO addition. These observations indicate that the MgO addition is very much beneficial in reducing corrosion rate. Due to unrestricted diffusion of oxygen ions to the metal surface, Cr formed Cr_2O_3 due to its high thermal stability. Once the

in the corrosion reaction hence it is present in the negligible amount in the scale as revealed by X-ray map (Fig 5.101c). Very little amount of iron has also been incorporated in the scale (Fig 5.101d). Probable hot corrosion mechanism for alloy A under Na_2SO_4 -60% V_2O_5 + MgO has been shown schematically in Fig 6.6.

6.5.2 Effect of MgO Addition on Hot Corrosion of Alloy B (Superni 75)

Wt. gain-time plot for Ni-base superalloy B after exposure for 24 cycles at 900°C with Na_2SO_4 - 60% V_2O_5 + MgO coating also shows similar trend of wt. change as observed with alloy A. Cr_2O_3 formation took place due to its high thermo dynamic stability during the initial stages and as soon as it became sufficient thick and protective the corrosion rate decreased. When the total wt. gain values, obtained with and without MgO addition to the salt mixture, were compared, it was observed that MgO addition decreased it from 6.75 to 5.0 mg/cm^2 . The thickness value of the scale also decreased from 45.0 to 43.0 micron. Thus it can be inferred from these observations that the MgO addition has a beneficial effect in reducing corrosion, although to a lower extent. This may be due to the inherent corrosion resistance property of the alloy B towards vanadic corrosion by the formation of thick protective Cr_2O_3 scale on its surface as observed in sec. 6.3 of this chapter.

Some unreacted salt mixture was visually observed which may be due to the incomplete consumption of the salt mixture during exposure. Due to the higher affinity of V_2O_5 for MgO as compared to Na_2SO_4 , it formed $\text{Mg}_3\text{V}_2\text{O}_8$ (m.p. 1190°C) which remained solid during studies. The amount of $\text{Mg}_3\text{V}_2\text{O}_8$ formation depends upon the Mg/MgO + V_2O_5 as shown in V_2O_5 - MgO phase diagram (Fig 2.9). 3 MgO : 1 V_2O_5 addition provides the maximum efficiency⁽⁷⁸⁾. The reaction for $\text{Mg}_3\text{V}_2\text{O}_8$ formation is shown in reaction (iv) of sec. 6.5.1. The mechanism of corrosion reactions might be similar to that described for alloy A in sec 6.5.1 of this chapter. SEM micrograph (Fig 5.77) reveals the irregular coarse grained structure of the scale with big cavities between them and is porous in nature. The XRD analysis (Tab 5.25, Fig 5.52) identified Cr_2O_3 , NiO, $\text{Ni}(\text{VO}_3)_2$ and $\text{Mg}_3\text{V}_2\text{O}_8$ as the prominent phases. The strong peaks are of Cr_2O_3 , NiO and $\text{Mg}_3\text{V}_2\text{O}_8$ while other peaks are weak. The EDAX analysis at areas 10 and 11 (Tab 5.30,

Fig 5.77) confirm the presence of these elements in the scale. The BSEI and X-ray maps (Fig 5.102) of alloy B indicates the presence of a duplex scale. The inner thin layer consists of Cr_2O_3 while the outer thick layer consists of oxides of Ni, Cr, Fe, V and MgO. The oxygen being present in higher concentration and also due to spalling of the outer porous scale, it could penetrate into the substrate by inward diffusion to form chromium oxide at the grain boundaries only at a limited area.

6.5.3 Effect of MgO Addition on Hot Corrosion of Alloy C (Superni 600).

The wt. change plots for Ni-base superalloy C also shows similar trend of rapid increase in wt. gain during the first two cycles and then a gradual decrease in wt. gain rate. The rapid increase may be due to Cr_2O_3 formation which is thermodynamically stable. The decrease in wt. gain may be attributed to the protective nature of the scale as well as spalling of the outer scale during cooling. Spalling was actually observed during experimentation. When the total wt. gain values, obtained with and without MgO addition, were compared it was observed that MgO addition reduced the total wt. gain value from 11.50 to 6.31 mg/cm^2 after 24 cycle exposure. The thickness of the scale also reduced from 75.0 to 62.0 micron. These observations suggest that MgO addition is beneficial in reducing the extent of corrosion caused by Na_2SO_4 - 60% V_2O_5 salt mixture coating. The mechanism by which corrosiveness is reduced for alloy A and B can be extended for this alloy also which are already described in 6.5.1 and 6.5.2 of this chapter. $\text{Mg}_3\text{V}_2\text{O}_8$ formation has taken place in preference to sodium vanadate. $\text{Mg}_3\text{V}_2\text{O}_8$ being solid only solid state reaction could occur. The diffusion rate is much slower in the solid state than in the liquid condition and also due to lesser defect concentration in the solid state. 3MgO : 1 V_2O_5 is a good proportion of MgO addition to achieve maximum efficiency⁽⁷⁷⁾. The phase diagram for MgO- V_2O_5 system (Fig 2.9) shows the effect of amount of MgO addition.

The bright particle of $\text{Mg}_3\text{V}_2\text{O}_8$ was revealed by the SEM micrograph (Fig 5.78) and X ray maps by EPMA (Fig 5.103). The SEM micrograph also shows that the scale consists of coarse rounded particles. Some big particles and cavities in between are also present which makes the scale porous. The XRD analysis (Tab 5.26, Fig 5.53) identified

the phases Cr_2O_3 , NiO , FeV_2O_4 , $\text{Ni}(\text{VO}_3)_2$ and $\text{Mg}_3\text{V}_2\text{O}_8$ and NiCr_2O_4 . The mechanism of formation of these oxides and the spinels has already been discussed in sec. 6.3 of the present chapter. The presence of the elements Mg, V, Fe, Ni and Cr has been indicated by the EDAX analysis at areas 11-13 (Tab 5.31, Fig 5.78). The BSEI and X-ray maps of alloy C (Fig 5.103) shows that the nature of the scale is duplex. The outer layer is rich in Mg, V and Cr elements. Cr is present in high concentrations near the alloy surface to form a protective Cr_2O_3 layer. The oxides of Ni, Cr, Mg, V and Fe are uniformly distributed throughout the scale. The scale near the alloy surface was nonadherent due to discontinuous Cr_2O_3 layer leading to an easy access of corroding species towards metal. Therefore the corrosion process could continue with a slower rate.

6.5.4 Effect of MgO Addition on Hot Corrosion of Alloy D (Superni 718)

The wt. change plots for Ni base alloy D after exposure at 900°C for 24 cycles with $\text{Na}_2\text{SO}_4 - 60\% \text{V}_2\text{O}_5 + \text{MgO}$ coating (Fig 5.24) shows that the corrosion rate is fast during the first two cycles and then the rate decreases. Due to Cr_2O_3 formation in the initial stage, the corrosion rate is faster and later it became protective leading to the reduction in corrosion rate. On comparison of the total wt. gain values obtained after 24 cycle exposure with and without MgO, it was observed that the MgO addition reduced the wt. gain value from 12.0 to 8.05 mg/cm^2 . Thus there is a reduction of 33% in the total wt. gain value. The thickness of the scale formed on the alloy surface after 24 cycle exposure at 900°C decreased from 67.5 to 62.7 micron. These observations suggest that MgO addition has a beneficial effect in reducing corrosiveness of the environment. The mechanism by which the extent of corrosion decreases is similar to that for alloys A, B and C, i.e., in place of a liquid NaVO_3 (m.p. 610°C), a solid magnesium orthovanadate, $\text{Mg}_2\text{V}_2\text{O}_8$ (m.p. 1190°C) is formed. Only solid state reaction might be possible. Mass transfer in solids is slower than in liquids due to difference in densities. The amount of MgO addition was $3\text{MgO} : 1\text{V}_2\text{O}_5$ to achieve maximum efficiency in reducing the extent of corrosion. Cracking of the scale and its spallation was observed during experimentation due to which fresh areas of the alloy might have been exposed to corrosive environment leading to continuation of corrosion upto the last cycle of exposure.

The SEM micrograph (Fig 5.79) shows the bright and dark particles 10-12 whose EDAX analysis (Tab 5.32) indicates the presence of Fe, Ni, Cr, V, Ti, Al and Mg. The XRD analysis (Tab 5.27, Fig 5.54) identified the phases Cr_2O_3 , Fe_2O_3 , NiO, $\text{Ni}(\text{VO}_3)_2$, $\text{Mg}_3\text{V}_2\text{O}_8$ and NiCr_2O_4 as the prominent ones.

The strong peaks were of $\text{Mg}_3\text{V}_2\text{O}_8$, Cr_2O_3 and NiO, while other peaks were weak. The BSEI and X-ray maps (Fig 5.104 a-g) of alloy D specimen shows two distinct layers of the scale. The top layer consists of magnesium vanadate and NiO in high concentration, while the scale beneath it consists of a homogeneous mixture of oxides of Fe, Ni, Cr, Mg and V. The scale near the surface of alloy is rich oxides of vanadium and chromium. Cr depletion in the substrate is also observed. The concentration of oxygen ion was high enough to diffuse even into the substrate to cause internal oxidation at the grain boundaries to a little extent. The probable corrosion mechanism for alloy D has been shown schematically in Fig 6.6a-c.

6.5.5 Effect of MgO addition on Hot Corrosion of Alloy E (Supercor 605)

When MgO was added in the ratio of 3MgO:1V₂O₅ in the Na₂SO₄ - 60% V₂O₅ salt mixture as recommended by Rhys-Jones et. al. (78) and then exposed for hot corrosion for 24 cycles at 900°C, it was observed that the extent of corrosiveness of the environment reduced considerably. The wt. change vs time plots (Fig 5.25) show that there is a rapid rate of reaction during the first two cycles, then the wt. gain rate decreases upto 10 cycles of exposure. Later the wt. gain value decreases with a high rate upto the last cycle.

By the comparison of the total wt. gain values, obtained with and without MgO addition to Na₂SO₄ - 60% V₂O₅, it was observed that the total wt. gain value decreased from 35.75 to 5.2 mg/cm² after exposure for 24 cycles. The thickness value of the scale formed on the alloy surface decreased from 96.6 to 55.0 micron after exposure for 24 cycles at 900°C with MgO addition. These observations indicate that the MgO addition is very much beneficial in reducing corrosion rate. Due to unrestricted diffusion of oxygen ions to the metal surface, Cr formed Cr_2O_3 due to its high thermal stability. Once the

chromia layer became protective, the corrosion rate decreased upto 10 cycles due to the separation of metal surface from the corrosive species as explained earlier. MgO reacts directly with V_2O_5 to form magnesium orthovanadate, $3MgO \cdot V_2O_5$ (m.p $1190^\circ C$). According to reaction (iv) of sec. 6.5.1, the product $Mg_3V_2O_8$ being solid at the reaction temperature $900^\circ C$, the reaction rate further decreased and the wt. gain value decreased significantly after 10 cycles till the end of the test. The effectiveness of MgO addition is due to : (i) the increase of melting point of deposits (ii) the counteraction of the effects of SO_3 in combustion gases. The increase in melting point of $Mg_3V_2O_8$ greatly increases its viscosity which reduces the diffusion of oxygen and counteracts the destruction of the protective oxide barrier film as Fichera et. al.⁽⁸¹⁾ have recommended after their studies with MgO addition.

The SEM micrograph (Fig 5.80) shows porous scale consisting of fine grained particles leading to the lower rate of diffusion of corroding species and cations through it. Co, Cr, W formed their respective oxides and then the formation of spinels might have occurred as described in sec. 6.3 of this chapter. The mechanism of formation of these oxides and spinels is already explained in sec. 6.3 of this chapter. The EDAX analysis at areas 9 and 10 (Tab 5.33, Fig 5.80) indicates the presence of the elements Fe, Cr, Ni, Co, W in high concentration. The XRD (Tab 5.28, Fig 5.55) identified the presence of Cr_2O_3 , CaO, WO_3 , FeV_2O_4 , $Co_3V_2O_8$, $(Cr,Fe)_2O_3$ and $NiCr_2O_4$ as the prominent phases. The BSEI and X ray maps for alloy E (Fig 5.105a-i) reveal the presence and distribution of these oxides and spinels. Due to the reduction of oxygen partial pressure, sulphur penetration has been observed in the substrate as NiS (Fig 5.105 c,h). Co, Cr, V and Fe are indicated to be present in the entire scale by the X-ray maps (Fig 5.105), while the presence of W, Ni are restricted to certain areas. S is segregated into the substrate near the surface (Fig 5.105h) and its presence in the scale is insignificant. EDAX analysis (Tab 5.33) has also indicated S to be absent in the scale of alloy E. Due to the porous nature of scale at the surface, spalling has occurred during experimentation specially during cooling which has added to the reduction in weight gain during 10-24 cycles of the test. The probable mechanism of corrosion for alloy E in Na_2SO_4 -60% V_2O_5 + MgO is shown schematically in Fig 6.6.

6.6 COMPREHENSIVE DISCUSSION

In this section an attempt has been made to compare the results of hot corrosion studies of alloys A, B, C, D and E with various $\text{Na}_2\text{SO}_4\text{-V}_2\text{O}_5$ salt coatings at different temperatures conducted in laboratory and in industrial atmospheres and to discuss the salient features.

The nature of kinetic plots for the alloys A, B, C, D and E after exposure in various salt mixtures of Na_2SO_4 and V_2O_5 is very similar. In general, a rapid corrosion rate during the first two cycle is followed by a decreased corrosion rate during the remaining cycles of the test of these alloys. It can be inferred from this observation that their behaviour towards the hot corrosion against these salts may also be similar. The initial fast rate of corrosion might be due to the chemical reaction by which a thermodynamically stable Cr_2O_3 formation on the alloy surface takes place and the slower rate of corrosion after two cycles might be due to the presence of protective Cr_2O_3 scale and also due to various other chemical reactions taking place by fluxing mechanism. Fluxing commonly means the dissolution of the protective oxides present in the salt at the scale/salt interface and then precipitation at the salt/air or salt/gas interface. In case of fluxing with thin film of salt Rapp and Goto⁽⁴⁾ have suggested the condition that the gradients in solubility of the protective oxide with distance into the salt layer should be negative at the oxide/salt interface so that accelerated attack could be sustained. To sustain steady corrosion, the protective oxide is fluxed as fast as it grows⁽⁷⁾. But in the present studies the corrosion rate decreases after two cycles which suggests that the rate of fluxing is slower than the rate of Cr_2O_3 formation. It means that a protective Cr_2O_3 layer is maintained. From this observation it can be inferred that these alloys, in general, have good corrosion resistance towards the $\text{Na}_2\text{SO}_4\text{-V}_2\text{O}_5$ environment.

In the alloy specimens exposed to Na_2SO_4 environment, the prominent phases identified by the XRD in their scales are common, e.g. $\alpha\text{-Fe}_2\text{O}_3$, NiO, Cr_2O_3 . Similar chemical reactions might have taken place in these alloys in the same sequence as mentioned in sec. 6.1-6.5 and as suggested by Luthra⁽⁷²⁾, Fryburg⁽⁴⁶⁾ and Malik et. al.⁽³¹⁾ under Na_2SO_4 environment. Then Cr_2O_3 might have basically got fluxed with Na_2SO_4 to

form Na_2CrO_4 which later evaporated⁽⁴⁶⁾. This observation might also have contributed to the reduction in wt. gain in later cycles. The solubilities of oxides are related to the concentration of oxygen ions as suggested by Bornstein and DeCrescente⁽¹⁴⁾.

Oxygen partial pressure is believed to be present in excess than its equilibrium value so as to cause oxidation of the various elements into their respective oxides, hence the main phases identified in the scales are oxides only. On the contrary, sulphur partial pressure might be less than its equilibrium partial pressure required for sulphidation to occur in the environment⁽¹⁰²⁾ due to which sulphidation, in general, has not been observed in these alloys except in alloys C and D at 700-900°C in pure Na_2SO_4 whereas CrS was identified.

The scale consisted of homogeneous mixture of oxides which then might have combined to form spinels $(\text{Cr, Fe})_2\text{O}_3$, NiCr_2O_4 which are found to exist in the outer layer of the scales.

The extent of attack was less at 700 and 800°C due to the existence of Na_2SO_4 (m.p. 884°C) in the solid state as observed by the lower wt. gain values. But at 900°C the attack was relatively more due to the liquid condition of Na_2SO_4 . Diffusion rate is higher in the liquid state than in the solid state of the salt. The chemical nature of the compounds formed did not change with increase in temperature. This suggests that similar reactions might have taken place in the same sequence at all these temperatures.

The Cr_2O_3 scale formed on the alloy surface was quite protective (dense) hence oxide ions (O^{2-}) could not penetrate it and so internal oxidation was not observed in the substrate of these alloys. All alloys have shown low corrosion rate against Na_2SO_4 . The probable mechanism of the Na_2SO_4 -induced corrosion has been shown schematically in the Fig. 6.1 indicating the interaction between the inward diffusion of the oxygen anions and the outward diffusion of the metal cations, the protective Cr_2O_3 layer on the alloy surface and the outer layer of oxides and spinels. The presence of these oxides were identified by XRD and the presence of elements have been indicated by EDAX analysis and are revealed by X-ray maps.

With Na_2SO_4 -15% V_2O_5 thin coating (4.0-5.0 mg/cm^2) the alloys have suffered moderate corrosion due to the formation of a low melting phase sodium metavanadate,

NaVO_3 (m.p. 610°C) thereby allowing higher diffusion rate. The mechanism of corrosion of these alloys might also be similar due to the identical nature of wt. change plots of these alloys at 700 , 800 and 900°C , except for the alloy D at 900°C where a wt. loss of 6.8 mg/cm^2 was observed. The average thickness values of the scale were also comparable varying in the range of 40 - 47 microns.

The higher corrosion observed in case of alloy D might be due to the presence of 3.05% Mo which supposedly led to formation of MoO_3 which subsequently got volatilized at 600°C ⁽⁸⁾. Absence of Mo in the scale was confirmed by EDAX and by EPMA in our studies. Also the scale formed on the alloy D surface was porous which cracked during cooling to room temperature causing fissures through which corrosive species could reach the alloy substrate and so corrosion continued by fluxing of Cr_2O_3 . The Na_2CrO_4 formed also might have evaporated. Part of the scale also spalled off as observed during experimentation. All these factors had a combined contribution towards the loss in wt. of alloy D. The probable mechanism of corrosion for alloy D has been explained with the help of a neat sketch (Fig. 6.3) showing the existence of oxides and spinels in the outer scale because they were formed in the early stages and moved away from the alloy surface as the time progressed⁽⁸⁵⁾.

With thin film of Na_2SO_4 - $60\%\text{V}_2\text{O}_5$, the fluxing action was more predominant by higher rate of dissolution of Cr_2O_3 in NaVO_3 than its rate of formation because of the low m.p. of the eutectic salt mixture (500°C) as observed in Na_2SO_4 - V_2O_5 diagram Fig. 2.7. Higher fluidity and low viscosity might also be a contributing factor. Due to this, higher corrosion rates were observed at 700 , 800 and 900°C but significantly higher at 900°C were indicated by the kinetic plots of these alloys (Fig. 5.11-5.15). This sulphate vanadate hot corrosion predominantly depends upon acid-base reactions between metal oxides and the acidic-basic constituents (NaVO_3 and SO_3) of the contaminants. Similar recommendations have been made by Jones et. al.⁽⁷³⁾. In the present investigation all the three Ni-base alloys B, C, and D have shown superior corrosion resistance than alloys A and E in this most severe environment because these alloys form protective layer of Cr_2O_3 on their surfaces and also Ni being the base material forms larger amount of $\text{Ni}(\text{VO}_3)_2$ by fluxing which is a solid phase at the test temperatures (700 - 900°C). Similar

findings of Ni-base alloy being superior to Fe-base alloy in $\text{Na}_2\text{SO}_4\text{-V}_2\text{O}_5$ environment has been reported by Kerby and Wilson⁽¹¹⁹⁾.

The presence of Fe and Na in the vanadate melts increases the non stoichiometry hence increases the oxygen diffusion⁽¹⁰⁸⁾, which may be the reason for poor corrosion resistance of Fe-base alloy A in $\text{Na}_2\text{SO}_4\text{-60}\%\text{V}_2\text{O}_5$. The mechanism of accelerated corrosion is most satisfactorily explained by Kerby and Wilson⁽¹⁰⁶⁾ where they suggested that catalytic action of V_2O_5 increased the defect concentration of the scale thereby allowing easy diffusion of reacting species. Thus due to the continuous dissolution of Cr_2O_3 , a heterogeneous brittle scale might have formed which cracked during cooling due to the difference in thermal expansion and contraction (thermal mismatch) and caused fissures through which fresh metal was exposed to corrosive species. The cracking of scale was also observed with this alloy in our investigation.

Co-base alloy E has also suffered severe corrosion in $\text{Na}_2\text{SO}_4\text{-60}\%\text{V}_2\text{O}_5$ which may be attributed to the higher fluidity of the melt⁽⁵⁹⁾ which adhere to the protective oxide and causes fluxing. The rate of corrosion might also increase by the formation of stable oxides of elements present in the alloy and environment, (e.g. Co, W, Cr, Ni, V). These oxides induce acidic fluxing hence the formation of these oxides are harmful⁽⁹⁹⁾. The spalling of porous scale might also contribute to the continuation of corrosion till the termination of the test. The probable mechanism of formation of these oxides by inward diffusion of oxygen and outward diffusion of metal cations, their spinel formation are shown schematically in Fig. 6.4 and the X-ray maps of the corroded alloy E also confirm the presence of these elements at definite locations.

The results of hot corrosion studies in combustion gas (c.g.) have shown that the corrosion kinetics obeyed parabolic law with two regions, the corrosion rate falling with the protective nature of Cr_2O_3 and $\text{Ni}(\text{VO}_3)_2$ layer. The kinetic data for these alloys also indicate the occurrence of similar trend of corrosion in these alloys that occurred in the tests conducted in air. The corrosion rate was higher as observed from the total wt. gain values which may be attributed to the higher temperature i.e. 1100°C as well as to the observed removal of some scale by impingement of high velocity of c.g. thereby exposing fresh areas of the alloy to the aggressive environment.

The extent of severe corrosion by Na_2SO_4 -60% V_2O_5 may be reduced by adding MgO as an inhibitor in the ratio of 3MgO:1 V_2O_5 as recommended by Rhys Jones et al.⁽⁷⁸⁾. The mechanism by which it reduces corrosion rate is explained by the formation of a solid phase, magnesium orthovanadate $\text{Mg}_3\text{V}_2\text{O}_8$ (m.p. 1190°C) by the reaction of V_2O_5 with MgO in preference to formation of liquid NaVO_3 . In our test MgO addition reduced the corrosion rate of all the alloys but its efficiency of inhibition was more for alloy A (90.51%) and for alloy E (85.33%).

The analysis of the wt. gain data shows that the Ni-base alloys B and C have superior corrosion resistance properties in all Na_2SO_4 - V_2O_5 environment which may be due to the formation of protective Cr_2O_3 and the solid phase $\text{Ni}(\text{VO}_3)_2$ identified in the scales. Also alloy C proved better than B at 700 and 800°C, while alloy B has proved to be the best at 900°C, even in the most corrosive environment of Na_2SO_4 -60% V_2O_5 .

From this investigation the suitability of these alloys for the various environments can be assessed.. All the alloys proved to be good corrosion resistant in pure Na_2SO_4 at 700-900°C, whereas with Na_2SO_4 -15% V_2O_5 the corrosion was moderate except for alloy D where the wt. loss was observed at 900°C. In Na_2SO_4 -60% V_2O_5 environment, all these alloys suffered only moderate corrosion at 700 and 800°C whereas at 900°C the corrosion was significant for alloys A and E.

In case of combustion gas (c.g.) environment in an industrial boiler at 1100°C with the above salt coatings these alloys have shown mild corrosion which is slightly higher than the laboratory studies under air except for Na_2SO_4 -60% V_2O_5 , where in laboratory tests at lower temperatures showed higher rate of corrosion for all the alloys.

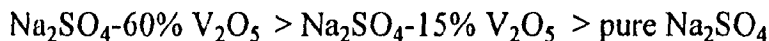
The existence of salt coatings under the turbulent environment cannot be ensured and also the fly ash deposits may interfere the corrosion process, hence it is difficult to comprehend the mode of corrosion.

The effects of MgO as an inhibitor in the ratio of 3:1 MgO: V_2O_5 has proved to be effective in all the alloys in Na_2SO_4 -60% V_2O_5 at 900°C in air.

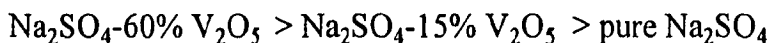
CONCLUSIONS

Based on the findings of hot corrosion studies carried out on Fe-base alloy A (Superfer 800H), Ni-base alloys B (Superni 75), C(Superni 600) and D(Superni 718) and a Co-base alloy E (Superco 605) in salt environments of pure Na_2SO_4 , Na_2SO_4 -15% V_2O_5 and Na_2SO_4 -60% V_2O_5 (for 24 cycles at 700, 800 and 900°C in air and also at 1100°C in c.g. for 6 cycles) and in Na_2SO_4 -60% V_2O_5 + MgO (for 24 cycles at 900°C in air), the following conclusions may be drawn.

1. On the basis of the total wt. gain measurements for alloys A, B, C, D and E after 24 cycles exposure at 700, 800 and 900°C in air in laboratory, corrosion in Na_2SO_4 - 60% V_2O_5 was higher than observed under other salts. The total wt. gain was observed to be in the following order:



2. The total wt. gain values observed for these alloys after hot corrosion for 6 cycles at 1100°C in c.g. was also in the same order as above:



3. The ranking of alloys in decreasing order of their wt. gain values observed in different salts and temperature conditions has been observed as follows:

A. Pure Na_2SO_4 in air for 24 cycles

a. 700°C → alloy A > alloy E > alloy D > alloy C > alloy B

b. 800°C → alloy A > alloy D > alloy C > alloy E > alloy B

c. 900°C → alloy A > alloy C > alloy E > alloy D > alloy B

B. Na_2SO_4 - 15% V_2O_5 in air for 24 cycles.

a. 700°C → alloy A > alloy E > alloy D > alloy B > alloy C

b. 800°C → alloy A > alloy E > alloy D > alloy B > alloy C

c. 900°C → alloy D > alloy C > alloy B > alloy E > alloy A

C. Na₂SO₄ - 60% V₂O₅ in air for 24 cycles

a. 700°C → alloy A > alloy E > alloy B > alloy D > alloy C

b. 800°C → alloy A > alloy E > alloy D > alloy B > alloy C

c. 900°C → alloy A > alloy E > alloy D > alloy C > alloy B.

D. Combustion gas at 1100°C for 6 cycles

a. With pure Na₂SO₄ → alloy A > alloy D > alloy C > alloy B > alloy E

b. With Na₂SO₄-15% V₂O₅ → alloy A > alloy D > alloy E > alloy C > alloy B

c. With Na₂SO₄-60% V₂O₅ → alloy D > alloy C > alloy B > alloy E > alloy A

E. Na₂SO₄ - 60% V₂O₅ + MgO at 900°C for 24 cycles.

alloy D > alloy C > alloy E > alloy B > alloy A.

4. These alloys have shown good corrosion resistance under pure Na₂SO₄ and Na₂SO₄-15%V₂O₅ at all temperatures and their wt. gain values are also comparable, except for the alloy D in Na₂SO₄-15%V₂O₅ at 900°C. This observation may be attributed to the high Cr content (15.5-21%) in these alloys.
5. Alloy D suffered moderate corrosion (6.8 mg/cm² wt. loss) in Na₂SO₄-15%V₂O₅ at 900°C. This may be attributed to the presence of 3.05% Mo which has deleterious effects due to the formation of MoO₃ which volatilises above 600° C^(52, 53, 87, 93) and to the formation of liquid sodium molybdate which served as a flux for the acidic dissolution of Cr₂O₃⁽⁴⁶⁾. Also, spalling of the scale observed during experiment might have added to the wt. loss.
6. Ni-base alloys B and C have shown good corrosion resistance at all temperatures in the most aggressive environment of Na₂SO₄-60% V₂O₅ which may be due to the observed thick, continuous, compact protective layer of Cr₂O₃ on the alloy surface and also due to the formation of refractory Ni-vanadate, Ni(VO₃)₂ in the scale as identified by XRD and revealed by X ray maps.
7. Fe-base alloy A has shown comparatively inferior corrosion resistance in nearly all the environments as their observed wt. gain values are higher as compared to other alloys. The reason for its inferior corrosion resistance may be due to the formation of a porous, non-protective oxide scale on its surface which allowed inward

diffusion of oxide ions (O^{2-}) towards the alloy substrate. The presence of Fe and Na in the vanadate melts increases the non stoichiometry of the scale causing higher diffusion of corrosive species. These observations might have led to the breakaway corrosion to cause wt. loss (23.2 mg/cm^2) in Na_2SO_4 -60% V_2O_5 at 900°C .

8. Co-base alloy E was also found to have inferior corrosion resistance than Ni-base alloys in nearly all the environments, on the basis of their wt. gain values, specially at 900°C in Na_2SO_4 - 60% V_2O_5 (35.5 mg/cm^2). The reason for this observation may be due to the porous non protective scale consisting of various oxide ingredients (e.g. CoO , WO_3 , Cr_2O_3 , TiO_2) as revealed by X-ray maps, containing numerous pores through which the corrosive species could continuously reach the alloy substrate and so corrosion continued till the last cycle.
9. The hot corrosion kinetics of these alloys in combustion gas (c.g.) are observed to obey parabolic rate law of oxidation at 1100°C as their (wt. gain)² - time plots were linear which consisted of two regions, one of higher rate and another of lower rate constants. The rate constant values increased with increase in V_2O_5 content in the salt mixture.
10. The addition of MgO as an inhibitor in the ratio 3 MgO : 1 V_2O_5 to Na_2SO_4 -60% V_2O_5 reduced sharply the rate of corrosion of these alloys by Na_2SO_4 -60% V_2O_5 at 900°C . This inhibiting effect may be ascribed to the formation of a solid phase $\text{Mg}_3\text{V}_2\text{O}_8$ (m.p. 1190°C) at the test temperature (900°C).
11. Although alloys B and C (Both Ni-base) have shown best corrosion resistance of all the alloys in nearly all conditions of test by the formation of protective Cr_2O_3 and refractory $\text{Ni}(\text{VO}_3)_2$ phases in the scale yet alloy B is superior to alloy C in Na_2SO_4 -60% V_2O_5 at 900°C on the basis of wt. gain values. The reason for this might be the higher Cr content (19.5%) than that of alloy C (15.5%).
12. Hot corrosion products observed in the scales of these alloys are mostly oxides of the elements present in the alloy and the environment from which it can be inferred that oxidation plays the predominant role in the hot corrosion in these tests.

13. Internal oxidation was observed in the substrates of many alloys in different environments, while internal sulphidation was observed only in the substrates of alloys A and E in $\text{Na}_2\text{SO}_4 - 60\% \text{V}_2\text{O}_5 + \text{MgO}$ at 900°C .
14. Greater Cr depletion was observed in the substrates below the oxide scales of alloys A, B, C, D and E in certain environments (pure Na_2SO_4 , $\text{Na}_2\text{SO}_4 - 15\% \text{V}_2\text{O}_5$, $\text{Na}_2\text{SO}_4 - 60\% \text{V}_2\text{O}_5$, $\text{Na}_2\text{SO}_4 - 60\% \text{V}_2\text{O}_5 + \text{MgO}$) which helped in maintaining the protective scale of Cr_2O_3 which perhaps was formed at a higher rate than the rate of its dissolution in the molten salt.

SUGGESTIONS FOR FUTURE WORK

1. Hot corrosion tests should be carried out in actual industrial environment for longer duration preferably 200-1000 hrs to predict the service life of a material and for comparison of hot corrosion resistance of various alloys.
2. Burner-rig set-up should be used to better simulate the actual service conditions for hot corrosion studies.
3. In-situ studies using hot stage microscope can be of great help in determining the actual mechanism of hot corrosion.
4. Role of gaseous environment on hot corrosion behaviour of superalloys should be studied.
5. Basic research efforts should be made to study the involvement of erosion-corrosion interactions to identify the type of coatings most resistant to combined effect of erosion-corrosion.
6. Investigation to improve existing coatings and to develop new coatings and a reliable and less expensive method for application is also needed.
7. To have better insight into the hot corrosion mechanism, reactions between oxides with oxides, sulphides with oxides and sulphides with sulphides should be studied.

REFERENCES

- [1] S. Prakash and V.K. Tiwari, "High Temperature Oxidation of Metals and Alloys, QIP Short Term Course Proceedings, University of Roorkee, Roorkee, June 23-July 7, (1992).
- [2] Y.S. Hwang and R.A. Rapp, *Corrosion*, 45(11), Nov.(1989), p. 933.
- [3] M. Seiersten and P. Kofstad, *High. Temp. Technol.*, 5,(3), Aug. (1987), p. 115.
- [4] R.A. Rapp and K.S. Goto, "The Hot Corrosion of Metals by Molten Salts", in *Symposium on Fused Salts*, J. Braunstein and J.R. Selman (Eds.), The Electrochemical Society, Pennington, N.J. (1979), p. 159.
- [5] R.A. Rapp and Y.S. Zhang, *JOM*, Dec. (1994), p. 47.
- [6] J.A. Goebel and F.S. Pettit, *Met. Trans.*, 1, (1970), p. 1943.
- [7] D.A. Shores, "New Perspectives on Hot Corrosion Mechanisms", in *High Temperature Corrosion*, R.A. Rapp (Ed.), NACE, Houston, TX, (1983), p. 493.
- [8] J. Swaminathan, S. Raghavan and S. Ramakrishna Iyer, *Trans. IIM*, 146(3), June (1993), p. 175.
- [9] J.G. Smeggil and N.S. Bornstein, "Study of Interdiffusion Effects on Oxidation/Corrosion Resistant Coatings for Advanced Single Crystal Superalloys", in *Symp. on High Temperature Protective Coatings*, Ed. S.C. Singhal, The Metallurgical Society of AIME, March 7-8 (1983), P.G.I.
- [10] J.A. Sprague, G.R. Johnston, F.A. Smidt, S.Y. Hwang, G.H. Meier and F.S. Pettit, "Oxidation of CoCrAlY and Y-Implanted CoCrAl Alloys", in *Symp. on High Temperature Protective Coatings*, Ed. S.C. Singhal, The Metallurgical Society of AIME, March 7-8, (1983), p. 93.
- [11] P. Hancock, *Mater Sci. Technol.*, 3, July (1987), p. 536.
- [12] W.T. Reid, *External Corrosion and Deposits: Boilers and Gas Turbines*, Elsevier, New York, USA, (1988).
- [13] N.S. Bornstein, M.A. DeCrescente and H. A. Roth, *Corrosion*, 28, (1972), p. 264.
- [14] N.S. Bornstein and M.A. DeCrescente, *Corrosion*, 26(7), July(1970), p. 209.

- [15] N.S. Bornstein and M.A. DeCrescente, *Trans. of Met. Soc., AIME*, 245, (1969), p. 1947.
- [16] K.L. Luthra and O.H. Leblanc, *Mater. Sci. Engrg.*, 87, (1987), p. 329.
- [17] J. Stringer, *Annual Review of Materials Science*, 7, Ed. R.A. Huggins (Palo Alto, C.A.): Annual Review Inc, (1977), p. 449.
- [18] K. L. Luthra and D.A. Shores, *J. Electrochem. Soc.*, 127(10), Oct. (1980), p. 2202.
- [19] K.L. Luthra and J.H. Wood, *Thin Solid Films*, 119, (1984), p. 271.
- [20] Y. S. Zhang, X. M. Li, T.L. Cao and S.T. Shih, *Corr. Sci. Protec. Tech.*, 4, (1992), p. 9.
- [21] F.S. Pettit and C.S. Giggins, *Hot Corrosion*, Ch. 12 in *Superalloys II*, C.T. Sims, N.S. Stoloff and W.C. Hagel (Eds.), Wiley Publ. N.Y. (1987), pp. 327-358.
- [22] F.S. Pettit and G.H. Meier, *Superalloys (1984)*, M.Gell, C.S. Kartovich, R.H. Bricknel, W.B. Kent, J.F. Radovich (Eds), *The Metallurgical Soc. of AIME*, Warrendale, Pennsylvania, (1984), p. 651.
- [23] C.T. Sims and W. C. Hagel, "The Superalloys Chapter 11 (Hot Corrosion), A Wiley Interscience Publication, John Wiley and Sons, N.Y. (1972).
- [24] F.S. Pettit and G.H. Meier, *Refractory Alloying Elements in Superalloys*, K.K. Tien, R. Reichman (Eds.), ASM, (1984), p. 165.
- [25] F. Gesmundo and F. Viani, *Materials Chemistry and Physics*, 20, (1988), pp. 513-528.
- [26] L. Shi, Y. Zhang and S. Shih, *Corros. Sci.*, 33(9), (1993), p. 1427-1438.
- [27] V. Buscaglia, P. Nanni and C. Bottino, *Corros. Sci.*, 30, (1990), pp. 327-349.
- [28] F. Gesmundo and P. Nanni, *Instituto Chimica, Fisica Applicata Dei Materiali*, Genova (Italia), pp. 54 ter-1-54 ter-6.
- [29] J. Le. Coze, U. Franzoni, O. Cayla, F. Devisme and A. Lefort, *Mater. Sci. Engng.*, A.120, (1989), pp. 293-300.
- [30] L.D. Paul and R.R. Seeley, *Corrosion*, Feb. (1991), pp. 152-159.
- [31] A.U. Malik, M.M. Amin and S. Ahmad, *Trans. Japan Inst. of Metals*, 25(3), (1984), pp. 168-178.

- [32] J.M. Oh, M.J. McNallan, G.Y. Lai, M.F. Rothman, *Met. Trans.*, 17A, Jun,(1986), pp. 1087-1094.
- [33] A.U. Malik and S. Ahmad, *High Temp. Technol.*, 2(4), Nov. (1984), pp. 217-223.
- [34] M. Misbahul Amin, *Thin Solid Films*, 237, (1994), pp. 172-174.
- [35] H.J. Grabke, E. Reese and M. Speigel, *Corros. Sci.*, 37(7), (1995), pp. 1023-1043.
- [36] Motihara Toshio Hisaichi, K. Itoh and Y. Shinata, *J. Japan Inst. of Metals*, 55(11), (1991), pp. 1207-1215.
- [37] J.A. Goebel, F.S. Pettit and G.W. Goward, *Met. Trans*, 4, (1973), p. 261.
- [38] M. Arbab and S.R. Shatynski, *J. Electrochem. Soc.*, 132(5), (1985), pp. 2264-2268.
- [39] P.S. Sidky and M.G. Hocking, *Corros. Sci.*, 27(5), (1987), pp. 499-530.
- [40] N. Otsuka and R.A. Rapp, *J. Electrochem. Soc.*, 137 (1), Jan. (1990), pp. 53-60.
- [41] R.L. Jones and S.T. Godmski, *J. Electrochem. Soc.*, 129(7), (1982), pp. 1613-1618.
- [42] K. Godlewski and E. Godlewska, *Mater. Sci. Engng.*, 88, (1987), pp. 103-109.
- [43] M. Levy, R. Huie and F. Pettit, *Corrosion*, 45(8), Aug. (1989), pp. 661-674.
- [44] D.M. Johnson, D.P. Whitle and J. Stringer, *Oxid. Met.*, 12(3), (1978), pp. 273-291.
- [45] G.C. Fryburg, F.J. Kohl, C. A. Stearns and W.L. Fielder, *J. Electrochem. Soc.*, 129(3), Mar.(1982), pp 571-585.
- [46] G.C. Fryburg, F.J. Kohl and C. A. Stearns, *J. Electrochem. Soc.*, 131(4), Dec.(1984), pp 2985-2997.
- [47] G.C. Fryburg, C. A. Stearns and F.J. Kohl, *J. Electrochem. Soc.*, (1977), pp. 1147-1148.
- [48] D.C. Chatterji, D.W. Mckee, G. Romeo, H.S. Spacil, *J. Electrochem. Soc.*, 122(7), July (1975), pp. 941-951.
- [49] A.U. Malik and S. Ahmad, *Z. Metallkunde*, BD74, H. 12, (1983), pp. 819-824.

- [50] A.U. Malik, N. Asrar, S. Ahmad and N. A. Siddiqui, *Z. Metallkunde*, BD79, H. 5, (1988), pp. 285-295.
- [51] Y.S. Zhang, *J. Electrochem. Soc.*, 133(3), Mar.(1986), pp. 655-657.
- [52] P.S. Sidky and M.G. Hocking, *Corros. Sci.*, 21(5), (1987), pp. 183-203.
- [53] M.G. Hocking and P.S. Sidky, *Corros. Sci.*, 21(5), (1987), pp. 205-214.
- [54] D.A. Shores and K.L. Luthra, *Proc. Conf., Corrosion-Erosion Behaviour of Materials*, K. Natesan (Ed.), (1980), pp. 86-102.
- [55] M. Mobin, A.U. Malik and S. Ahmad, *Bull. Mater. Sci.*, 19(5), Oct(1996), pp. 807-821.
- [56] P. Lambert, B. Champagne and B. Arseneault, *Canadian Metallurgical Quarterly*, 30(2), (1991), pp 125-130.
- [57] V.N. Krasilnikov, M.P. Glazyrin, A.P. Palkin, L.A. Perelyaeva and A.A. Ivakin, *Russian J. Inorg. Chem.*, 32(3), (1987), pp. 425-428.
- [58] E. Otero, M. C. Merina, A. Pardo, M.V. Beizma and G. Buitrago, *Proc. Conf. International Conf. on Metallic Corrosion, Delhi*, (1987), pp. 3583-3591.
- [59] E. Otero, A. Pardo, J. Hernaez and F. J. Perez, *Corros. Sci.*, 30, (1990), pp. 677-683.
- [60] E. Otero, A. Pardo, J. Hernaez and F. J. Perez, *Corros. Sci.*, 34, (1992), pp. 1747-1757.
- [61] Y. Longa and M. Takemoto, *Corrosion*, 48, Jly. (1992).
- [62] K.L. Luthra and H.S. Spacil, *J. Electrochem. Soc.*, 129(3), Mar.(1982), pp. 649-656.
- [63] R. L. Jones, *J. Electrochem. Soc.*, 139(10), Oct. (1992), pp. 2794-2799.
- [64] R.L. Jones, *Materials at High Temp.*, 9(4), Nov. (1991), pp. 228-236.
- [65] R.L. Jones, *American Ceram. Soc.*, 76(6), (1993), pp. 1635-1637.
- [66] G.A. Kolta, I.F. Hewaidy and N.S. Felix, *Thermochimica Acta*, 4(1972), pp. 151-164.
- [67] Hideaki Suito and D.R. Gaskel, *Met. Trans.*, 2, Doc. (1971), pp. 3299-3303.
- [68] N.S. Bornstein, M.A. DeCrescente and H.A. Roth, *Proc. Conf. on Gas Turbine Materials in the Marine*, MCIC-75-27, Columbus, OH USA, (1975), pp. 115-160.

- [69] K.L. Luthra, *Met. Trans.*, 13A, Oct. (1982), pp. 1843-1852.
- [70] K.L. Luthra, *J. Electrochem Soc.*, 132(6), (1985), pp. 1293-1298.
- [71] R.L. Jones, C.E. Williams and S.R. Jones, *J. Electrochem. Soc.*, 133(1), Jan. (1986), pp 227-230.
- [72] K.L. Luthra, *Met. Trans.*, 13A, Oct. (1982), pp. 1853-1864.
- [73] R. L. Jones and C.E. Williams, *Mater. Sci. Engng.*, 87, (1987), pp. 353-360.
- [74] W.D. Niles and H.R. Sanders, *Trans. ASME*, April (1962), pp. 178-186.
- [75] R.L. Jones, R.F. Reidy, Derck Mess, *Am. Ceram. Soc.*, 76(10), Oct., (1993), pp. 2660-2662.
- [76] R.L. Jones, R.F. Reidy, Derck Mess, *Am. Ceram. Soc.*, 75(7), July(1992), pp. 1818-1821.
- [77] P.J. Hancock, H.A. Hancock, W.F. Caley and R.S. Hollingshead, *Mater. Sci. Engng.*, 120A, (1989), pp. 313-318.
- [78] T.N. Rhys-Jones, J.R. Nicholls and P. Hancock, *Corros. Sci.*, 123(2), (1983), pp. 139-149.
- [79] R.K. Sinha, *Metallic Protection*, Apr. (1982), pp. 44-48.
- [80] G.M. Clark and R. Morley, *Solid State Chem.*, 10, (1976), pp. 429-435.
- [81] M. Fichera, R. Leonard and C.A. Farina, *Electrochimica. Acta.*, 32(6), (1987).
- [82] D.N.H. Trafford and D.P. Whittle, *Corros. Sci.*, 20, (1980), pp. 499-530.
- [83] M.M. Barbooti, H. Suham, Al Madfai and Hudda J. Nassouri, *Thermochimica Acta.*, 126, (1988), pp. 43-49.
- [84] V.M. Radhakrishnan, R. Srinivasan and S. Das, *Proc. Symp. SOLSEC, IGCAR, Kalpakkam*, 22-24 Jan. (1997), p. C29.
- [85] Deepak Saxena, "Effect of Zr and Y Addition on High Temperature Sulphidation Behaviour of Fe-15Cr-4Al Alloy", Ph.D. Thesis, University of Roorkee, (1986).
- [86] R.N. Sharma, "Hot Corrosion Behaviour of Iron and Nickel base Superalloys in Salt Environments at Elevated Temperatures", Ph.D. Thesis, University of Roorkee, (1996).
- [87] J. Swaminathan and S. Raghavan, *High Temperature Mater. Processes*, 13 (4), (1994), pp. 277-297.

- [88] P.S. Sidky and M.G. Hocking, *Corros. Sci.*, 21(5), (1987), pp. 499-530.
- [89] P.Y. Hou and J. Stringer, *J. Electrochem. Soc.*, 134(7), (1981), pp. 1836-1849.
- [90] McAdam and Young, *Oxid. Met.*, 28(3/4), (1987), pp. 165-181.
- [91] J.L. Smialek and D.L. Humphrey, *Scripta Met.*, 26(1992), p. 1763.
- [92] Y. Niu, F. Gesmundo, F. Viani and W. Wu, *Oxid. Met.*, 42(3/4), (1994), pp. 265-284.
- [93] K.R. Peters, D.P. Whittle and J. Stringer, *Corros. Sci.*, 16, (1976), pp. 791-804.
- [94] Gilbert J. Santoro, *Oxid. Met.*, 13(5), (1979).
- [95] S.F.C. Stewart and S.R. Shatynski, *Oxid. Met.*, 18(3/4), (1982), pp. 163-185.
- [96] R.A. Rapp, *Corrosion, NACE*, 42(10), Oct. (1986).
- [97] K.J.L. Iyer, S.R. Iyer and V.M. Radhakrishnan, *High Temp. Technol.*, 5(3), Aug. (1987), pp. 145-150.
- [98] S.N. Tiwari, R.N. Sharma, Satya Prakash, Review on Fireside Corrosion in Boilers Proc. Conf. NML Jamshedpur, 11-12 Apr. (1995), pp. D1-D10.
- [99] F.S. Pettit and G.H. Meier, *The Met. Soc. of AIME*, Warrendale, pp. 651-687.
- [100] S.N. Tiwari, Satya Prakash, Proc. Symp. on Metals and Materials Research, IIT Madras, 4-5, July (1996), pp. 107-117.
- [101] R.A. Rapp, D.L. Douglass, F.S. Pettit and D.P. Whittle, *Mater. Sci. Engng.*, 50, (1981), pp. 1-17.
- [102] M.F. Stroosnijder and W.J. Quadackers, *High Temp. Technol.*, 4(3), Aug. (1986), pp. 141-151.
- [103] S.N. Tiwari and Satya Prakash, Proc. Conf. on Advanced Thermochemistry and Ferrous Metallurgy, BHU, Varanasi, 14-16 Oct. (1996), p. C6.
- [104] K.L. Luthra, *Met. Trans.*, 13A, Oct. (1982), pp. 1853-1864.
- [105] L. Fairman, *Corrosion Sci.*, 2,(1962), pp. 293-296.
- [106] R.C. Kerby and J.R. Wilson, *Canadian J. Chemistry*, 150, (1972), pp. 2865-2870.
- [107] S.N. Tiwari and Satya Prakash, Proc. Symp., Localised Corrosion and Environmental Cracking, IGCAR, Kalpakkam, 22-24 Jan. (1997), C-33.
- [108] R.C. Kerby and J.R. Wilson, *Trans. ASME*, Jan. (1973), pp. 36-44.

- [109] C.J. Valdes, R.B. Dooley and J.R. Wilson, *Canadian J. Chem.*, 150, (1972), pp. 2877-2881.
- [110] K. Sachs, *Metallurgia*, Apr. (1958), pp. 167-173.
- [111] S.N. Tiwari and Satya Prakash, Review on the Role of Magnesium Oxide as an Inhibitor of Hot Oil Ash Corrosion, *J. Mater. Sci. Technol*, (To be Published).
- [112] U.R. Evans, *The Corrosion and Oxidation of Metals, Scientific Principles and Practical Applications*, Edward Arnold Publishers Ltd., London, (1961).
- [113] K. Upadhy and K.N. Strafford, *Proc. Symp. on Hig Temp. Protective Coatings* Ed. S.C. Singhal. The Met. Soc. AIME, Mar. 7-8, (1983), p. 159.
- [114] H.R. Thilkan, A.K. Lahiri and T. Banerjee, *N.M.L. Tech. Journal*, May (1967), pp. 20-25.
- [115] K.J.L. Iyer, S.R. Iyer and V.M. Radhakrishnan, *Prakt. Metallography*, 24, (1987), pp. 164-174.
- [116] P. Kofstad, "High Temperature Corrosion, Elsevier Applied Science, New York (1988), Chapter 14.
- [117] P. Elliot, *Mater. Perform.*, 28, 4, (1989), pp. 57-66.
- [118] C.S. Giggins and F.S. Pettit, *Oxid. Met.*, 14, (1980), p. 363.
- [119] A.K. Mishra, *Oxid. Met.*, 25(5/6), (1986), pp. 373-396.
- [120] D.A. Pantomy and K.I. Vasu, *J. Inorg. Nucl. Chem.*, 30, (1968), pp. 423-432.
- [121] D.A. Pantomy and K.I. Vasu, *J. Inorg., Nucl. Chem.*, 30, (1968), pp. 755-779.
- [122] P. Kofstad, *Microscopy of Oxidation. (Proc. Conf.) LONDON, U.K., March (1990) p.p. 1-9*
- [123] R.B. Dooley and J.R. Wilson, *Trans. ASME*, July (1975), pp. 422-428.
- [124] R.E. Lobnig and H.J. Grabke, *Corros. Sci.*, 30, 10, (1990), pp. 1045-1071.

TABLE 4.1 : NOMINAL COMPOSITION OF THE ALLOYS USED

Alloy Nomenclature	Alloy Midhani Grade (Similar Grade)	Chemical Composition (wt %)												
		Fe	Ni	Co	Cr	Ti	Al	Mo	W	Mn	Si	Cu	Ta	C
A	Superfer 800H (Incoloy 800H)	Bal	32	-	21	0.3	0.3	-	-	1.5	1.0	-	-	0.1
B	Superni-75 (Nimonic 75)	3.0	Bal	-	19.5	0.3	-	-	-	-	-	-	-	0.1
C	Superni-600 (Inconel 600)	10.0	Bal	-	15.5	-	0.6	-	0.5	-	-	-	-	0.2
D	Superni 718 (Inconel 718)	18.5	Bal	-	19.0	0.9	0.5	3.05	-	0.18	0.13	0.15	5.13	0.04
E	Superc 605 (KC20WN/L605)	3.0	10.0	Bal	20.0	-	-	-	15.0	1.5	0.3	-	-	0.08

TABLE 4.2 : ENVIRONMENTAL CONDITIONS OF HOT CORROSION TESTS

S. No.	Condition of test	Salt mixture	Temperature (°C)	Period of test	Environments
1	Laboratory	(i) Pure Na ₂ SO ₄ (ii) Na ₂ SO ₄ -15%V ₂ O ₅ (iii) Na ₂ SO ₄ -60%V ₂ O ₅ (iv) Na ₂ SO ₄ -60%V ₂ O ₅ + MgO	700, 800, 900 700, 800, 900 700, 800, 900 900	24Cycles(1h heating, 20 min. cooling) --do-- --do-- --do--	Air Air Air Air
2	Industry	(i) Pure Na ₂ SO ₄ (ii) Na ₂ SO ₄ -15%V ₂ O ₅ (iii) Na ₂ SO ₄ -60%V ₂ O ₅	1100 1100 1100	6Cycles(24h heating, 1 h cooling) --do-- --do--	Combustion gases in boiler, wt% CO ₂ - 16.4 O ₂ - 0.2 CO - 31-59 ppm SO ₂ - 133-592 ppm NO ₂ - Nil NO - 157-396 ppm N ₂ - Balance

Table 5.1 : Weight Change (mg/cm^2) for Alloys A, B, C, D and E in Different Salts and Temperatures.

Time of Exposure (No. of Cycles)	Environment	Temp. ($^{\circ}\text{C}$)	Alloys Wt. gain (mg/cm^2)				
			A	B	C	D	E
24	Pure Na_2SO_4	700	0.29	0.15	0.21	0.22	0.24
		800	0.35	0.25	0.32	0.35	0.29
		900	0.52	0.27	0.47	0.37	0.42
24	Na_2SO_4 -15% V_2O_5	700	2.2	0.60	0.50	0.60	1.05
		800	2.75	1.20	0.65	1.40	2.20
		900	2.95	3.76	3.90	-6.80	3.15
24	Na_2SO_4 -60% V_2O_5	700	11.40	2.55	2.25	2.45	4.90
		800	11.60	5.10	2.85	6.15	8.20
		900	-23.20	6.75	11.55	12.00	35.75
6 (144 h)	Pure Na_2SO_4 + c.g.	1100	1.25	0.90	1.05	1.25	0.65
6 (144 h)	Na_2SO_4 -15% V_2O_5 + c.g.	1100	2.90	2.30	2.55	2.80	2.75
6 (144 h)	Na_2SO_4 -60% V_2O_5 + c.g.	1100	4.50	5.10	5.10	5.40	4.75
24	Na_2SO_4 -60% V_2O_5 + MgO	900	2.20	5.00	6.30	8.05	5.2

Table 5.2 : Parabolic Rate Constants ($\text{gm}^2\text{cm}^{-4}\text{sec}^{-1}$) for Alloys A, B, C, D and E in Combustion Gas at 1100°C

S. No.	Material	Temp. °C	Environment		
			Pure Na ₂ SO ₄	Na ₂ SO ₄ -15%V ₂ O ₅	Na ₂ SO ₄ -60%V ₂ O ₅
1	Alloy A (Superfer 800H)	1100	1.105 x 10 ⁻¹⁰	7.302 x 10 ⁻¹⁰	2.083 x 10 ⁻⁹
			4.972 x 10 ⁻¹¹	2.925 x 10 ⁻¹⁰	3.641 x 10 ⁻¹⁰
2	Alloy B (Superni 75)	1100	7.277 x 10 ⁻¹¹	5.252 x 10 ⁻¹⁰	1.147 x 10 ⁻⁹
			2.138 x 10 ⁻¹¹	3.505 x 10 ⁻¹⁰	5.819 x 10 ⁻¹⁰
3	Alloy C (Superni 600)	1100	8.751 x 10 ⁻¹¹	4.052 x 10 ⁻¹⁰	2.025 x 10 ⁻⁹
			5.833 x 10 ⁻¹²	7.977 x 10 ⁻¹¹	1.161 x 10 ⁻⁹
4	Alloy D (Superni 718)	1100	1.547 x 10 ⁻¹⁰	5.680 x 10 ⁻¹⁰	7.500 x 10 ⁻¹⁰
			2.416 x 10 ⁻¹¹	1.677 x 10 ⁻¹⁰	7.369 x 10 ⁻¹⁰
5	Alloy E (Superco 605)	1100	2.722 x 10 ⁻¹¹	3.976 x 10 ⁻¹⁰	1.596 x 10 ⁻⁹
			8.333 x 10 ⁻¹²	1.597 x 10 ⁻¹⁰	4.547 x 10 ⁻¹⁰

Table 5.3 : Average Scale Thickness of Alloys A, B, C, D and E After Exposure in Salt Environments at 900°C

Environment	Alloy				
	A	B	C	D	E
	Thickness (microns)				
Pure Na ₂ SO ₄	17.00	7.50	9.00	10.00	8.00
Na ₂ SO ₄ -15%V ₂ O ₅	40.30	43.30	42.50	47.00	40.00
Na ₂ SO ₄ -60%V ₂ O ₅	62.50	45.00	75.00	67.50	96.60
Na ₂ SO ₄ -60%V ₂ O ₅ + c.g.	18.00	33.00	31.60	42.00	37.00
Na ₂ SO ₄ -60%V ₂ O ₅ + MgO	33.30	43.00	62.00	62.70	55.00

TABLE 5.4 : XRD Analysis of Alloy A (Superfer 800H) after Hot Corrosion for 24 Cycles at 700, 800 and 900°C in Pure Na₂SO₄.

S.No.	'd' values			Phases Identified
	700°C	800°C	900°C	
1.	-	-	3.688	$\alpha\text{Fe}_2\text{O}_3$
2.	-	3.673	-	$\alpha\text{Fe}_2\text{O}_3$
3.	3.658	-	-	$\alpha\text{Fe}_2\text{O}_3$
4.	2.947	-	-	Ni Cr ₂ O ₄
5.	-	2.936	-	Ni Cr ₂ O ₄
6.	-	-	2.710	$\alpha\text{Fe}_2\text{O}_3$
7.	-	2.706	-	$\alpha\text{Fe}_2\text{O}_3$
8.	2.695	-	-	$\alpha\text{Fe}_2\text{O}_3$
9.	-	-	2.633	Cr ₂ O ₃ , Na ₂ SO ₄
10.	-	2.628	-	Cr ₂ O ₃ , Na ₂ SO ₄
11.	2.623	-	-	Cr ₂ O ₃ , Na ₂ SO ₄
12.	2.525	2.525	-	$\alpha\text{Fe}_2\text{O}_3$
13.	-	-	2.512	$\alpha\text{Fe}_2\text{O}_3$
14.	-	-	2.129	Cr ₂ O ₃
15.	1.835	1.835	-	(Cr,Fe) ₂ O ₃
16.	-	-	1.713	$\alpha\text{Fe}_2\text{O}_3$
17.	-	1.698	-	$\alpha\text{Fe}_2\text{O}_3$
18.	-	1.495	-	Na ₂ SO ₄
19.	1.490	-	-	Na ₂ SO ₄
20.	1.331	-	1.331	$\alpha\text{Fe}_2\text{O}_3$

TABLE 5.5 : XRD Analysis of Alloy B (Superni 75) after Hot Corrosion for 24 Cycles at 700, 800 and 900°C in Pure Na₂SO₄.

S.No.	'd' values			Phases Identified
	700°C	800°C	900°C	
1.	3.862	3.862	-	Cr ₂ O ₃
2.	3.502	3.502	-	Cr ₂ O ₃
3.	3.085	-	3.085	Cr ₂ O ₃
4.	2.946	-	2.946	Ni Cr ₂ O ₄
5.	-	2.819	-	Cr ₂ O ₃
6.	-	-	2.785	Cr ₂ O ₃
7.	-	2.505	2.505	Ni Cr ₂ O ₄
8.	-	-	2.129	Cr ₂ O ₃
9.	2.110	-	-	Cr ₂ O ₃
10.	-	-	2.087	NiO
11.	-	2.073	-	Cr ₂ O ₃
12.	2.064	-	-	NiO
13.	1.691	-	-	Ni Cr ₂ O ₄
14.	-	1.680	1.680	Ni Cr ₂ O ₄
15.	-	1.632	-	NiCr ₂ O ₄
16.	-	1.477	-	NiO, NiCr ₂ O ₄
17.	1.474	-	1.474	NiO, NiCr ₂ O ₄
18.	1.257	1.257	-	NiO, NiCr ₂ O ₄
19.	-	-	1.254	NiO, NiCr ₂ O ₄
20.	-	1.085	-	NiCr ₂ O ₄
21.	1.073	-	-	NiO, NiCr ₂ O ₄
22.	-	-	1.067	NiO, NiCr ₂ O ₄

TABLE 5.6 : XRD Analysis of Alloy C (Superni 600) after Hot Corrosion for 24 Cycles at 700, 800 and 900°C in Pure Na₂SO₄.

S.No.	'd' values			Phases Identified
	700°C	800°C	900°C	
1.	3.299	3.299	3.299	Cr ₂ O ₃
2.	2.819	2.819	-	Cr ₂ O ₃
3.	-	-	2.664	CrS, αFe ₂ O ₃
4.	2.656	2.656	-	CrS, αFe ₂ O ₃
5.	-	-	2.505	Ni Cr ₂ O ₄
6.	-	2.492	-	Ni Cr ₂ O ₄
7.	2.389	2.389	-	CrS
8.	2.106	2.106	2.106	Cr ₂ O ₃ , CrS, NiO
9.	2.064	-	-	αFe ₂ O ₃
10.	-	-	2.055	CrS
11.	-	-	1.867	CrS
12.	-	-	1.744	CrS
13.	1.473	-	1.473	Ni O
14.	-	1.343	-	CrS
15.	1.258	1.258	1.258	NiO
16.	-	1.073	-	NiCr ₂ O ₄ , αFe ₂ O ₃
17.	-	-	1.071	Ni Cr ₂ O ₄
18.	1.044	-	-	αFe ₂ O ₃

TABLE 5.7 : XRD Analysis of Alloy D (Superni 718) after Hot Corrosion for 24 Cycles at 700, 800 and 900°C in Pure Na₂SO₄.

<i>S.No.</i>	<i>'d' values</i>			<i>Phases Identified</i>
	<i>700°C</i>	<i>800°C</i>	<i>900°C</i>	
1.	3.488	3.488	-	Cr ₂ O ₃
2.	3.299	3.299	3.299	Cr ₂ O ₃
3.	3.277	-	-	TiO ₂
4.	-	3.274	3.274	TiO ₂
5.	3.171	3.171	3.171	CrS
6.	2.727	-	2.727	Cr ₂ O ₃
7.	-	2.690	2.690	αFe ₂ O ₃
8.	2.505	2.505	2.505	NiCr ₂ O ₄ , TiO ₂
9.	-	-	2.219	TiO ₂
10.	2.129	2.129	-	NiCr ₂ O ₄ , CrS, αFe ₂ O ₃
11.	-	-	2.100	NiCr ₂ O ₄ , Cr ₂ O ₃ , CrS
12.	-	-	1.839	αFe ₂ O ₃
13.	-	1.822	-	αFe ₂ O ₃
14.	-	-	1.696	αFe ₂ O ₃
15.	1.629	-	1.629	TiO ₂
16.	-	1.444	1.444	CrS
17.	1.272	-	-	NiCr ₂ O ₄
18.	1.087	-	1.087	NiCr ₂ O ₄

TABLE 5.8 : XRD Analysis of Alloy E (Superco 605) after Hot Corrosion for 24 Cycles at 700, 800 and 900°C in Pure Na₂SO₄.

S.No.	'd' values			Phases Identified
	700°C	800°C	900°C	
1.	3.862	-	3.862	Cr ₂ O ₃
2.	-	3.644	3.644	αFe ₂ O ₃
3.	3.274	3.274	3.274	Cr ₂ O ₃
4.	2.854	2.854	2.854	Co ₃ O ₄
5.	-	-	2.695	αFe ₂ O ₃
6.	-	2.672	2.672	αFe ₂ O ₃
7.	2.505	2.505	2.505	NiCr ₂ O ₄ , Co ₃ O ₄ , αFe ₂ O ₃
8.	2.284	-	2.284	WO ₃
9.	-	2.225	-	WO ₃
10.	2.101	-	2.101	Cr ₂ O ₃ , NiCr ₂ O ₄ , WO
11.	-	2.087	-	WO ₃ , αFe ₂ O ₃ , Cr ₂ O ₃
12.	-	-	1.680	αFe ₂ O ₃
13.	1.679	-	-	αFe ₂ O ₃
14.	1.478	1.478	-	NiCr ₂ O ₄ , Co ₃ O ₄
15.	-	-	1.444	NiCr ₂ O ₄ , Co ₃ O ₄
16.	1.226	1.226	-	NiCr ₂ O ₄
17.	1.114	-	-	WO ₃ , NiCr ₂ O ₄
18.	-	1.087	1.087	NiCr ₂ O ₄ , WO ₃

TABLE 5.9 : XRD Analysis of Alloy A (Superfer 800H) after Hot Corrosion for 24 Cycles at 700, 800 and 900°C in Na₂SO₄-15%V₂O₅.

S.No.	'd' values			Phases Identified
	700°C	800°C	900°C	
1.	4.0710	-	-	Cr ₂ O ₃
2.	3.6584	-	3.6584	αFe ₂ O ₃
3.	-	3.5024	3.5024	Cr ₂ O ₃
4.	3.2864	-	-	Cr ₂ O ₃
5.	-	3.2052	-	Cr ₂ O ₃
6.	-	3.0962	3.0962	Cr ₂ O ₃
7.	-	-	2.8279	Cr ₂ O ₃
8.	2.6873	2.6873	2.6873	αFe ₂ O
9.	2.5052	2.5052	2.5052	FeV ₂ O ₄ , αFe ₂ O ₃ , Ni Cr ₂ O ₄
10.	2.1292	-	-	Cr ₂ O ₃ , αFe ₂ O ₃ , FeV ₂ O ₄
11.	-	2.0916	2.0916	αFe ₂ O ₃ , Cr ₂ O ₃
12.	1.7137	-	-	αFe ₂ O ₃ , (Cr,Fe) ₂ O ₃ , Ni Cr ₂ O ₄
13.	-	1.6845	1.6845	FeV ₂ O ₄ , αFe ₂ O ₃
14.	1.6189	1.6189	1.6189	FeV ₂ O ₄ , NiCr ₂ O ₄
15.	1.4778	1.4778	1.4778	FeV ₂ O ₄ , NiCr ₂ O ₄
16.	-	1.3037	-	NiCr ₂ O ₄
17.	1.2691	-	1.2691	αFe ₂ O ₃ , (Cr,Fe) ₂ O ₃ , Ni Cr ₂ O ₄

TABLE 5.10 : XRD Analysis of Alloy B (Superni 75) after Hot Corrosion for 24 Cycles at 700, 800 and 900°C in Na₂SO₄-15%V₂O₅.

<i>S.No.</i>	<i>'d' values</i>			<i>Phases Identified</i>
	<i>700°C</i>	<i>800°C</i>	<i>900°C</i>	
1.	3.4490	-	-	Cr ₂ O ₃
2.	-	2.9752	2.9752	Cr ₂ O ₃
3.	2.8279	2.8279	-	Cr ₂ O ₃
4.	2.5257	2.5257	2.5257	Ni Cr ₂ O ₄
5.	2.4203	2.4203	2.4203	NiO
6.	2.0963	2.0963	2.0963	Cr ₂ O ₃ , NiO
7.	1.6902	-	-	Ni Cr ₂ O ₄
8.	-	1.6137	1.6137	Ni Cr ₂ O ₄
9.	1.4800	1.4800	1.4800	NiO, Ni Cr ₂ O ₄
10.	-	-	1.2619	NiO, Ni Cr ₂ O ₄
11.	1.2577	1.2577	-	NiO, Ni Cr ₂ O ₄
12.	-	1.0686	-	NiO, Ni Cr ₂ O ₄
13.	1.0461	-	1.0461	NiO, Ni Cr ₂ O ₄

TABLE 5.11 : XRD Analysis of Alloy C (Superni 600) after Hot Corrosion for 24 Cycles at 700, 800 and 900°C in Na₂SO₄-15%V₂O₅.

S.No.	'd' values			Phases Identified
	700°C	800°C	900°C	
1.	2.9460	2.9460	2.9460	NiCr ₂ O ₄ , FeV ₂ O ₄ , Ni(VO ₃) ₂
2.	2.6790	2.6790	-	(Cr,Fe) ₂ O ₃
3.	2.5050	2.5050	2.5050	NiCr ₂ O ₄ , FeV ₂ O ₄ , Ni(VO ₃) ₂
4.	-	-	2.4140	NiO, Ni(VO ₃) ₂
5.	2.1808	2.1808	-	(Cr,Fe) ₂ O ₃
6.	2.0870	2.0870	2.0870	NiO, FeV ₂ O ₄ , Ni(VO ₃) ₂
7.	1.6980	1.6980	1.6980	FeV ₂ O ₄ , (Cr,Fe) ₂ O ₃ , NiCr ₂ O ₄
8.	1.6000	1.6000	1.6000	FeV ₂ O ₄ , NiCr ₂ O ₄
9.	1.4950	-	-	NiO, FeV ₂ O ₄ , NiCr ₂ O ₄
10.	-	1.4730	1.4730	NiO, (Cr,Fe) ₂ O ₃ , NiCr ₂ O ₄
11.	1.2670	-	1.2670	NiO, FeV ₂ O ₄ , NiCr ₂ O ₄
12.	-	1.2600	-	NiO, FeV ₂ O ₄ , (Cr,Fe) ₂ O ₃
13.	-	-	1.2060	(Cr,Fe) ₂ O ₃ , NiO, NiCr ₂ O ₄
14.	1.0830	1.0830	1.0830	NiCr ₂ O ₄ , NiO

TABLE 5.12 : XRD Analysis of Alloy D (Superni 718) after Hot Corrosion for 24 Cycles at 700, 800 and 900°C in Na₂SO₄-15%V₂O₅.

S.No.	'd' values			Phases Identified
	700°C	800°C	900°C	
1.	3.322	-	-	Ni(VO ₃) ₂
2.	2.975	2.975	2.975	NiCr ₂ O ₄ , Fe ₃ O ₄
3.	2.836	-	-	Al ₂ O ₃ , TiO ₂ , Ni(VO ₃) ₂
4.	2.532	2.532	2.532	TiO ₂ , Fe ₃ O ₄ , NiCr ₂ O ₄
5.	2.426	-	2.426	Al ₂ O ₃ , Fe ₃ O ₄
6.	-	2.193	-	TiO ₂
7.	2.100	2.100	2.100	Fe ₃ O ₄ , NiO, Cr ₂ O ₃
8.	1.828	1.828	-	Al ₂ O ₃
9.	-	1.684	-	TiO ₂
10.	1.608	-	1.608	TiO ₂ , Fe ₃ O ₄ , NiCr ₂ O ₄
11.	-	1.600	-	TiO ₂ , NiCr ₂ O ₄
12.	-	-	1.477	Fe ₃ O ₄ , NiCr ₂ O ₄
13.	1.473	1.473	-	Fe ₃ O ₄ , Ni(VO ₃) ₂
14.	-	1.444	-	Al ₂ O ₃
15.	1.270	-	1.270	Fe ₃ O ₄ , Ni Cr ₂ O ₄
16.	-	1.261	-	Fe ₃ O ₄ , Ni Cr ₂ O ₄
17.	-	1.183	-	Al ₂ O ₃ , Ni Cr ₂ O ₄
18.	-	-	1.081	Al ₂ O ₃ , Fe ₃ O ₄ , Ni Cr ₂ O ₄

TABLE 5.13 : XRD Analysis of Alloy E (Superco 605) after Hot Corrosion for 24 Cycles at 700, 800 and 900°C in Na₂SO₄-15%V₂O₅.

<i>S.No.</i>	<i>'d' values</i>			<i>Phases Identified</i>
	<i>700°C</i>	<i>800°C</i>	<i>900°C</i>	
1.	3.0753	3.0753	-	Cr ₂ O ₃
2.	-	-	2.9558	FeWO ₄
3.	2.9180	2.9180	2.9180	FeWO ₄
4.	-	-	2.5257	Ni Cr ₂ O ₄
5.	2.4394	2.4394	2.4394	NiO, FeWO ₄ , CoO
6.	-	2.1150	2.1150	CoO, Cr ₂ O ₃ , FeWO ₄
7.	2.0825	-	-	NiO, Cr ₂ O ₃ , FeWO ₄
8.	2.0644	-	2.0644	NiO, FeWO ₄
9.	-	2.0335	-	CoO
10.	1.5661	1.5661	-	CoO
11.	-	1.4950	1.4950	NiO, CoO, FeWO ₄
12.	1.4715	-	-	FeWO ₄ , NiO
13.	-	1.2765	1.2765	Ni Cr ₂ O ₄
14.	1.2619	-	1.2619	CoO, NiO, FeWO ₄
15.	-	-	1.2222	CoO, FeWO ₄
16.	1.1386	-	-	CoO, FeWO ₄

TABLE 5.14 : XRD Analysis of Alloy A (Superfer 800H) after Hot Corrosion for 24 Cycles at 700, 800 and 900°C in Na₂SO₄-60%V₂O₅.

S.No.	'd' values			Phases Identified
	700°C	800°C	900°C	
1.	-	-	3.6883	α Fe ₂ O ₃ , (Cr,Fe) ₂ O ₃
2.	2.9462	2.9462	2.9462	FeV ₂ O ₄
3.	2.6952	2.6952	2.6952	Cr ₂ O ₃ , α Fe ₂ O ₃
4.	2.5120	2.5120	2.5120	FeV ₂ O ₄ , α Fe ₂ O ₃ , (Cr,Fe) ₂ O ₃
5.	2.4078	2.4078	2.4078	NiO
6.	2.0825	2.0825	2.0825	FeV ₂ O ₄ , NiO, α Fe ₂ O ₃ , (Cr,Fe) ₂ O ₃
7.	1.8357	1.8357	-	α Fe ₂ O ₃
8.	1.6989	1.6989	1.6989	FeV ₂ O ₄ , α Fe ₂ O ₃
9.	1.6902	-	-	FeV ₂ O ₄
10.	1.6034	1.6034	1.6034	FeV ₂ O ₄ , (Cr,Fe) ₂ O ₃
11.	1.4736	1.4736	1.4736	NiO, FeV ₂ O ₄ , (Cr,Fe) ₂ O ₃
12.	-	1.2824	-	FeV ₂ O ₄ , NiO
13.	1.2706	1.2706	1.2706	(Cr,Fe) ₂ O ₃ , NiO, FeV ₂ O ₄
14.	-	-	1.1114	α Fe ₂ O ₃
15.	-	1.1015	-	α Fe ₂ O ₃
16.	1.0851	-	1.0851	α Fe ₂ O ₃
17.	-	-	1.0418	α Fe ₂ O ₃

TABLE 5.15 : XRD Analysis of Alloy B (Superni 75) after Hot Corrosion for 24 Cycles at 700, 800 and 900°C in Na₂SO₄-60%V₂O₅.

S.No.	'd' values			Phases Identified
	700°C	800°C	900°C	
1.	-	-	4.1281	Cr ₂ O ₃
2.	3.6733	-	3.6733	(Cr, Fe) ₂ O ₃
3.	3.5297	-	-	Ni(VO ₃) ₂
4.	3.2864	3.2864	3.2864	Ni(VO ₃) ₂ , Cr ₂ O ₃
5.	2.9558	-	2.9558	Ni(VO ₃) ₂ , NiCr ₂ O ₄
6.	2.8020	2.8020	2.8020	Ni(VO ₃) ₂
7.	2.5188	2.5188	2.5188	Ni(VO ₃) ₂ , NiCr ₂ O ₄
8.	-	2.4203	2.4203	NiO, Ni(VO ₃) ₂
9.	-	2.0918	2.0918	NiO, Cr ₂ O ₃
10.	2.0644	2.0644	2.0644	Ni(VO ₃) ₂ , (Cr,Fe) ₂ O ₃ , NiO
11.	1.8084	-	1.8084	(Cr, Fe) ₂ O ₃
12.	1.6931	-	-	NiCr ₂ O ₄ , Ni(VO ₃) ₂
13.	1.6008	-	1.6008	Ni Cr ₂ O ₄ , (Cr, Fe) ₂ O ₃
14.	1.4778	1.4778	1.4778	NiO, (Cr, Fe) ₂ O ₃ , NiCr ₂ O ₄
15.	1.3179	-	-	NiCr ₂ O ₄
16.	1.2591	1.2591	1.2591	NiO, NiCr ₂ O ₄
17.	-	1.2041	-	NiO, (Cr, Fe) ₂ O ₃
18.	1.2029	-	1.2029	Ni Cr ₂ O ₄ , (Cr, Fe) ₂ O ₃

TABLE 5.16 : XRD Analysis of Alloy C (Superni 718) after Hot Corrosion for 24 Cycles at 700, 800 and 900°C in Na₂SO₄-60%V₂O₅.

S.No.	'd' values			Phases Identified
	700°C	800°C	900°C	
1.	3.3470	3.3470	-	Ni(VO ₃) ₂
2.	-	-	3.1717	FeV ₂ O ₄
3.	2.9750	2.9750	-	FeV ₂ O ₄ , Ni(VO ₃) ₂
4.	-	2.8810	-	Ni(VO ₃) ₂
5.	2.5180	2.5180	-	FeV ₂ O ₄ , NiCr ₂ O ₄ , Ni(VO ₃) ₂
6.	-	-	2.4394	NiO, FeV ₂ O ₄ , NiCr ₂ O ₄ , Ni(VO ₃) ₂
7.	2.4200	2.4200	-	Ni(VO ₃) ₂ , NiO, FeV ₂ O ₄ , NiCr ₂ O ₄
8.	-	-	2.1340	NiCr ₂ O ₄ , FeV ₂ O ₄ , Ni(VO ₃) ₂
9.	2.0910	2.0910	-	NiO, NiCr ₂ O ₄ , FeV ₂ O ₄
10.	-	2.0590	-	NiCr ₂ O ₄ , Ni(VO ₃) ₂
11.	-	-	2.0125	NiCr ₂ O ₄
12.	1.7250	1.7250	-	Ni(VO ₃) ₂
13.	1.6960	-	-	FeV ₂ O ₄ , NiCr ₂ O ₄
14.	1.6030	1.6030	-	NiCr ₂ O ₄ , FeV ₂ O ₄
15.	-	-	1.5541	NiCr ₂ O ₄ , FeV ₂ O ₄
16.	1.4710	1.4710	-	NiCr ₂ O ₄ , FeV ₂ O ₄
17.	-	1.4490	1.4490	NiO, FeV ₂ O ₄
18.	1.2563	1.2563	1.2563	FeV ₂ O ₄
19.	-	-	1.1904	NiO
20.	1.0810	1.0810	-	NiO, NiCr ₂ O ₄
21.	-	-	1.0668	NiO

TABLE 5.17 : XRD Analysis of Alloy D (Superni 600) after Hot Corrosion for 24 Cycles at 700, 800 and 900°C in Na₂SO₄-60%V₂O₅.

S.No.	'd' values			Phases Identified
	700°C	800°C	900°C	
1.	-	-	4.0536	Cr ₂ O ₃
2.	-	3.8130	-	Cr ₂ O ₃
3.	3.6580	3.6580	-	(Cr, Fe) ₂ O ₃
4.	3.5290	3.5290	-	NaVO ₃
5.	-	3.2860	-	Cr ₂ O ₃ , NaVO ₃ , Ni(VO ₃) ₂
6.	3.1940	-	3.1940	NaVO ₃ , FeV ₂ O ₄
7.	2.9650	2.9650	-	Ni Cr ₂ O ₄ , FeV ₂ O ₄ , Ni(VO ₃) ₂
8.	2.5180	2.5180	-	NaVO ₃ , Ni Cr ₂ O ₄ , Ni(VO ₃) ₂ , FeV ₂ O ₄
9.	-	2.4145	2.4145	NiO, FeV ₂ O ₄
10.	-	-	2.1292	Cr ₂ O ₃ , NiO
11.	-	2.0960	-	Cr ₂ O ₃ , Ni Cr ₂ O ₄
12.	2.0590	2.0590	-	NiO, FeV ₂ O ₄ , Ni Cr ₂ O ₄
13.	-	-	1.5059	NiO
14.	1.4530	1.4530	1.4530	FeV ₂ O ₄ , Ni Cr ₂ O ₄
15.	1.2720	-	1.2720	Ni Cr ₂ O ₄ , FeV ₂ O ₄
16.	1.2520	1.2520	1.2520	NiO, NiCr ₂ O ₄
17.	-	-	1.2004	NiO, (Cr, Fe) ₂ O ₃
18.	1.0720	1.0720	1.0720	NiO, NiCr ₂ O ₄

TABLE 5.18 : XRD Analysis of Alloy E (Supercor 605) after Hot Corrosion for 24 Cycles at 700, 800 and 900°C in Na₂SO₄-60%V₂O₅.

S.No.	'd' values			Phases Identified
	700°C	800°C	900°C	
1.	4.0905	-	4.0905	Cr ₂ O ₃
2.	-	-	3.4490	Cr ₂ O ₃
3.	3.2746	3.2746	3.2746	Cr ₂ O ₃
4.	3.0547	3.0547	3.0547	WO ₃ , Co ₃ V ₂ O ₈
5.	-	2.7112	2.7112	WO ₃ , Co ₂ O ₃
6.	2.5395	2.5395	-	Co ₃ V ₂ O ₈ , NiCr ₂ O ₄
7.	2.4917	2.4917	2.4917	WO ₃ , (Cr,Fe) ₂ O ₃ , NiCr ₂ O ₄
8.	-	-	2.3472	CoV ₃ , Co ₂ O ₃
9.	-	-	2.1486	WO ₃ , (Cr,Fe) ₂ O ₃
10.	-	-	2.1340	Cr ₂ O ₃
11.	-	2.1103	-	Cr ₂ O ₃ , CoV ₃
12.	2.0825	2.0825	2.0825	WO ₃ , CoV ₃ , Co ₃ V ₂ O ₈
13.	-	-	1.9080	CoV ₃
14.	-	-	1.8288	(Cr,Fe) ₂ O ₃
15.	1.8084	-	1.8084	Co ₂ O ₃
16.	1.5517	-	1.5517	WO ₃ , Co ₂ O ₃ , NiCr ₂ O ₄
17.	1.3914	1.3914	1.3914	Co ₂ O ₃ , Co ₃ V ₂ O ₈
18.	1.2765	1.2765	1.2765	CoV ₃ , Co ₃ V ₂ O ₈

TABLE 5.19 : XRD Analysis of Alloy A (Superfer 800H) after Hot Corrosion for 24 Cycles in Industrial Atmosphere at 1100°C with Different Salt Coatings.

S.No.	'd' values			Phase Identified
	Na ₂ SO ₄	Na ₂ SO ₄ -15% V ₂ O ₅	Na ₂ SO ₄ -60% V ₂ O ₅	
1.	-	4.0900	-	Cr ₂ O ₃
2.	4.0720	-	-	Cr ₂ O ₃
3.	-	-	4.0536	Cr ₂ O ₃
4.	-	-	3.6880	αFe ₂ O ₃
5.	-	3.6730	-	αFe ₂ O ₃
6.	-	2.9650	-	FeV ₂ O ₄ , Cr ₂ O ₃
7.	-	-	2.7270	Cr ₂ O ₃ , Al ₂ O ₃ , αFe ₂ O ₃
8.	2.6950	2.6950	-	αFe ₂ O ₃
9.	-	-	2.5390	TiO ₂ , αFe ₂ O ₃ , Cr ₂ O ₃
10.	2.5180	2.5180	-	TiO ₂ , FeV ₂ O ₄ , αFe ₂ O ₃ , Cr ₂ O ₃
11.	-	2.2140	-	Al ₂ O ₃ , αFe ₂ O ₃
12.	2.1830	-	-	TiO ₂ ,
13.	-	-	2.0820	αFe ₂ O ₃ , Cr ₂ O ₃ , Ni Cr ₂ O ₄
14.	2.0730	2.0730	-	NiO, αFe ₂ O ₃ , Cr ₂ O ₃
15.	-	-	1.8530	NiCr ₂ O ₄ , αFe ₂ O ₃ ,
16.	-	-	1.7010	NiCr ₂ O ₄ , αFe ₂ O ₃ ,
17.	1.6960	1.6960	-	FeV ₂ O ₄ , TiO ₂ , Cr ₂ O ₃
18.	-	-	1.6870	TiO ₂ , αFe ₂ O ₃
19.	-	-	1.4950	NiCr ₂ O ₄
20.	1.4880	-	-	Al ₂ O ₃ , Cr ₂ O ₃ , NiO
21.	-	1.4860	-	FeV ₂ O ₄ , Ni O, Al ₂ O ₃
22.	1.4370	-	-	Al ₂ O ₃
23.	-	-	1.3690	TiO ₂ , Al ₂ O ₃
24.	1.2700	-	1.2730	Ni Cr ₂ O ₄ ,
25.	1.0740	1.0720	1.0750	Ni Cr ₂ O ₄ , αFe ₂ O ₃ ,

TABLE 5.20 : XRD Analysis of Alloy B (Superni 75) after Hot Corrosion for 24 Cycles at 1100°C in Industrial Atmosphere with Different Salt Coatings.

S.No.	'd' values			Phase Identified
	Na_2SO_4	$Na_2SO_4-15\% V_2O_5$	$Na_2SO_4-60\% V_2O_5$	
1.	4.0536	4.0536	4.0536	Cr_2O_3
2.	-	-	3.7030	αFe_2O_3
3.	-	-	2.7190	$Cr_2O_3, \alpha Fe_2O_3$
4.	2.5250	-	2.5180	$NiCr_2O_4, \alpha Fe_2O_3, FeV_2O_4$
5.	-	2.2190	-	TiO_2
6.	-	-	2.0770	$Cr_2O_3, FeV_2O_4, NiCr_2O_4$
7.	2.0550	-	-	NiO
8.	-	2.0510	-	$FeV_2O_4, NiCr_2O_4$
9.	-	-	1.8390	$\alpha Fe_2O_3,$
10.	-	1.7010	-	Cr_2O_3, FeV_2O_4, TiO_2
11.	1.6960	-	-	TiO_2, Cr_2O_3
12.	-	-	1.6930	$FeV_2O_4, \alpha Fe_2O_3$
13.	-	1.6080	-	Cr_2O_3, TiO_2, FeV_2O_4
14.	1.6030	-	-	$Cr_2O_3, TiO_2,$
15.	-	-	1.6000	$NiCr_2O_4, FeV_2O_4$
16.	-	1.4840	-	$NiO, NiCr_2O_4$
17.	-	1.4530	1.4530	FeV_2O_4
18.	1.3470	-	-	TiO_2
19.	-	-	1.2630	$NiCr_2O_4, FeV_2O_4$
20.	1.2560	-	-	NiO, Cr_2O_3
21.	-	1.2500	-	NiO, Cr_2O_3, FeV_2O_4
22.	1.0690	1.0700	-	NiO, Cr_2O_3

TABLE 5.21 : XRD Analysis of Alloy C (Superni 600) after Hot Corrosion for 24 Cycles in Industrial Atmosphere at 1100°C with Different Salt Coatings.

S.No.	'd' values			Phase Identified
	Na ₂ SO ₄	Na ₂ SO ₄ -15% V ₂ O ₅	Na ₂ SO ₄ -60% V ₂ O ₅	
1.	4.072	-	4.090	Cr ₂ O ₃
2.	3.703	3.703	-	αFe ₂ O ₃
3.	-	-	3.359	NiO
4.	3.205	-	-	CrS
5.	-	2.936	-	FeV ₂ O ₄
6.	2.703	2.703	2.703	Cr ₂ O ₃ , αFe ₂ O ₃
7.	2.525	-	2.518	αFe ₂ O ₃ , Cr ₂ O ₃
8.	-	2.525	-	αFe ₂ O ₃ , Cr ₂ O ₃ , Ni(VO ₃) ₂ , FeV ₂ O ₄
9.	2.064	-	-	CrS, NiO
10.	-	-	2.059	Cr ₂ O ₃ , NiO
11.	-	2.059	-	Cr ₂ O ₃ , NiO, Ni(VO ₃) ₂ , FeV ₂ O ₄
12.	1.846	-	1.821	αFe ₂ O ₃
13.	-	1.698	-	αFe ₂ O ₃ , Ni(VO ₃) ₂
14.	-	-	1.681	αFe ₂ O ₃
15.	-	1.490	-	αFe ₂ O ₃ , Cr ₂ O ₃
16.	1.490	-	-	αFe ₂ O ₃ , Cr ₂ O ₃ , CrS, NiO
17.	-	-	1.473	NiO
18.	-	1.457	-	αFe ₂ O ₃ , NiO, FeV ₂ O ₄
19.	1.311	-	-	αFe ₂ O ₃ , CrS
20.	1.264	1.261	1.261	NiO, αFe ₂ O ₃ , Cr ₂ O ₃
21.	-	1.074	-	Cr ₂ O ₃
22.	-	-	1.074	αFe ₂ O ₃ , NiO

TABLE 5.22 : XRD Analysis of Alloy D (Superni 718) after Hot Corrosion for 24 Cycles in Industrial Atmosphere at 1100°C with Different Salt Coatings.

S.No.	'd' values			Phase Identified
	Na_2SO_4	$Na_2SO_4-15\% V_2O_5$	$Na_2SO_4-60\% V_2O_5$	
1.	-	-	4.0536	Cr_2O_3
2.	3.6430	3.7030	-	αFe_2O_3
3.	2.6950	2.7030	2.7030	αFe_2O_3
4.	-	2.5250	-	$TiO_2, Cr_2O_3, Ni(VO_3)_2$
5.	2.4910	-	2.4910	$\alpha Fe_2O_3, TiO_2$
6.	2.2030	2.2090	-	TiO_2, NiO
7.	-	2.0820	-	$Al_2O_3, Ni(VO_3)_2$
8.	2.0770	-	-	Cr_2O_3, CrS, NiO
9.	-	-	2.0730	Cr_2O_3, NiO
10.	-	1.8420	-	$Ni(VO_3)_2$
11.	1.7440	-	-	CrS
12.	1.6930	1.6960	1.6930	$\alpha Fe_2O_3, TiO_2, Cr_2O_3$
13.	1.5900	-	-	αFe_2O_3
14.	-	1.4860	-	Al_2O_3, Cr_2O_3, NiO
15.	1.4860	-	-	$\alpha Fe_2O_3, NiO, Cr_2O_3$
16.	1.2700	1.2700	1.2700	NiO
17.	-	1.1910	1.2220	NiO, αFe_2O_3
18.	-	1.0850	-	Al_2O_3, Cr_2O_3
19.	-	-	1.0390	NiO

TABLE 5.23 : XRD Analysis of Alloy E (Superco 605) after Hot Corrosion for 24 Cycles in Industrial Atmosphere at 1100°C with Different Salt Coatings.

S.No.	'd' values			Phase Identified
	Na ₂ SO ₄	Na ₂ SO ₄ -15% V ₂ O ₅	Na ₂ SO ₄ -60% V ₂ O ₅	
1.	4.0900	4.0536	4.0536	Cr ₂ O ₃
2.	3.6880	3.6880	3.6730	αFe ₂ O ₃
3.	-	-	3.3720	Co ₃ V ₂ O ₈
4.	-	-	2.9650	Cr ₂ O ₃ , Co ₃ V ₂ O ₈
5.	-	-	2.7110	Cr ₂ O ₃ , αFe ₂ O ₃ , Co ₃ V ₂ O ₈
6.	2.7030	2.6950	-	Cr ₂ O ₃ , αFe ₂ O ₃
7.	-	-	2.5250	Cr ₂ O ₃ , Ni Cr ₂ O ₄ , Co ₃ V ₂ O ₈
8.	-	2.5180	-	CoO, Cr ₂ O ₃ , Co ₃ V ₂ O ₈
9.	2.5180	-	-	Cr ₂ O ₃ , αFe ₂ O ₃
10.	-	-	2.1340	CoO, Cr ₂ O ₃
11.	2.0680	-	-	WO ₃ , αFe ₂ O ₃
12.	-	2.0640	-	CoO, Co ₃ V ₂ O ₈ , FeWO ₄ , NiO
13.	-	1.6960	-	Cr ₂ O ₃ , Co ₃ V ₂ O ₈
14.	1.6930	-	-	αFe ₂ O ₃
15.	-	-	1.5010	CoO, Co ₃ V ₂ O ₈
16.	-	1.4860	-	FeWO ₄ , Co ₃ V ₂ O ₈ , NiO, Cr ₂ O ₃
17.	1.4860	-	-	Cr ₂ O ₃
18.	-	-	1.4570	CoO, Ni Cr ₂ O ₄ , αFe ₂ O ₃
19.	-	1.4530	-	Co ₃ V ₂ O ₈
20.	1.4530	-	-	Co ₃ O ₄
21.	1.2630	-	-	Cr ₂ O ₃
22.	-	1.2570	-	FeWO ₄ , CoO, NiO
23.	-	1.0770	-	NiO, Cr ₂ O ₃
24.	1.0770	-	-	WO ₃ , Co ₃ O ₄ , αFe ₂ O ₃ , Cr ₂ O ₃

TABLE 5.24 : XRD Analysis of Alloy A (Superfer 800H) after Hot Corrosion for 24 Cycles at 700, 800 and 900°C in Na₂SO₄-60%V₂O₅+MgO.

S.No.	'd' values	Phases Identified
1.	3.6733	α Fe ₂ O ₃
2.	2.8106	Cr ₂ O ₃
3.	2.6952	α Fe ₂ O ₃ , FeS
4.	2.5326	FeV ₂ O ₄ , Cr ₂ O ₃ , Ni Cr ₂ O ₄ , FeS
5.	2.1103	Cr ₂ O ₃
6.	2.0916	FeS, Mg ₃ V ₂ O ₈ , FeV ₂ O ₄
7.	1.7256	Cr ₂ O ₃ , FeS
8.	1.7168	Ni Cr ₂ O ₄ , FeV ₂ O ₄ , Cr ₂ O ₃
9.	1.6137	Ni Cr ₂ O ₄
10.	1.4907	Mg ₃ V ₂ O ₈ , FeS
11.	1.4800	Cr ₂ O ₃ , Ni Cr ₂ O ₄
12.	1.2706	Mg ₃ V ₂ O ₈ , FeV ₂ O ₄ , Ni Cr ₂ O ₄
13.	1.0823	Mg ₃ V ₂ O ₈

TABLE 5.25 : XRD Analysis of Alloy B (Superni 75) after Hot Corrosion for 24 Cycles at 700, 800 and 900°C in Na₂SO₄-60%V₂O₅+MgO.

S.No.	'd' values	Phases Identified
1.	3.3845	Ni(VO ₃) ₂
2.	3.2984	Ni(VO ₃) ₂
3.	2.9653	Cr ₂ O ₃ , Ni(VO ₃) ₂
4.	2.5257	Cr ₂ O ₃ , Ni(VO ₃) ₂
5.	2.4266	NiO, Ni(VO ₃) ₂
6.	2.0963	Cr ₂ O ₃ , NiO, Mg ₃ V ₂ O ₈
7.	1.6085	Cr ₂ O ₃
8.	1.4821	NiO, Cr ₂ O ₃ , Mg ₃ V ₂ O ₈
9.	1.2634	NiO, Cr ₂ O ₃ , Mg ₃ V ₂ O ₈
10.	1.2105	Mg ₃ V ₂ O ₈
11.	1.0477	Mg ₃ V ₂ O ₈

TABLE 5.26 : XRD Analysis of Alloy C (Superni 600) after Hot Corrosion for 24 Cycles at 700, 800 and 900°C in Na₂SO₄-60%V₂O₅+MgO.

S.No.	'd' values	Phases Identified
1.	2.955	Cr ₂ O ₃ , FeV ₂ O ₄ , Ni(VO ₃) ₂
2.	2.512	Ni Cr ₂ O ₄ , FeV ₂ O ₄ , Ni(VO ₃) ₂
3.	2.420	NiO, Mg ₃ V ₂ O ₈
4.	2.091	Ni(VO ₃) ₂ , Mg ₃ V ₂ O ₈ , Cr ₂ O ₃
5.	1.707	Cr ₂ O ₃ , FeV ₂ O ₄
6.	1.605	Ni Cr ₂ O ₄ , FeV ₂ O ₄
7.	1.480	Mg ₃ V ₂ O ₈ , NiO, FeV ₂ O ₄
8.	1.261	NiO, FeV ₂ O ₄
9.	1.086	Ni Cr ₂ O ₄
10.	1.069	NiO, Mg ₃ V ₂ O ₈

TABLE 5.27 : XRD Analysis of Alloy D (Superni 718) after Hot Corrosion for 24 Cycles at 700, 800 and 900°C in Na₂SO₄-60%V₂O₅+MgO.

<i>S.No.</i>	<i>'d' values</i>	<i>Phases Identified</i>
1.	3.6596	α Fe ₂ O ₃
2.	2.9558	Cr ₂ O ₃ , Ni(VO ₃) ₂
3.	2.5188	α Fe ₂ O ₃ , Ni(VO ₃) ₂ , Ni Cr ₂ O ₄
4.	2.4203	NiO, Mg ₃ V ₂ O ₈ , Ni(VO ₃) ₂
5.	2.0870	Cr ₂ O ₃ , NiO, Mg ₃ V ₂ O ₈
6.	1.7077	Cr ₂ O ₃ , α Fe ₂ O ₃
7.	1.6085	Cr ₂ O ₃ , NiO
8.	1.4821	α Fe ₂ O ₃ , NiO, Cr ₂ O ₃ , Mg ₃ V ₂ O ₈
9.	1.4449	α Fe ₂ O ₃
10.	1.2630	Cr ₂ O ₃ , NiO
11.	1.2090	NiO, Mg ₃ V ₂ O ₈
12.	1.0470	NiO, Mg ₃ V ₂ O ₈

TABLE 5.28 : XRD Analysis of Alloy E (Supercor 605) after Hot Corrosion for 24 Cycles at 700, 800 and 900°C in Na₂SO₄-60%V₂O₅+MgO.

<i>S.No.</i>	<i>'d' values</i>	<i>Phases Identified</i>
1.	2.4653	Cr ₂ O ₃ , CoO, FeV ₂ O ₄ , Ni Cr ₂ O ₄
2.	2.1340	WO ₃ , CoO, Cr ₂ O ₃ , Co ₃ V ₂ O ₈
3.	1.5126	WO ₃ , CoO, Ni Cr ₂ O ₄ , Co ₃ V ₂ O ₈
4.	1.2854	CoO, Cr ₂ O ₃ , Co ₃ V ₂ O ₈
5.	1.2824	Co ₃ V ₂ O ₈ , Ni Cr ₂ O ₄
6.	1.2301	FeV ₂ O ₄ , Ni Cr ₂ O ₄ , Co ₃ V ₂ O ₈

Table 5.29 : EDAX Analysis of Alloy A (Superfer 800H) After Cyclic Hot Corrosion Under Different Salts and Temperatures.

Analysis Area	Environment	No. of Cycles	Temp °C	Element wt. %													
				Fe	Ni	Cr	Co	Na	V	S	Ti	Al	Si	Mn	Mg		
1	Pure Na ₂ SO ₄	24	900	7.58	2.42	82.38	-	2.56	2.62	2.44	-	-	-	-	-	-	-
2		24	900	6.02	2.08	65.23	-	2.25	2.01	7.33	15.08	-	-	-	-	-	-
3	Na ₂ SO ₄ -15%V ₂ O ₅	24	900	18.04	1.80	67.01	-	3.09	4.49	4.12	3.09	1.28	1.54	-	-	-	-
4		24	900	8.98	1.68	80.89	-	4.49	2.27	1.12	1.68	1.12	-	-	-	-	-
5	Na ₂ SO ₄ -60%V ₂ O ₅	24	900	46.17	20.81	26.01	-	2.27	2.05	-	-	2.27	2.43	-	-	-	-
6		24	900	48.04	19.50	30.39	-	-	-	-	-	-	-	-	-	-	-
7	Na ₂ SO ₄ -60%V ₂ O ₅	6	1100	5.75	21.49	55.73	-	4.00	-	-	4.86	2.80	3.62	5.75	-	-	-
8		6	1100	11.58	22.46	38.34	-	-	-	-	9.79	3.57	1.51	8.75	-	-	-
9	Na ₂ SO ₄ -60%V ₂ O ₅ + MgO	24	900	-	4.69	10.43	-	43.13	-	-	-	-	-	17.35	24.34	-	-
10		24	900	16.40	5.41	41.88	-	11.86	-	13.26	2.79	-	-	6.98	2.79	-	-
11		24	900	16.69	1.33	41.06	-	9.01	-	13.85	3.00	-	-	8.68	6.34	-	-
12		24	900	15.43	1.66	44.17	-	20.72	-	4.84	3.47	-	-	9.68	-	-	-

Table 5.30 : EDAX Analysis of Alloy B (Superni 75) After Cyclic Hot Corrosion Under Different Salts and Temperatures.

Analysis Area	Environment	No. of Cycles	Temp °C	Element wt. %													
				Fe	Ni	Cr	Co	Na	V	S	Ti	Al	Si	Mn	Mg		
1	Pure Na ₂ SO ₄	24	900	-	4.59	84.62	-	2.53	-	-	8.24	-	-	-	-	-	-
2		24	900	-	3.42	52.46	-	2.49	-	-	4.10	-	-	-	-	-	-
3		24	900	-	7.16	83.17	-	-	-	-	7.16	-	-	-	-	-	-
4	Na ₂ SO ₄ -15%V ₂ O ₅	24	900	-	91.34	7.90	-	-	-	-	-	-	1.37	-	-	-	-
5		24	900	-	94.28	4.94	-	-	-	-	-	-	0.772	-	-	-	-
6	Na ₂ SO ₄ -60%V ₂ O ₅	24	900	-	81.45	9.72	-	6.07	-	-	-	-	2.73	-	-	-	-
7		24	900	-	40.11	34.76	-	19.91	-	-	2.37	-	-	2.82	-	-	-
8	Na ₂ SO ₄ -60%V ₂ O ₅	6	1100	-	61.78	26.57	-	4.12	-	-	-	-	5.02	2.51	-	-	-
9		6	1100	-	40.91	39.07	-	6.21	-	-	5.47	-	4.62	3.72	-	-	-
10	Na ₂ SO ₄ -60%V ₂ O ₅	24	900	-	57.25	19.02	-	16.57	-	-	-	-	-	-	-	-	-
11	+ MgO	24	900	-	56.23	26.91	-	14.87	-	-	1.96	-	-	-	-	-	-

Table 5.31 : EDAX Analysis of Alloy C (Superni 600) After Cyclic Hot Corrosion Under Different Salts and Temperatures.

Analysis Area	Environment	No. of Cycles	Temp °C	Element wt. %													
				Fe	Ni	Cr	Co	Na	V	S	Ti	Al	Si	Mn	Mg		
1	Pure Na ₂ SO ₄	24	900	6.43	4.28	82.38	-	-	-	-	-	3.98	-	2.90	-	-	-
2		24	900	2.32	3.98	89.70	-	-	-	-	-	3.98	-	-	-	-	-
3		24	900	2.53	2.89	23.91	-	-	-	-	13.76	-	-	6.88	-	-	-
4	Na ₂ SO ₄ - 15%V ₂ O ₅	24	900	8.21	65.58	16.42	-	-	-	-	-	2.47	-	3.25	1.95	-	-
5		24	900	16.89	29.22	44.99	-	-	-	-	-	6.64	-	2.24	-	-	-
6	Na ₂ SO ₄ - 60%V ₂ O ₅	24	900	18.04	36.21	33.73	-	-	-	-	-	4.00	-	2.92	2.35	-	-
7		24	900	2.62	84.83	6.12	-	-	-	-	-	4.08	-	2.33	-	-	-
8	Na ₂ SO ₄ - 60%V ₂ O ₅	24	900	6.79	21.16	19.90	-	-	-	-	-	46.60	-	2.21	3.31	-	-
9		6	1100	4.26	62.08	27.31	-	-	-	-	-	-	-	3.63	2.72	-	-
10	Na ₂ SO ₄ - 60%V ₂ O ₅	6	1100	4.96	53.02	23.48	-	-	-	-	-	-	-	4.42	7.51	-	-
11		24	900	3.28	73.46	4.85	-	-	-	-	-	3.28	-	-	-	-	-
12	Na ₂ SO ₄ - 60%V ₂ O ₅ + MgO	24	900	8.54	34.30	24.52	-	-	-	-	-	14.42	-	2.91	2.84	-	-
13		24	900	10.50	67.27	14.97	-	-	-	-	-	4.46	-	-	-	-	-

Table 5.32 : EDAX Analysis of Alloy D (Superni 718) After Cyclic Hot Corrosion Under Different Salts and Temperatures.

Analysis Area	Environment	No. of Cycles	Temp °C	Element wt. %													
				Fe	Ni	Cr	Co	Na	V	S	Ti	Al	Si	Mn	Mg		
1	Pure Na ₂ SO ₄	24	900	2.43	2.28	43.37	-	-	-	-	-	7.91	-	43.98	-	-	-
2		24	900	2.07	2.07	74.61	-	-	-	-	-	3.88	-	17.35	-	-	-
3		24	900	2.16	3.08	72.83	-	-	-	-	-	2.16	13.88	-	5.86	-	-
4	Na ₂ SO ₄ - 15%V ₂ O ₅	24	900	30.58	14.98	44.81	-	-	-	-	-	2.34	-	4.23	3.02	-	-
5		24	900	31.99	16.56	41.86	-	-	-	-	-	2.81	-	5.49	1.26	-	-
6	Na ₂ SO ₄ - 60%V ₂ O ₅	24	900	7.05	58.82	8.23	-	-	-	-	-	8.23	-	8.23	9.41	-	-
7		24	900	8.15	54.34	9.78	-	-	-	-	-	8.69	-	9.23	9.78	-	-
8	Na ₂ SO ₄ - 60%V ₂ O ₅	6	1100	5.48	11.06	63.84	-	-	-	-	-	3.04	-	6.55	5.32	4.71	-
9		6	1100	15.57	1.256	69.84	-	-	-	-	-	-	-	5.52	2.26	5.52	-
10	Na ₂ SO ₄ - 60%V ₂ O ₅ + MgO	24	900	26.05	29.48	30.62	-	-	-	-	-	5.14	-	3.77	2.74	-	2.00
11		24	900	7.22	80.06	6.90	-	-	-	-	-	2.35	-	-	1.72	-	1.41
12	MgO	24	900	19.94	22.92	47.97	-	-	-	-	-	3.37	-	3.66	1.15	-	0.963

Table 5.33 : EDAX Analysis of Alloy E (Superco 605) After Cyclic Hot Corrosion Under Different Salts and Temperatures.

Analysis Area	Environment	No. of Cycles	Temp °C	Element wt. %														
				Fe	Ni	Cr	Co	Na	V	S	Ti	Al	Si	Mn	Mg	W		
1	Pure Na ₂ SO ₄	24	900	3.50	-	68.12	28.36	-	-	-	-	-	-	-	-	-	-	-
2		24	900	2.67	-	78.27	19.04	-	-	-	-	-	-	-	-	-	-	-
3	Na ₂ SO ₄ -15%V ₂ O ₅	24	900	1.89	29.73	2.84	59.59	-	-	-	-	-	1.42	-	-	-	-	4.50
4		24	900	3.85	22.70	5.33	58.56	-	-	-	-	-	-	-	-	-	-	9.53
5	Na ₂ SO ₄ -60%V ₂ O ₅	24	900	2.22	4.17	40.66	31.05	-	5.57	-	-	-	2.36	4.87	7.10	-	-	1.94
6		24	900	2.58	5.16	37.32	34.75	-	5.42	-	-	-	-	1.55	8.01	-	-	4.78
7	Na ₂ SO ₄ -60%V ₂ O ₅	6	1100	8.88	11.11	17.77	44.44	-	-	-	-	-	7.50	10.27	-	-	-	-
8		6	1100	7.72	5.00	65.68	21.59	-	-	-	-	-	-	-	-	-	-	-
9	Na ₂ SO ₄ -60%V ₂ O ₅	24	900	3.24	3.97	42.14	25.99	-	7.22	-	-	-	-	6.22	9.38	-	-	1.80
10	+ MgO	24	900	3.07	4.02	48.41	26.68	-	4.53	-	-	-	-	1.02	10.43	-	-	1.79

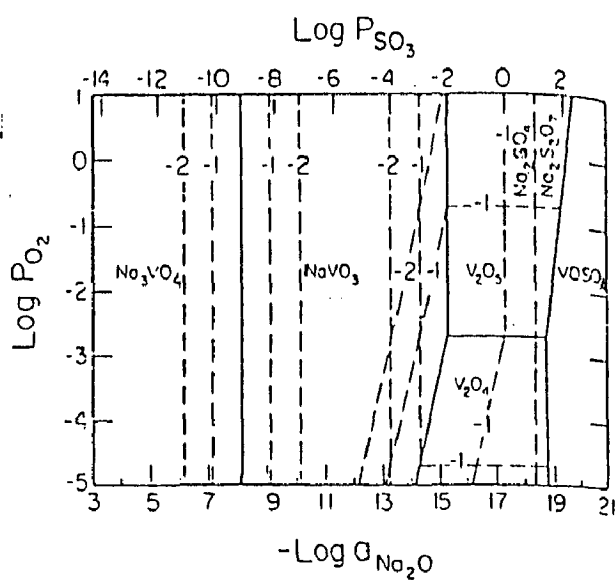


Fig. 2.1: Phase stability diagram for Na-V-S-O system at 900°C⁽¹⁷⁾.

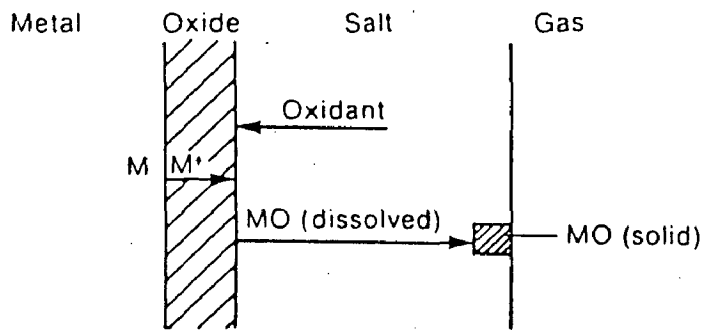


Fig. 2.2(a): Schematic diagram for fluxing. Metal oxide dissolves at the oxide/salt interface and migrates down a concentration gradient to a region of lower solubility, where MO precipitates. At steady state the oxide is dissolved and transported away just as fast as it grows⁽⁴⁾.

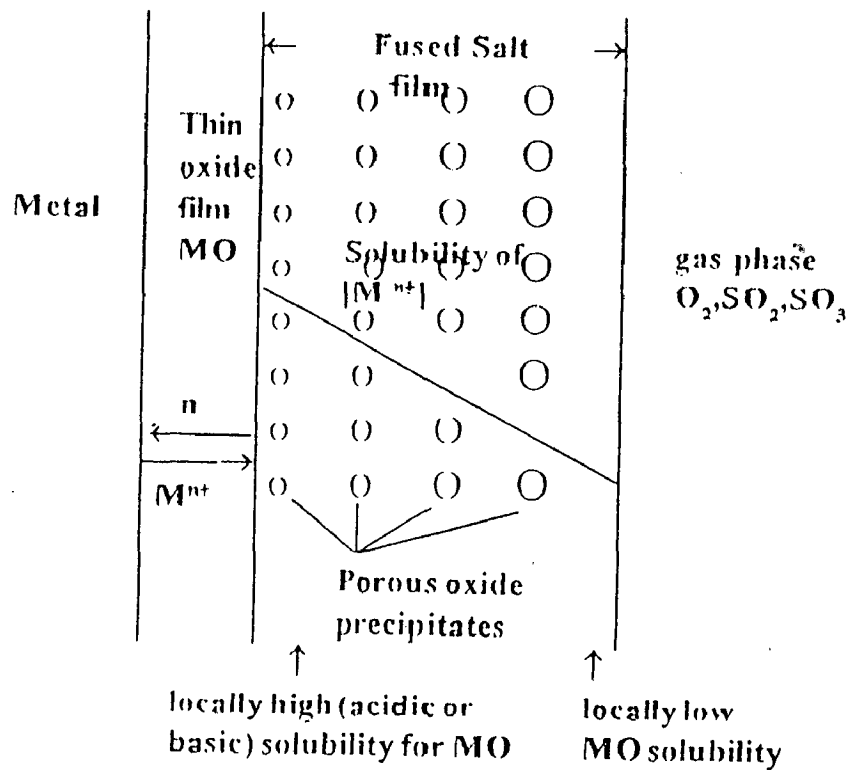


Fig. 2.2(b) Precipitation of a porous MO oxide supported by the solubility gradient in a fused salt film⁽⁴⁾.

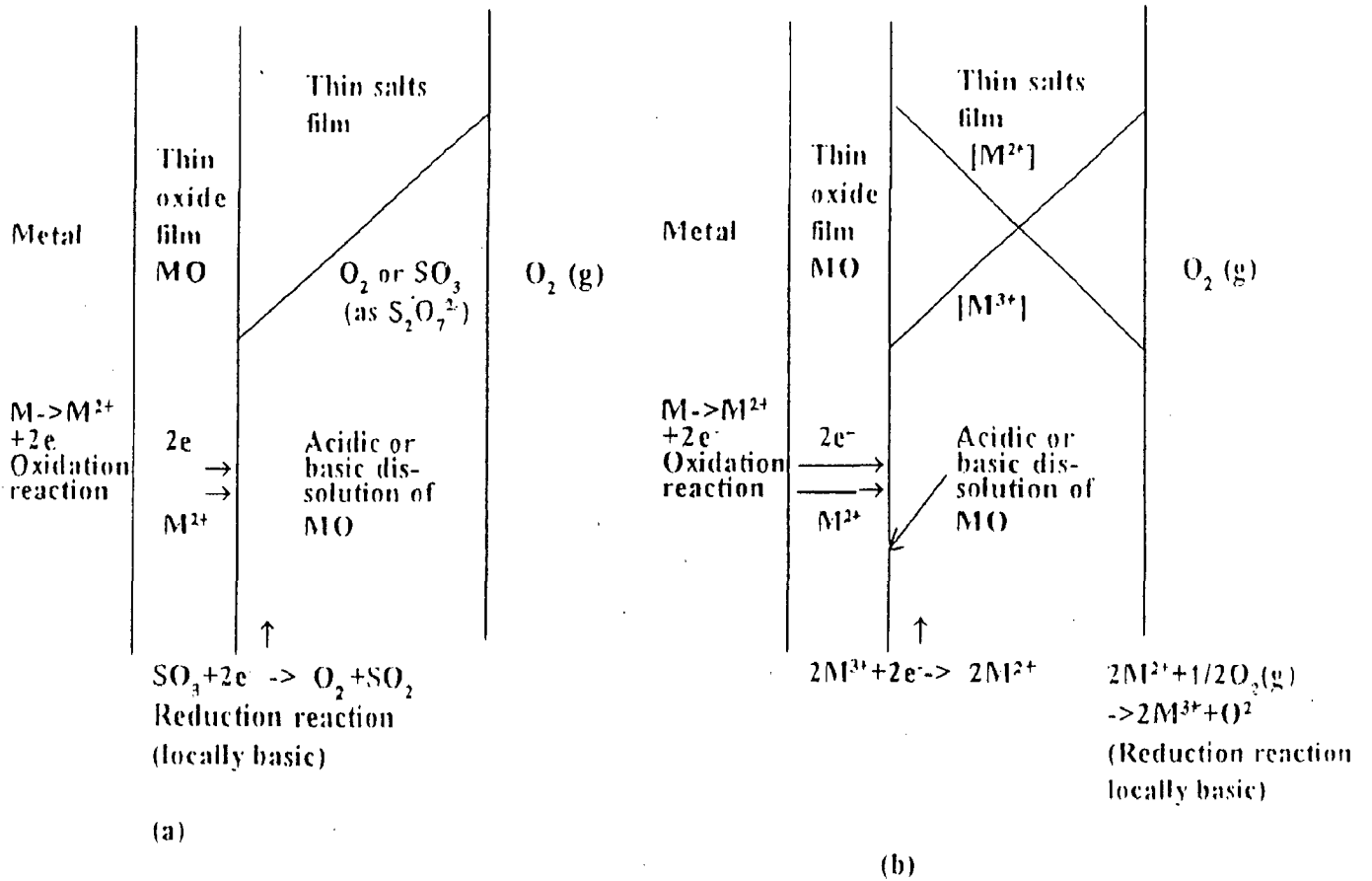


Fig. 2.3 : Cathodic reduction of SO₃ (as S₂O₇²⁻) or molecular oxygen for
 (a) a high permeability of SO₃ or O₂ in the salt film⁽⁴⁾
 (b) high concentration and diffusivities of M²⁺ and M³⁺ or electronic conduction in the salt film⁽⁴⁾.

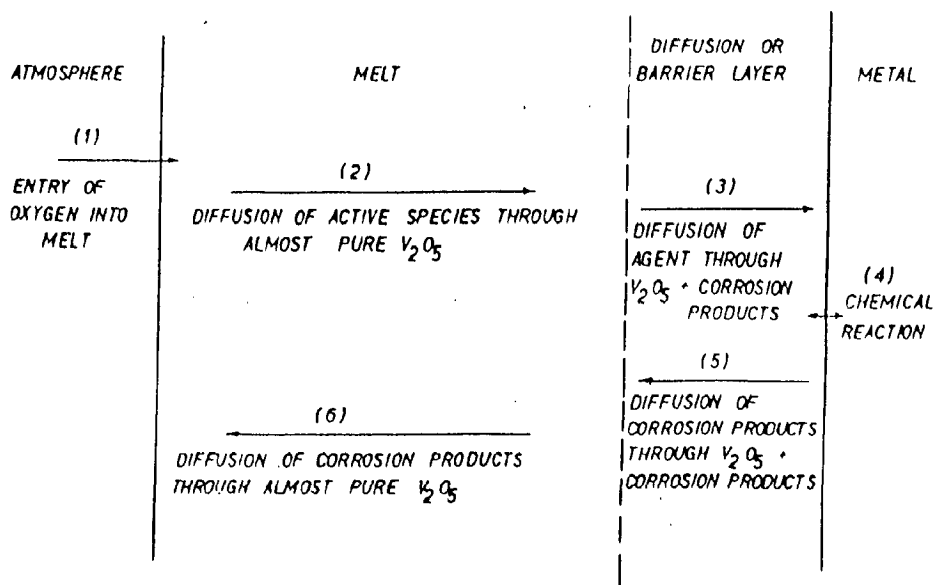


Fig. 2.4 : Sequential steps in the vanadic corrosion of metals⁽¹¹⁸⁾.

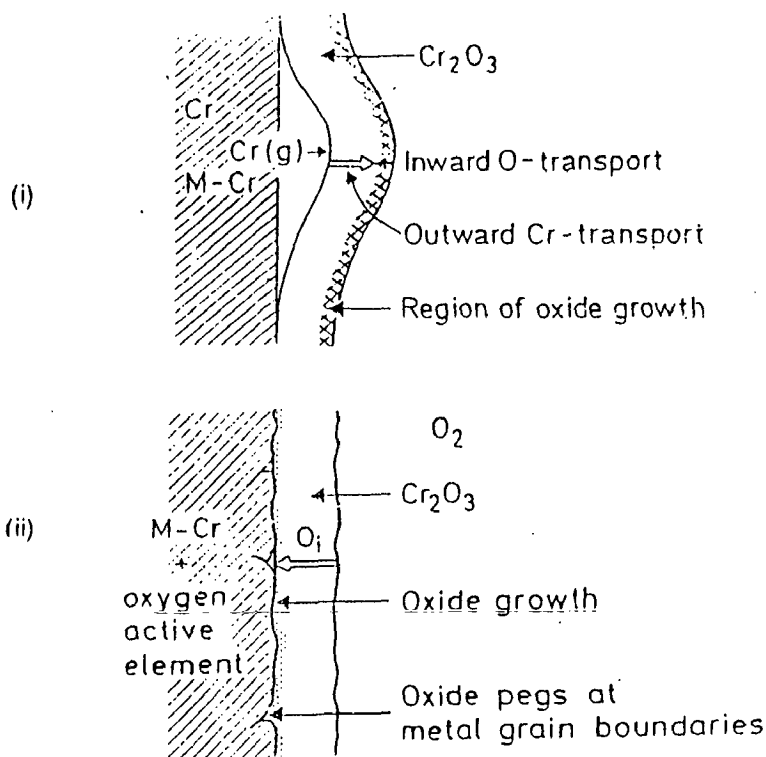


Fig. 2.5: Schematic illustration of the growth of chromia scales in (i) the absence of oxygen active element and with predominant outward transport of chromium through the scale, and (ii) the presence of oxygen active elements and with predominant inward transport of oxygen⁽¹²²⁾.

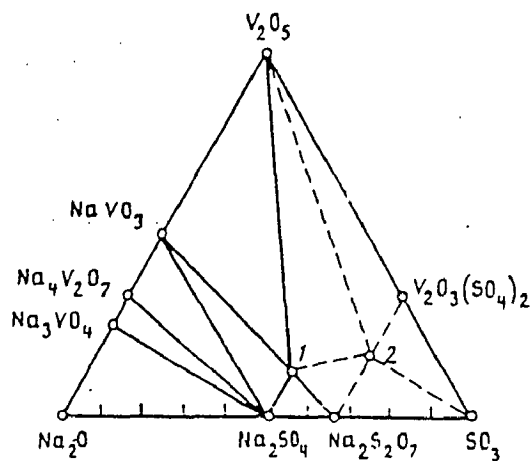


Fig. 2.6 : Phase diagram of the $\text{Na}_2\text{O}-\text{V}_2\text{O}_5-\text{SO}_3$ system.

(1) $\text{Na}_3\text{VO}_2(\text{SO}_4)_2$, (2) $\text{NaVO}(\text{SO}_4)_2$ ⁽⁵⁷⁾.

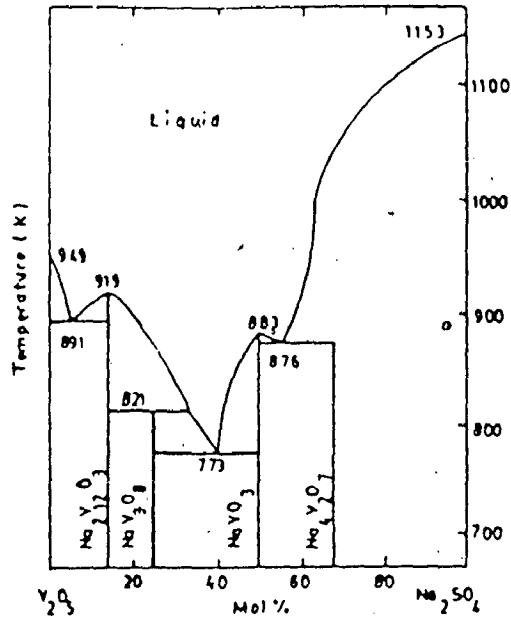


Fig. 2.7 : Equilibrium diagram V_2O_5 - Na_2SO_4 mixture⁽⁵⁸⁾.

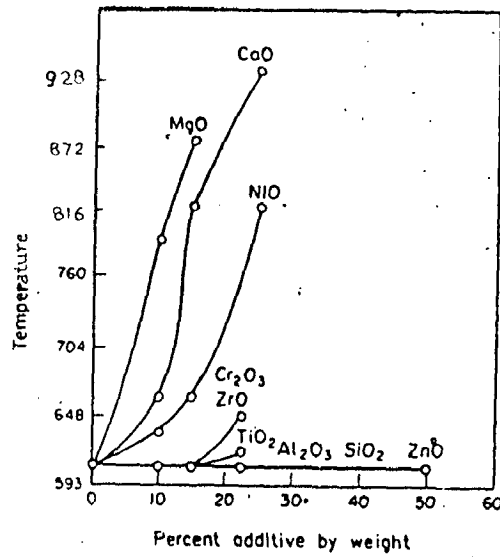


Fig. 2.8 : Effect of adding various oxides on melting point of a typical crude oil ash. Initial oil ash composition ; 60% V_2O_5 , 15% Na_2SO_4 , 10% CaO, 5% PbO, 5% SiO_2 , 5% Fe_2O_3 ⁽⁸¹⁾

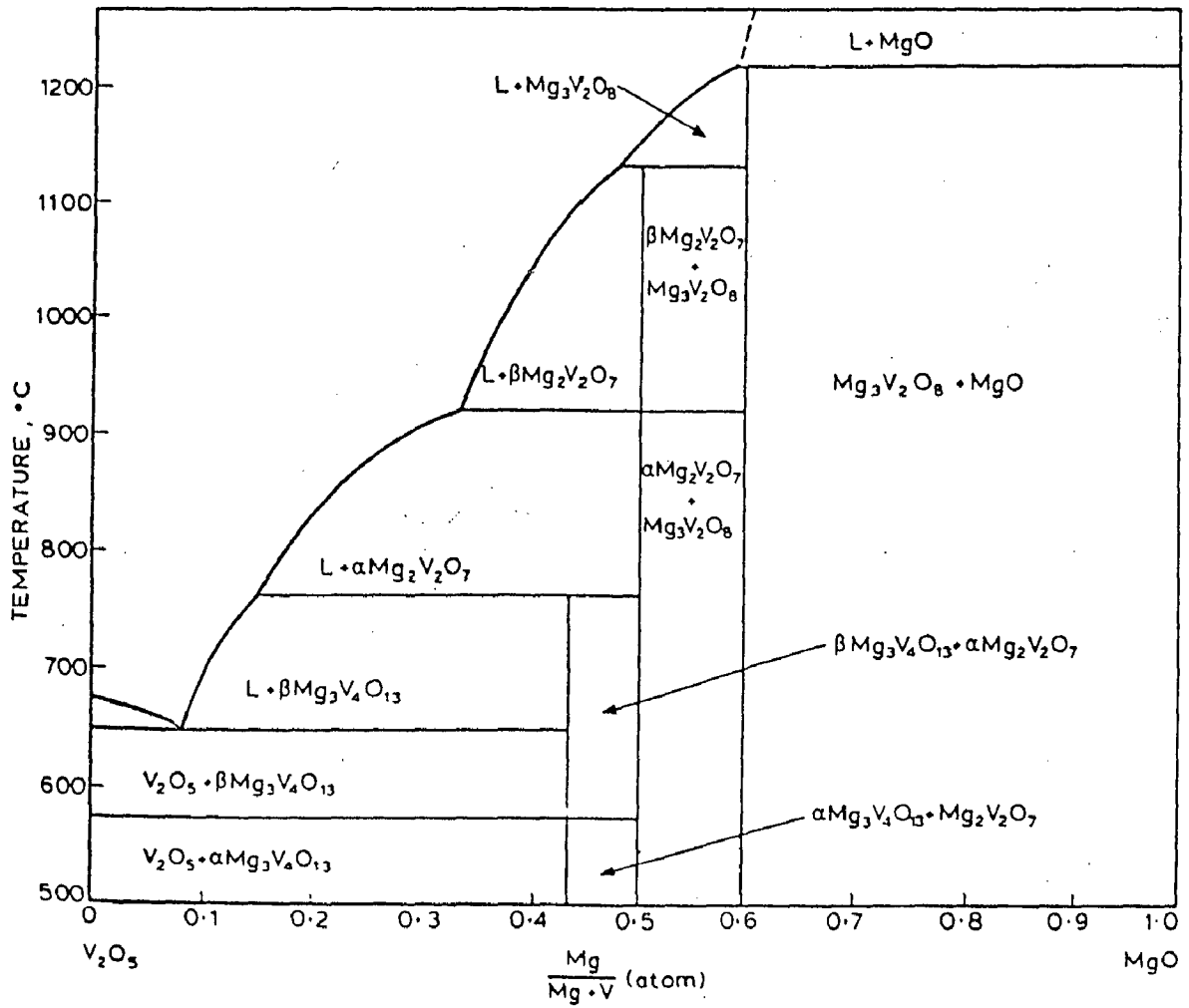


Fig. 2.9 : Phase diagram for MgO - V₂O₅ system⁽¹¹⁾.

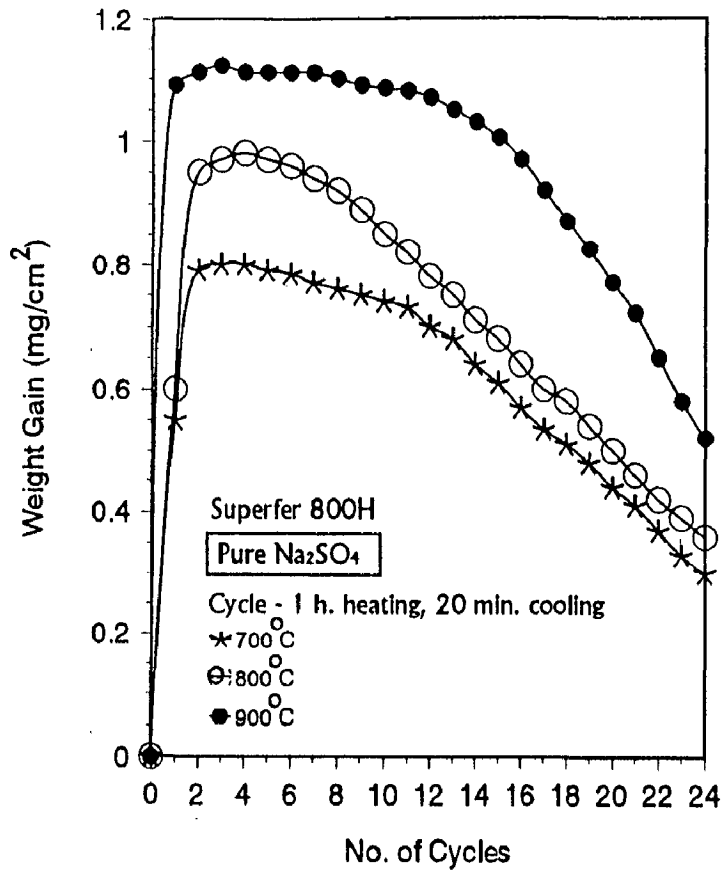


Fig. 5.1 : Weight change plots for the alloy A(Superfer 800H) In pure Na₂SO₄

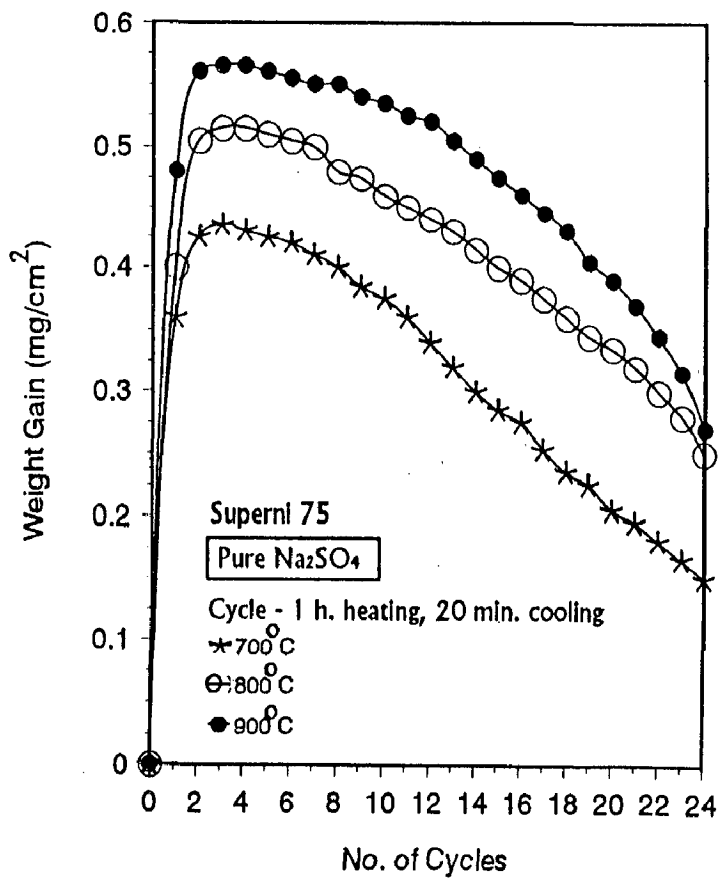


Fig. 5.2 : Weight change plots for the alloy B (Superni 75) in pure Na₂SO₄

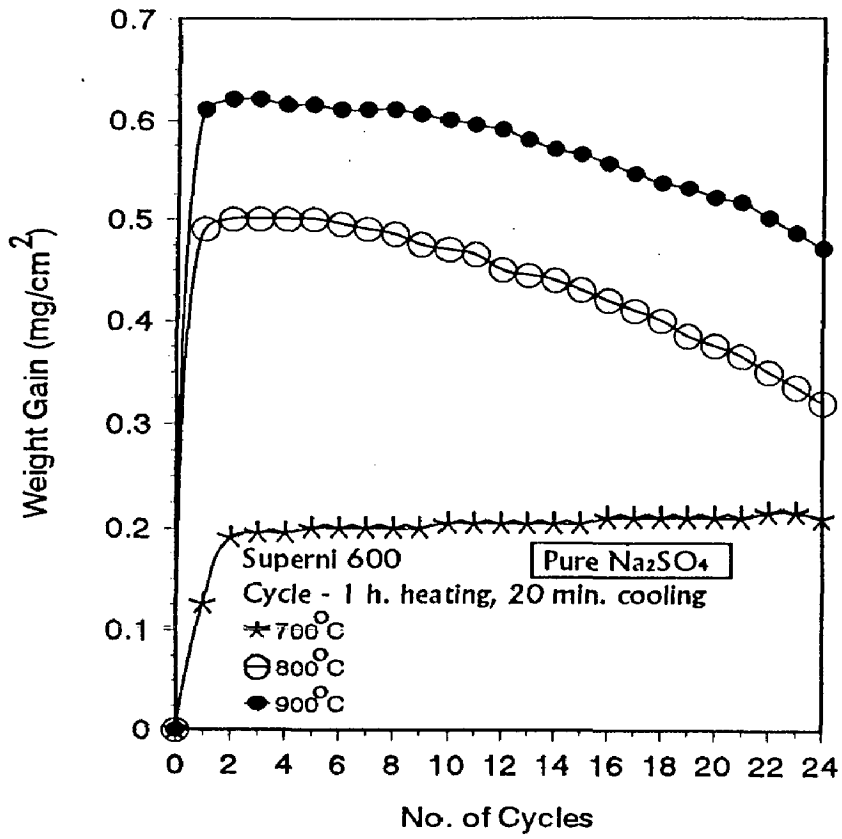


Fig. 5.3 : Weight change plots for the alloy C (Superni 600) in pure Na₂SO₄

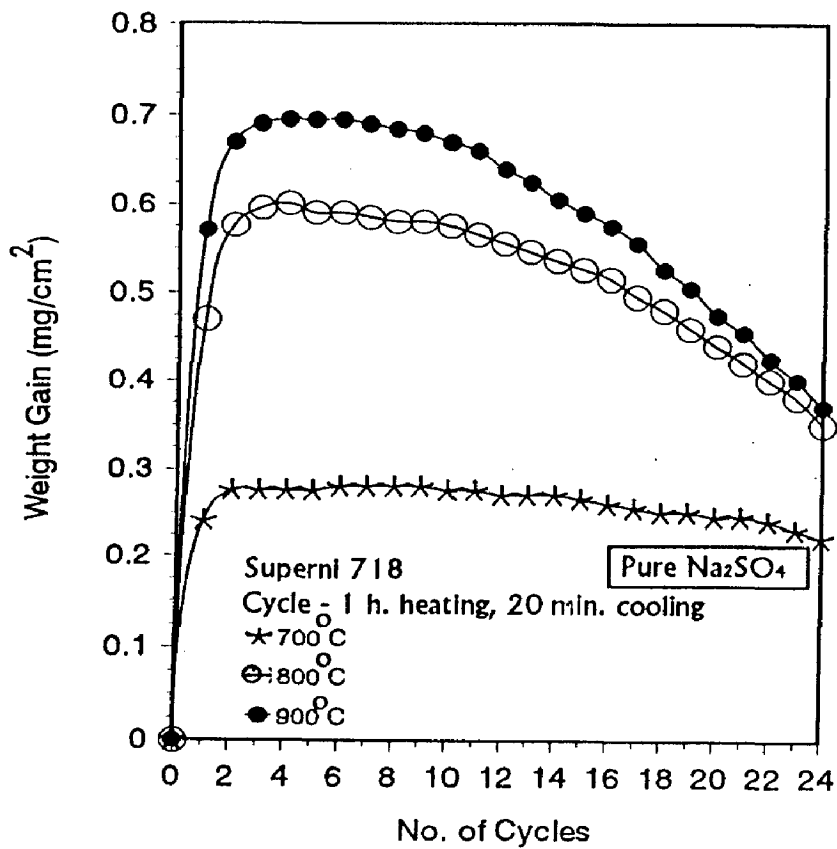


Fig. 5.4 : Weight change plots for the alloy D (Superni 718) in pure Na₂SO₄

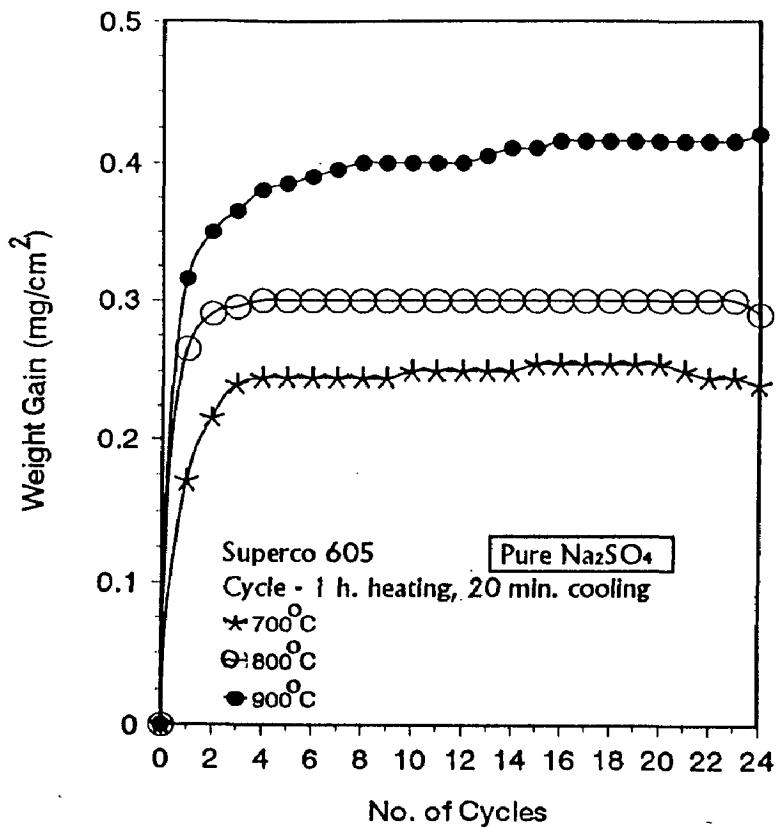


Fig. 5.5 : Weight change plots for the alloy E (Superco 605) in pure Na₂SO₄

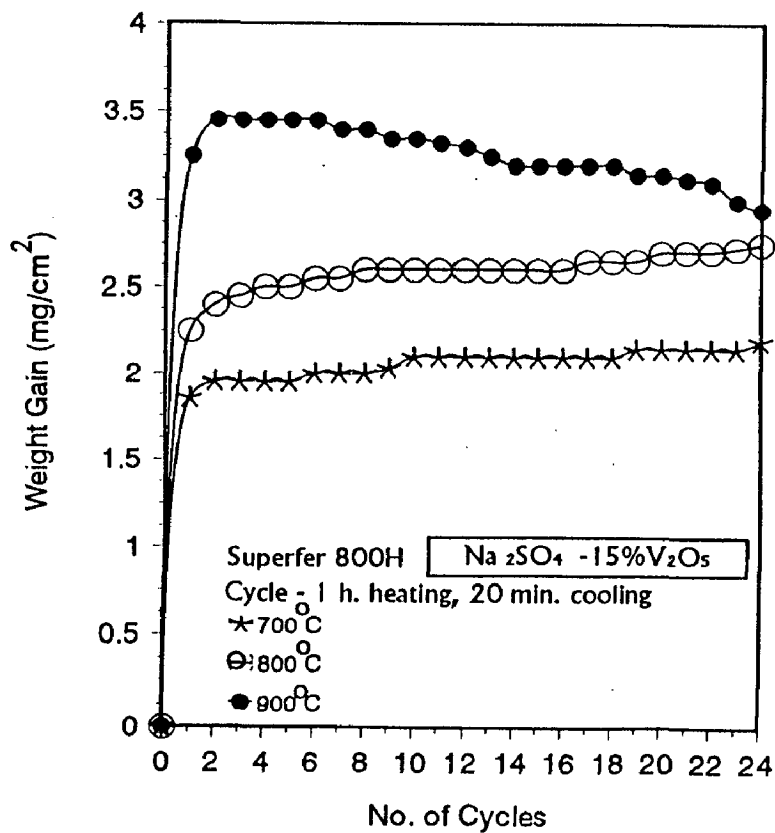


Fig. 5.6 : Weight change plots for the alloy A (Superfer 800H) in Na₂SO₄-15% V₂O₅

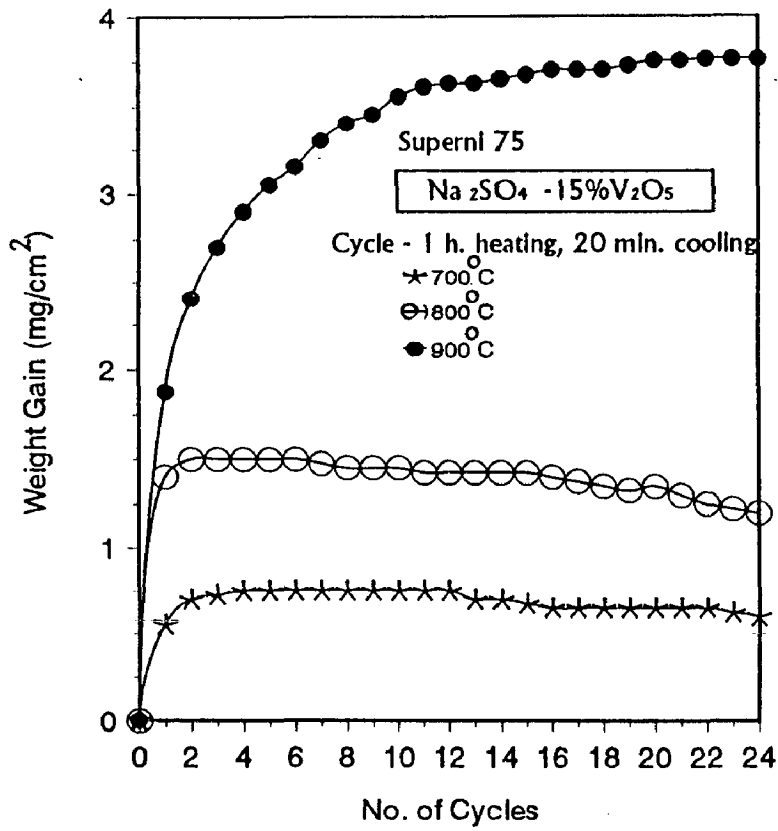


Fig. 5.7 : Weight change plots for the alloy C (Superni 75) in $\text{Na}_2\text{SO}_4-15\% \text{V}_2\text{O}_5$

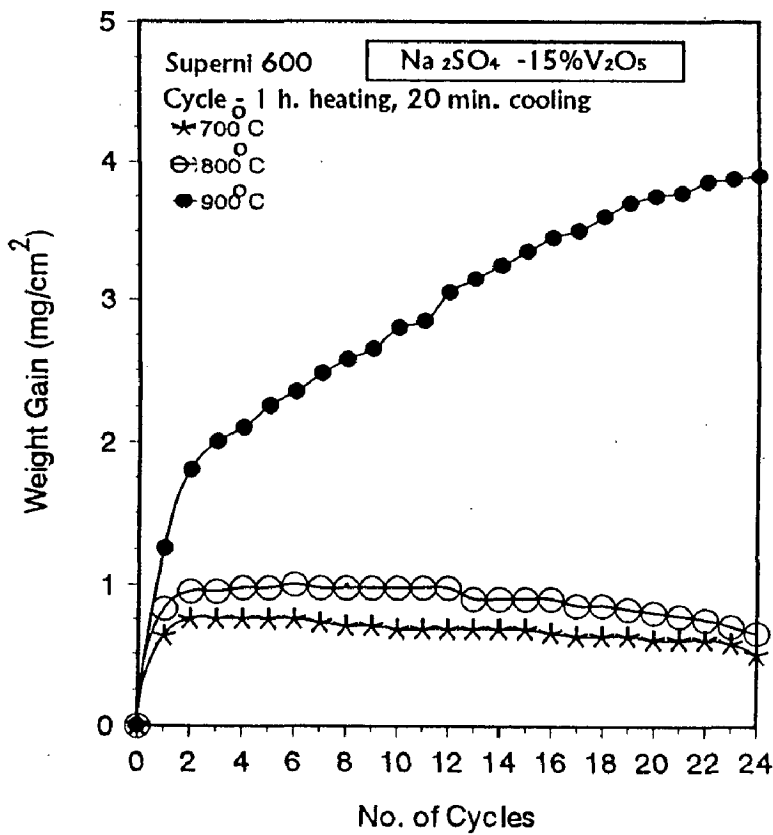


Fig. 5.8 : Weight change plots for the alloy C (Superni 600) in $\text{Na}_2\text{SO}_4-15\% \text{V}_2\text{O}_5$

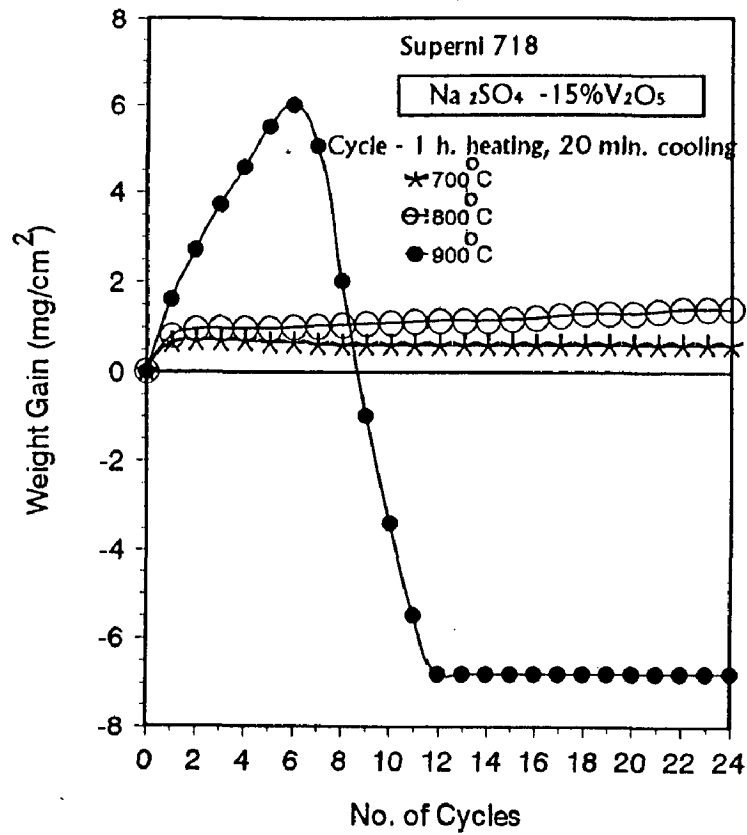


Fig. 5.9 : Weight change plots for the alloy D (Supernl 718) in Na_2SO_4 -15% V_2O_5

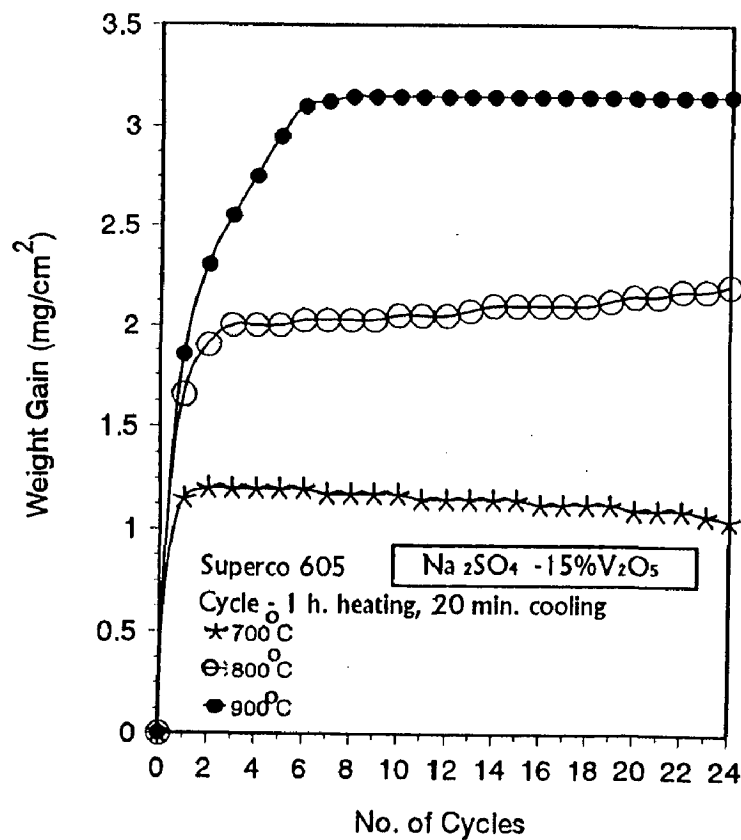


Fig. 5.10 : Weight change plots for the alloy E (Superco 605) in Na_2SO_4 -15% V_2O_5

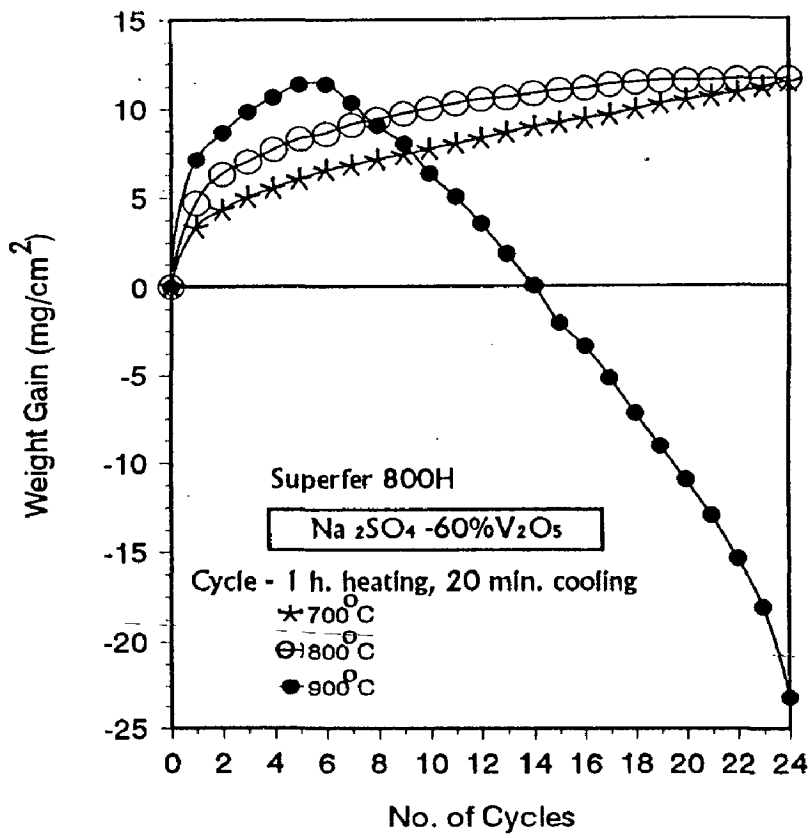


Fig. 5.11 : Weight change plots for the alloy A (Superfer 800H) in Na_2SO_4 -60% V_2O_5

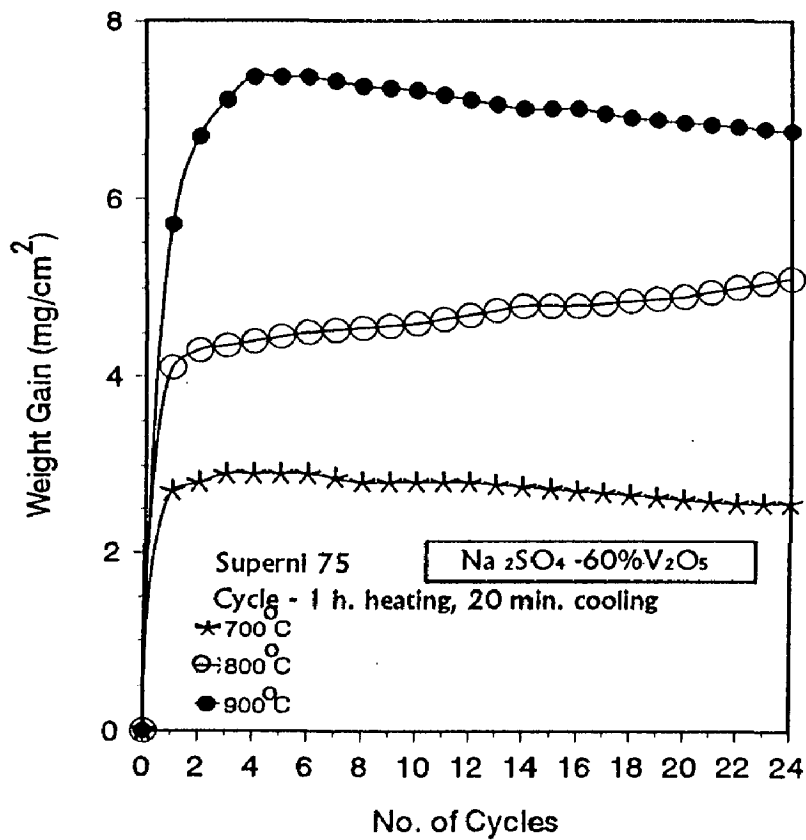


Fig. 5.12 : Weight change plots for the alloy B (Superni 75) in Na_2SO_4 -60% V_2O_5

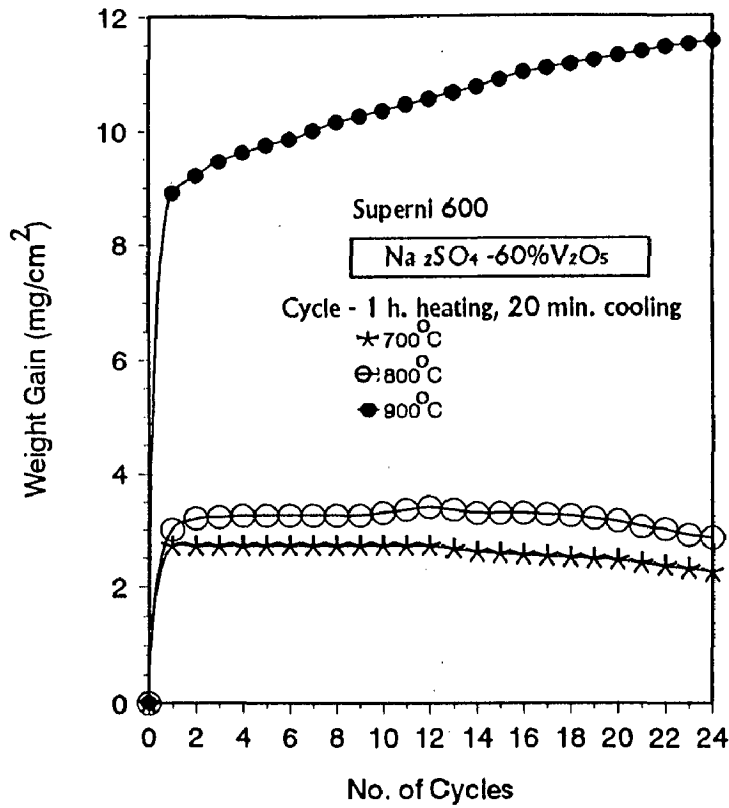


Fig. 5.13 : Weight change plots for the alloy C (Superni 600) in Na_2SO_4 -60% V_2O_5

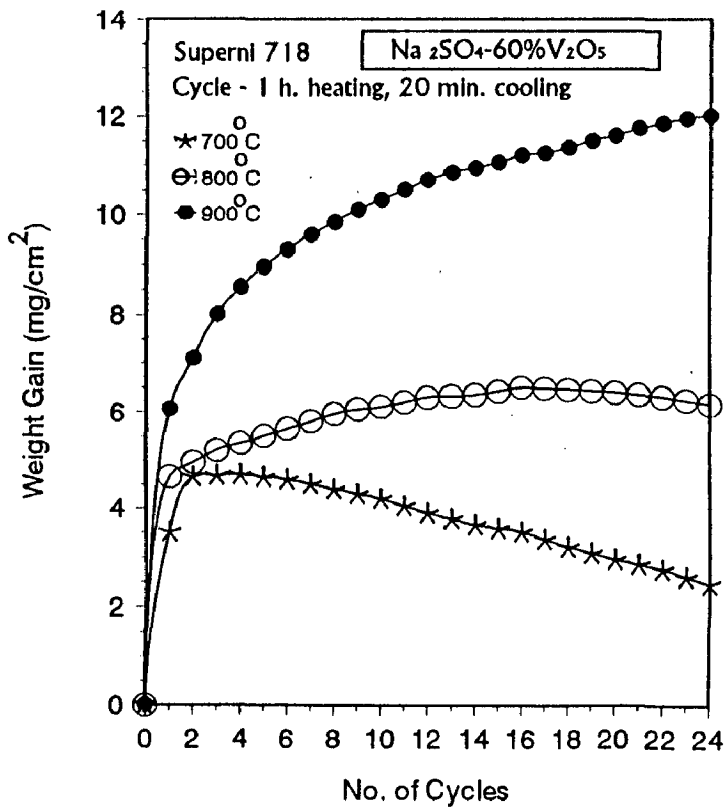


Fig. 5.14 : Weight change plots for the alloy D (Superni 718) in Na_2SO_4 -60% V_2O_5

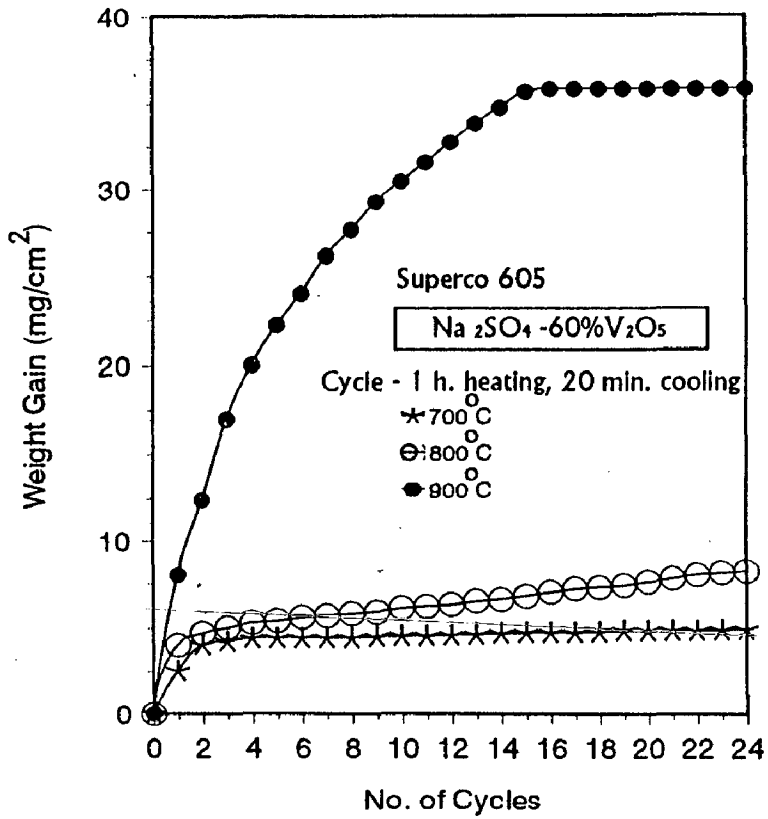


Fig. 5.15 : Weight change plots for the alloy E (Superco 605) in Na_2SO_4 -60% V_2O_5

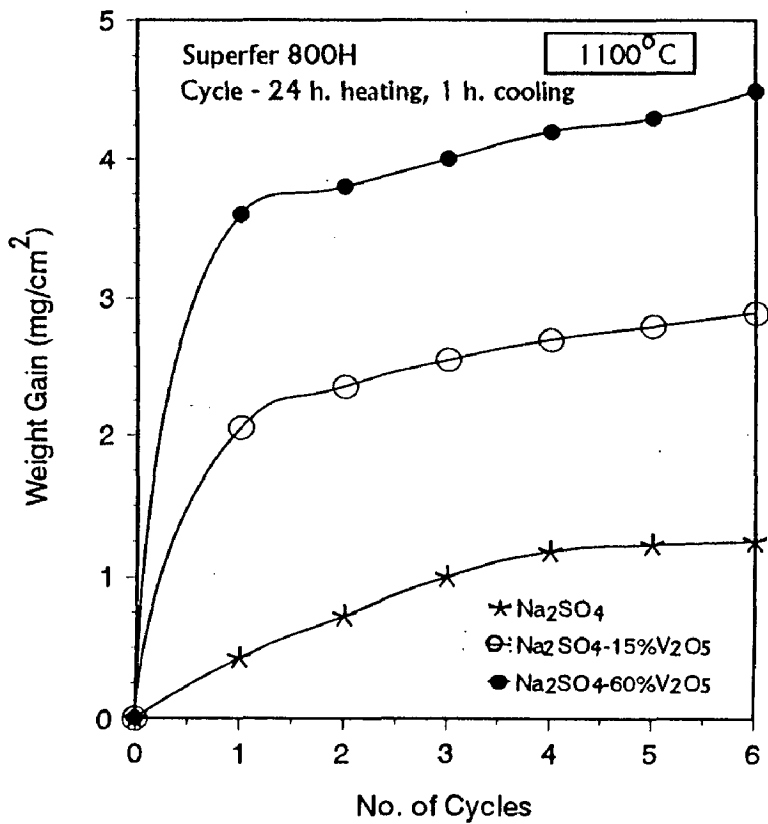


Fig. 5.16 : Weight change plots for the alloy A (Superfer 800H) in combustion gas at 1100°C

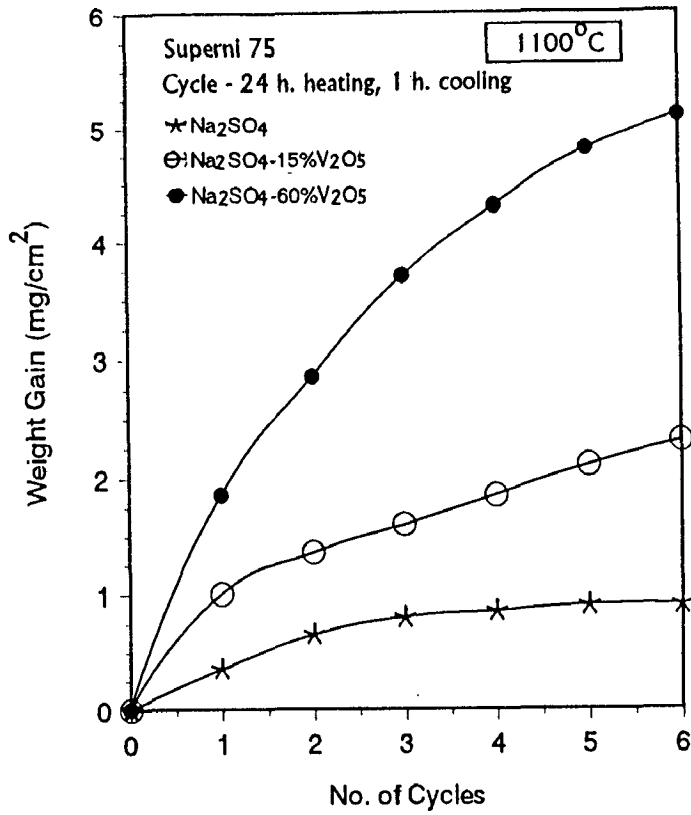


Fig. 5.17 : Weight change plots for the alloy B (Superni 75) in combustion gas at 1100°C

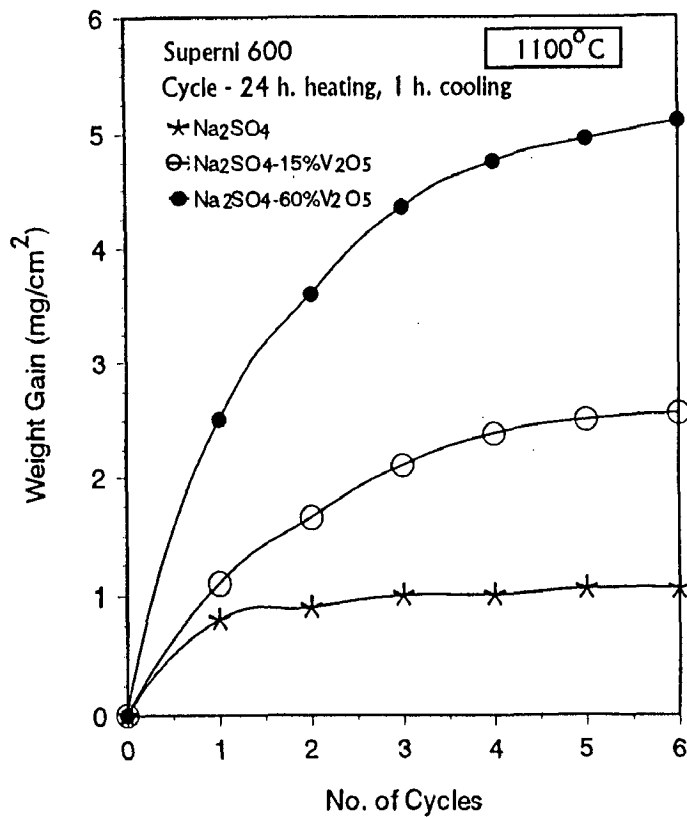


Fig. 5.18 : Weight change plots for the alloy C (Superni 600) in combustion gas at 1100°C

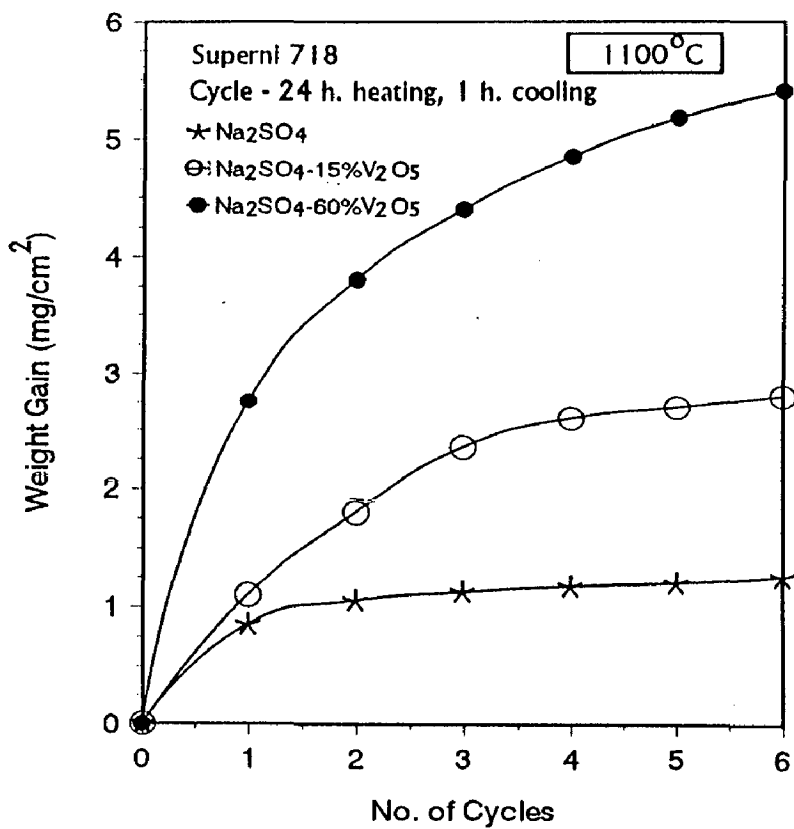


Fig. 5.19 : Weight change plots for the alloy D (Superni 718) in combustion gas at 1100°C.

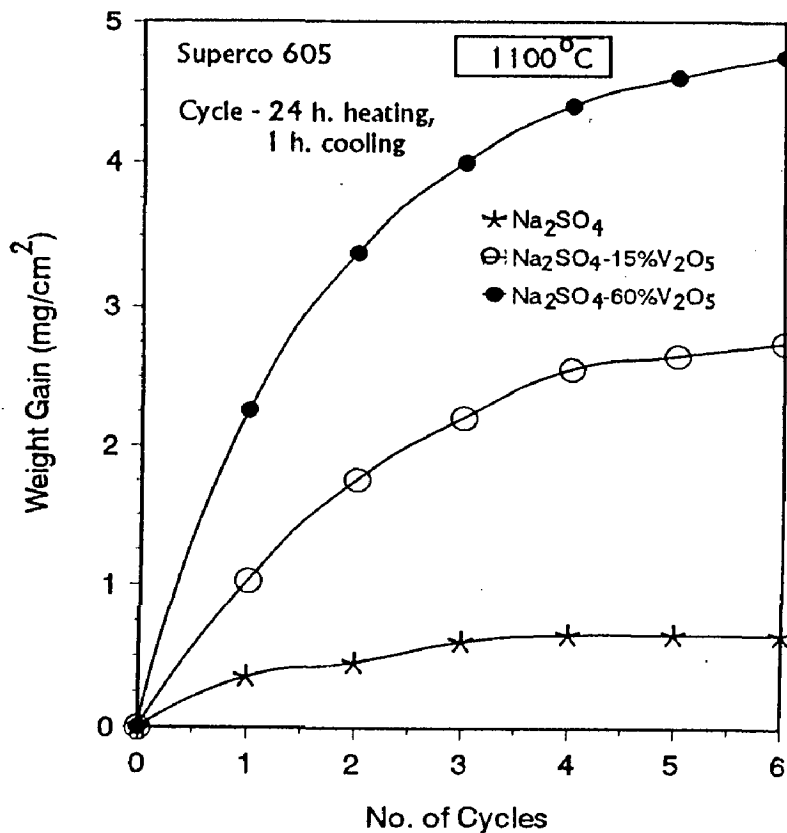


Fig. 5.20 : Weight change plots for the alloy E (Superco 605) in combustion gas at 1100°C

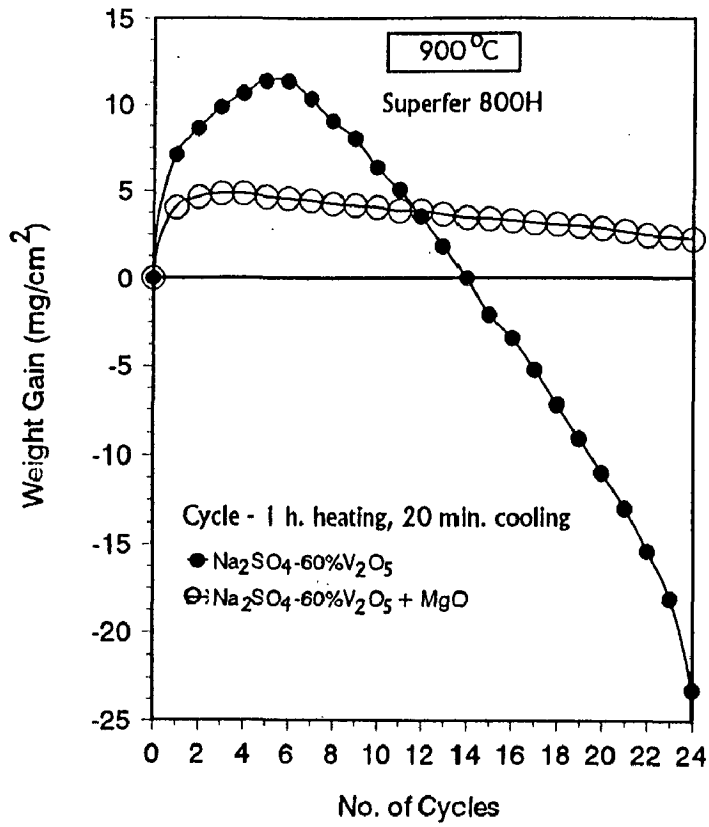


Fig. 5.21 : Weight change plots for the alloy A (Superfer 800H) in Na₂SO₄-60% V₂O₅ + MgO at 900°C

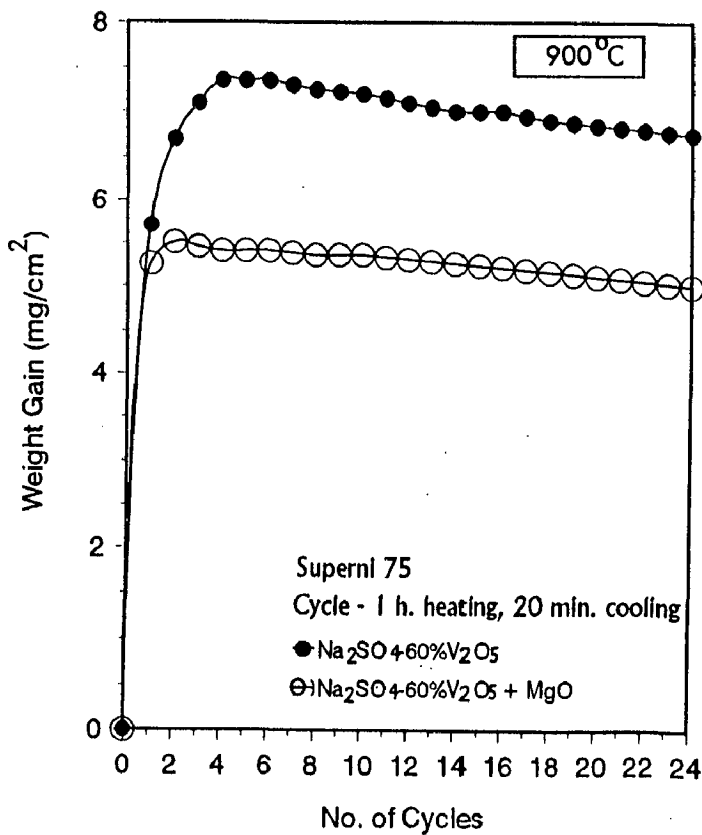


Fig. 5.22 : Weight change plots for the alloy B (Superni 75) in Na₂SO₄-60% V₂O₅ + MgO at 900°C.

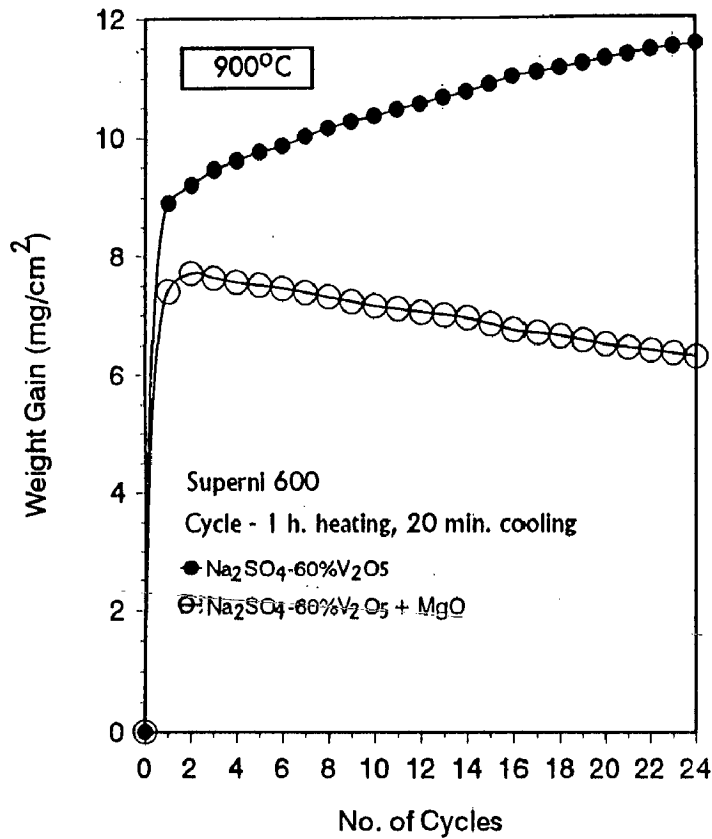


Fig. 5.23 : Weight change plots for the alloy C (Superni 600) Na₂SO₄-60%V₂O₅ + MgO at 900°C

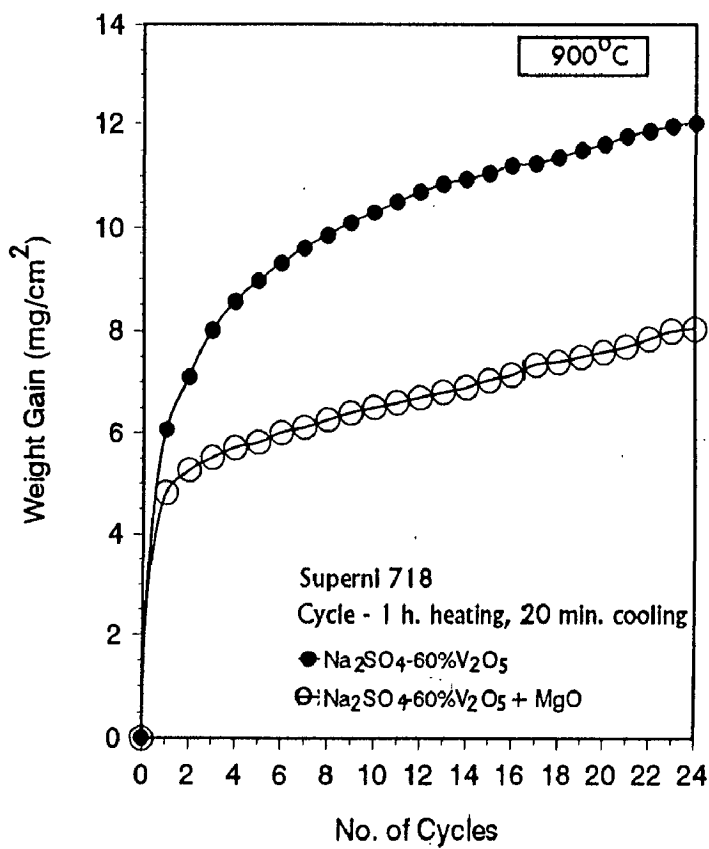


Fig. 5.24 : Weight change plots for the alloy D (Superni 718) in Na₂SO₄-60%V₂O₅ + MgO at 900°C.

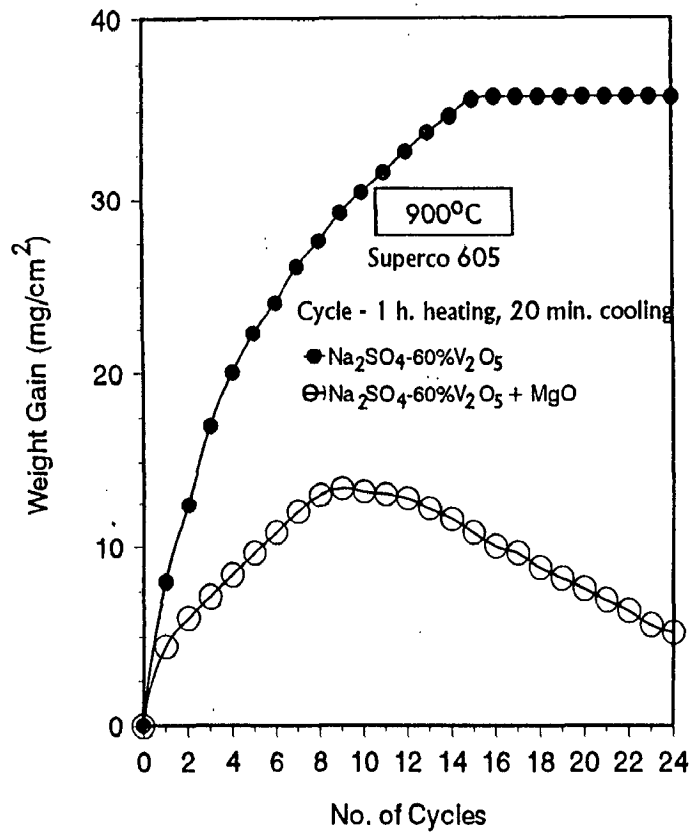


Fig. 5.25 : Weight change plots for the alloy E (Superco 605) in Na₂SO₄+60%V₂O₅+ MgO at 900°C













Salt Coating	Exposure (No. of Cycles)	Temperature ($^{\circ}\text{C}$)			
		700	800	900	1100
Pure Na_2SO_4	24				
Na_2SO_4 -15% V_2O_5	24				
Na_2SO_4 -60% V_2O_5	24				
Pure Na_2SO_4 + c.g.	6				
Na_2SO_4 -15% V_2O_5 + c.g.	6				
Na_2SO_4 -60% V_2O_5 + c.g.	6				
Na_2SO_4 -60% V_2O_5 + MgO	24				

Fig. 5.26 : Macrographs of Alloy A (Superfer 800H) after cyclic hot corrosion under different salts and temperatures





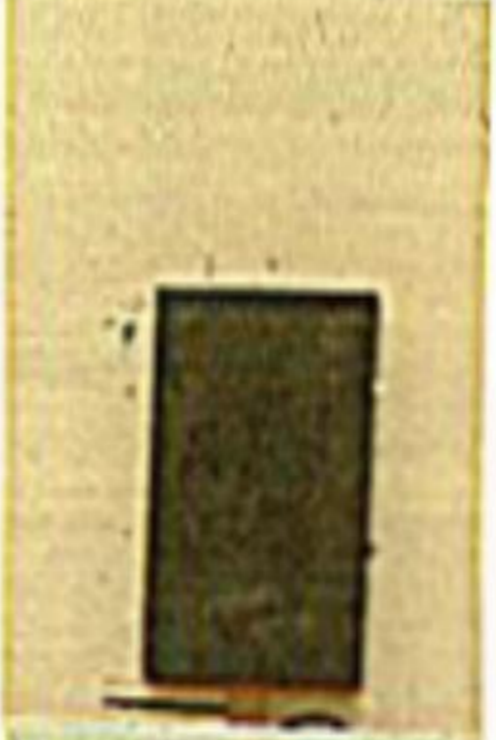



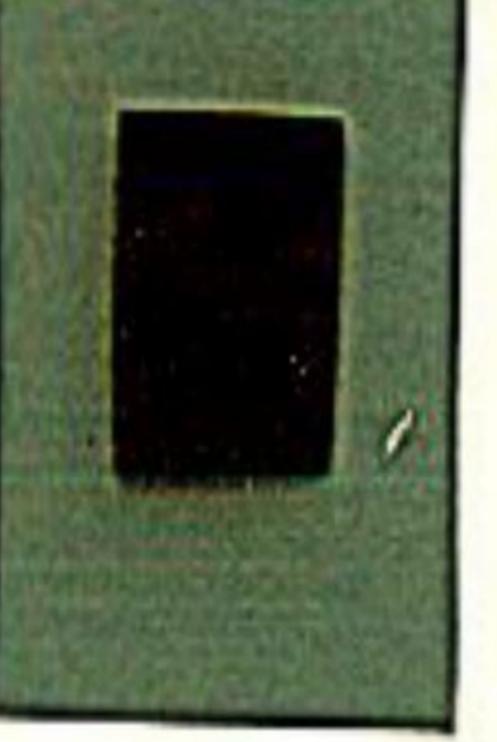
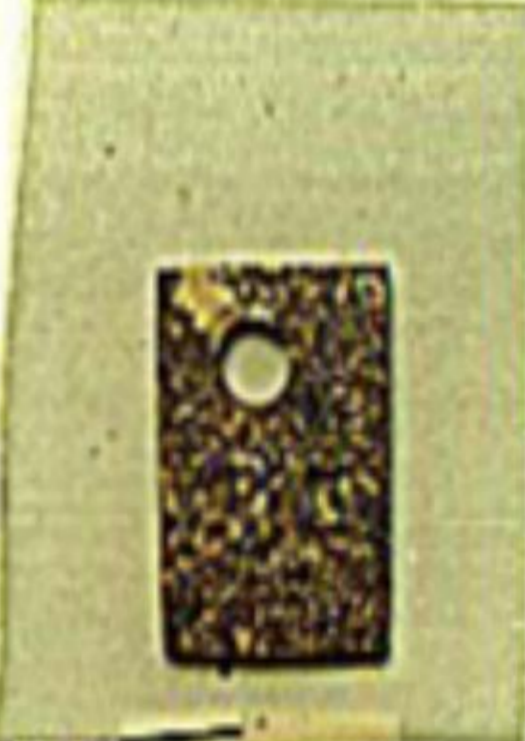



Salt Coating	Exposure (No. of Cycles)	Temperature (°C)			
		700	800	900	1100
Pure Na ₂ SO ₄	24				
Na ₂ SO ₄ -15%V ₂ O ₅	24				
Na ₂ SO ₄ -60%V ₂ O ₅	24				
Na ₂ SO ₄ + c.g.	6				
Na ₂ SO ₄ -15%V ₂ O ₅ + c.g.	6				
Na ₂ SO ₄ -60%V ₂ O ₅ + c.g.	6				
Na ₂ SO ₄ -60%V ₂ O ₅ + MgO	24				

Fig. 5.27 : Macrographs of Alloy B (Superni 75) after cyclic hot corrosion under











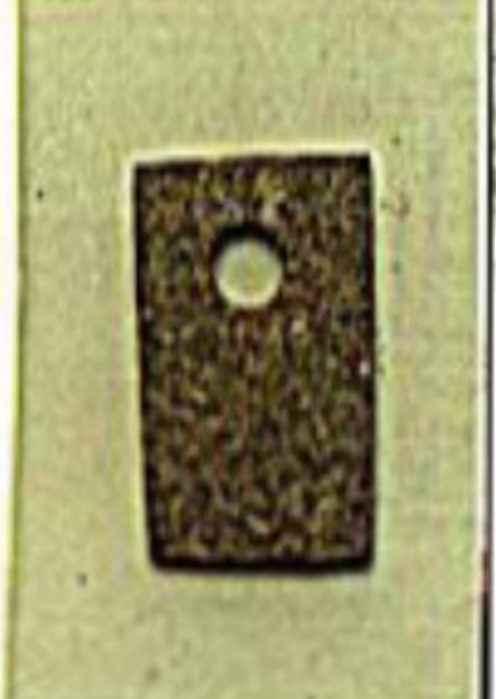



Salt Coating	Exposure (No. of Cycles)	Temperature (°C)			
		700	800	900	1100
Pure Na ₂ SO ₄	24				
Na ₂ SO ₄ -15%V ₂ O ₅	24				
Na ₂ SO ₄ -60%V ₂ O ₅	24				
Na ₂ SO ₄ + c.g.	6				
Na ₂ SO ₄ -15%V ₂ O ₅ + c.g.	6				
Na ₂ SO ₄ -60%V ₂ O ₅ + c.g.	6				
Na ₂ SO ₄ -60%V ₂ O ₅ + MgO	24				

Fig. 5.28 : Macrographs of Alloy C (Superni 600) after cyclic hot corrosion under different salts and temperatures.

Salt Coating	Exposure (No. of Cycles)	Temperature (°C)			
		700	800	900	1100
Pure Na ₂ SO ₄	24				
Na ₂ SO ₄ -15%V ₂ O ₅	24				
Na ₂ SO ₄ -60%V ₂ O ₅	24				
Na ₂ SO ₄ + c.g.	6				
Na ₂ SO ₄ -15%V ₂ O ₅ + c.g.	6				
Na ₂ SO ₄ -60%V ₂ O ₅ + c.g.	6				
Na ₂ SO ₄ -60%V ₂ O ₅ + MgO	24				

Fig. 5.29 : Macrographs of Alloy D (Superni 718) after cyclic hot corrosion under




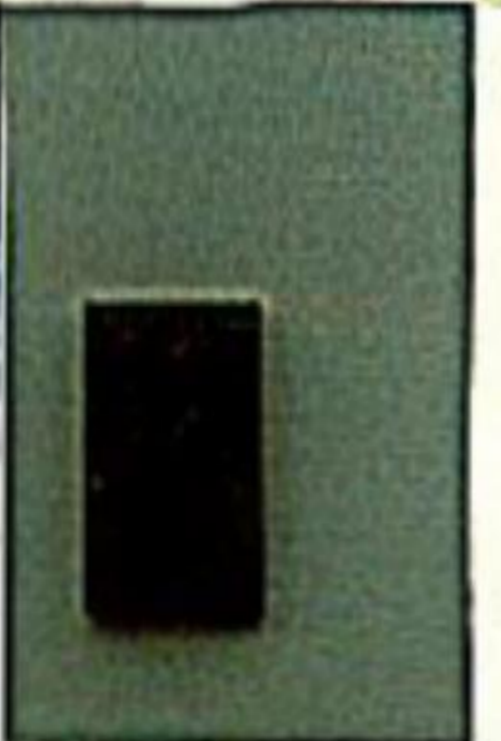
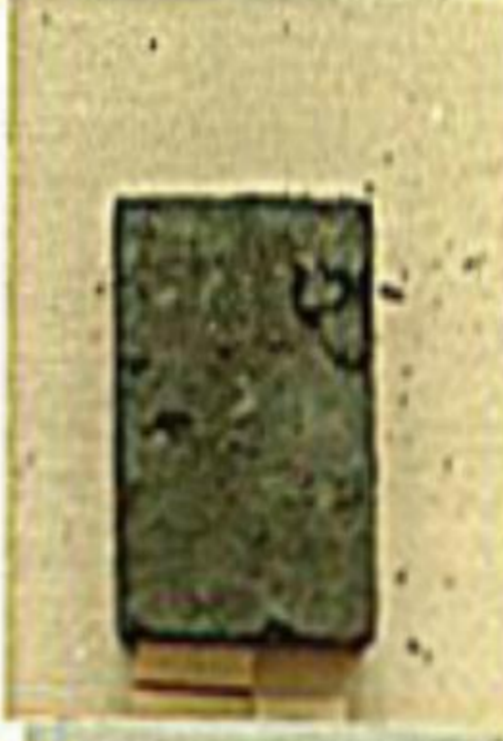








Salt Coating	Exposure (No. of Cycles)	Temperature (°C)			
		700	800	900	1100
Pure Na ₂ SO ₄	24				
Na ₂ SO ₄ -15%V ₂ O ₅	24				
Na ₂ SO ₄ -60%V ₂ O ₅	24				
Na ₂ SO ₄ + c.g.	6				
Na ₂ SO ₄ -15%V ₂ O ₅ + c.g.	6				
Na ₂ SO ₄ -60%V ₂ O ₅ + c.g.	6				
Na ₂ SO ₄ -60%V ₂ O ₅ + MgO	24				

Fig. 5.30 : Macrographs of Alloy E (Supercor 605) after cyclic hot corrosion under different salts and temperatures.

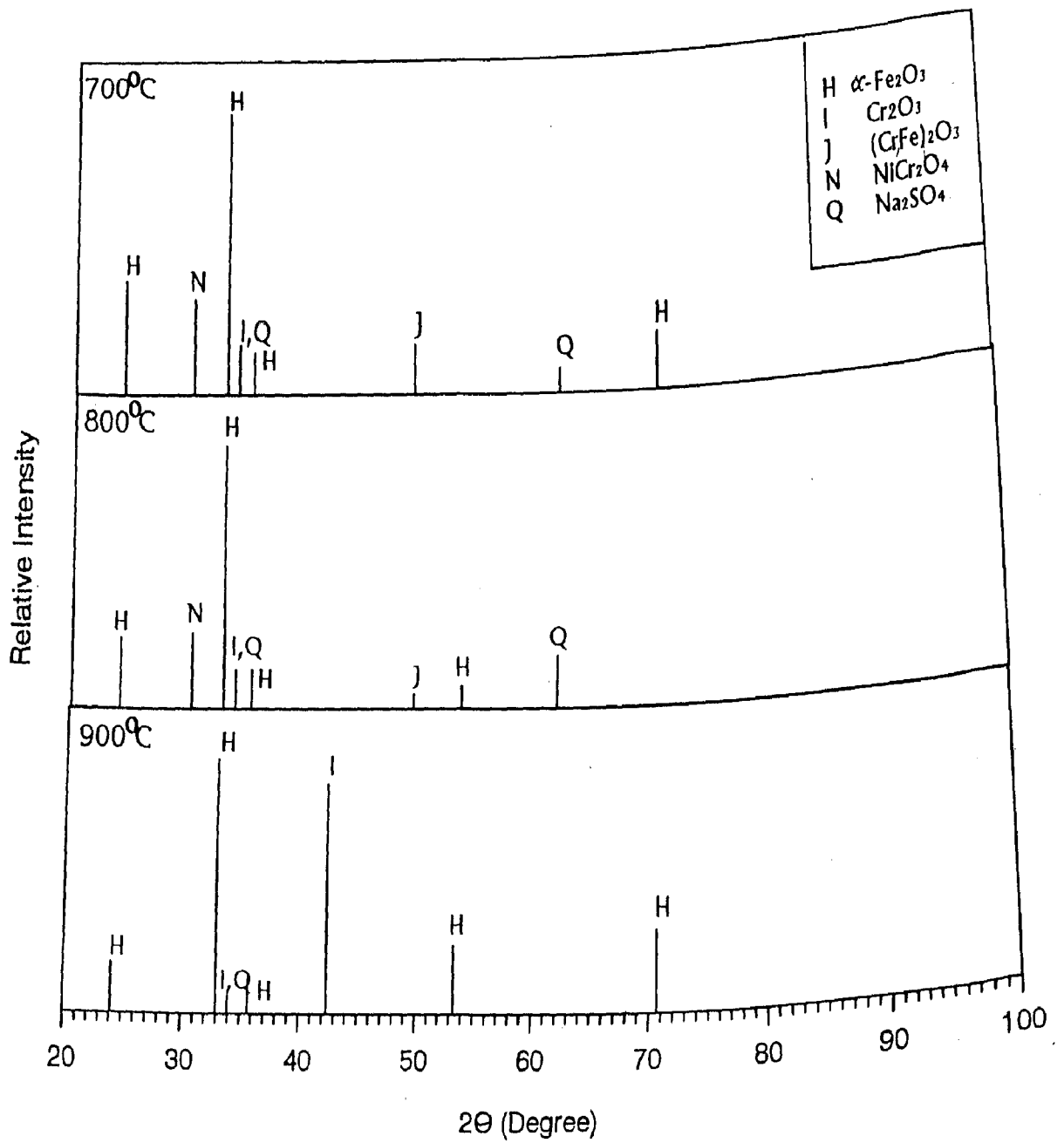


Fig. 5.31 : X-Ray Diffraction profile for alloy A (Superfer 800H) after hot corrosion at 700, 800 and 900 °C in pure Na₂SO₄.

Fig. 5.56 : SEM of alloy A (Superfer 800H) after cyclic hot corrosion in pure

Na₂SO₄ at

(a) 900°C, (X640)

(b) 800°C, (X640)

(c) 700°C, (X640)

Fig. 5.57 : SEM of alloy A (Superfer 800H) after cyclic hot corrosion in

Na₂SO₄-15%V₂O₅ at

(a) 900°C, (X640)

(b) 800°C, (X640)

(c) 700°C, (X640)

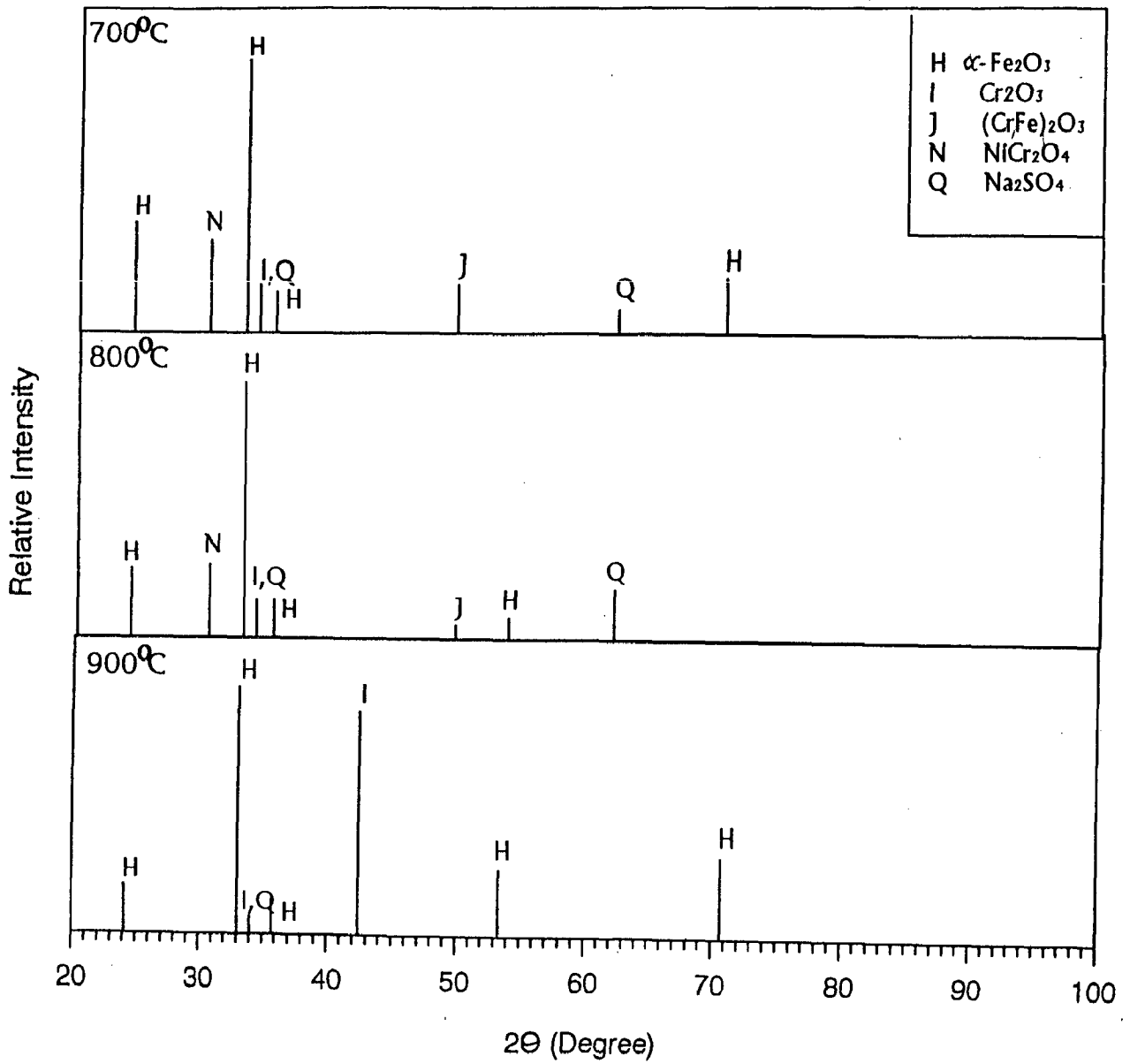


Fig. 5.31 : X-Ray Diffraction profile for alloy A (Superfer 800H) after hot corrosion at 700, 800 and 900 °C in pure Na₂SO₄.

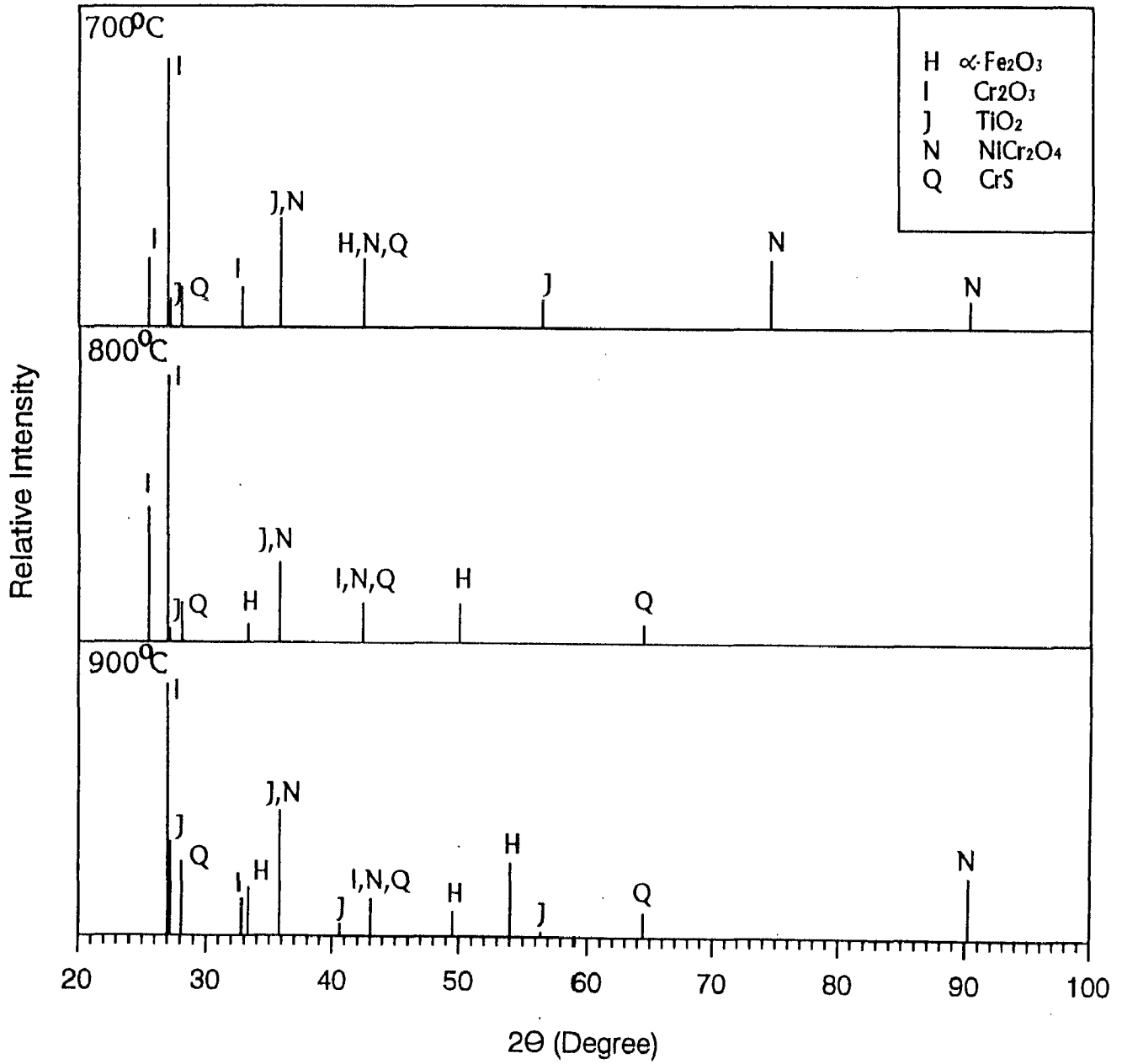


Fig. 5.34 : X-Ray Diffraction profile for alloy D (Superni 718) after hot corrosion at 700, 800 and 900°C in pure Na₂SO₄.

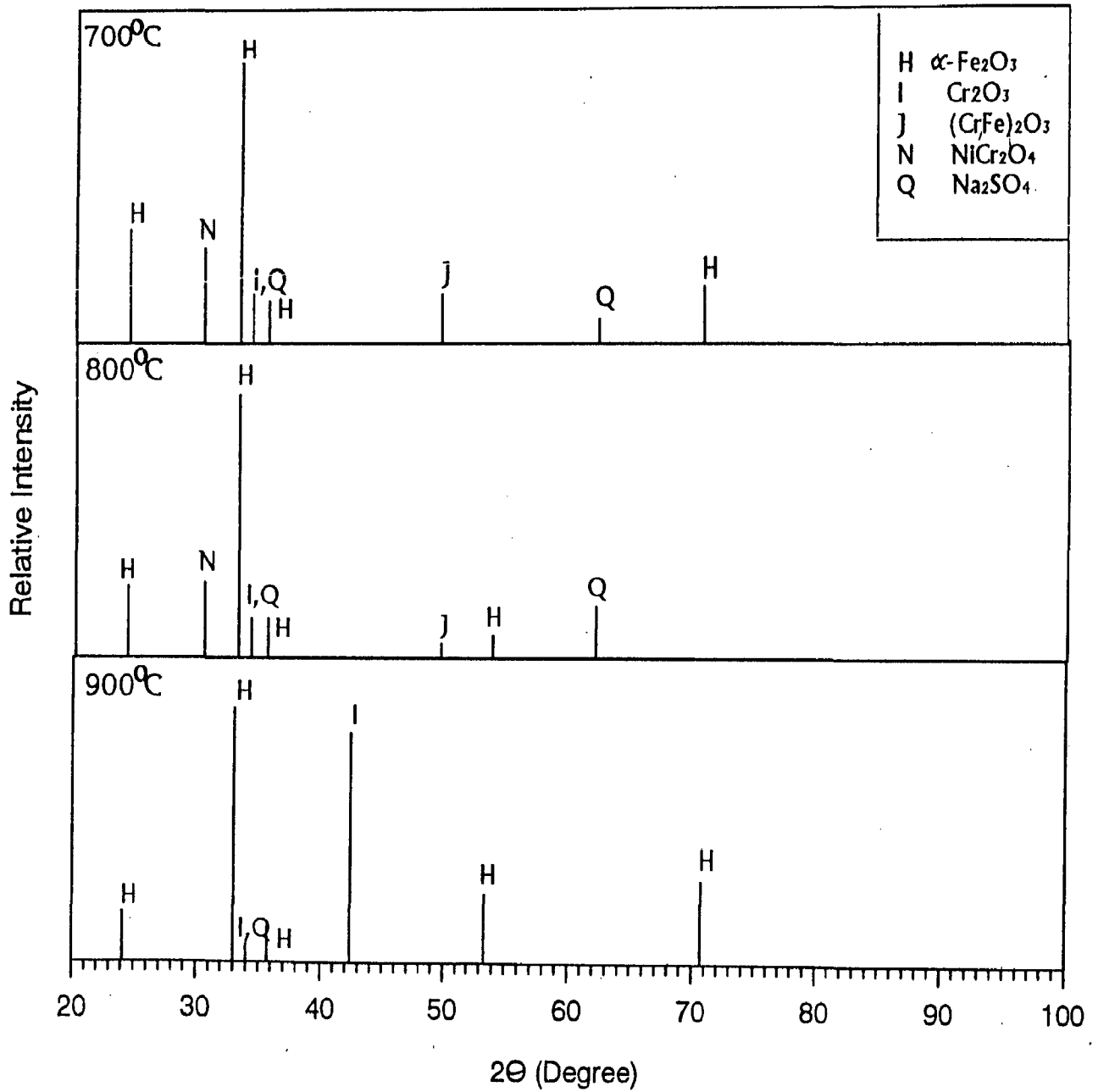


Fig. 5.31 : X-Ray Diffraction profile for alloy A (Superfer 800H) after hot corrosion at 700, 800 and 900 °C in pure Na₂SO₄.

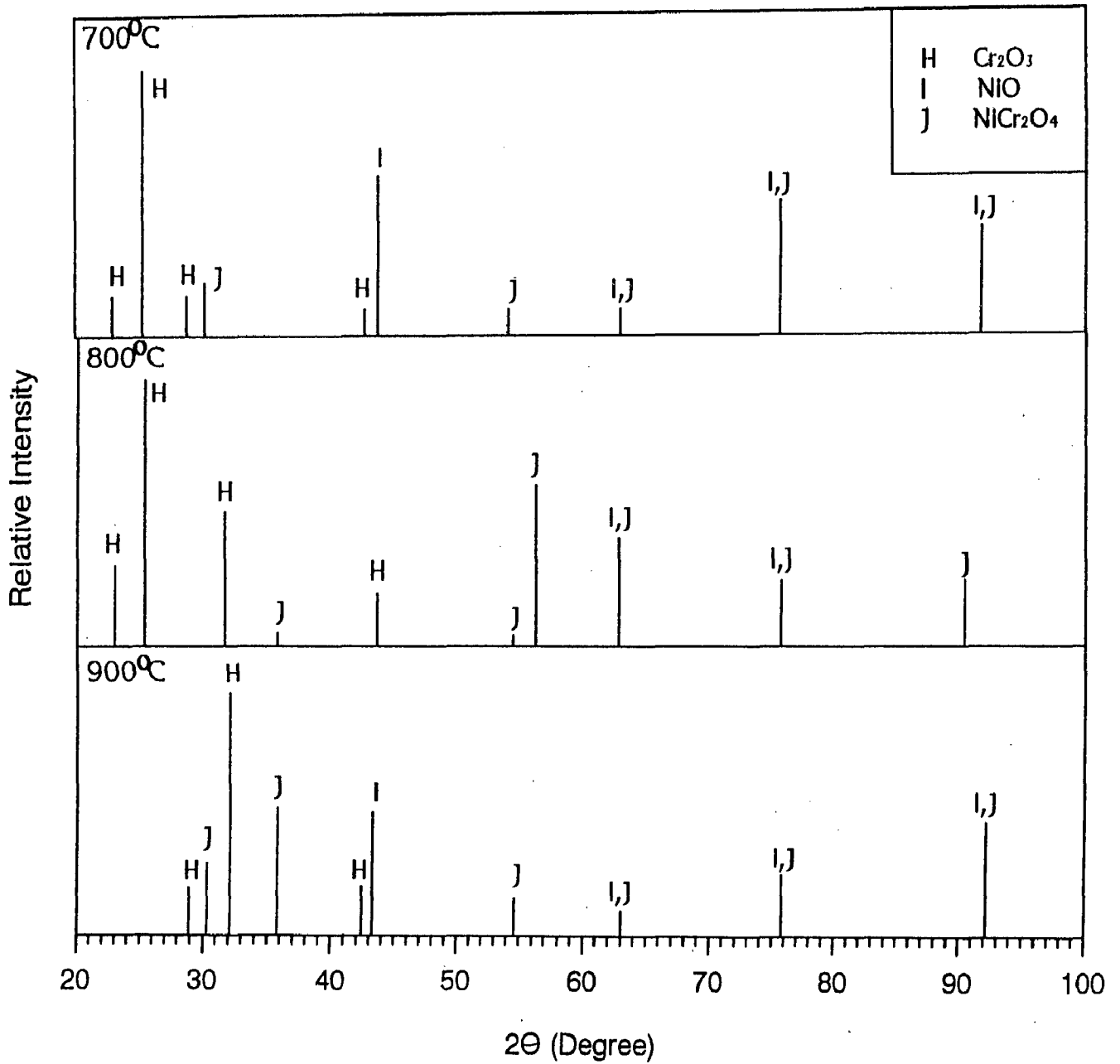


Fig. 5.32 : X-Ray Diffraction profile for alloy B (Superni 75) after hot corrosion at 700, 800 and 900 °C in pure Na₂SO₄.

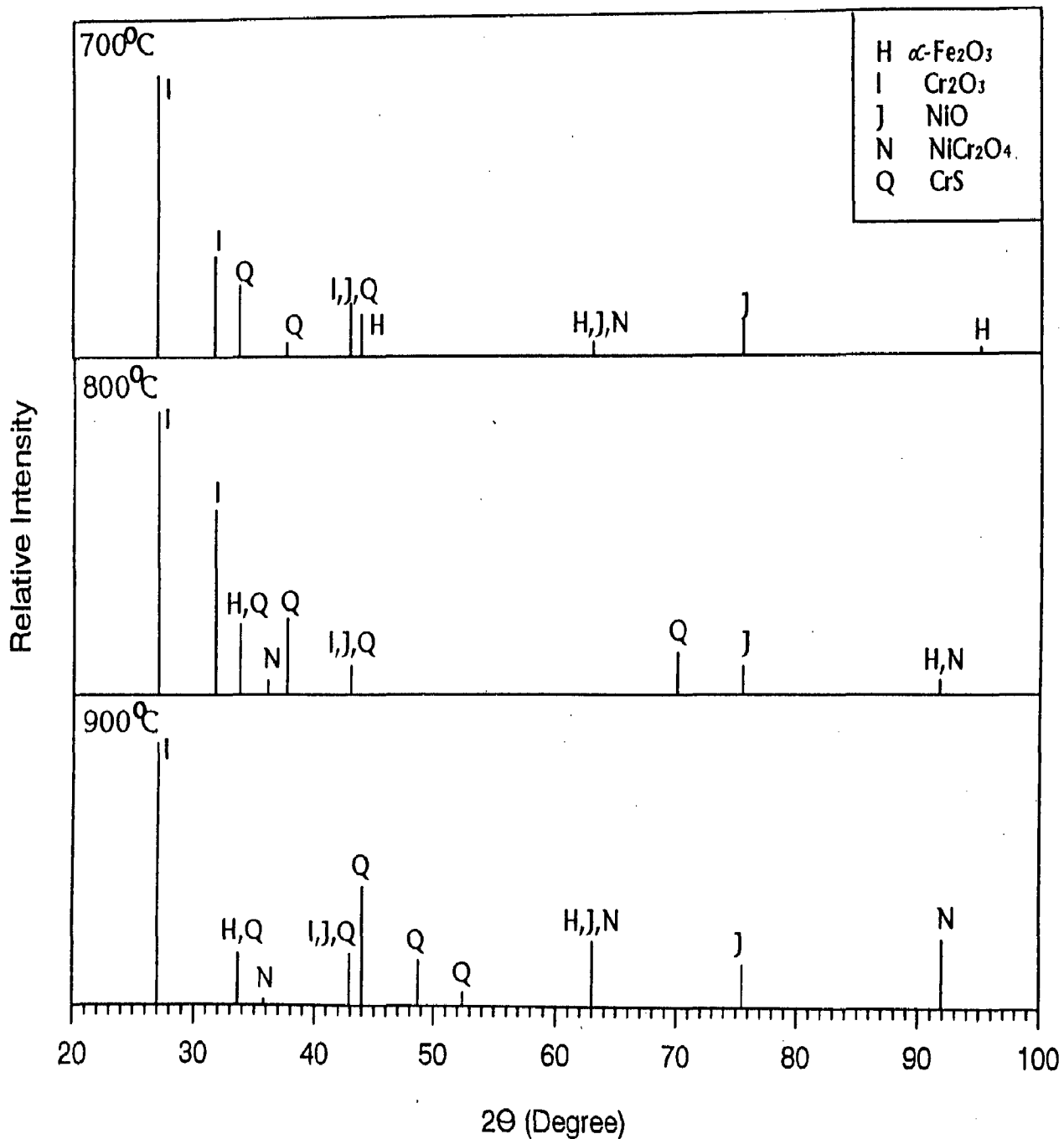


Fig. 5.33 : X-Ray Diffraction profile for alloy C (Superni 600) after hot corrosion at 700, 800 and 900°C in pure Na₂SO₄.

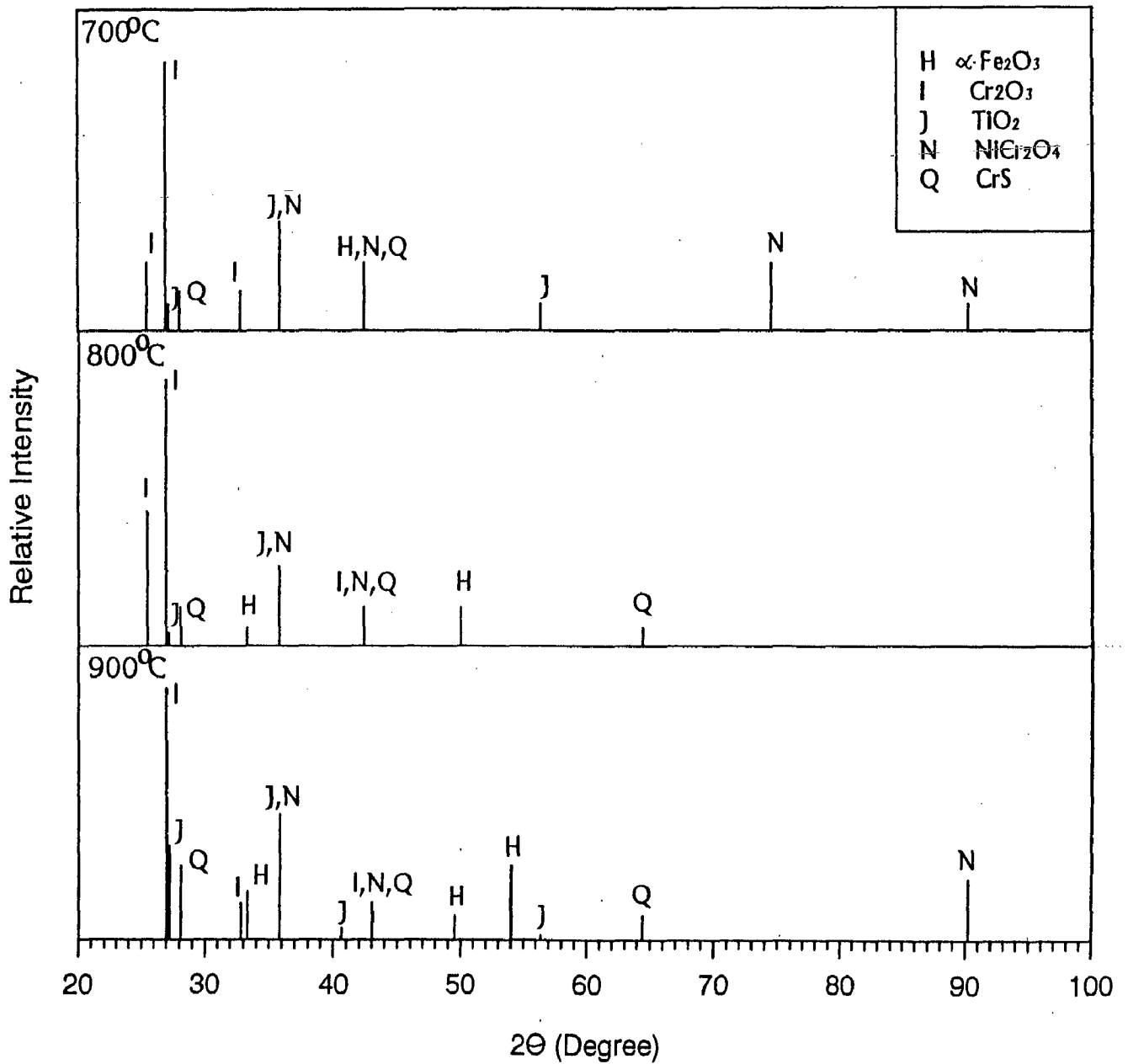


Fig. 5.34 : X-Ray Diffraction profile for alloy D (Superni 718) after hot corrosion at 700, 800 and 900°C in pure Na₂SO₄.

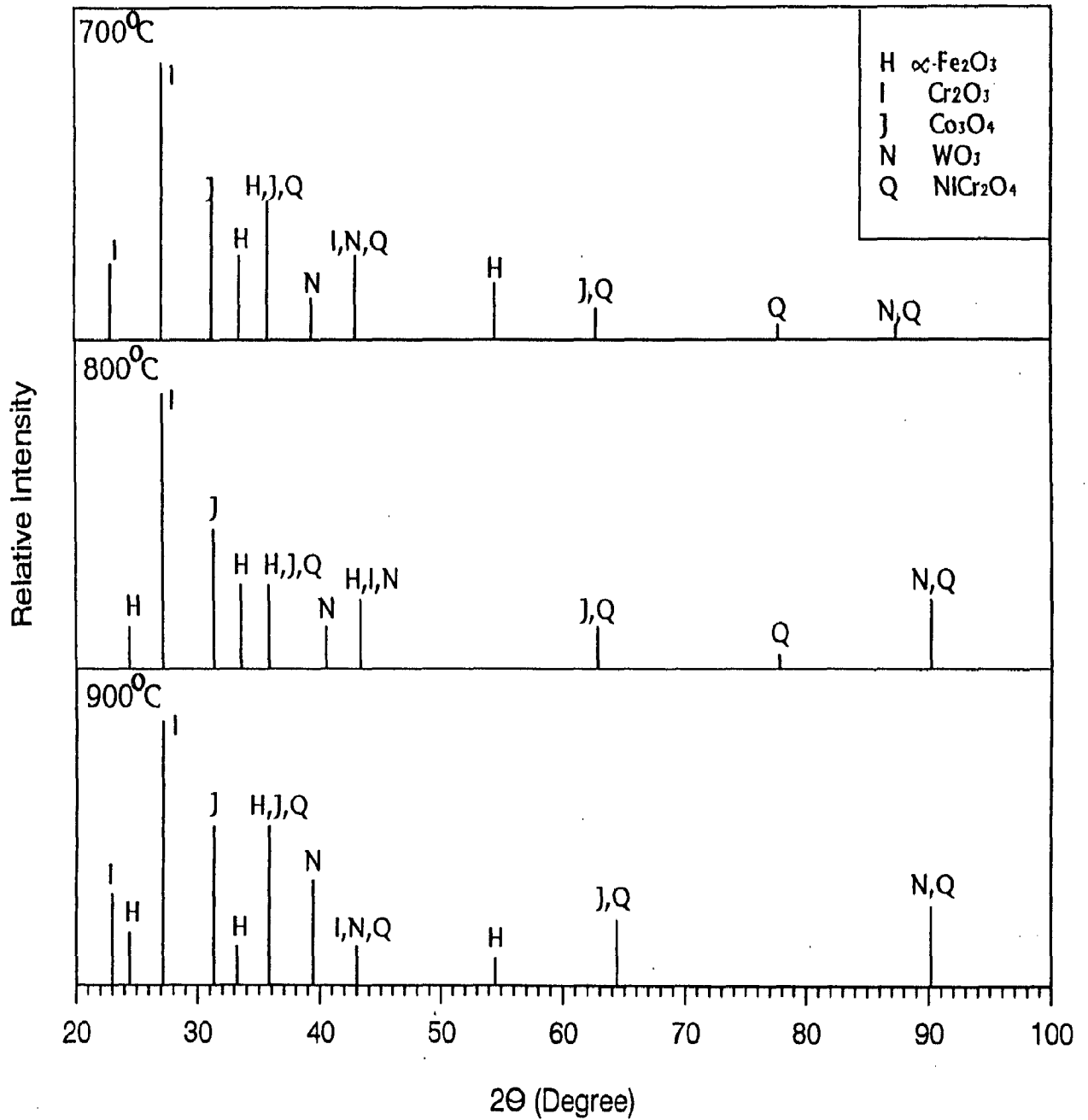


Fig. 5.35 : X-Ray Diffraction profile for alloy E (Superco 605) after hot corrosion at 700, 800 and 900°C in pure Na₂SO₄.

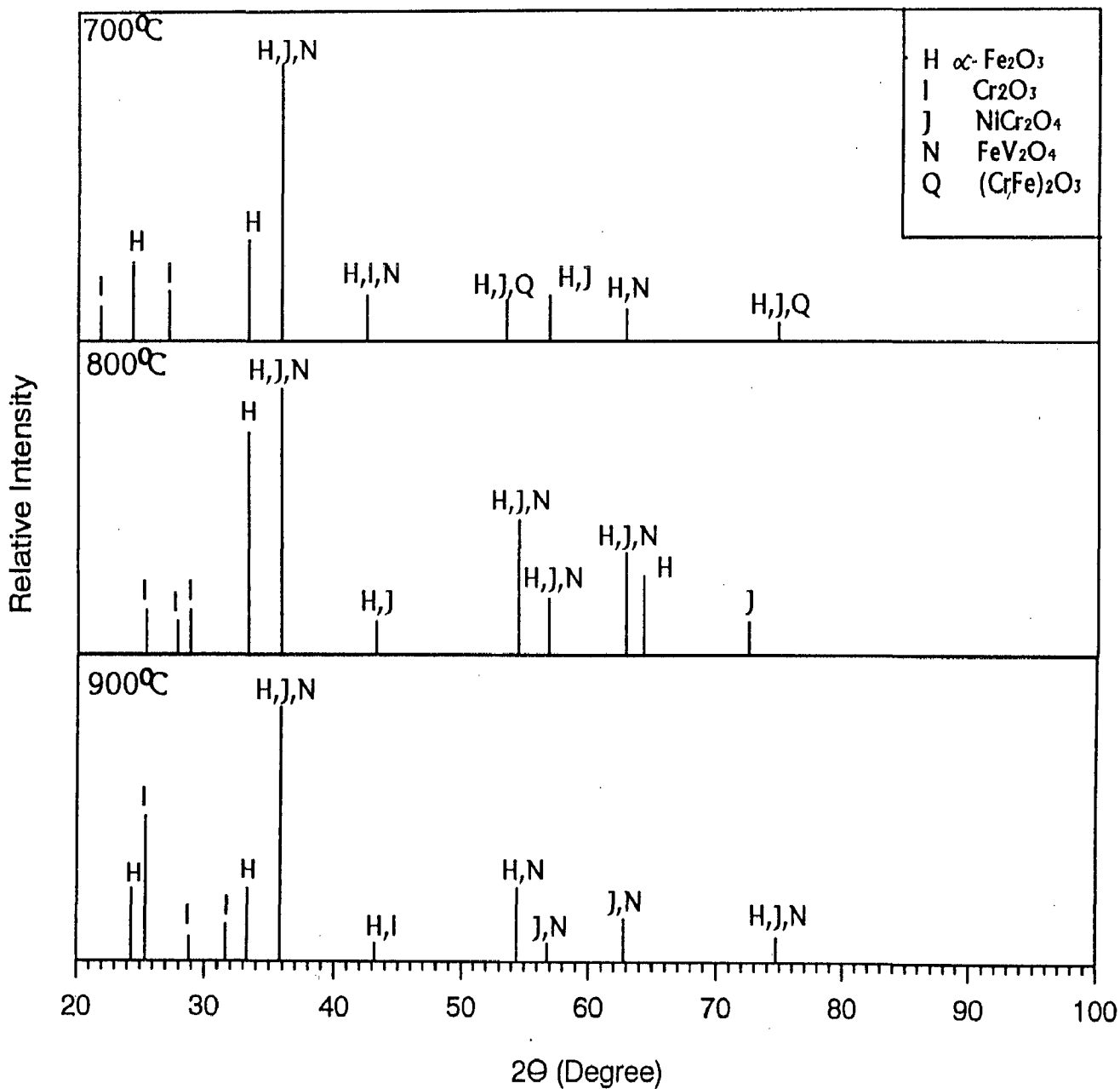


Fig. 5.36 : X-Ray Diffraction profile for alloy A (Superfer 800H) after hot corrosion at 700, 800 and 900 °C in Na₂SO₄-15% V₂O₅

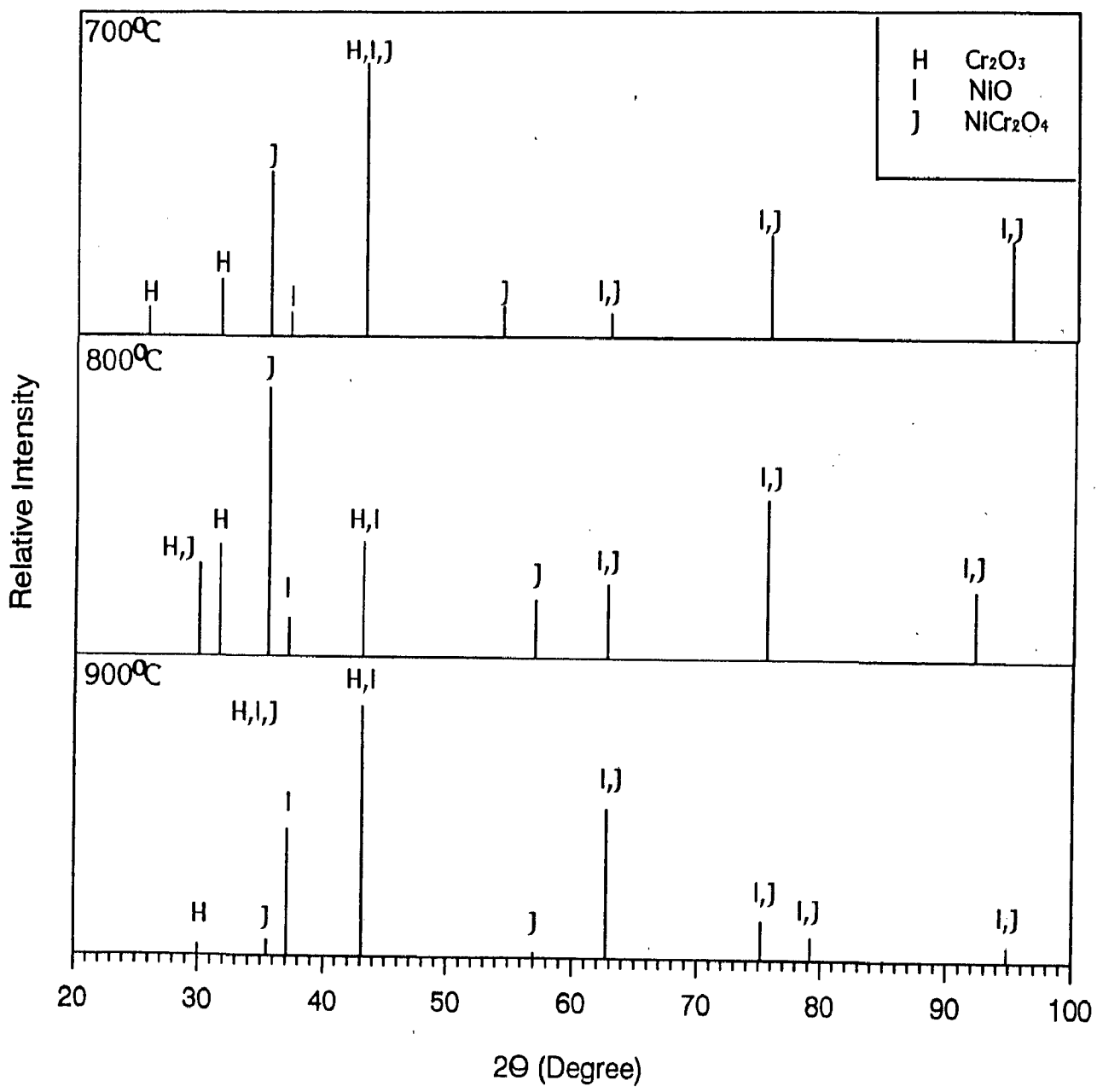


Fig. 5.37 : X-Ray Diffraction profile for alloy B (Superni 75) after hot corrosion at 700, 800 and 900 °C in Na₂SO₄-15% V₂O₅

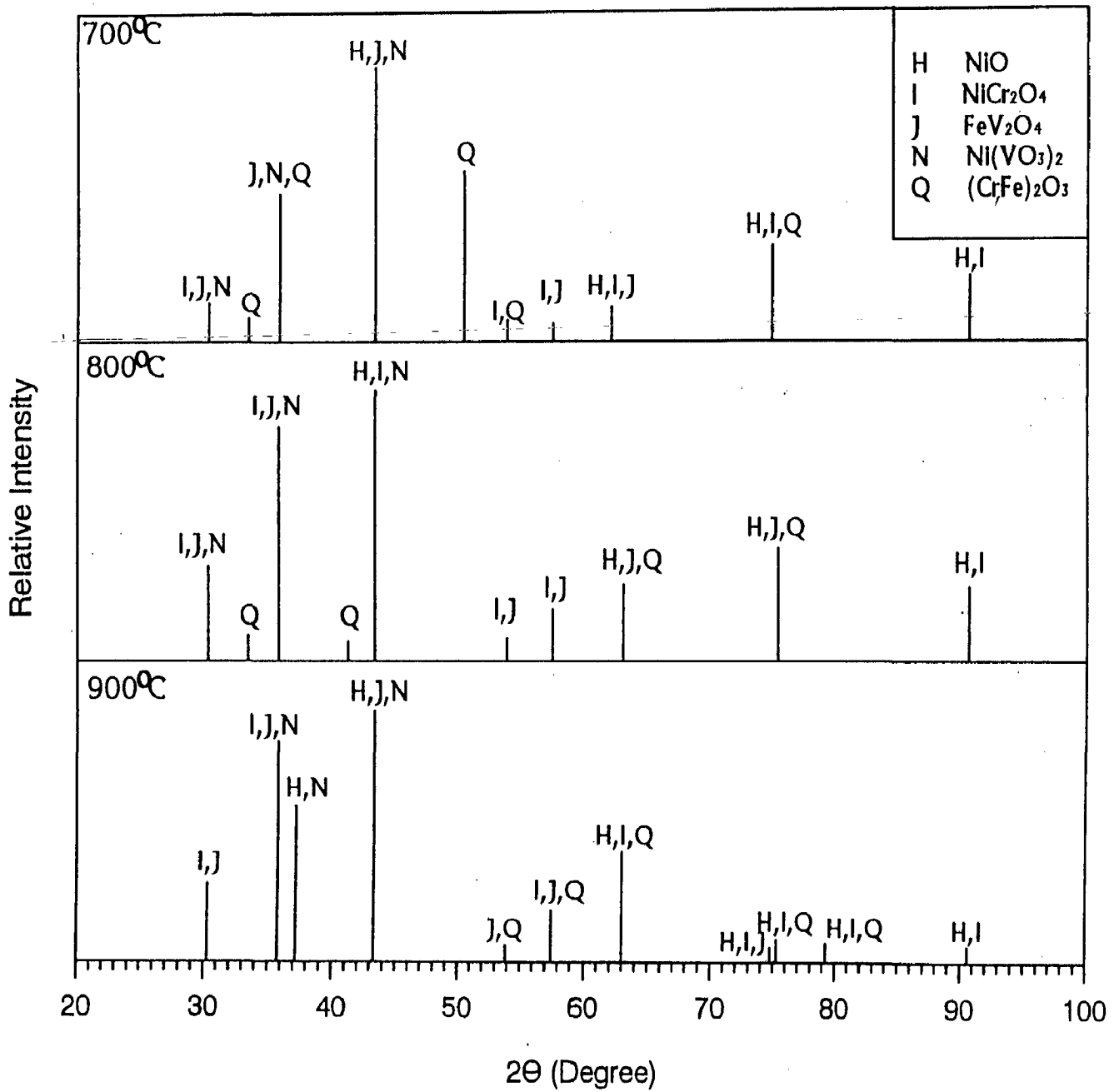


Fig. 5.38 : X-Ray Diffraction profile for alloy C (Superni 600) after hot corrosion at 700, 800 and 900 °C in Na₂SO₄-15% V₂O₅

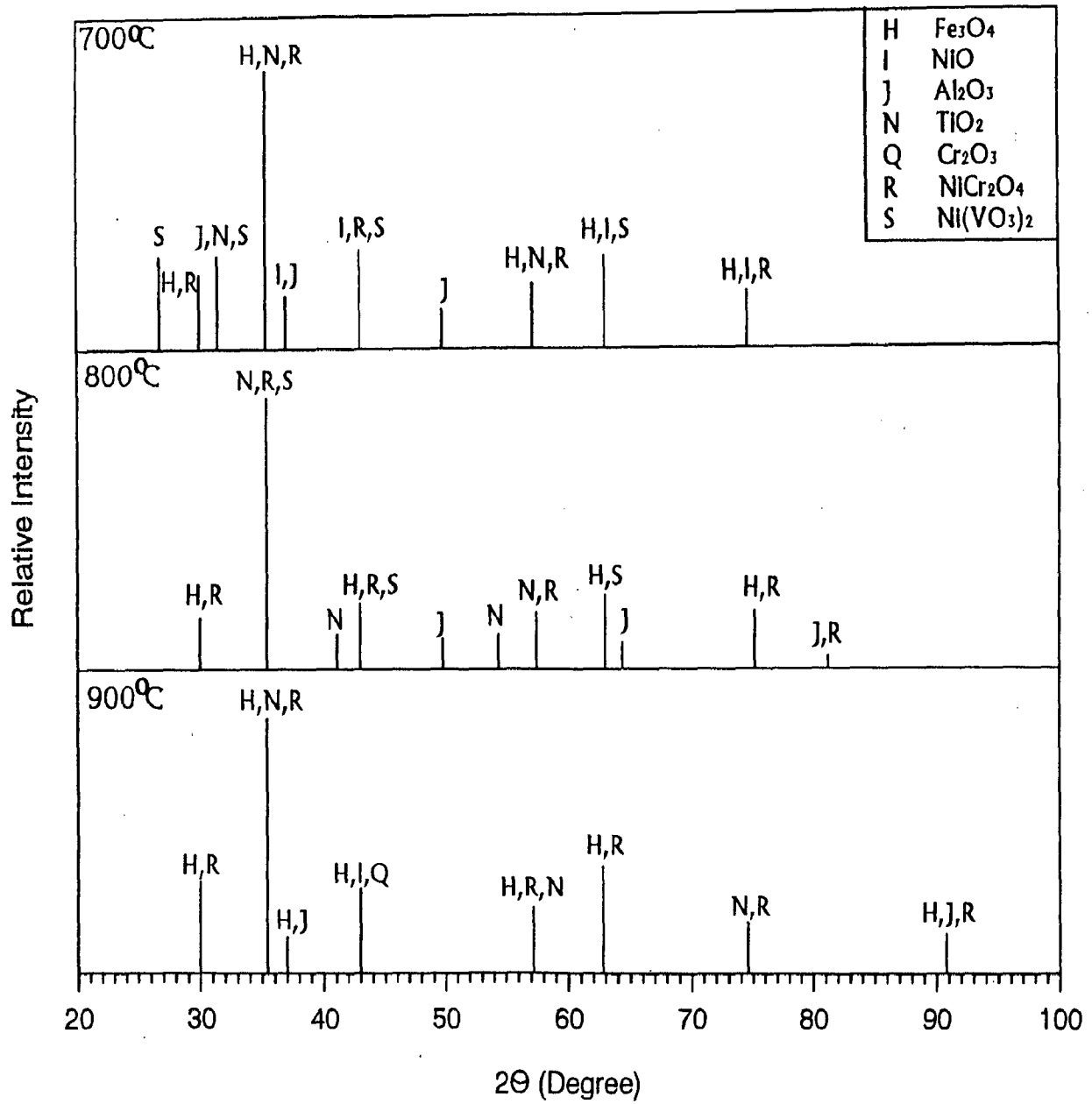


Fig. 5.39 : X-Ray Diffraction profile for alloy D (Superni 718) after hot corrosion at 700, 800 and 900 °C in Na₂SO₄-15% V₂O₅

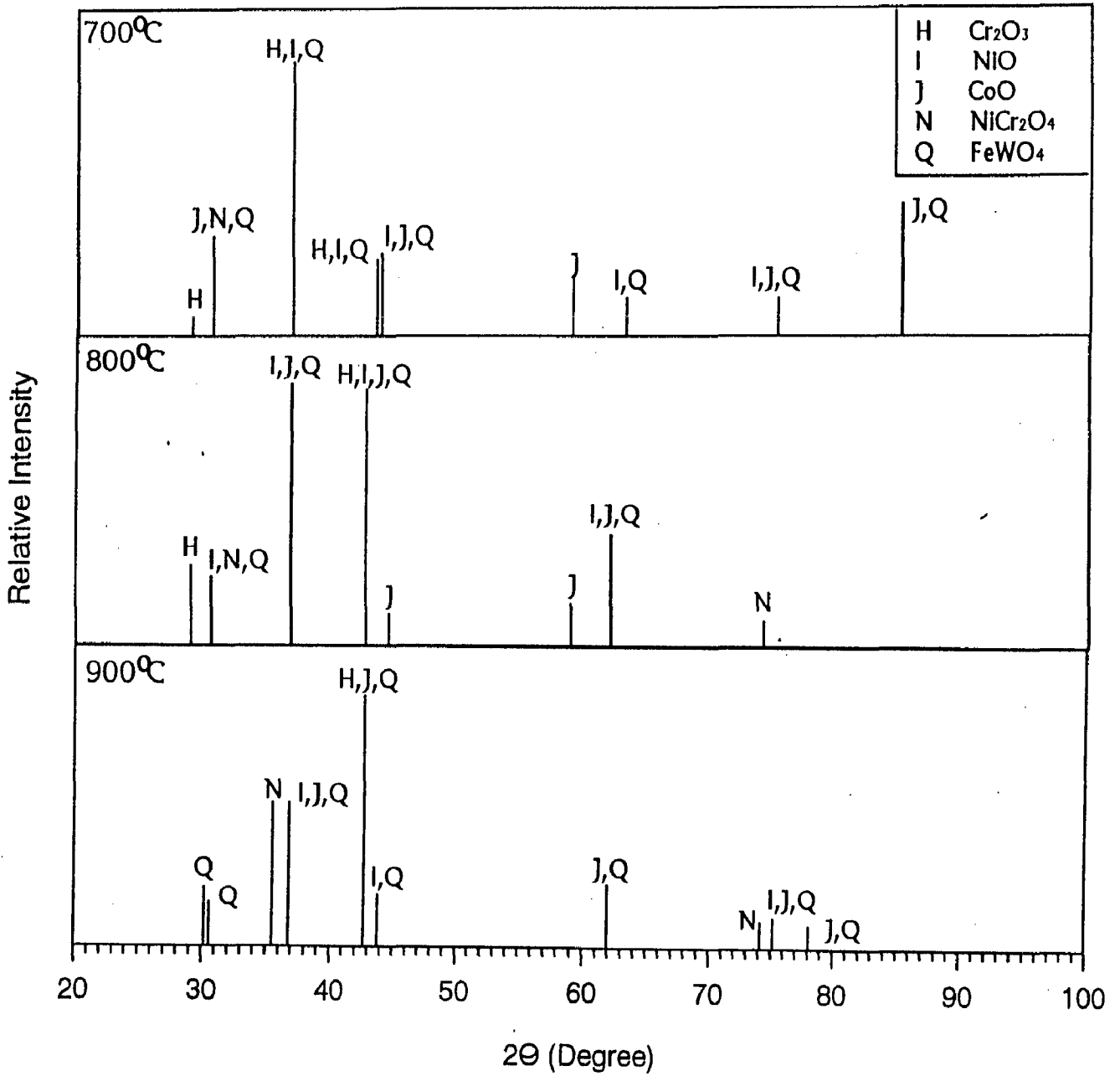


Fig. 5.40 : X-Ray Diffraction profile for alloy E (Supercor 605) after hot corrosion at 700, 800 and 900 °C in Na₂SO₄-15% V₂O₅

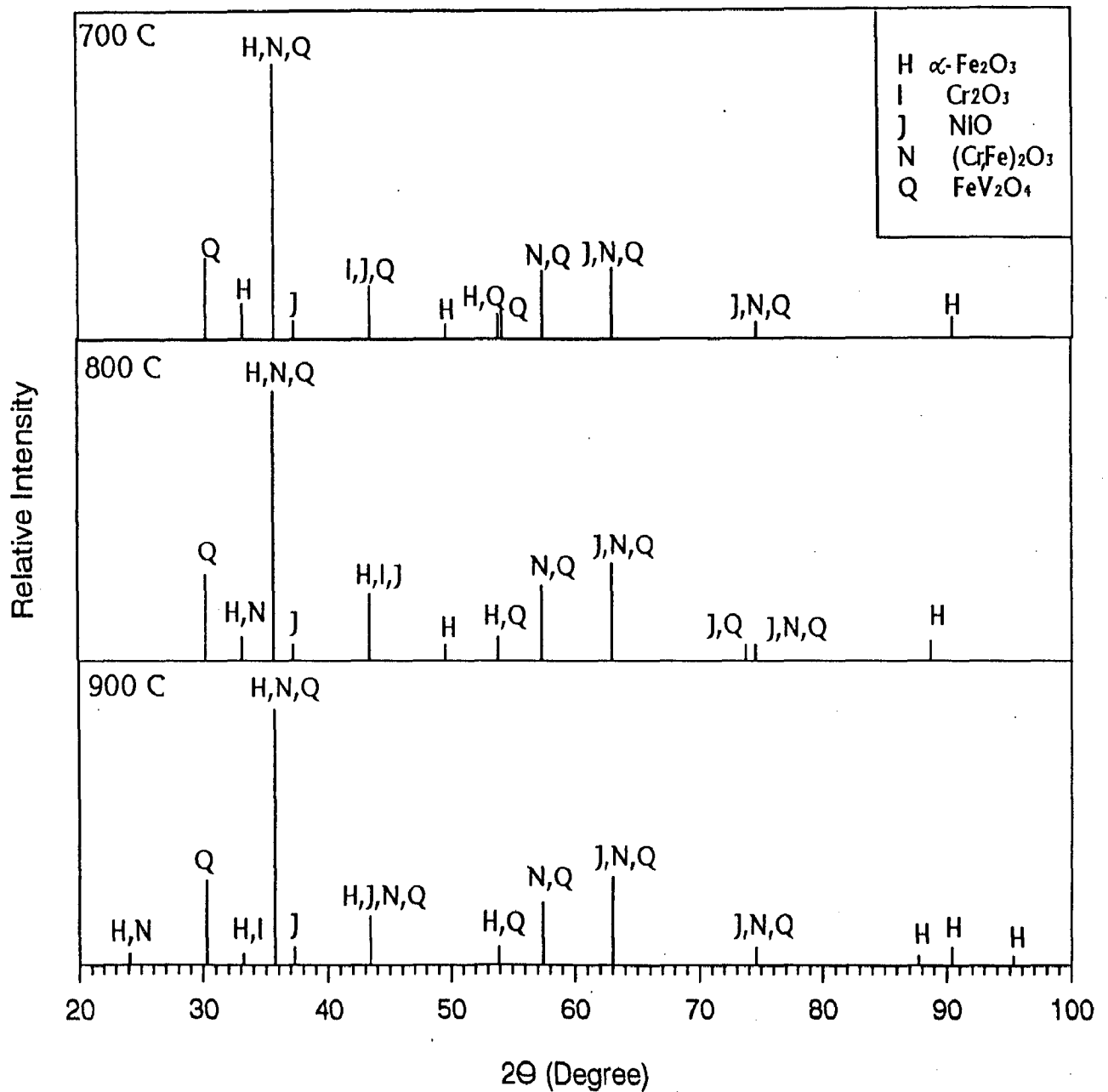


Fig. 5.41 : X-Ray Diffraction profile for alloy A (Superfer 800H) after hot corrosion at 700, 800 and 900 °C in Na₂SO₄-60% V₂O₅

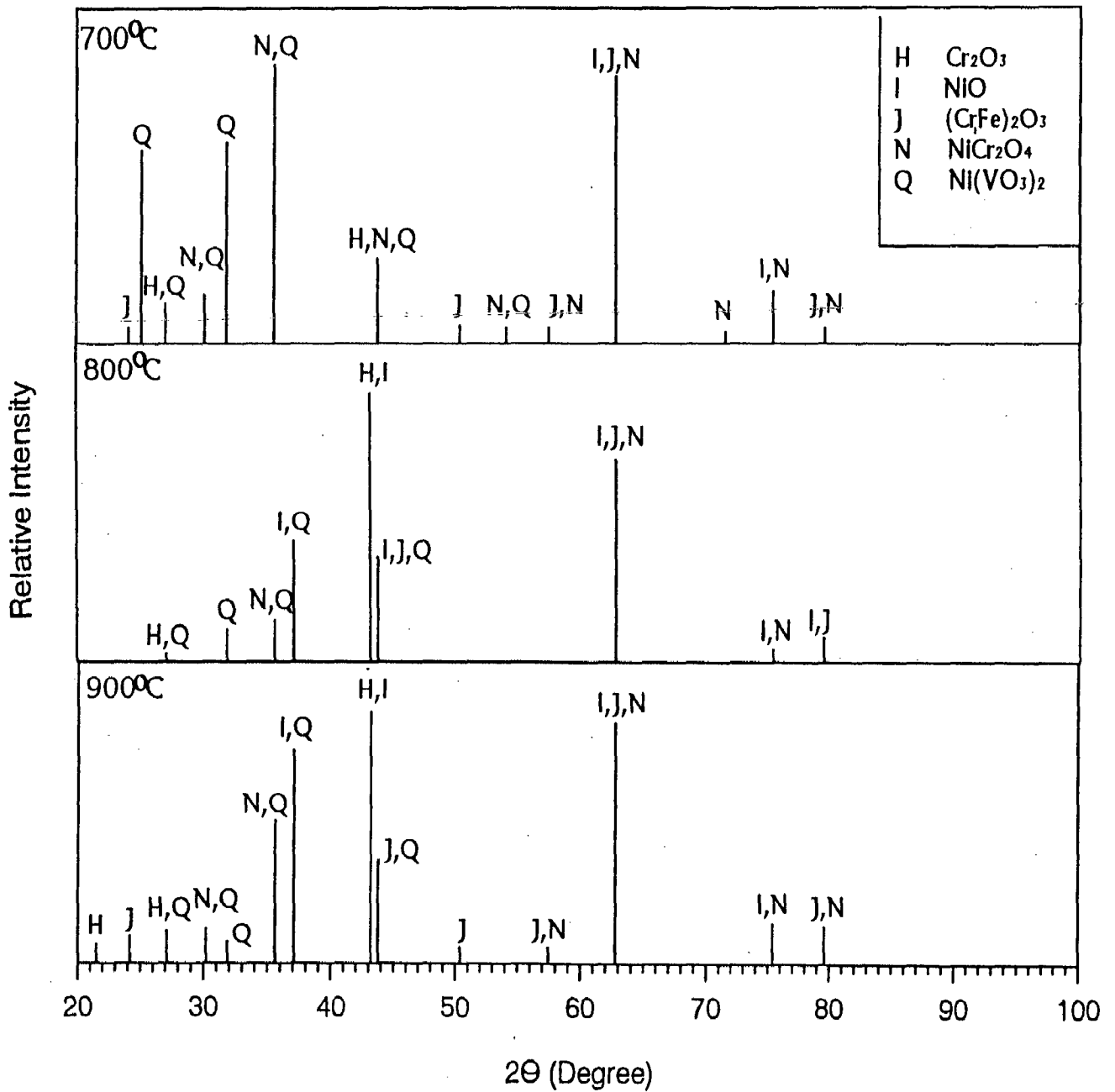


Fig. 5.42 : X-Ray Diffraction profile for alloy B (Superni 75) after hot corrosion at 700, 800 and 900 °C in Na₂SO₄-60% V₂O₅

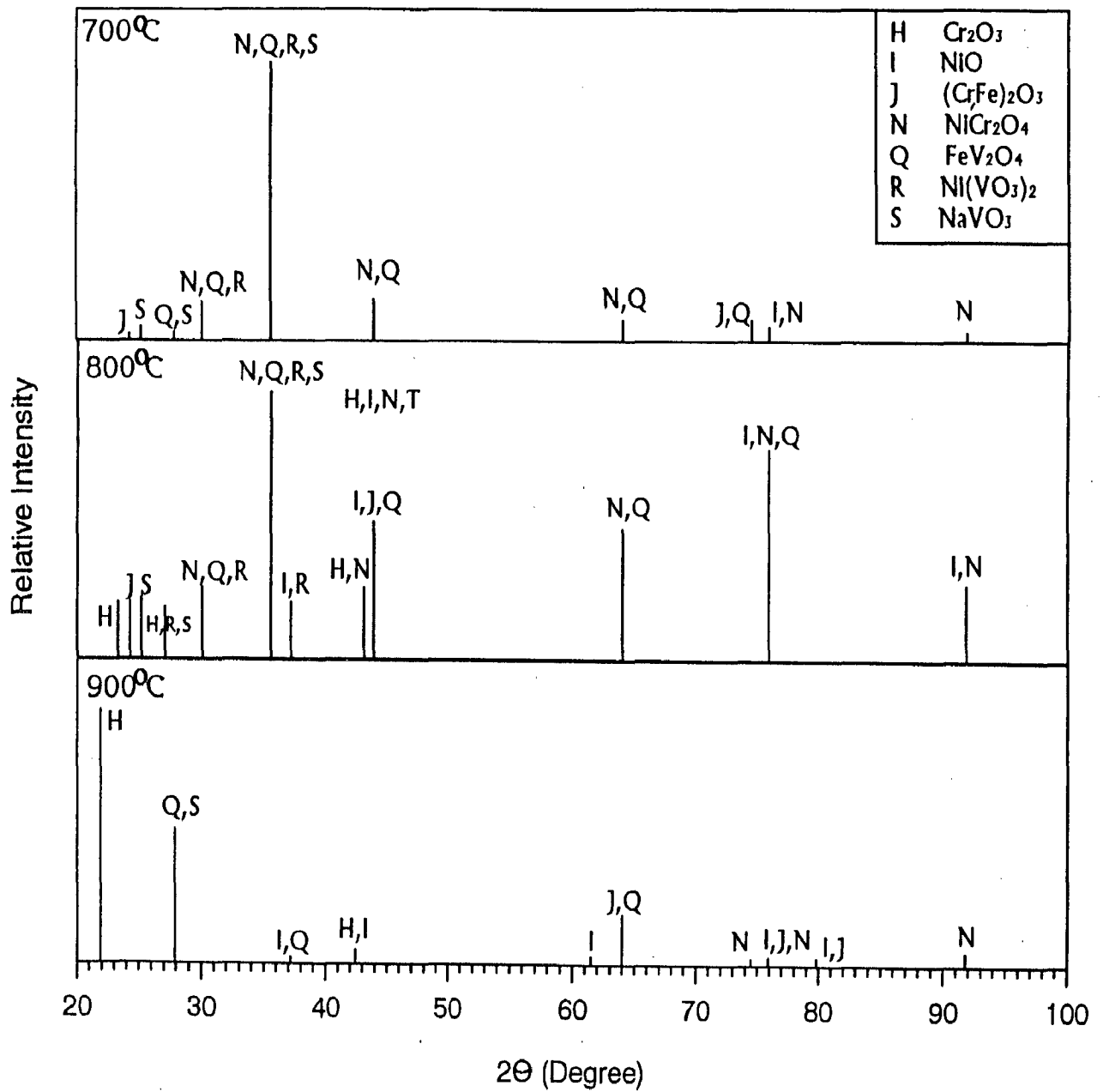


Fig. 5.43 : X-Ray Diffraction profile for alloy C (Superni 600) after hot corrosion at 700, 800 and 900 °C in Na₂SO₄-60% V₂O₅

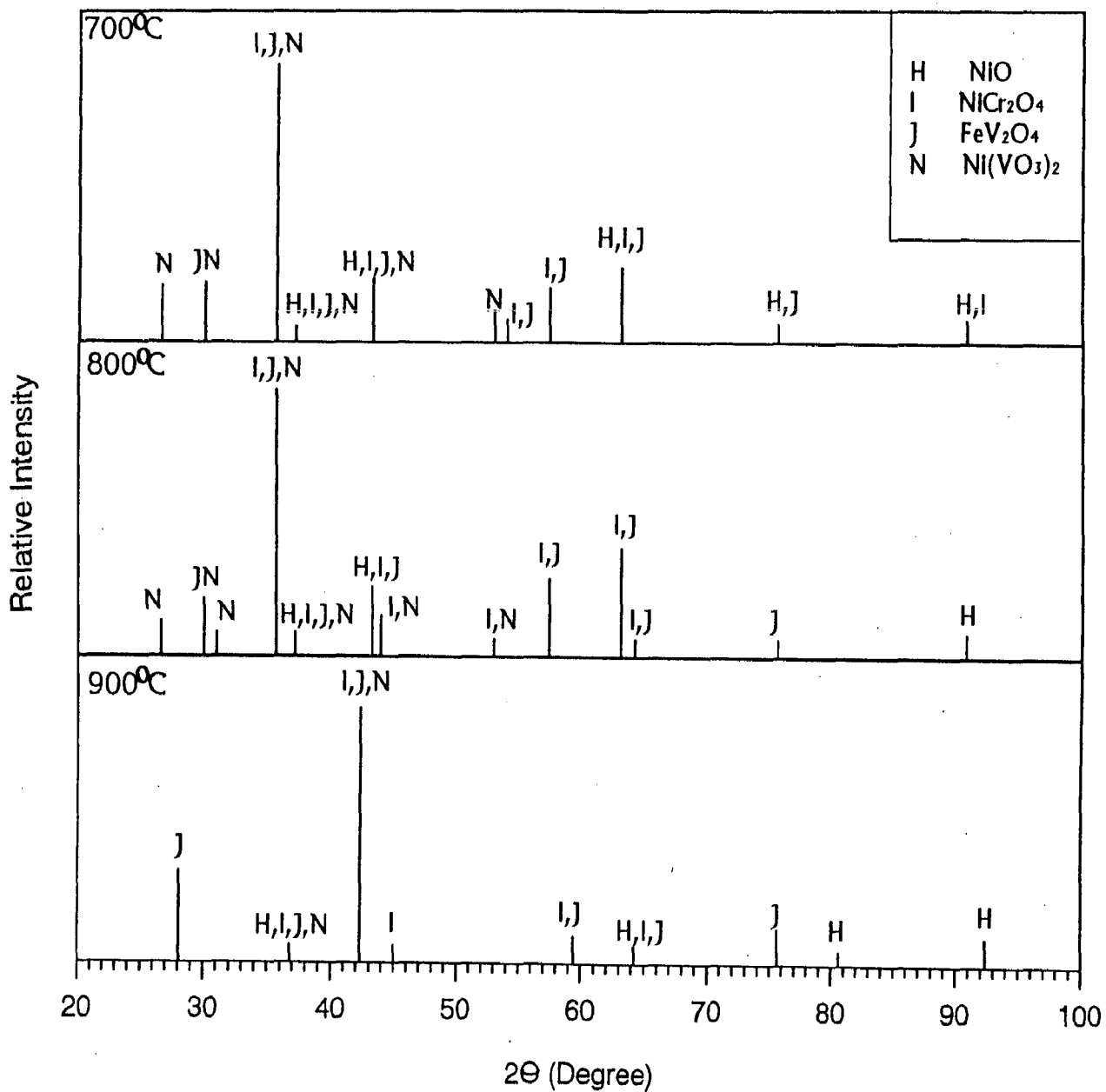


Fig. 5.44 : X-Ray Diffraction profile for alloy D (Superni 718) after hot corrosion at 700, 800 and 900 °C in Na₂SO₄-60% V₂O₅

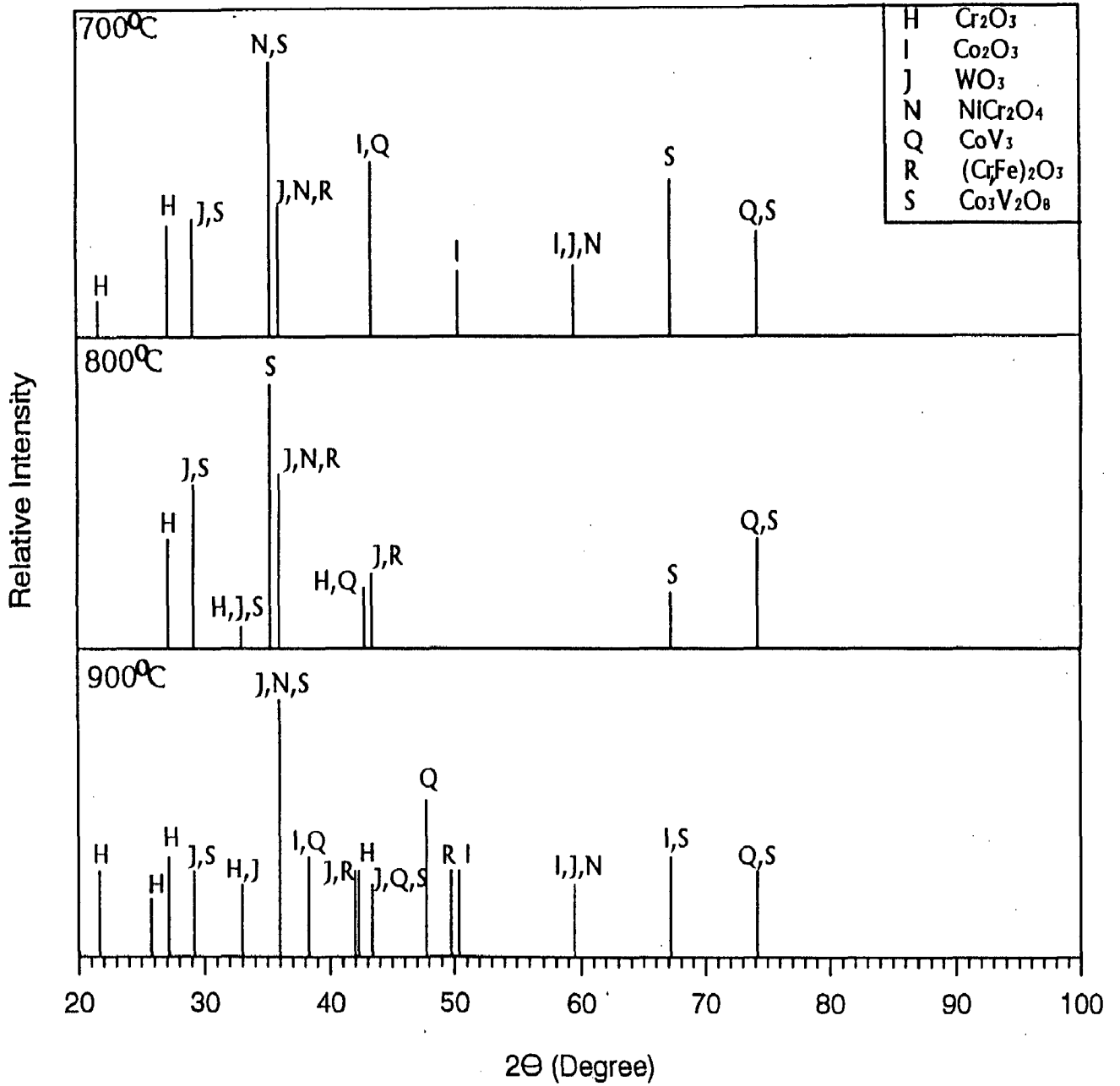


Fig. 5.45 : X-Ray Diffraction profile for alloy E (Superco 605) after hot corrosion at 700, 800 and 900 °C in Na₂SO₄-60% V₂O₅

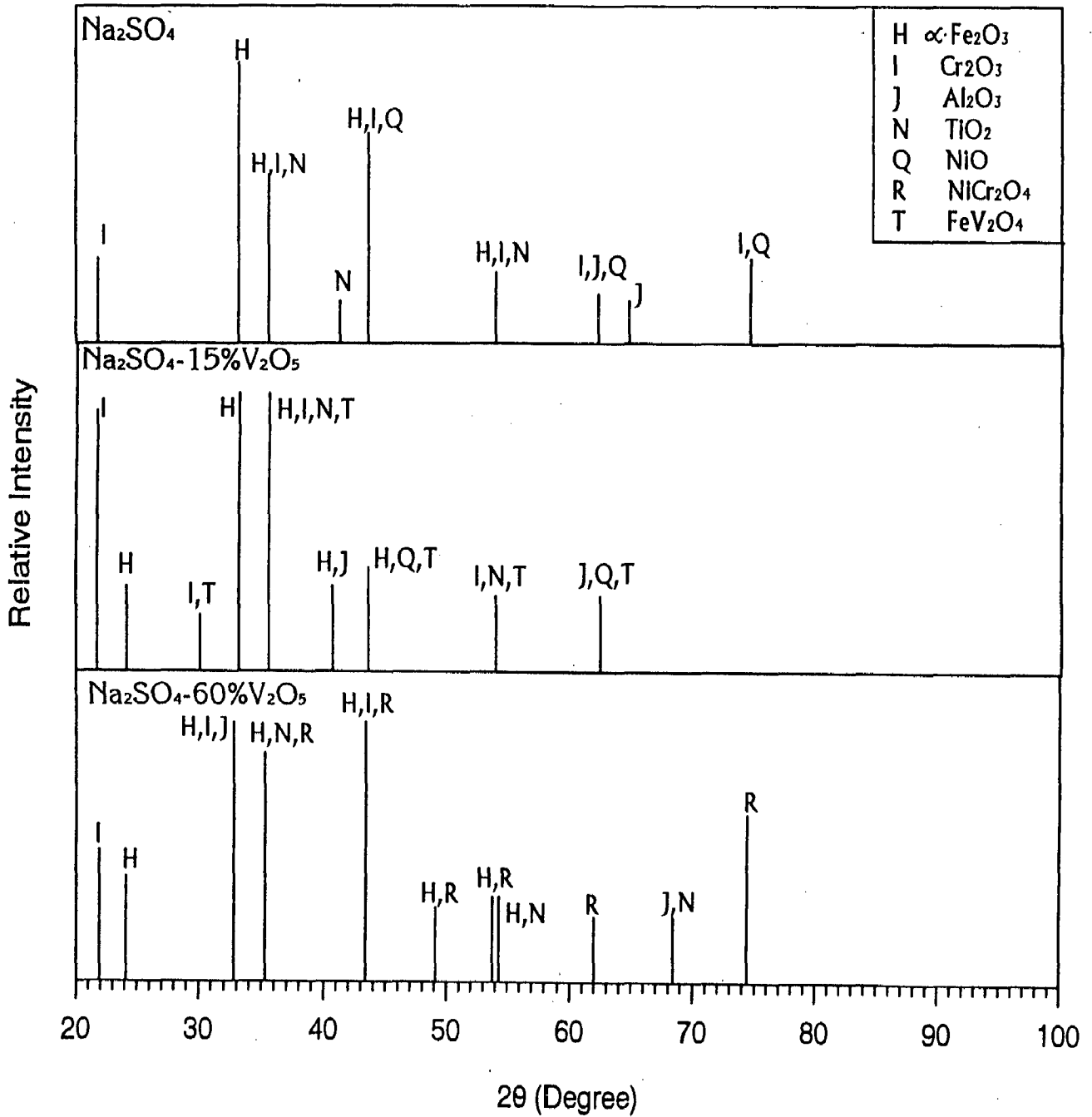


Fig. 5.46 : X-Ray Diffraction profile for alloy A (Superfer 800H) after hot corrosion at 1100°C in industrial Atmosphere.

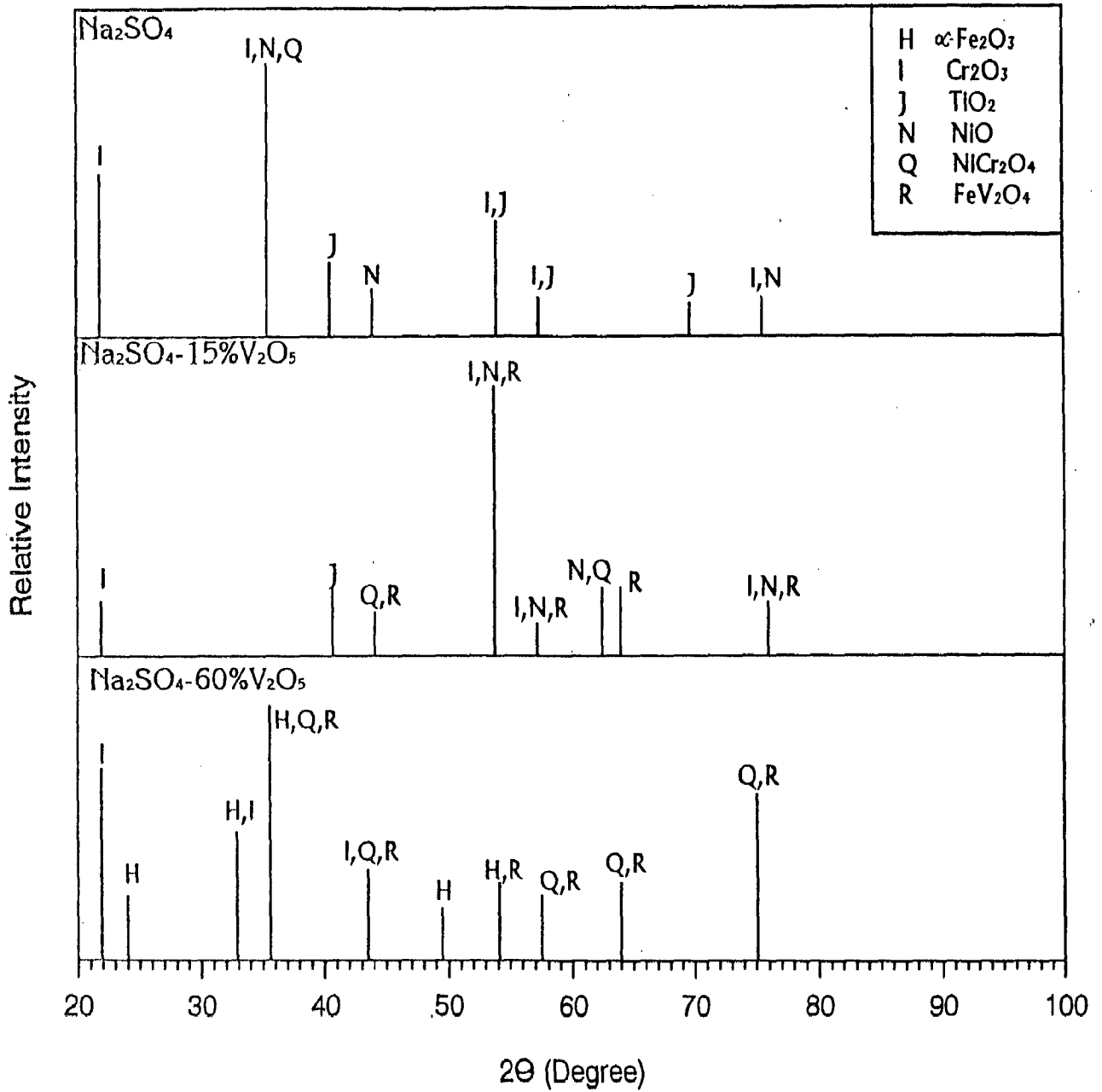


Fig. 5.47 : X-Ray Diffraction profile for alloy B (Superni 75) after hot corrosion at 1100°C in industrial atmosphere.

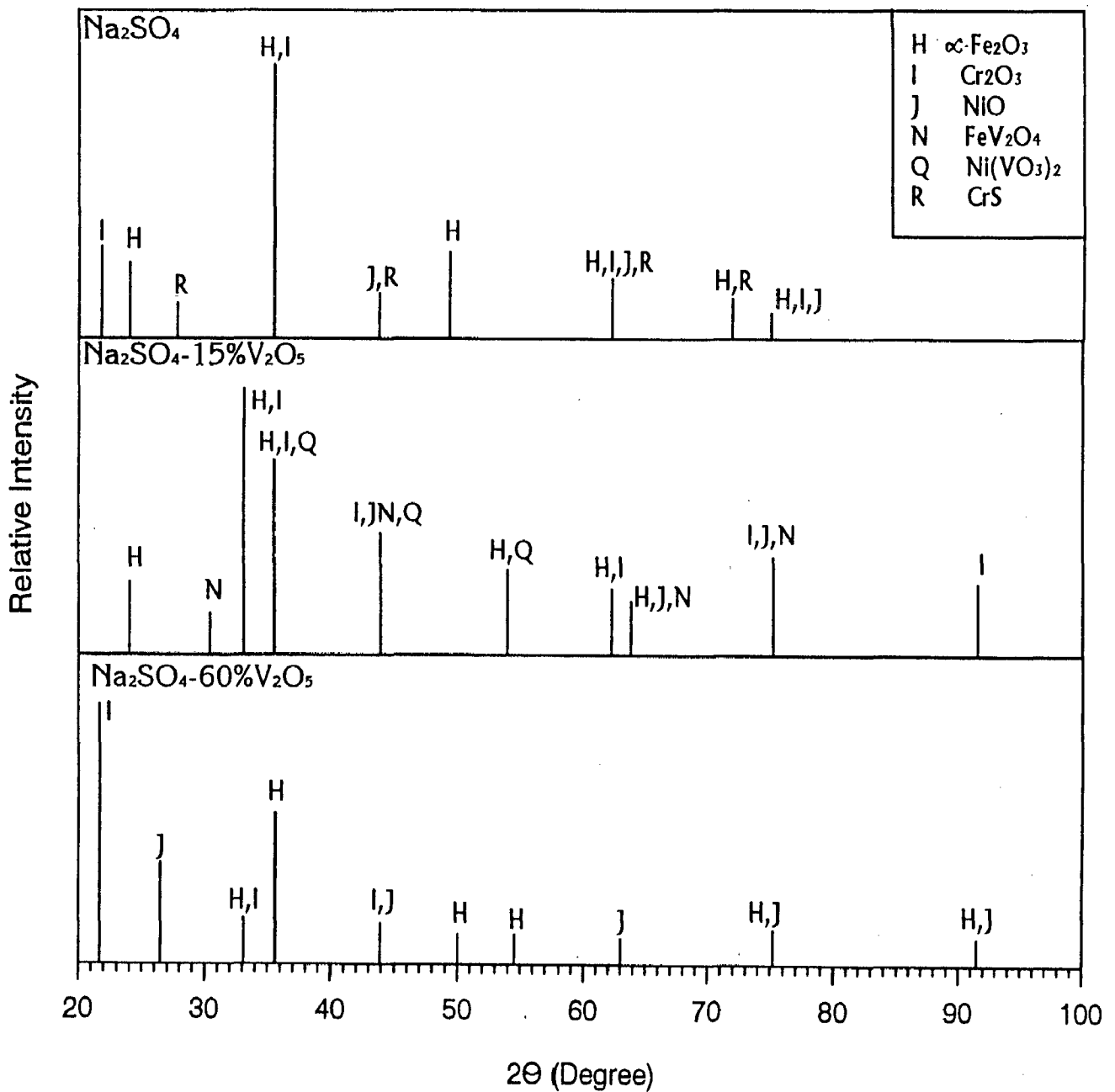


Fig. 5.48 : X-Ray Diffraction profile for alloy C (Superni 600) after hot corrosion at 1100°C in industrial atmosphere.

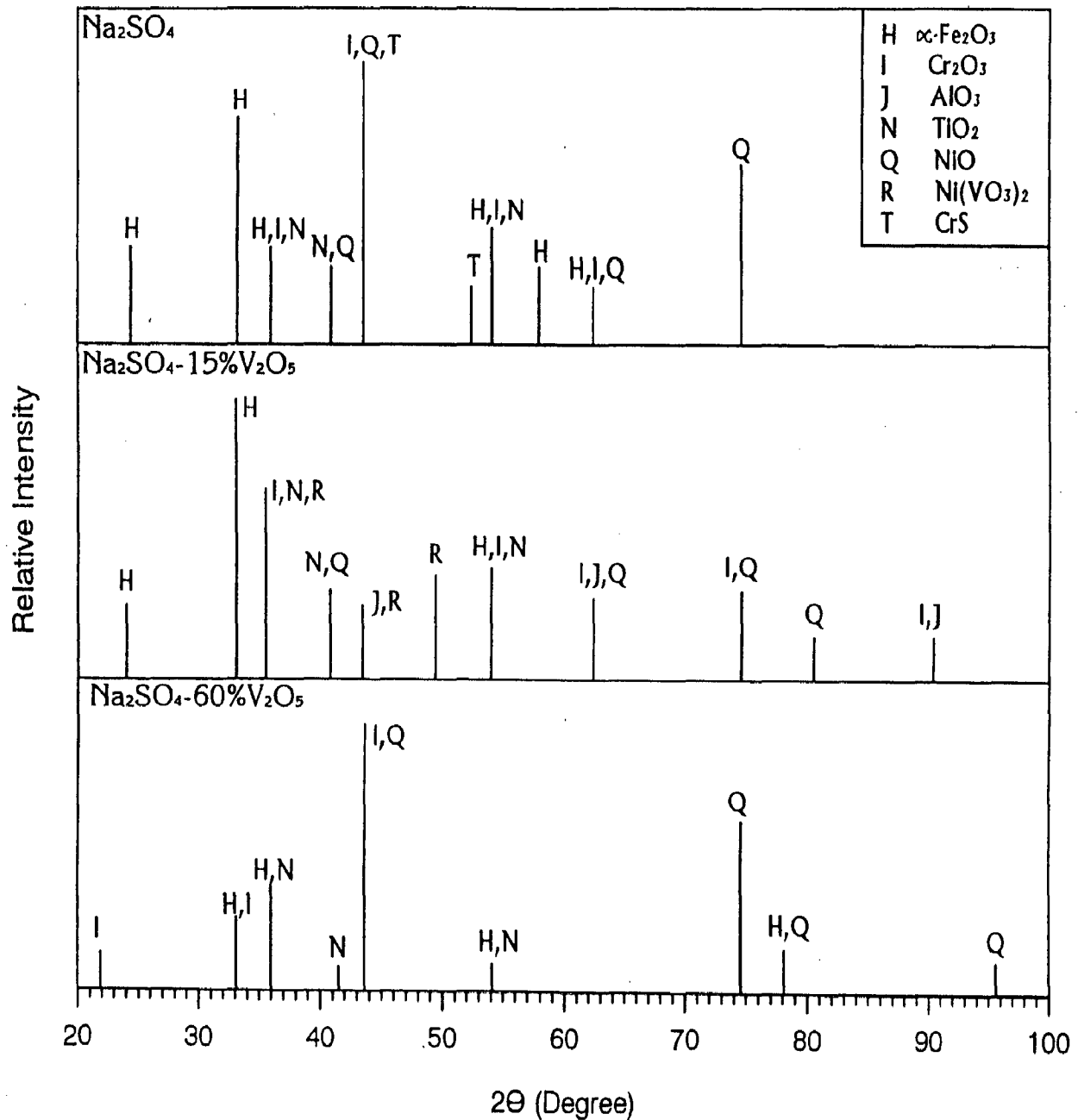


Fig. 5.49 : X-Ray Diffraction profile for alloy D (Superni 718) after hot corrosion at 1100°C in industrial atmosphere.

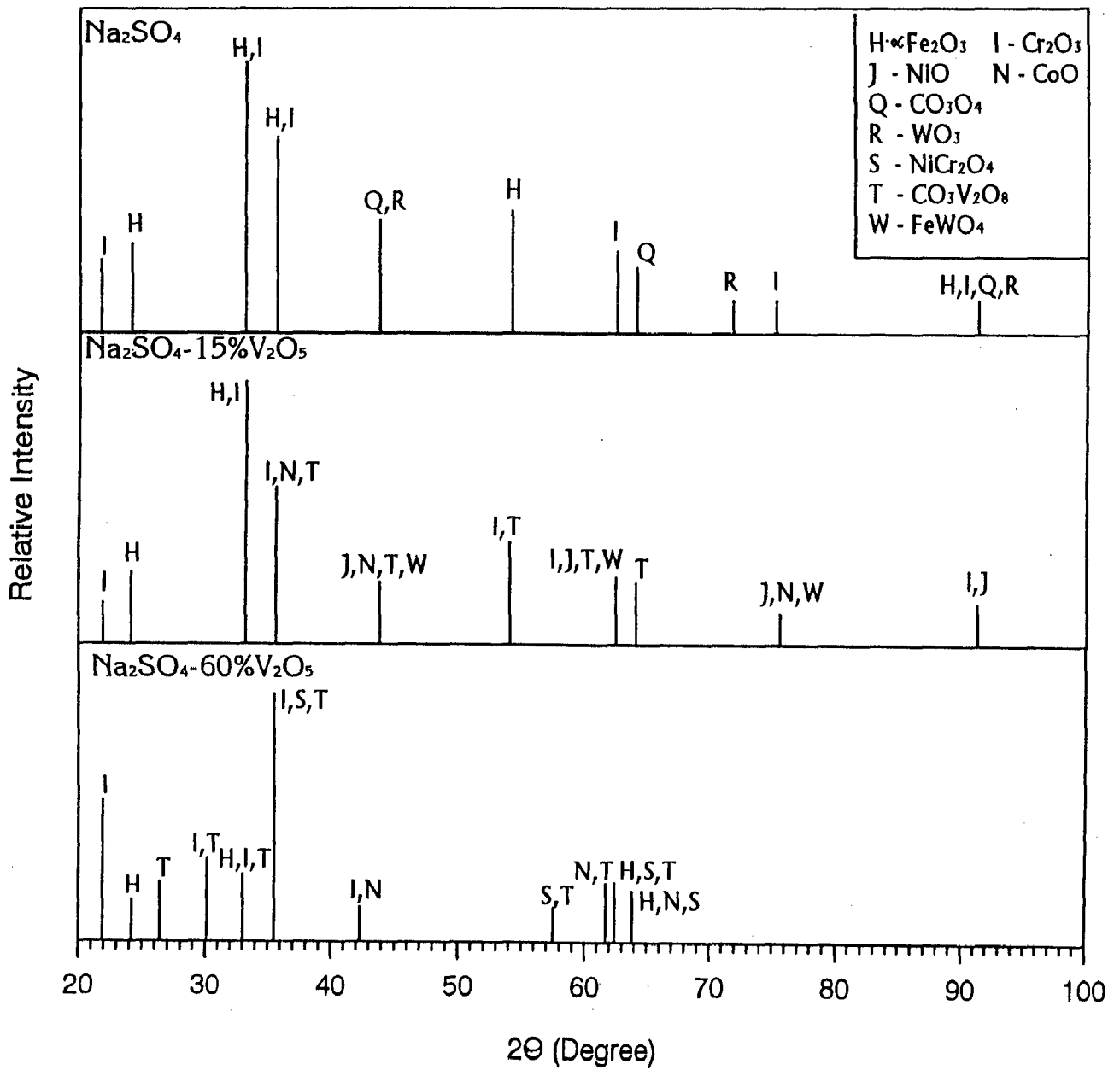


Fig. 5.50 : X-Ray Diffraction profile for alloy E (Superco 605) after hot corrosion at 1100°C in industrial atmosphere.

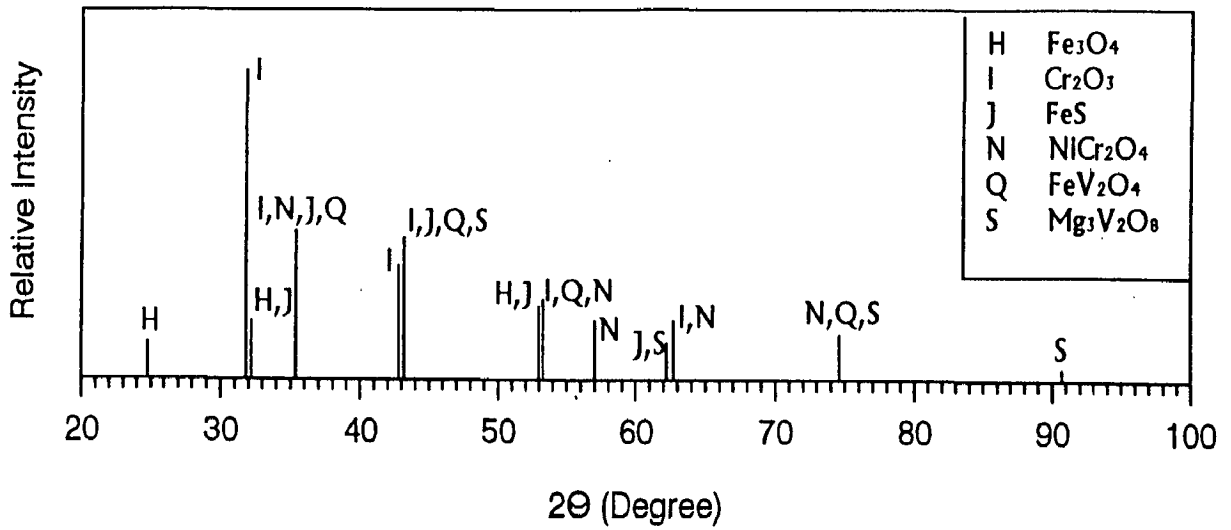


Fig. 5.51 : X-Ray Diffraction profile for alloy A (Superfer 800H) after hot corrosion at 900 °C in Na₂SO₄.-60%V₂O₅+MgO.

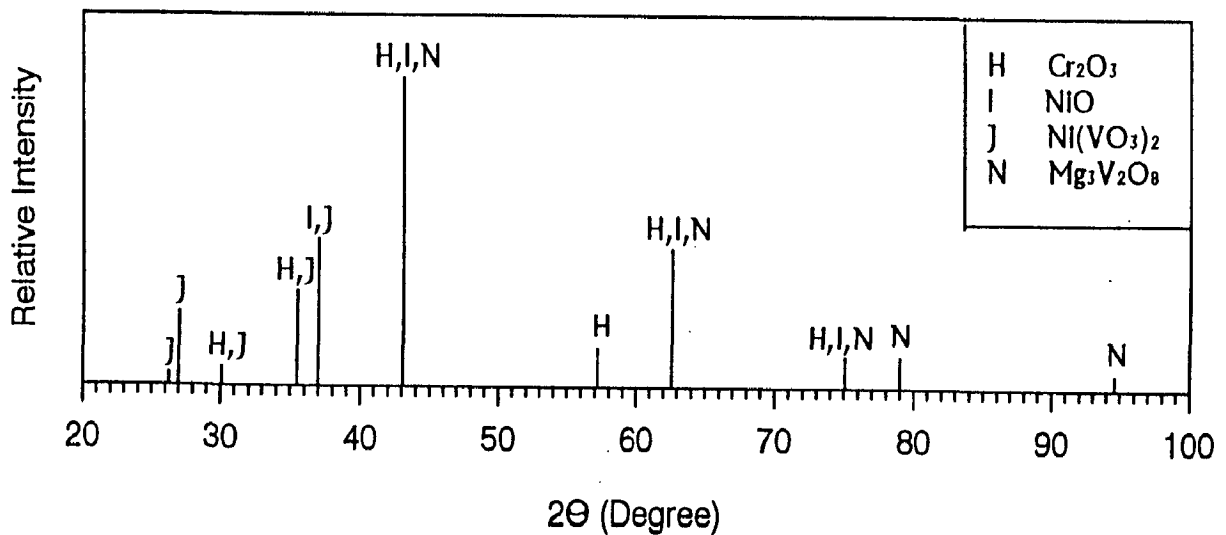


Fig. 5.52 : X-Ray Diffraction profile for alloy B (Superni 75) after hot corrosion at 900 °C in Na₂SO₄.-60%V₂O₅+MgO.

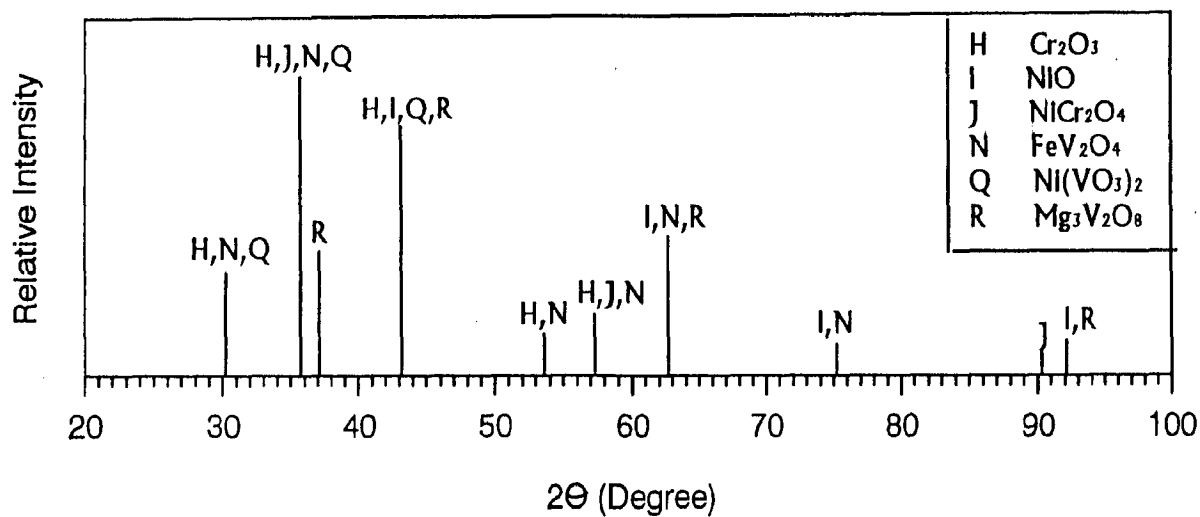


Fig. 5.53 : X-Ray Diffraction profile for alloy C (Superni 600) after hot corrosion at 900 °C in Na₂SO₄.-60%V₂O₅+MgO.

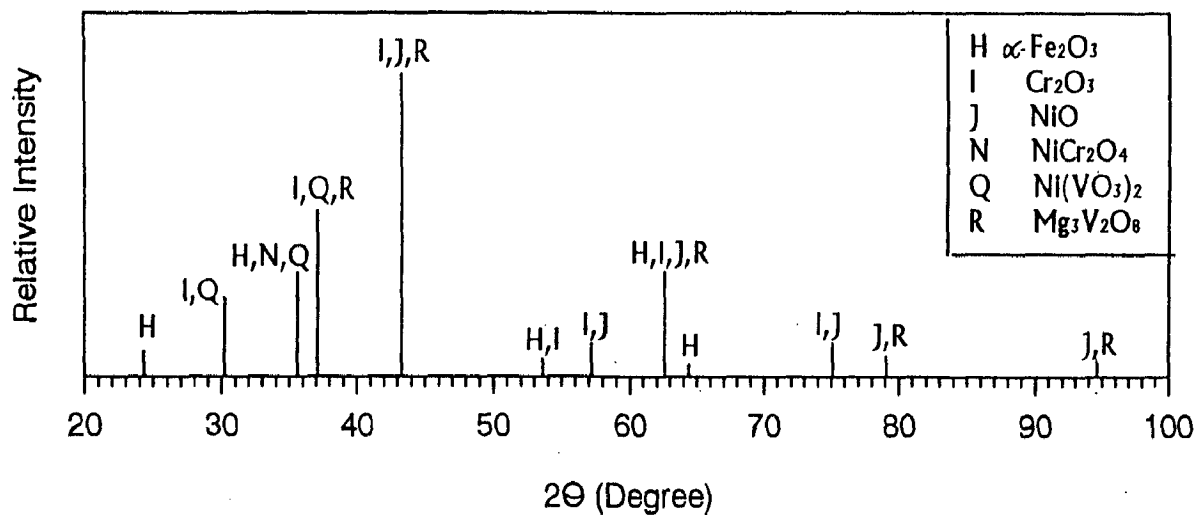


Fig. 5.54 : X-Ray Diffraction profile for alloy D (Superni 718) after hot corrosion at 900 °C in Na₂SO₄.-60%V₂O₅+MgO.

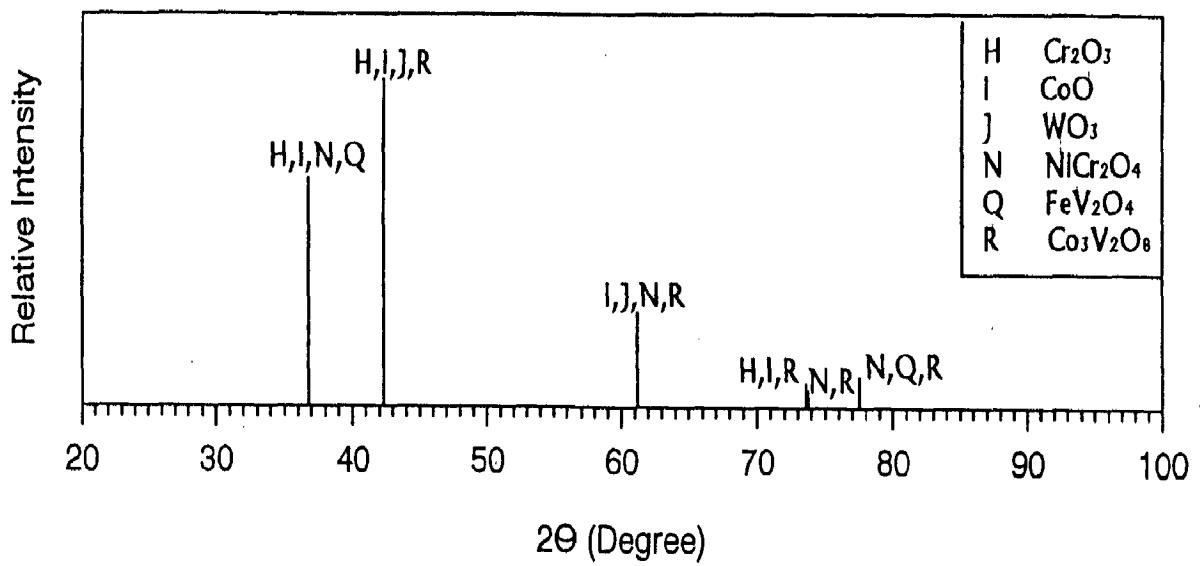


Fig. 5.55 : X-Ray Diffraction profile for alloy E (Superco 605) after hot corrosion at 900°C in Na₂SO₄-60%V₂O₅+MgO.

Fig. 5.56 : SEM of alloy A (Superfer 800H) after cyclic hot corrosion in pure

Na_2SO_4 at

(a) 900°C, (X640)

(b) 800°C, (X640)

(c) 700°C, (X640)

Fig. 5.57 : SEM of alloy A (Superfer 800H) after cyclic hot corrosion in

Na_2SO_4 -15% V_2O_5 at

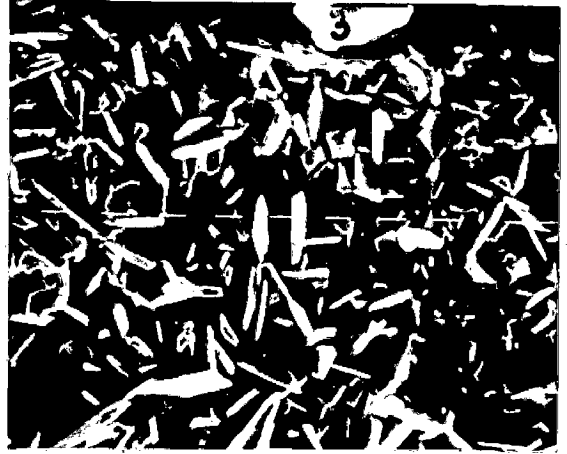
(a) 900°C, (X640)

(b) 800°C, (X640)

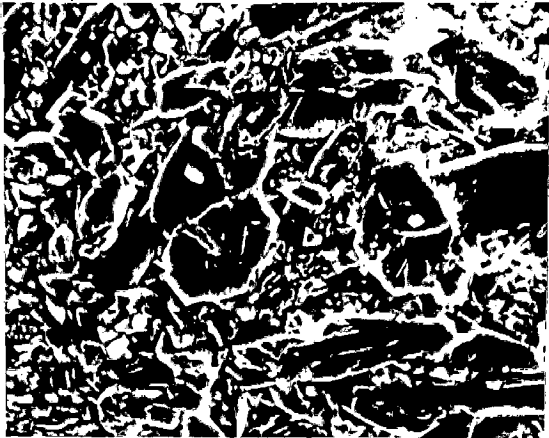
(c) 700°C, (X640)



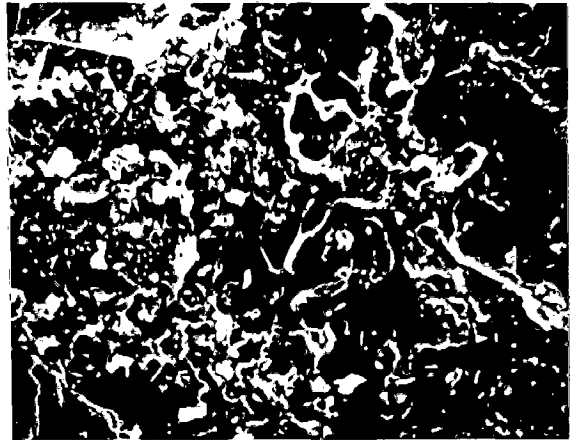
a



a



b

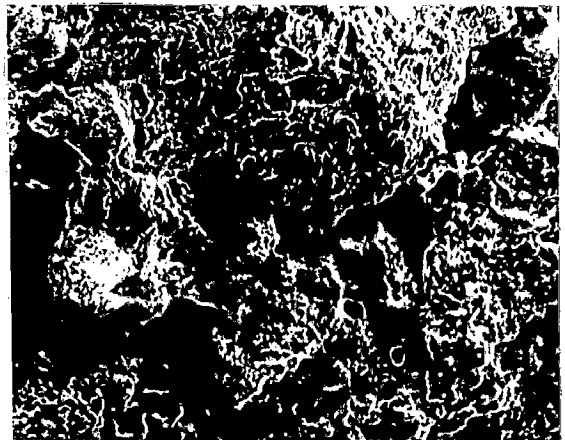


b



c

Fig. 5-56



c

Fig. 5-57

Fig. 5.58 : SEM of alloy B (Superni 75) after cyclic hot corrosion in pure Na_2SO_4 at

(a) 900°C, (X640)

(b) 800°C, (X640)

(c) 700°C, (X640)

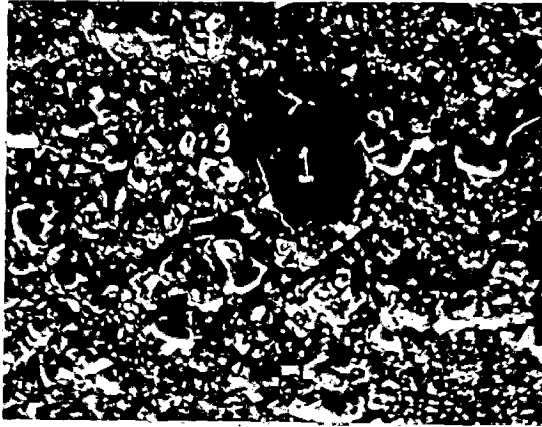
Fig. 5.59 : SEM of alloy B (Superni 75) after cyclic hot corrosion in Na_2SO_4 -

15% V_2O_5 at

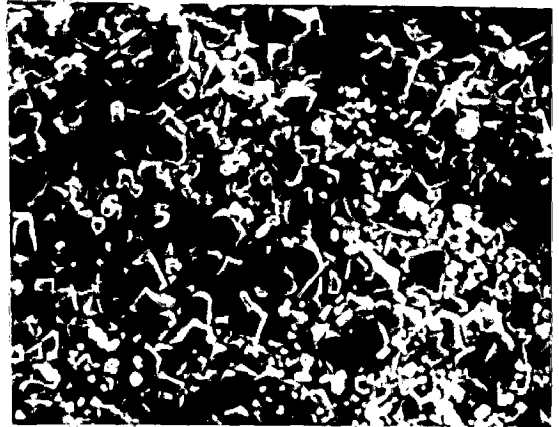
(a) 900°C, (X640)

(b) 800°C, (X640)

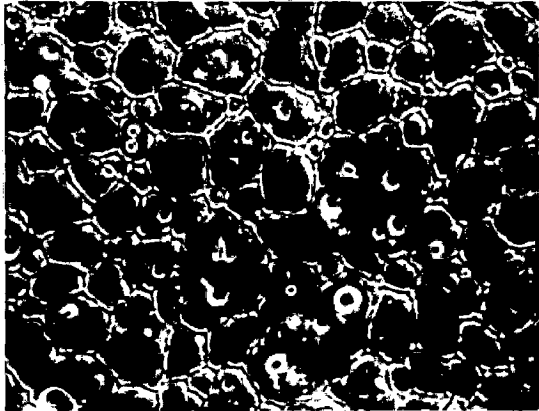
(c) 700°C, (X640)



a



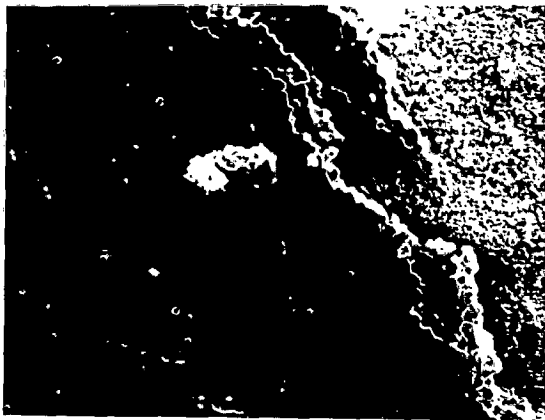
a



b



b



c

Fig. 5-58



c

Fig. 5-59

Fig. 5.60 : SEM of alloy C (Superni 600) after cyclic hot corrosion in pure

Na₂SO₄ at

(a) 900°C, (X640)

(b) 800°C, (X640)

(c) 700°C, (X640)

Fig. 5.61 : SEM of alloy C (Superni 600) after cyclic hot corrosion in Na₂SO₄-

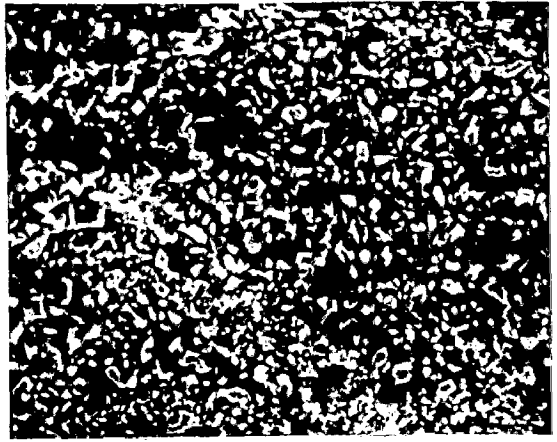
15%V₂O₅ at

(a) 900°C, (X640)

(b) 800°C, (X640)

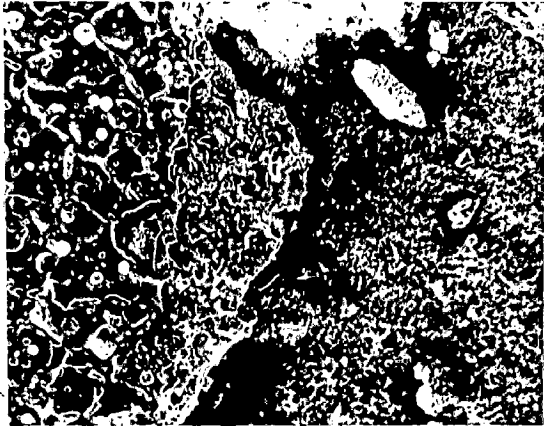
(c) 700°C, (X640)





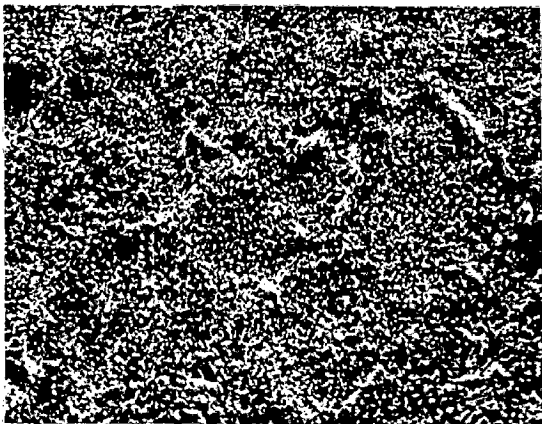
a

a



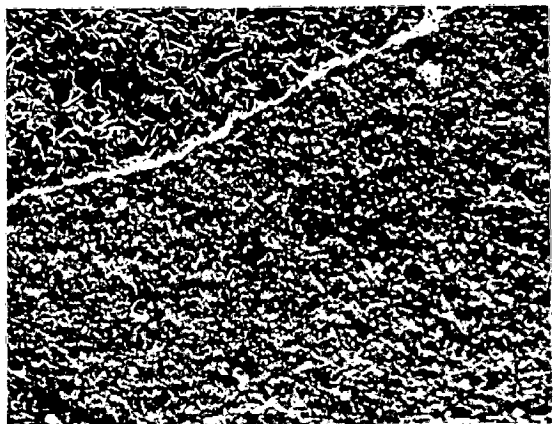
b

b



c

Fig. 5-60



c

Fig. 5-61

Fig. 5.62 : SEM of alloy D (Superni 718) after cyclic hot corrosion in pure

Na₂SO₄ at

(a) 900°C, (X640)

(b) 800°C, (X640)

(c) 700°C, (X640)

Fig. 5.63 : SEM of alloy D (Superni 718) after cyclic hot corrosion in Na₂SO₄-

15%V₂O₅ at

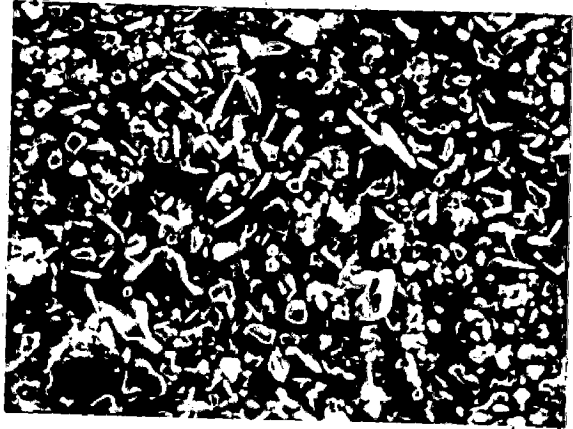
(a) 900°C, (X640)

(b) 800°C, (X640)

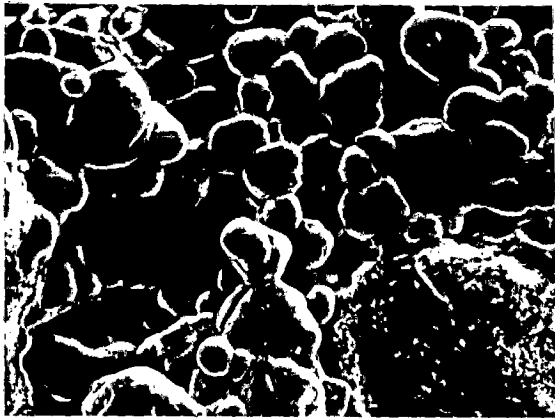
(c) 700°C, (X640)



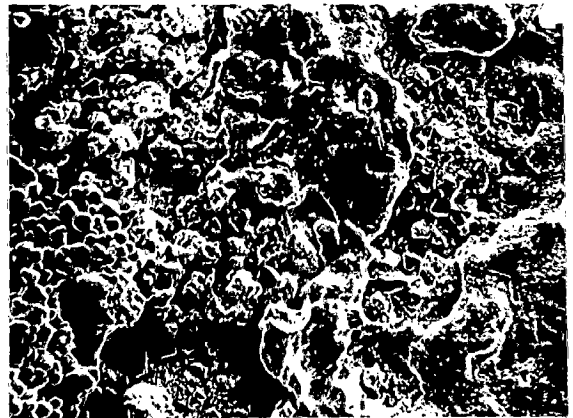
a



a



b



b



c

Fig. 5-62



Fig. 5.64 : SEM of alloy E (Superco 605) after cyclic hot corrosion in pure

Na₂SO₄ at

(a) 900°C, (X640)

(b) 800°C, (X640)

(c) 700°C, (X640)

Fig. 5.65 : SEM of alloy E (Superco 605) after cyclic hot corrosion in Na₂SO₄-

15%V₂O₅ at

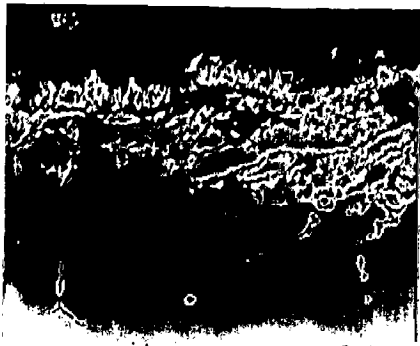
(a) 900°C, (X640)

(b) 800°C, (X640)

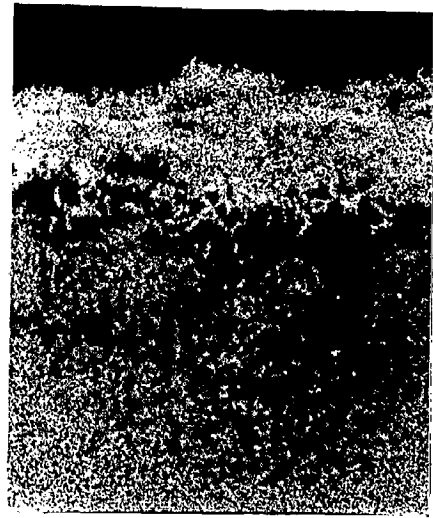
(c) 700°C, (X640)

Fig. 5.89 BSEI and X-ray mappings of the cross-section of Alloy D (Superni 718) after cyclic-hot corrosion test (X1000).

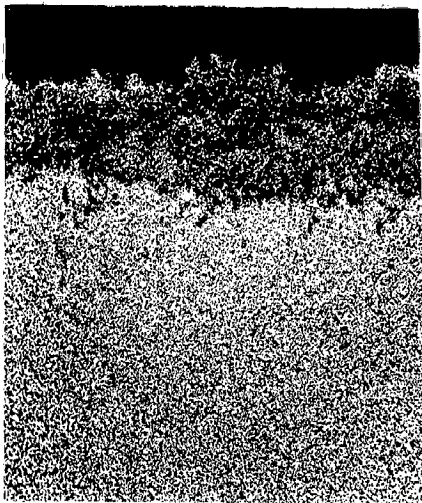
- (a) Composition image (BSEI)
- (b) Cr K_{α} x-ray image
- (c) Ni K_{α} x-ray image
- (d) Fe K_{α} x-ray image
- (e) Al K_{α} x-ray image
- (f) Ti K_{α} x-ray image
- (g) O K_{α} x-ray image



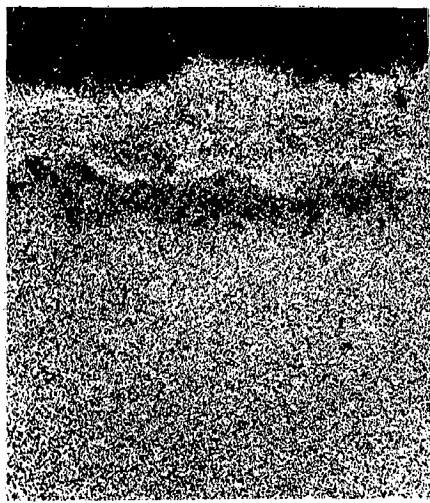
a



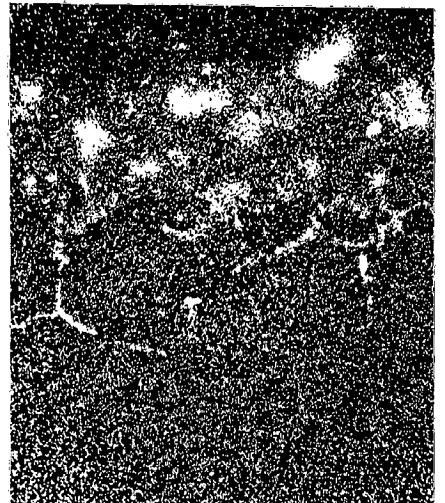
b



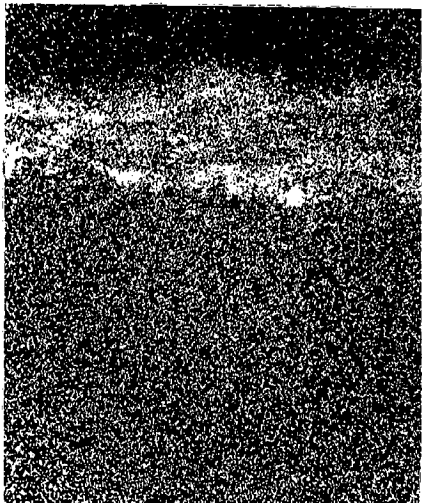
c



d



e



f



g

Fig. 5.88 BSEI and X-ray mappings of the cross-section of Alloy C (Superni 600) after cyclic hot corrosion at 900°C in Na₂SO₄-15% V₂O₅ (X400).

(a) Composition image (BSEI)

(b) Cr K_α x-ray image

(c) Ni K_α x-ray image

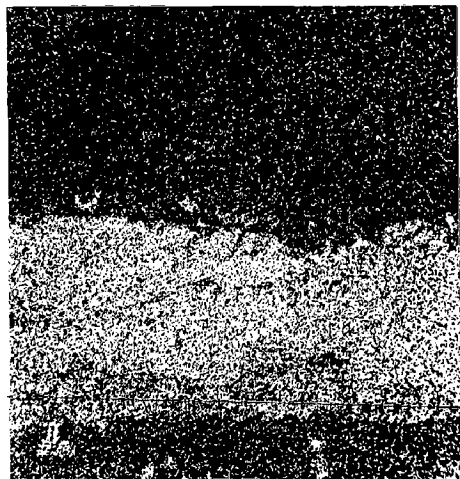
(d) Fe K_α x-ray image

(e) Al K_α x-ray image

(f) V K_α x-ray image

(g) O K_α x-ray image

p



o



q



d

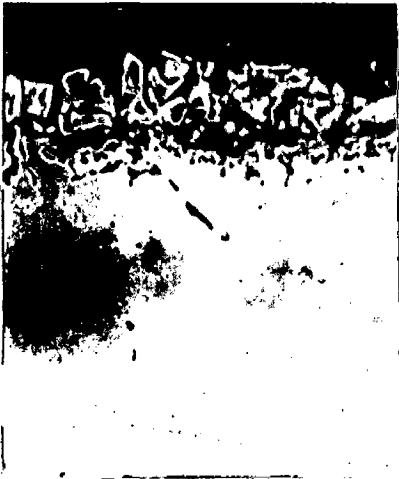
Fig. 5.87 BSEI and X-ray mappings of the cross-section of Alloy B (Superni 75) after cyclic hot corrosion at 900°C in Na₂SO₄-15% V₂O₅ (X300).

(a) Composition image (BSEI)

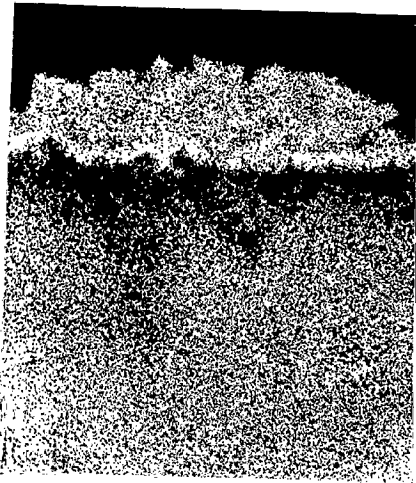
(b) Cr K_α x-ray image

(c) Ni K_α x-ray image

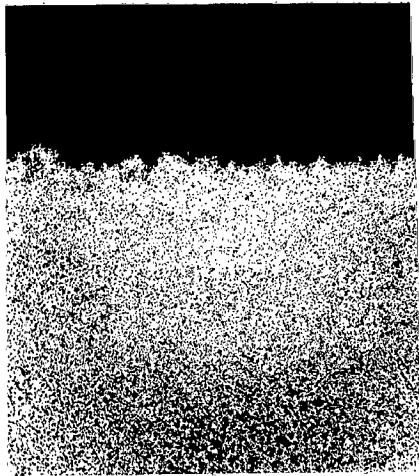
(d) O K_α x-ray image



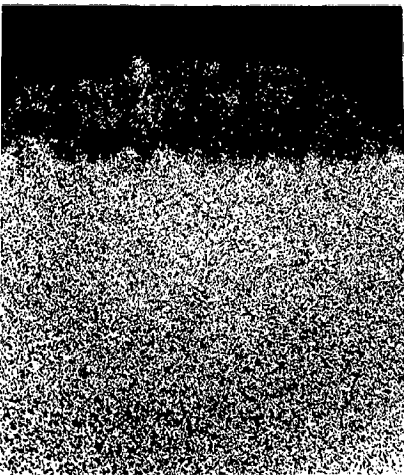
a



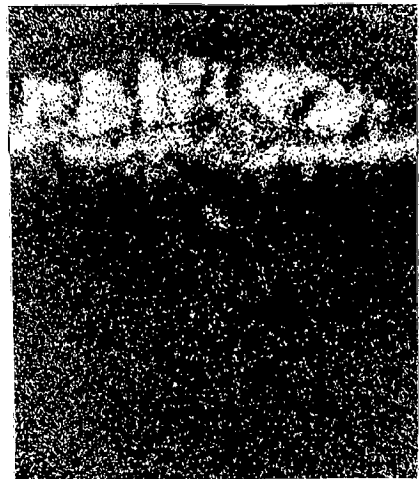
b



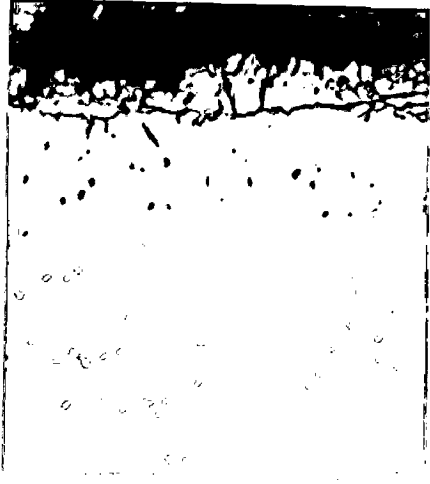
c



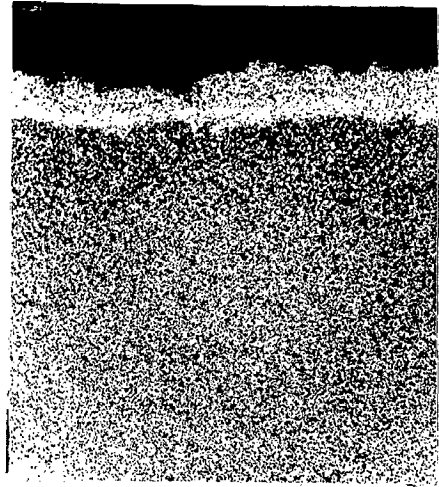
d



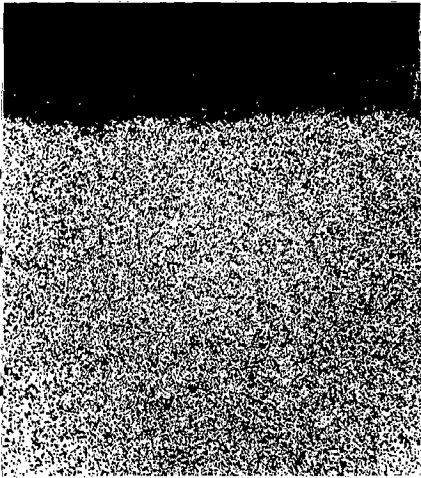
e



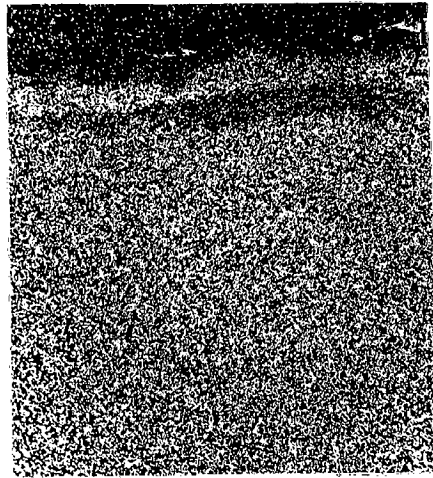
a



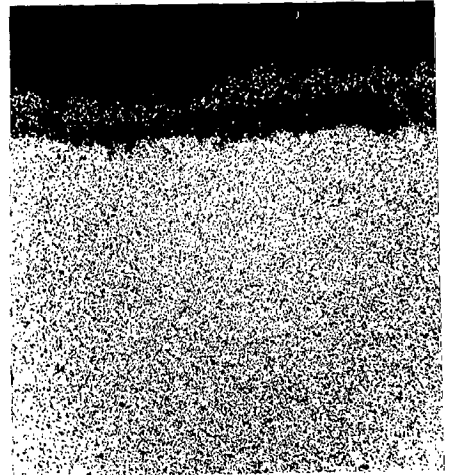
b



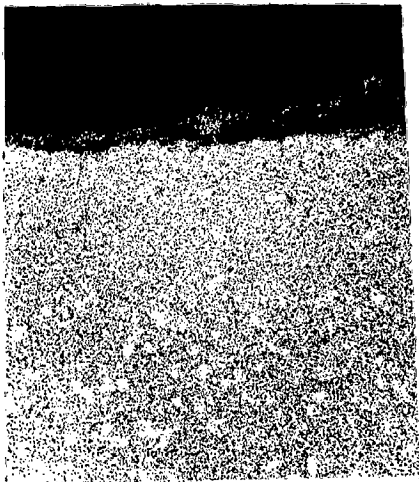
c



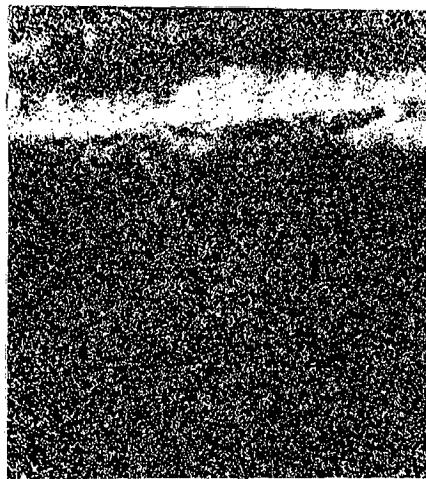
d



e



f



g

Fig. 5.86 BSEI and X-ray mappings of the cross-section of Alloy A (Superfer 800H) after cyclic hot corrosion at 900°C in Na₂SO₄-15% V₂O₅ (X1000).

(a) Composition image (BSEI)

(b) Cr K_α x-ray image

(c) Ni K_α x-ray image

(d) Fe K_α x-ray image

(e) O K_α x-ray image

Fig. 5.85 BSEI and X-ray mappings of the cross-section of Alloy E (Superco 605) after cyclic hot corrosion at 900°C in pure Na₂SO₄ (X1000).

(a) Composition image (BSEI)

(b) Cr K_α x-ray image

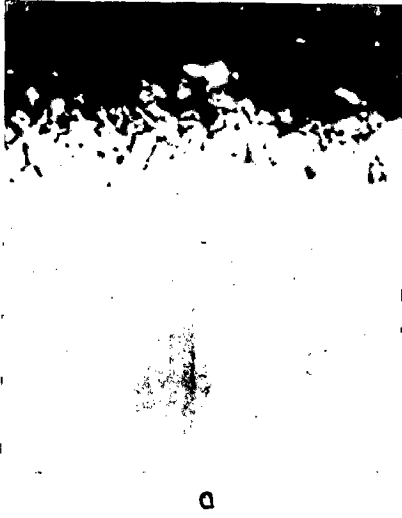
(c) Ni K_α x-ray image

(d) Fe K_α x-ray image

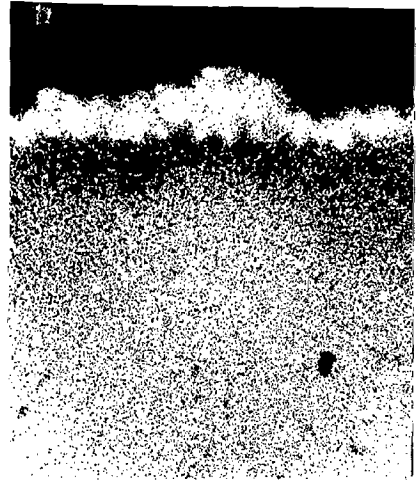
(e) Co K_α x-ray image

(f) W K_α x-ray image

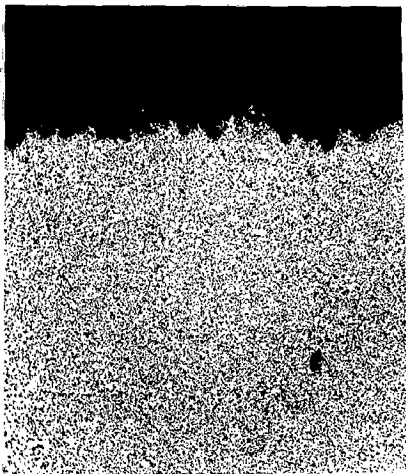
(g) O K_α x-ray image



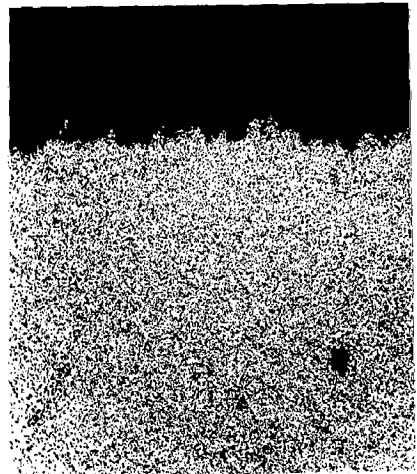
a



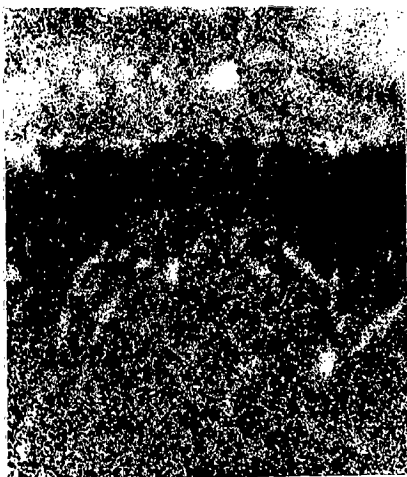
b



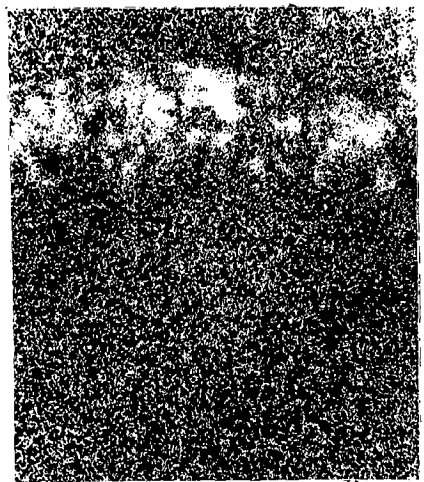
c



d



e



f

Fig. 5.84 BSEI and X-ray mappings of the cross-section of Alloy D (Superni 718) after cyclic hot corrosion at 900°C in pure Na₂SO₄ (X1000).

(a) Composition image (BSEI)

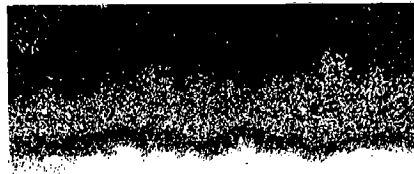
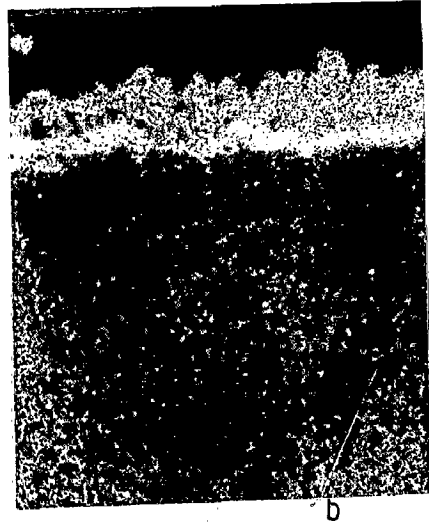
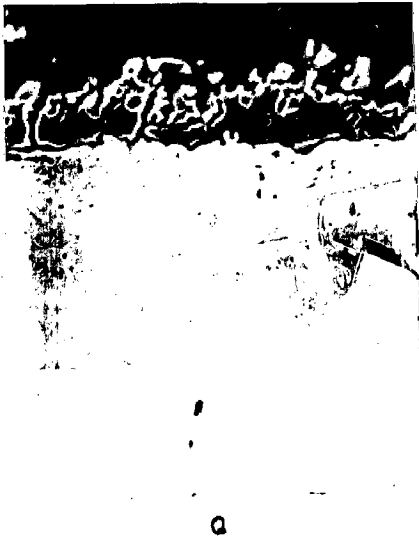
(b) Cr K_α x-ray image

(c) Ni K_α x-ray image

(d) Fe K_α x-ray image

(e) Ti K_α x-ray image

(f) O K_α x-ray image



c

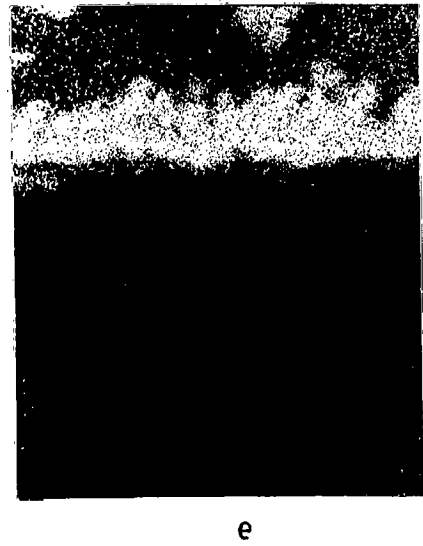
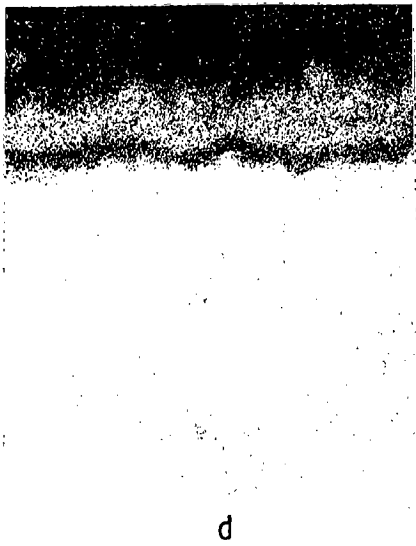


Fig. 5.83 BSEI and X-ray mappings of the cross-section of Alloy C (Superni 600) after cyclic hot corrosion at 900°C in pure Na₂SO₄ (X1000).

(a) Composition image (BSEI)

(b) Cr K_α x-ray image

(c) Ni K_α x-ray image

(d) Fe K_α x-ray image

(e) O K_α x-ray image

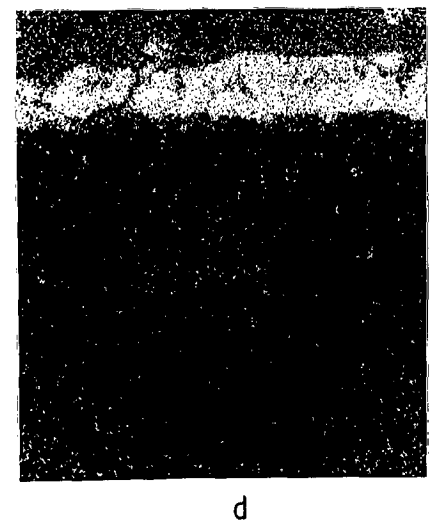
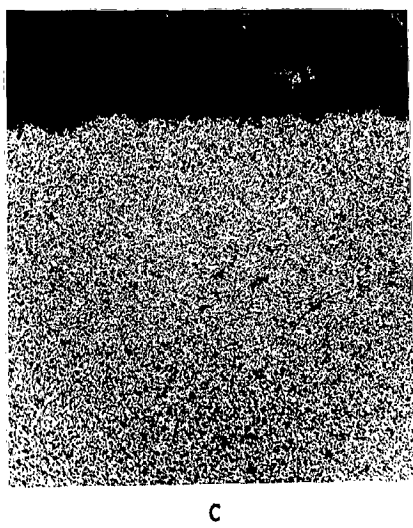
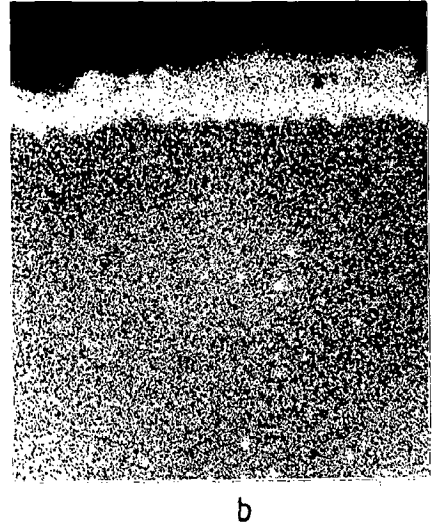
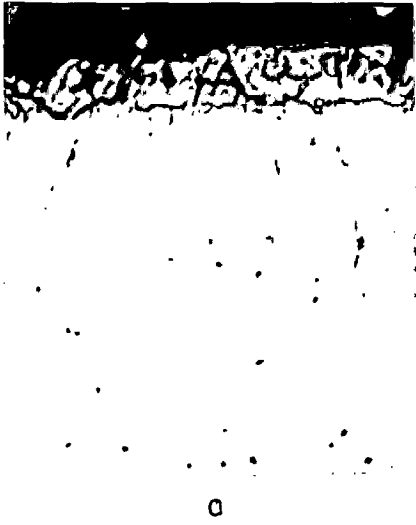


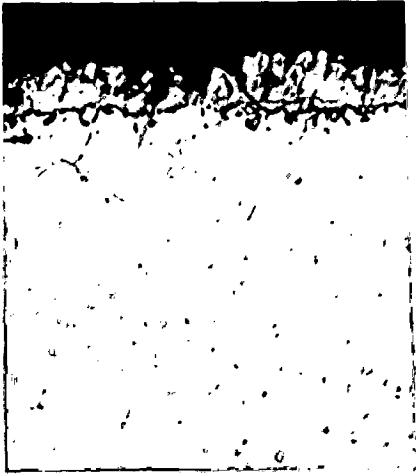
Fig. 5.82 BSEI and X-ray mappings of the cross-section of Alloy B (Superni 75) after cyclic hot corrosion at 900°C in pure Na₂SO₄ (X1000).

(a) Composition image (BSEI)

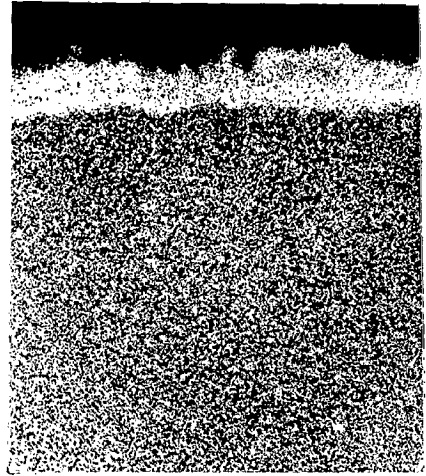
(b) Cr K_α x-ray image

(c) Ni K_α x-ray image

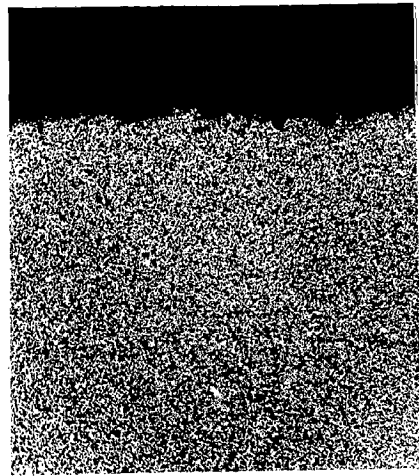
(d) O K_α x-ray image



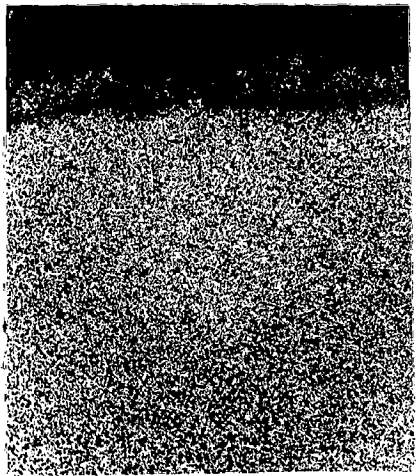
a



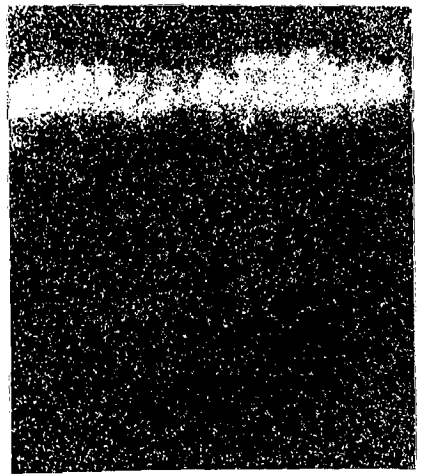
b



c



d



e

Fig. 5.81 BSEI and X-ray mappings of the cross-section of Alloy A (Superfer 800H) after cyclic hot corrosion at 900°C in pure Na₂SO₄ (X1000).

(a) Composition image (BSEI)

(b) Cr K_α x-ray image

(c) Ni K_α x-ray image

(d) Fe K_α x-ray image

(e) O K_α x-ray image

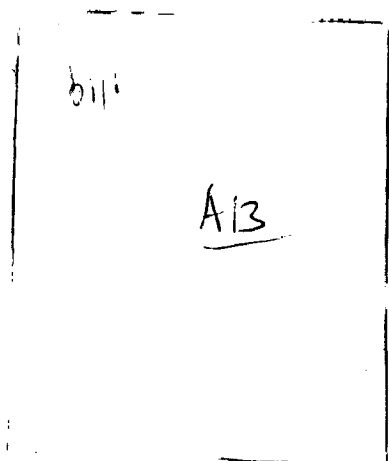


Fig - 5-76

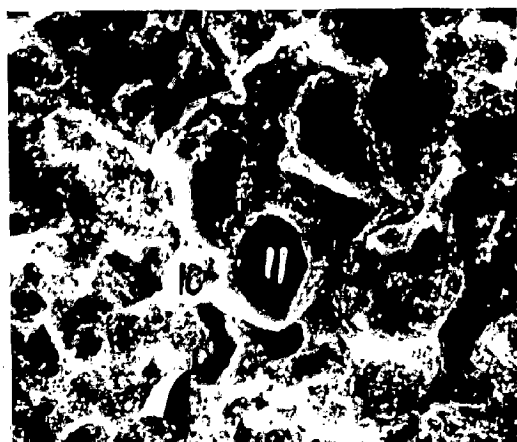


Fig - 5-77

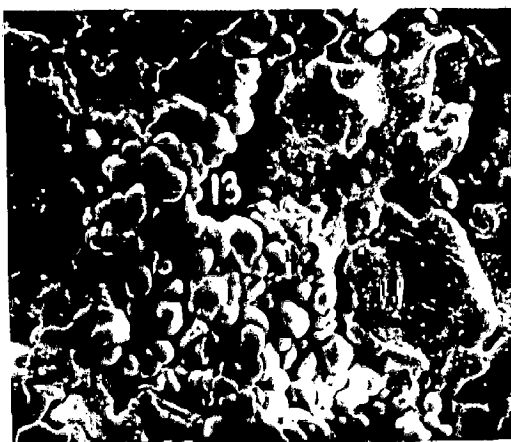


Fig - 5-78

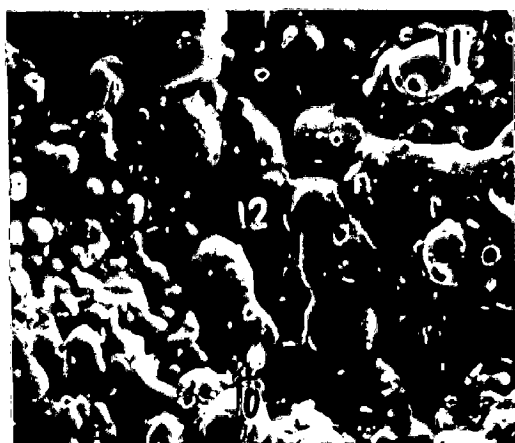
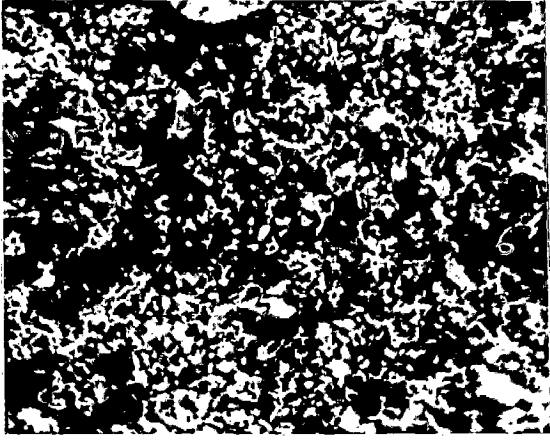


Fig - 5-79

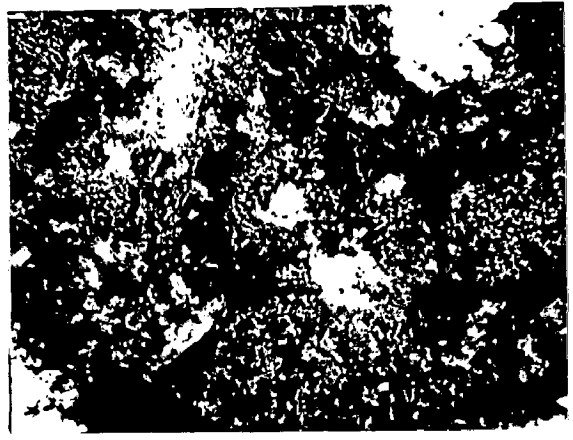


Fig - 5-80

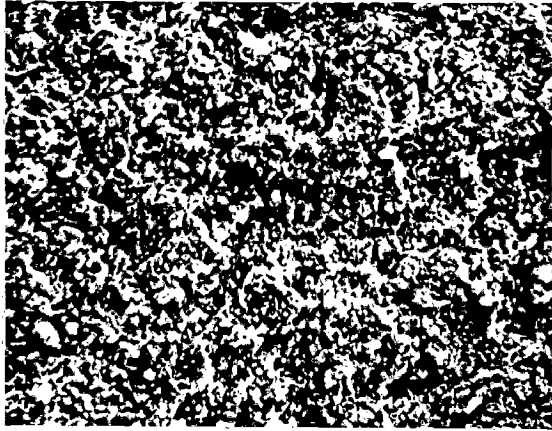
- Fig. 5.76 Scanning electron micrographs of Alloy A (Superfer 800H) after cyclic hot corrosion at 900°C in Na₂SO₄-60% V₂O₅ + MgO (X640).
- Fig. 5.77 Scanning electron micrographs of Alloy B (Superni 75) after cyclic hot corrosion at 900°C in Na₂SO₄-60% V₂O₅ + MgO (X640).
- Fig. 5.78 Scanning electron micrographs of Alloy C (Superni 600) after cyclic hot corrosion at 900°C in Na₂SO₄-60% V₂O₅ + MgO (X640).
- Fig. 5.79 Scanning electron micrographs of Alloy D (Superni 718) after cyclic hot corrosion at 900°C in Na₂SO₄-60% V₂O₅ + MgO (X640).
- Fig. 5.80 Scanning electron micrographs of Alloy E (Superco 605) after cyclic hot corrosion at 900°C in Na₂SO₄-60% V₂O₅ + MgO (X640).



a



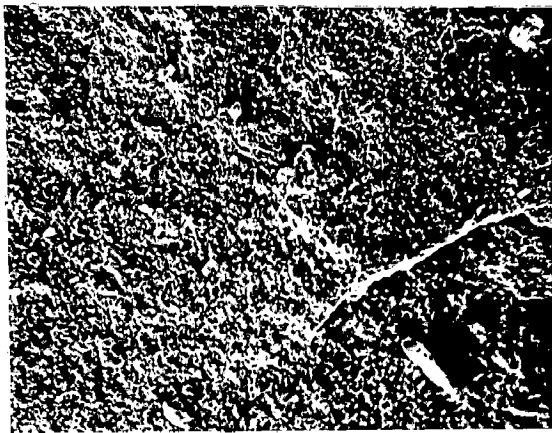
a



b

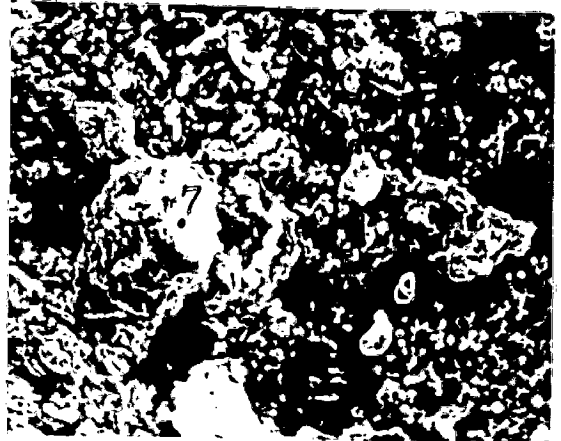


b



c

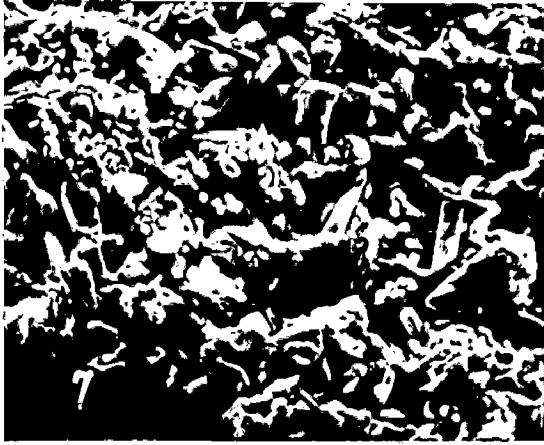
Fig. 5-74



c

Fig. 5-75

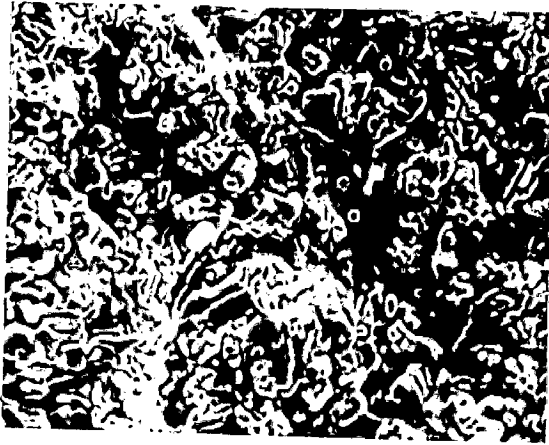




a



a



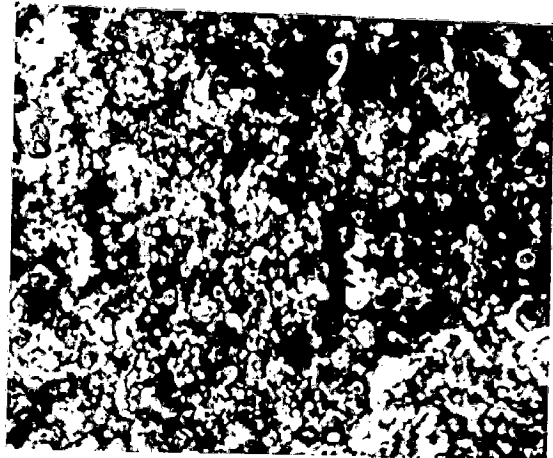
b

b



c

Fig. 5-72



c

Fig. 5-73

**Fig. 5.74 : SEM of alloy E (Superco 605) after cyclic hot corrosion in Na_2SO_4 -
60% V_2O_5 at**

- | | |
|------------|--------|
| (a) 900°C, | (X640) |
| (b) 800°C, | (X640) |
| (c) 700°C, | (X640) |

**Fig. 5.75 : SEM of alloy E (Superco 605) after cyclic hot corrosion in c.g. at
1100°C with**

- | | |
|--|--------|
| (a) Pure Na_2SO_4 , | (X640) |
| (b) Na_2SO_4 -15% V_2O_5 , | (X640) |
| (c) Na_2SO_4 -60% V_2O_5 , | (X640) |

**Fig. 5.72 : SEM of alloy D (Superni 718) after cyclic hot corrosion in Na_2SO_4 -
60% V_2O_5 at**

(a) 900°C, (X640)

(b) 800°C, (X640)

(c) 700°C, (X640)

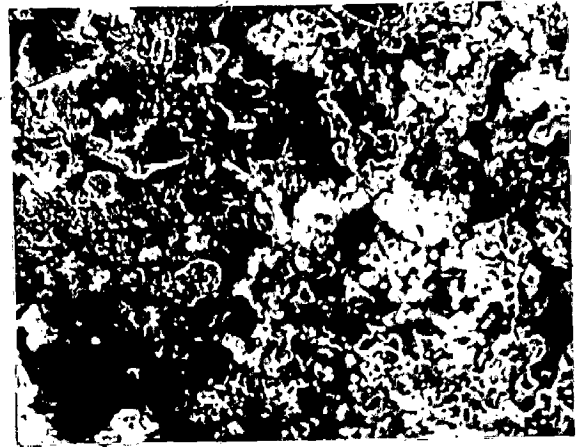
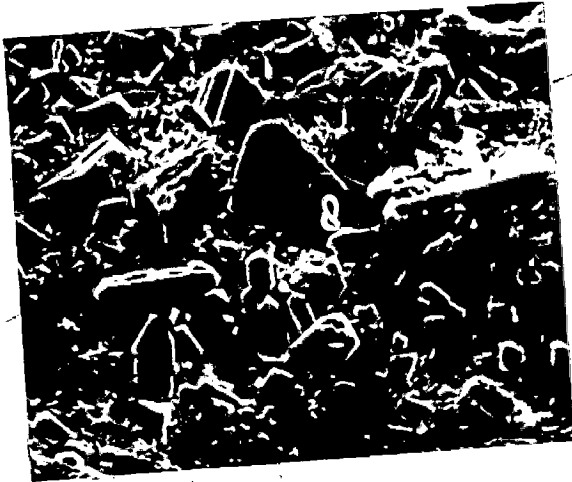
**Fig. 5.73 : SEM of alloy D (Superni 718) after cyclic hot corrosion in c.g. at
1100°C with**

(a) Pure Na_2SO_4 , (X640)

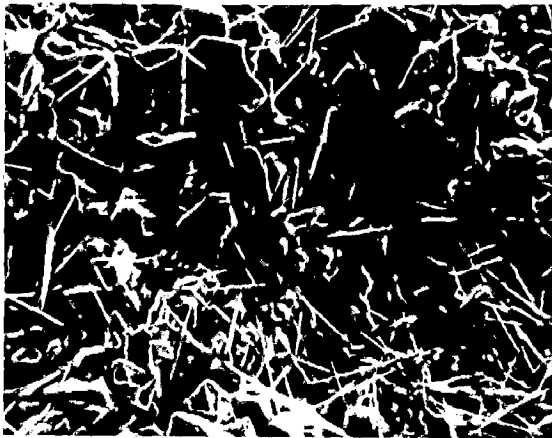
(b) Na_2SO_4 -15% V_2O_5 , (X640)

(c) Na_2SO_4 -60% V_2O_5 , (X640)



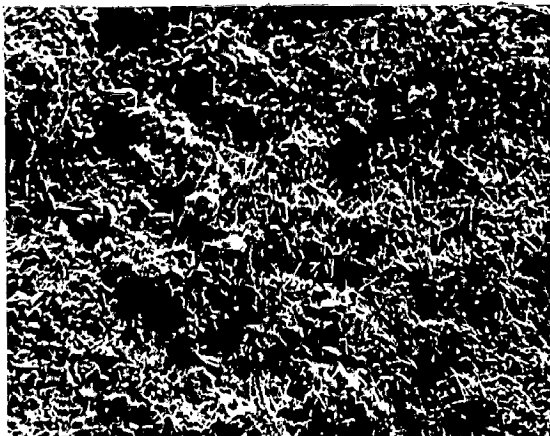


a



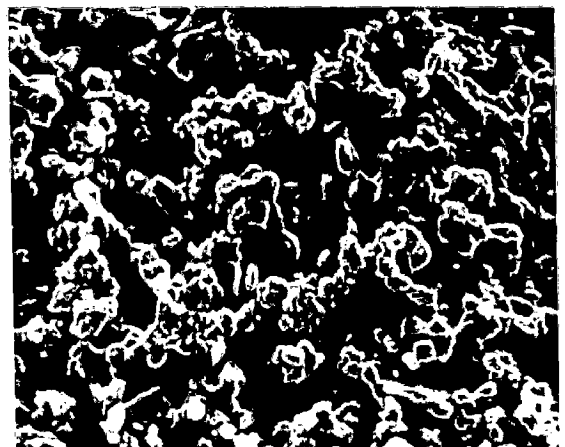
b

b



c

Fig. 5-70



c

Fig. 5-71

Fig. 5.70 : SEM of alloy C (Superni 600) after cyclic hot corrosion in Na₂SO₄-60%V₂O₅ at

(a) 900°C, (X640)

(b) 800°C, (X640)

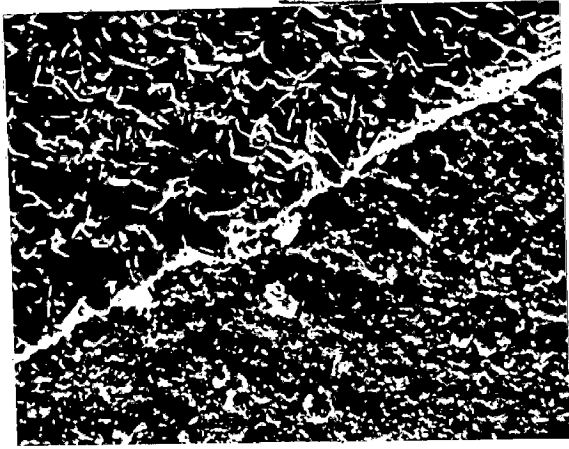
(c) 700°C, (X640)

Fig. 5.71 : SEM of alloy C (Superni 600) after cyclic hot corrosion in c.g. at 1100°C with

(a) Pure Na₂SO₄ , (X640)

(b) Na₂SO₄-15%V₂O₅, (X640)

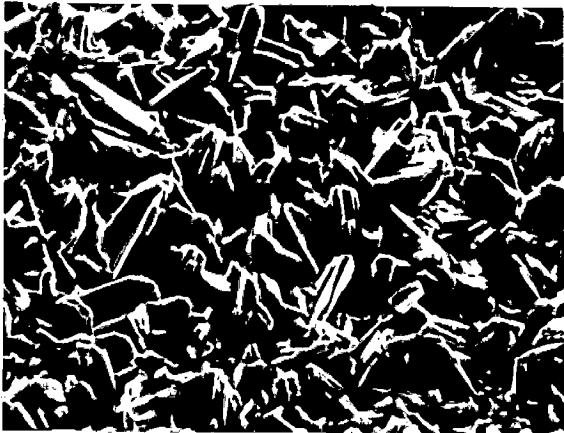
(c) Na₂SO₄-60%V₂O₅, (X640)



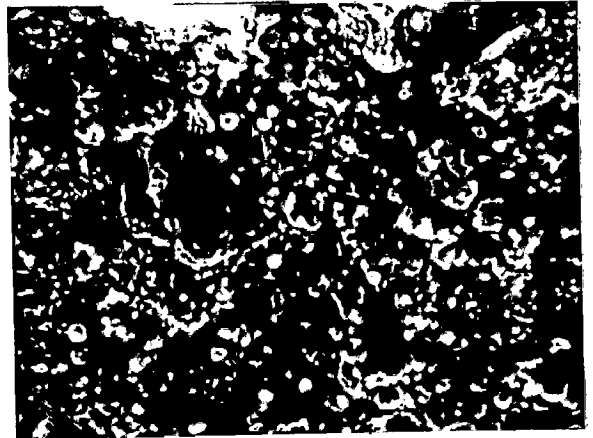
a



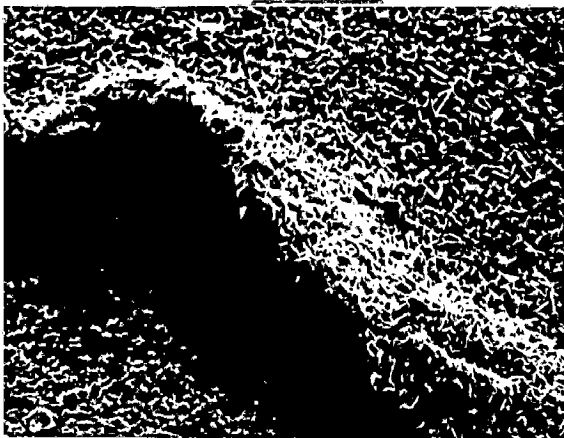
a



b



b



c

Fig. 5-68



c

Fig. 5-69

**Fig. 5.68 : SEM of alloy B (Superni 75) after cyclic hot corrosion in Na_2SO_4 -
60% V_2O_5 at**

(a) 900°C, (X640)

(b) 800°C, (X640)

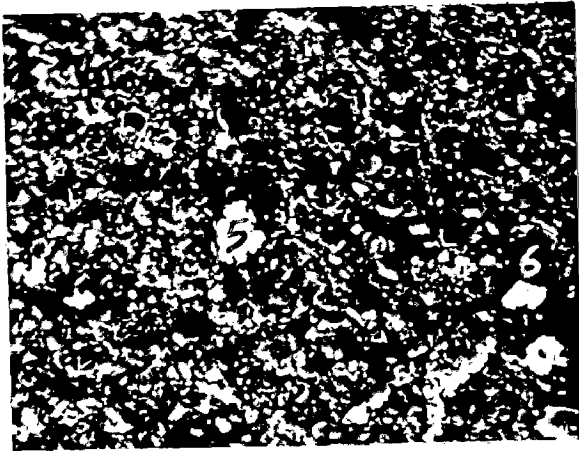
(c) 700°C, (X640)

**Fig. 5.69 : SEM of alloy B (Superni 75) after cyclic hot corrosion in c.g. at
1100°C with**

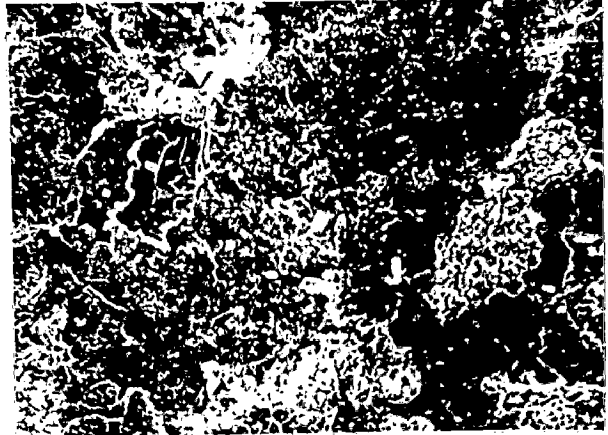
(a) Pure Na_2SO_4 , (X640)

(b) Na_2SO_4 -15% V_2O_5 , (X640)

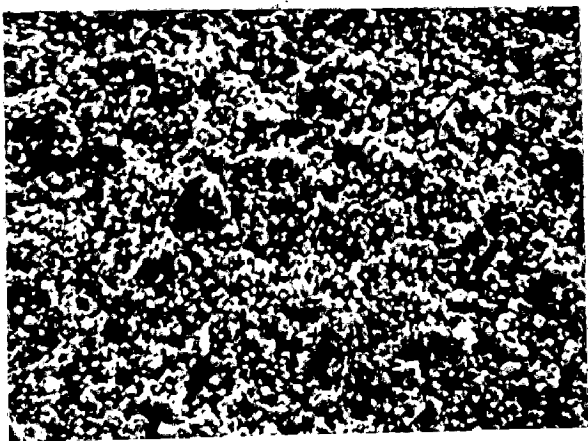
(c) Na_2SO_4 -60% V_2O_5 , (X640)



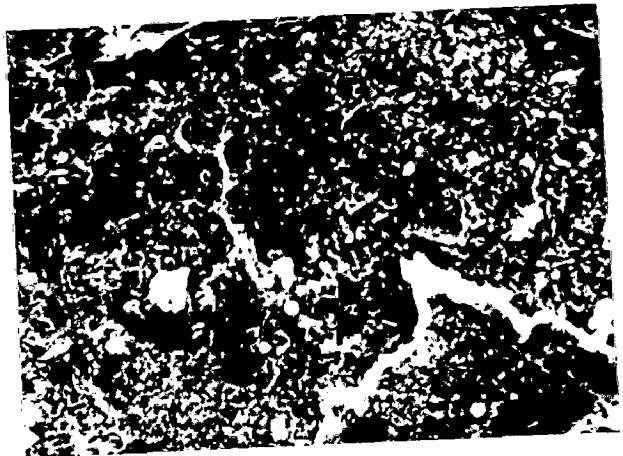
a



a



b

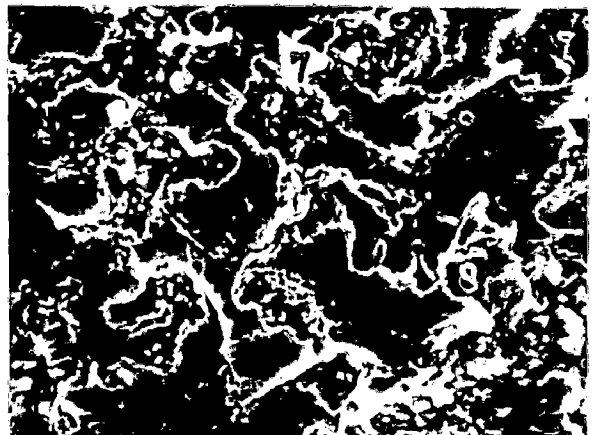


b



c

Fig. 5-66



c

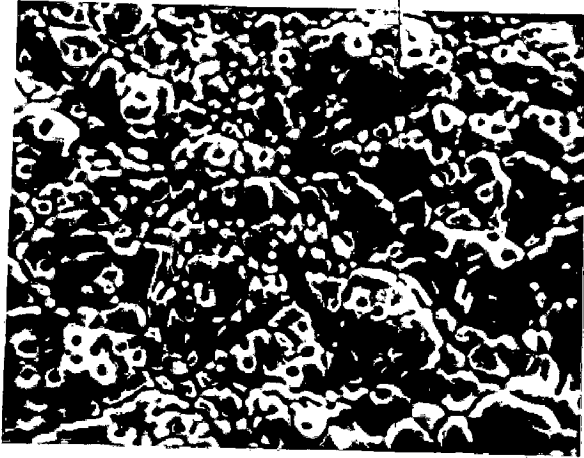
Fig. 5-67

Fig. 5.66 : SEM of alloy A (Superfer 800H) after cyclic hot corrosion in Na_2SO_4 -60% V_2O_5 at

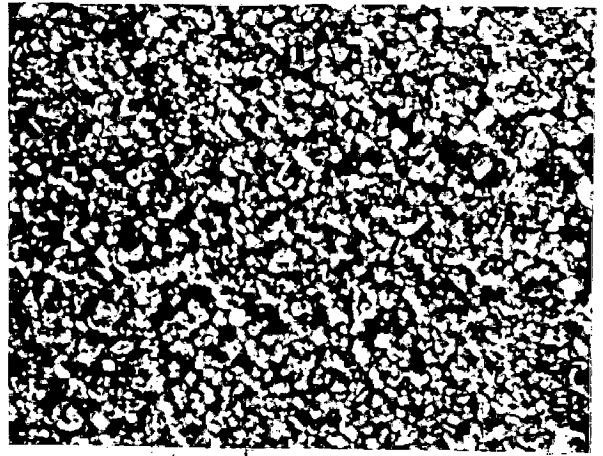
- (a) 900°C, (X640)
- (b) 800°C, (X640)
- (c) 700°C, (X640)

Fig. 5.67 : SEM of alloy A (Superfer 800H) after cyclic hot corrosion in c.g. at 1100°C with

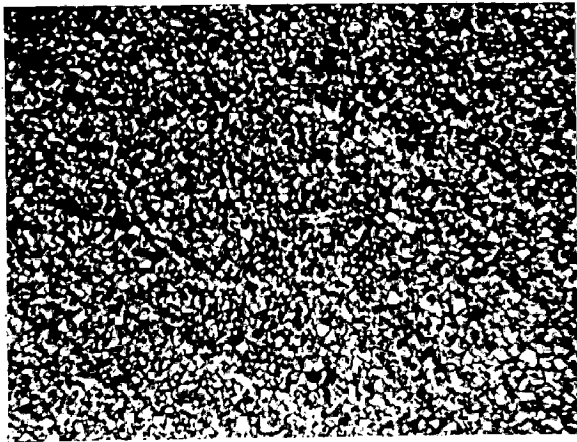
- (a) Pure Na_2SO_4 , (X640)
- (b) Na_2SO_4 -15% V_2O_5 , (X640)
- (c) Na_2SO_4 -60% V_2O_5 , (X640)



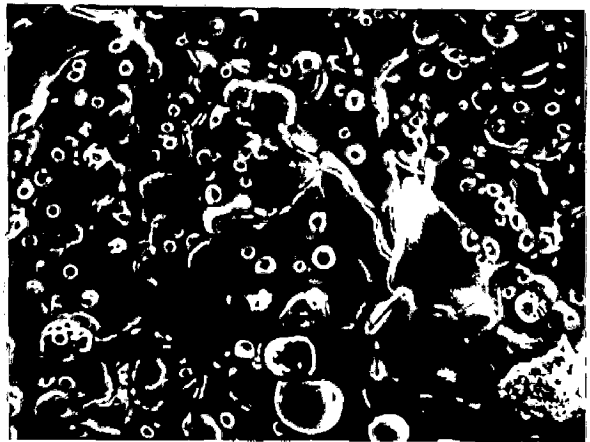
a



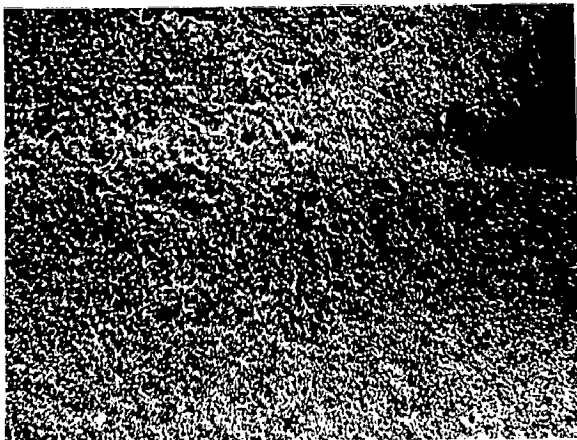
a



b

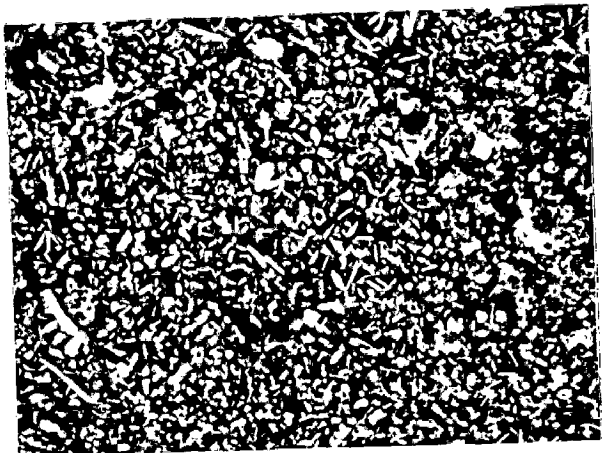


b



c

Fig. 5-64



c

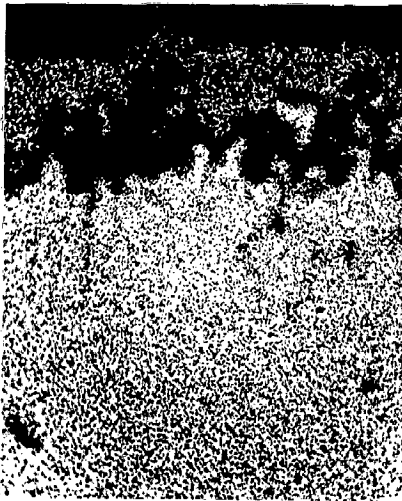
Fig. 5-65



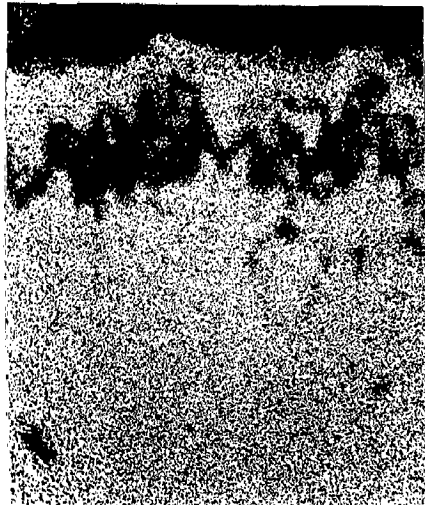
a



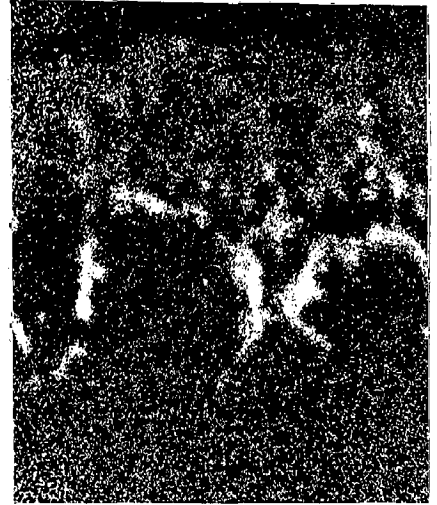
b



c



d



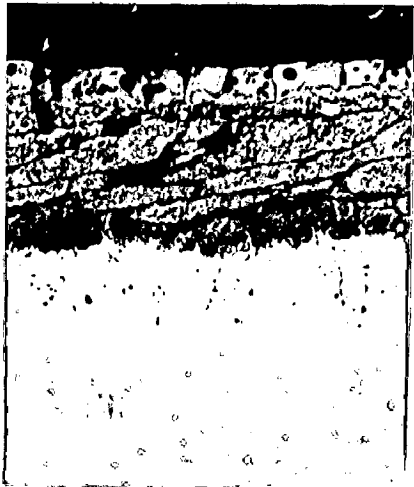
e



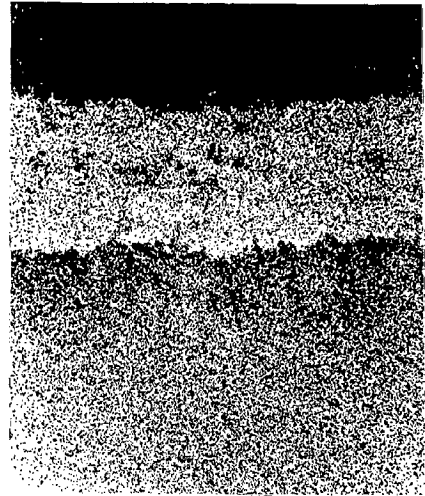
f



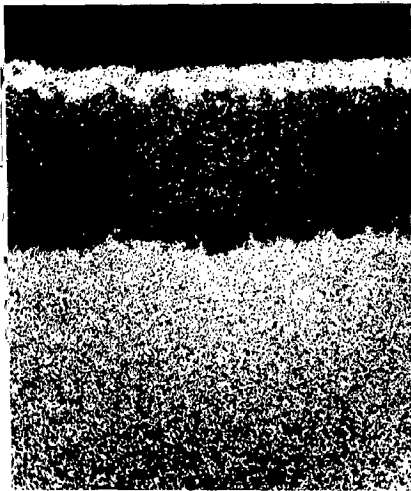
g



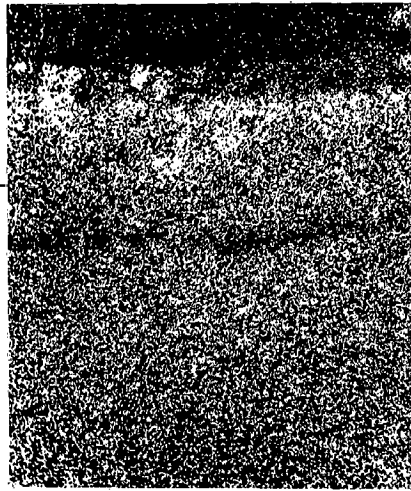
a



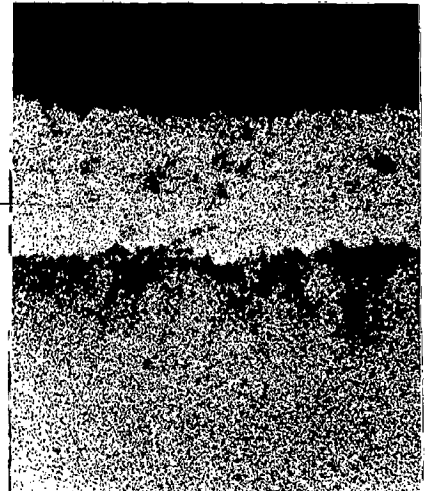
b



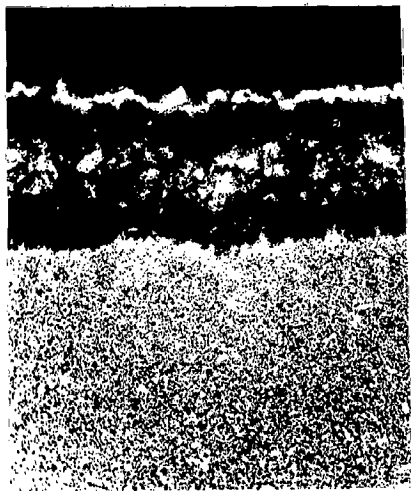
c



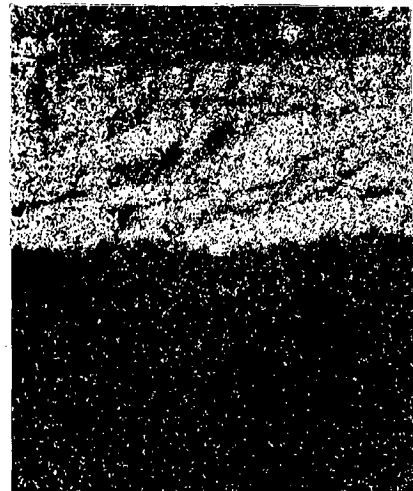
d



e



f



g

Fig. 5.91 BSEI and X-ray mappings of the cross-section of Alloy A (Superfer 800H) after cyclic hot corrosion at 900°C in Na₂SO₄-60% V₂O₅ (X400).

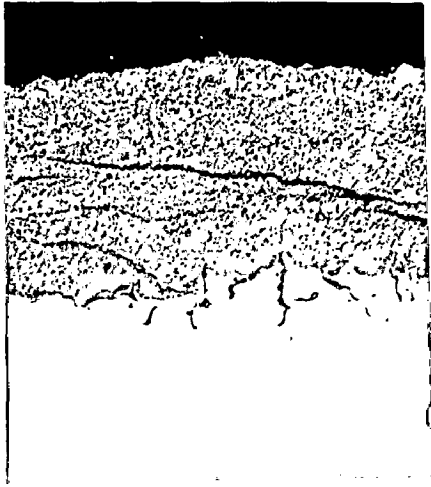
(a) Composition image (BSEI)

(b) Cr K_α x-ray image

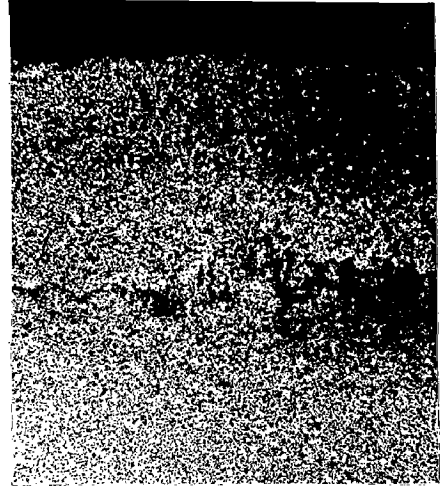
(c) Ni K_α x-ray image

(d) Fe K_α x-ray image

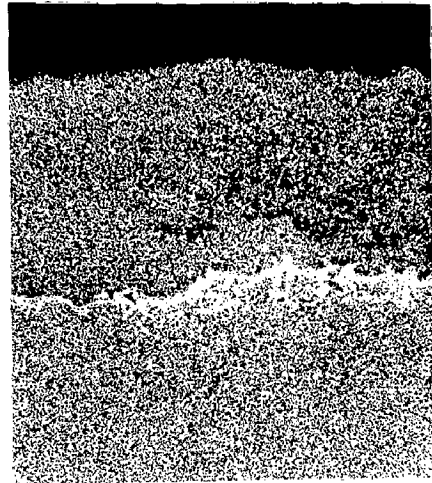
(e) O K_α x-ray image



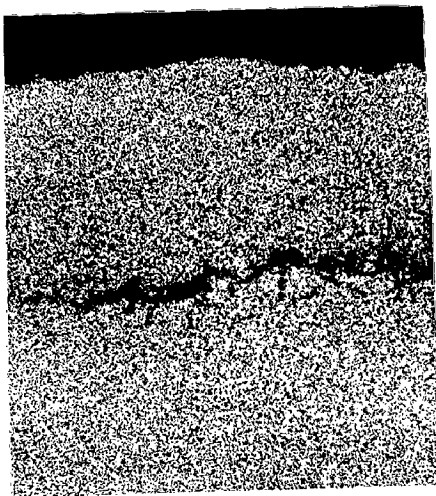
a



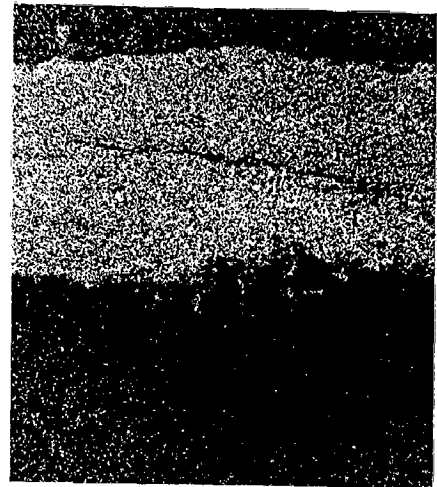
b



c



d



e

Fig. 5.92 BSEI and X-ray mappings of the cross-section of Alloy B (Superni 75) after cyclic hot corrosion at 900°C in Na₂SO₄-60% V₂O₅ (X600).

(a) Composition image (BSEI)

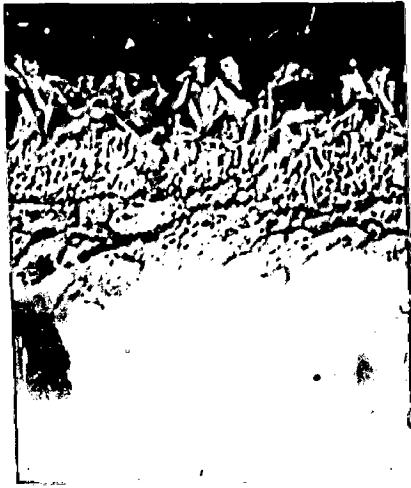
(b) Cr K_α x-ray image

(c) Ni K_α x-ray image

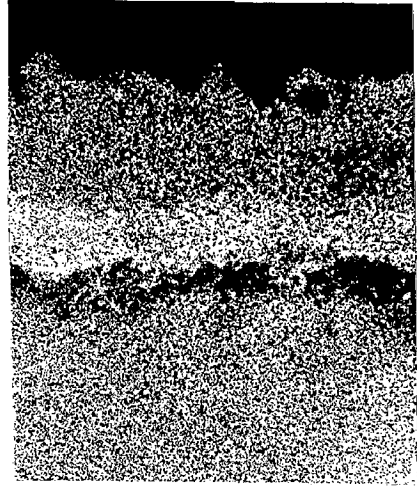
(d) Fe K_α x-ray image

(e) V K_α x-ray image

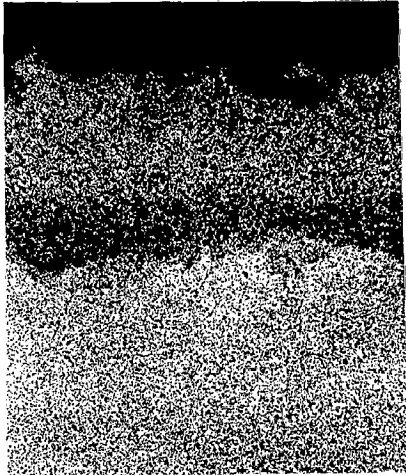
(f) O K_α x-ray image



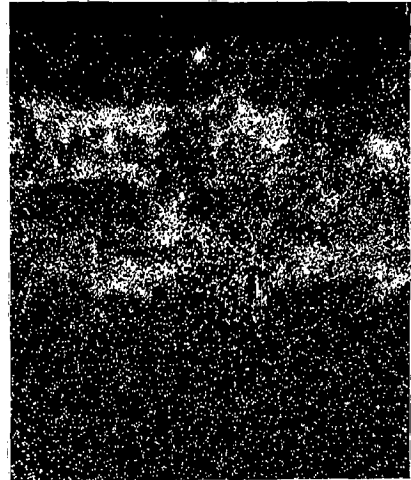
a



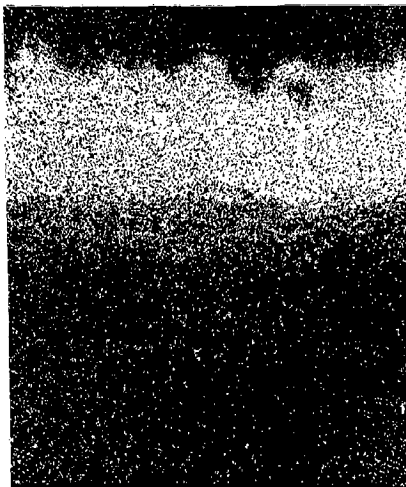
b



c



d



e



f

Fig. 5.93 BSEI and X-ray mappings of the cross-section of Alloy C (Superni 600) after cyclic hot corrosion at 900°C in Na₂SO₄-60% V₂O₅ (X400).

(a) Composition image (BSEI)

(b) Cr K_α x-ray image

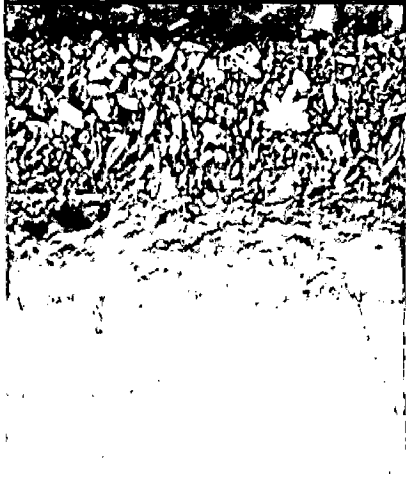
(c) Ni K_α x-ray image

(d) Fe K_α x-ray image

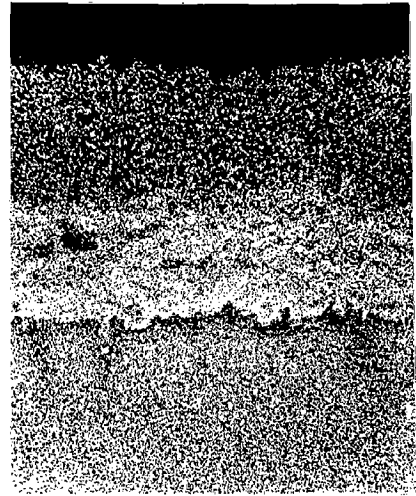
(e) Na K_α x-ray image

(f) V K_α x-ray image

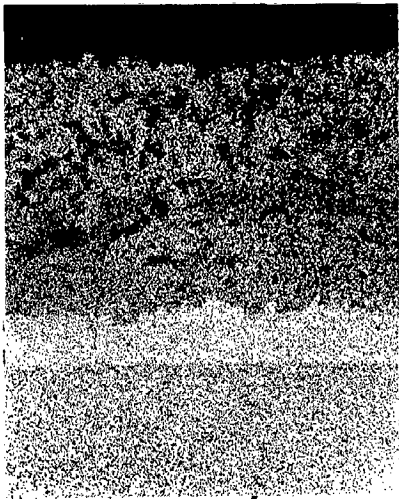
(g) O K_α x-ray image



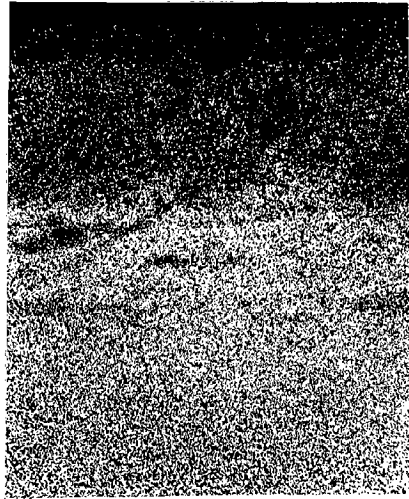
a



b



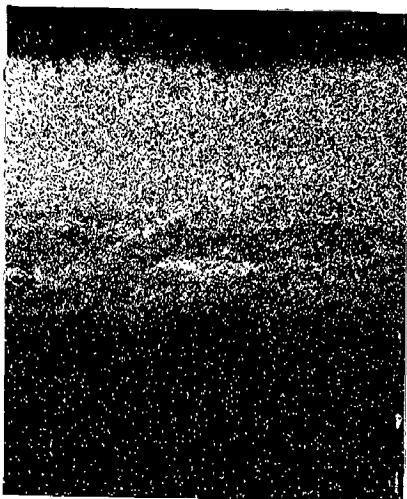
c



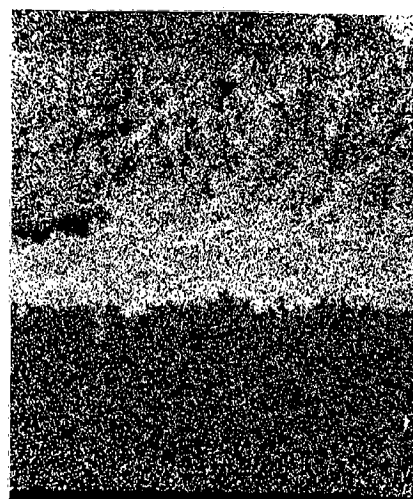
d



e



f



g

Fig. 5.94 BSEI and X-ray mappings of the cross-section of Alloy D (Superni 718) after cyclic hot corrosion at 900°C in Na₂SO₄-60% V₂O₅ (X400).

(a) Composition image (BSEI)

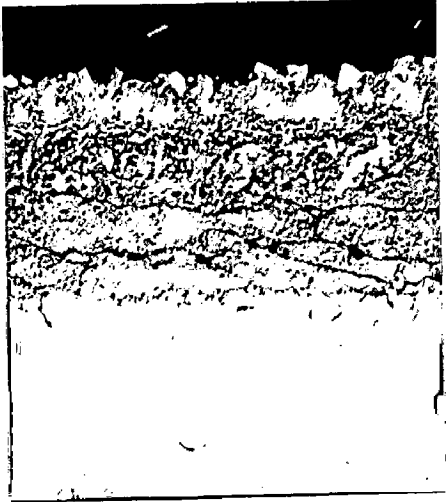
(b) Cr K_α x-ray image

(c) Ni K_α x-ray image

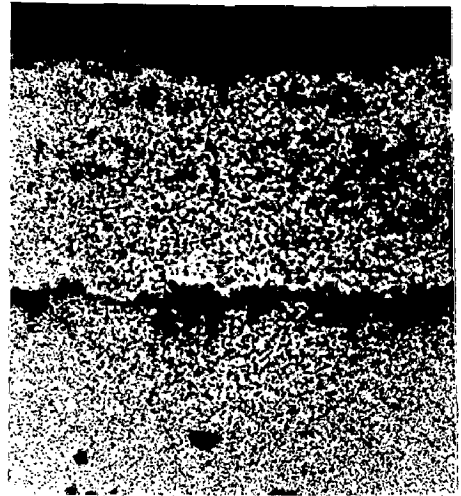
(d) Fe K_α x-ray image

(e) V K_α x-ray image

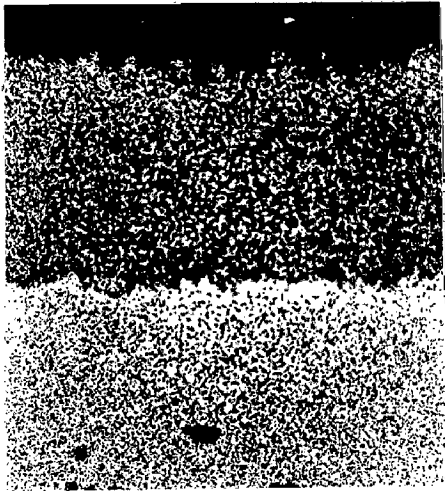
(f) O K_α x-ray image



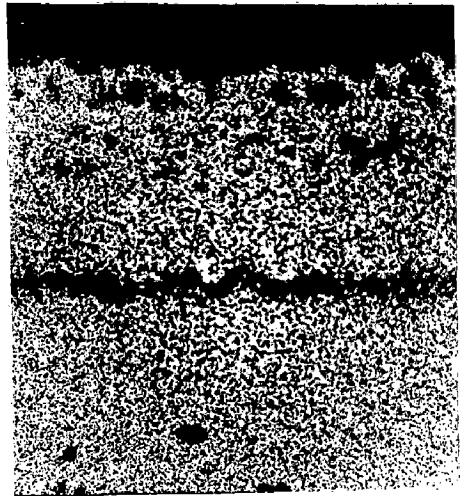
a



b



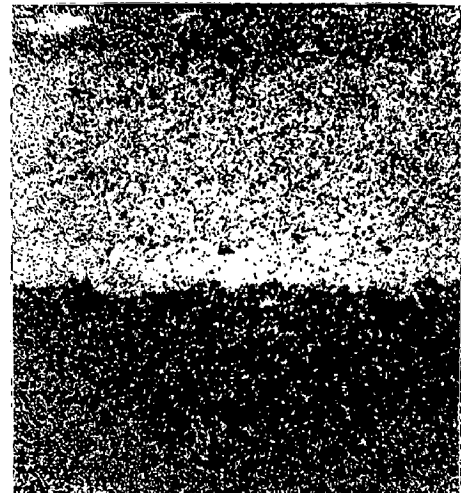
c



d



e



f

Fig. 5.95 BSEI and X-ray mappings of the cross-section of Alloy E (Superalloy 605) after cyclic hot corrosion at 900°C in Na₂SO₄-60% V₂O₅ (X300).

(a) Composition image (BSEI)

(b) Cr K_α x-ray image

(c) Ni K_α x-ray image

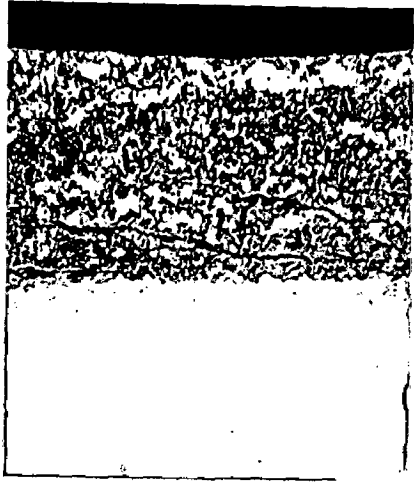
(d) Fe K_α x-ray image

(e) Co K_α x-ray image

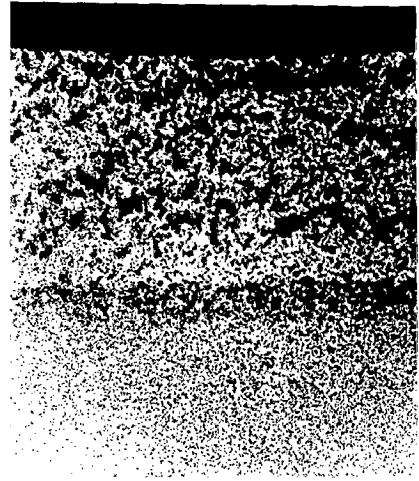
(f) W K_α x-ray image

(g) V K_α x-ray image

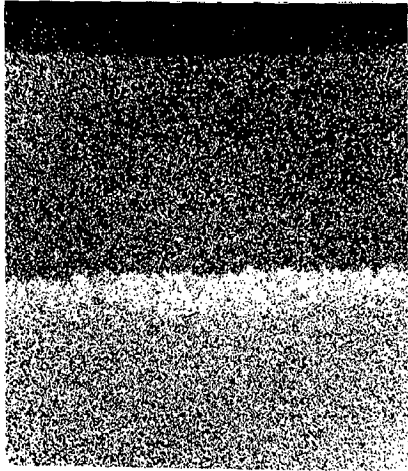
(h) O K_α x-ray image



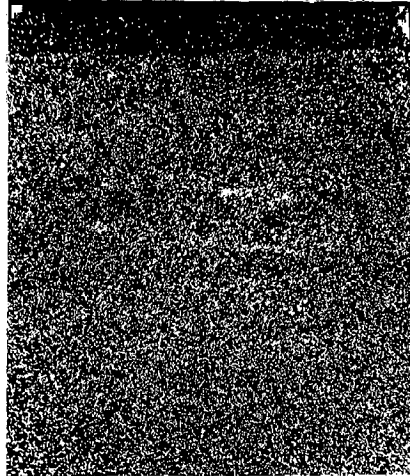
a



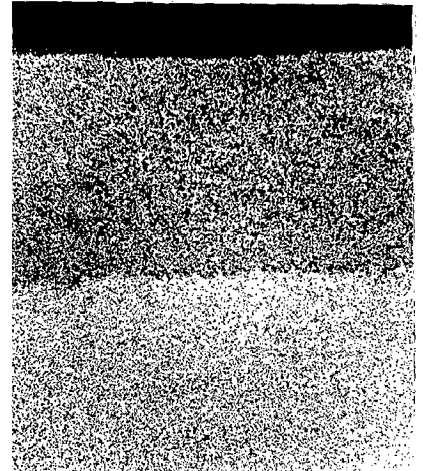
b



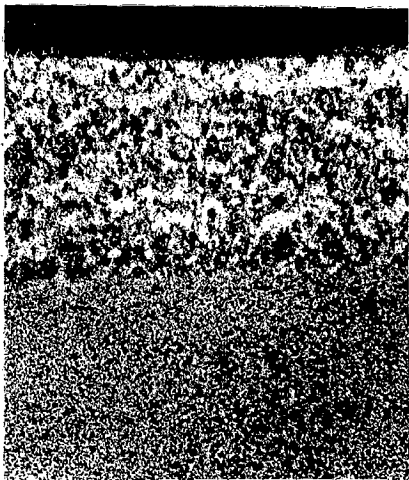
c



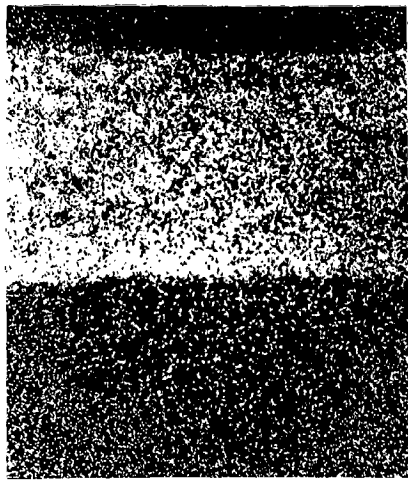
d



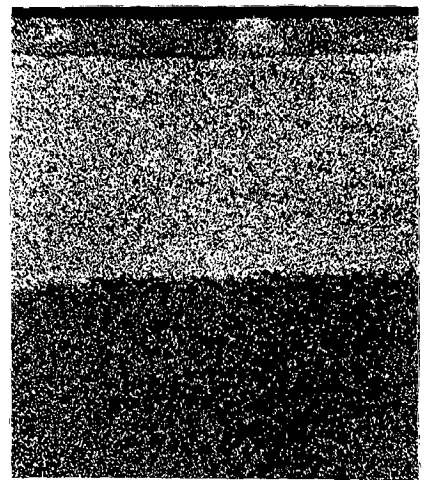
e



f



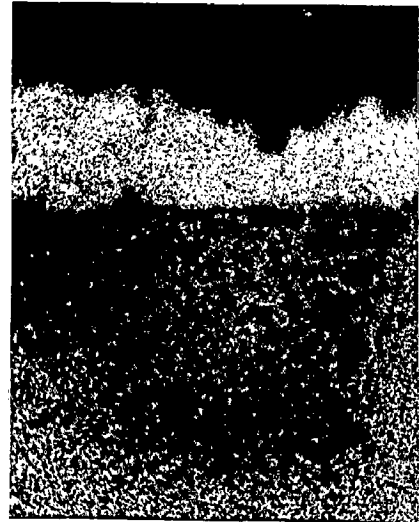
g



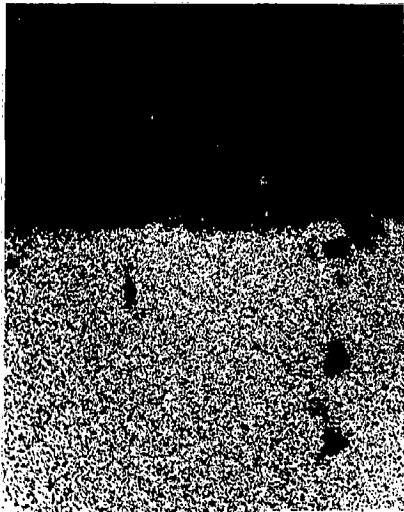
h



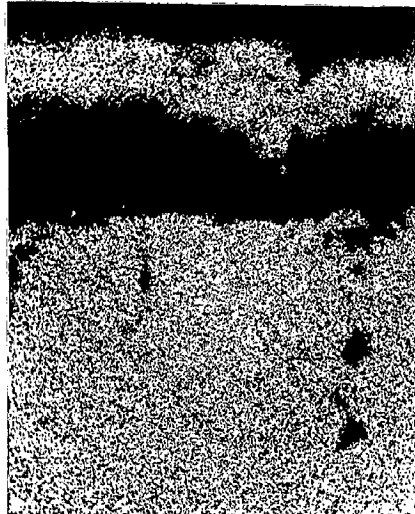
a



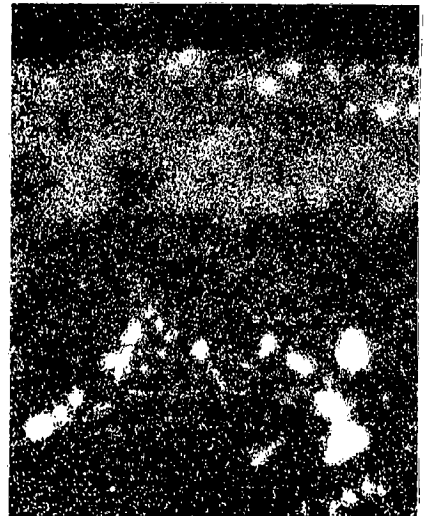
b



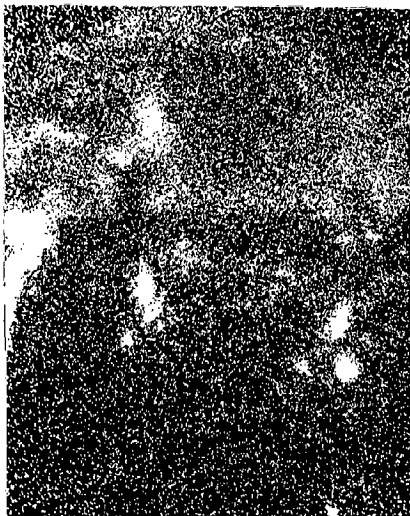
c



d



e



f



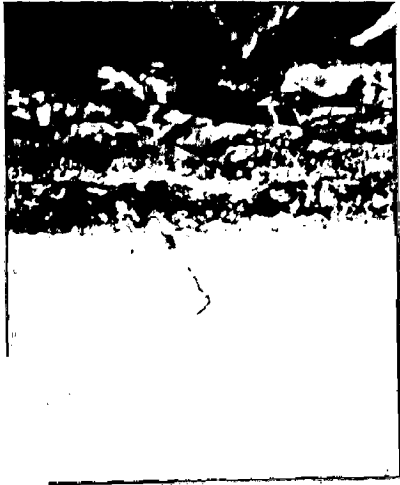
g

Fig. 5.97 BSEI and X-ray mappings of the cross-section of Alloy B (Superni 75) after cyclic hot corrosion at 1100°C in industrial atmosphere (X600).

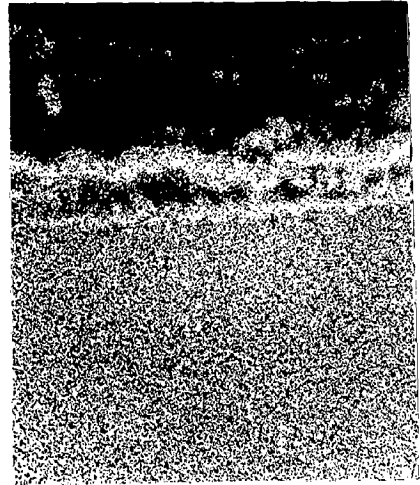
- (a) Composition image (BSEI)
- (b) Cr K_{α} x-ray image
- (c) Ni K_{α} x-ray image
- (d) Fe K_{α} x-ray image
- (e) V K_{α} x-ray image
- (f) O K_{α} x-ray image

Fig. 5.90 BSEI and X-ray mappings of the cross-section of Alloy E (Superco 605) after cyclic hot corrosion at 900°C in Na₂SO₄-15% V₂O₅ (X500).

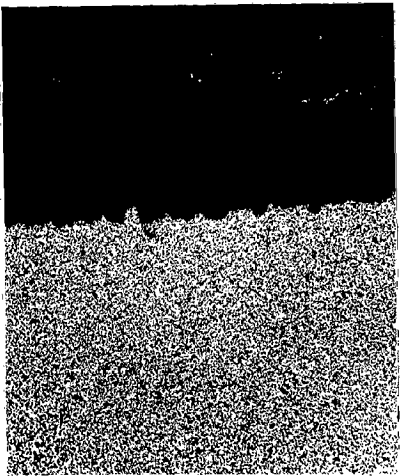
- (a) Composition image (BSEI)
- (b) Cr K_α x-ray image
- (c) Ni K_α x-ray image
- (d) Fe K_α x-ray image
- (e) Co K_α x-ray image
- (f) W K_α x-ray image
- (g) O K_α x-ray image



a



b



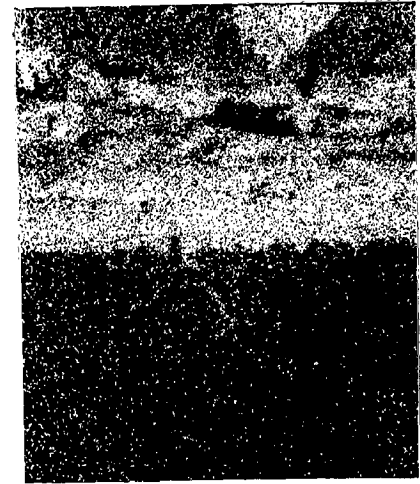
c



d



e



f

Fig. 5.98 BSEI and X-ray mappings of the cross-section of Alloy C (Superni 600) after cyclic hot corrosion at 1100°C in industrial atmosphere (X600).

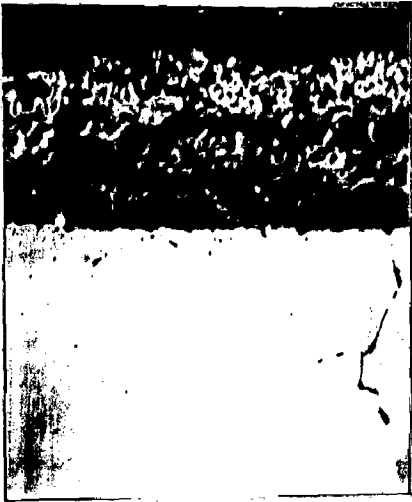
(a) Composition image (BSEI)

(b) Cr K_{α} x-ray image

(c) Ni K_{α} x-ray image

(d) Fe K_{α} x-ray image

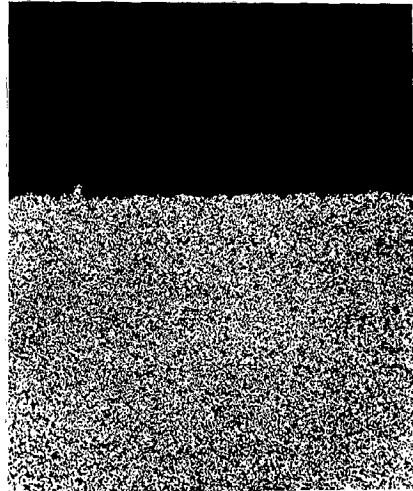
(e) O K_{α} x-ray image



a



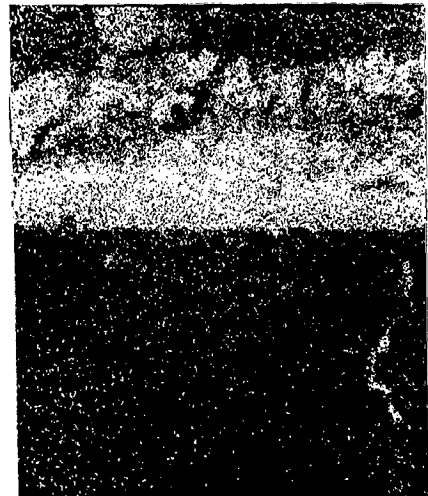
b



c



d



e

Fig. 5.99 BSEI and X-ray mappings of the cross-section of Alloy D (Superni 718) after cyclic hot corrosion at 1100°C in industrial atmosphere (X600).

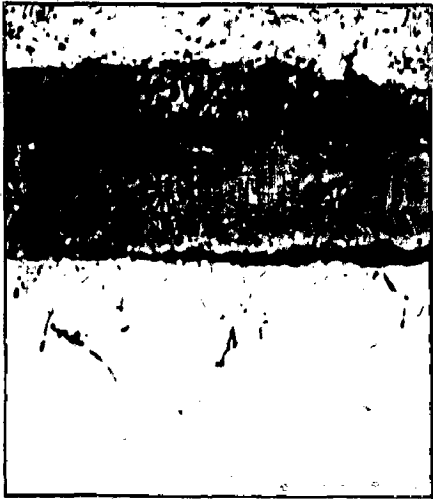
(a) Composition image (BSEI)

(b) Cr K_{α} x-ray image

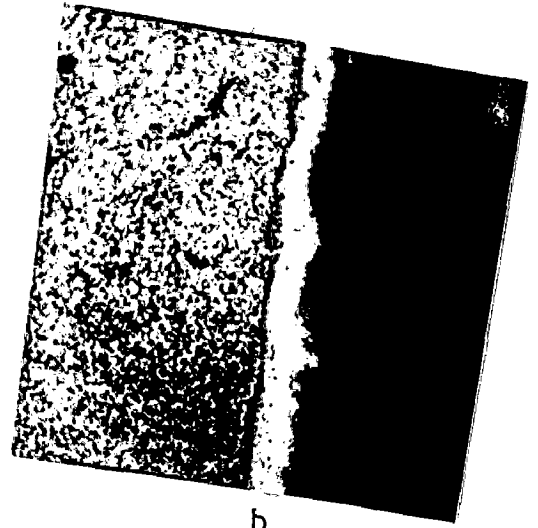
(c) Ni K_{α} x-ray image

(d) Fe K_{α} x-ray image

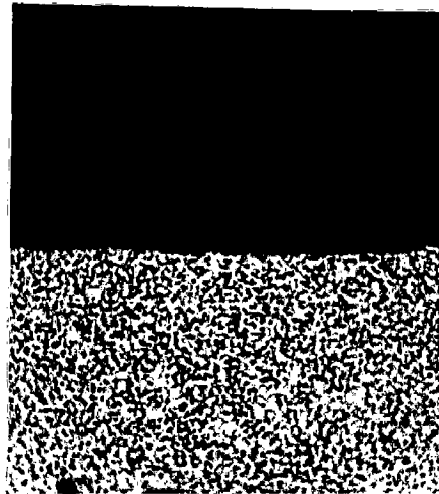
(e) O K_{α} x-ray image



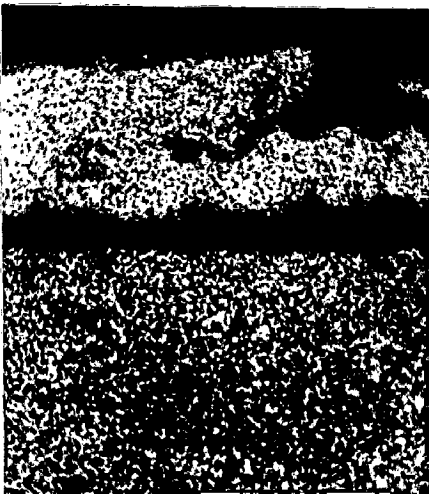
a



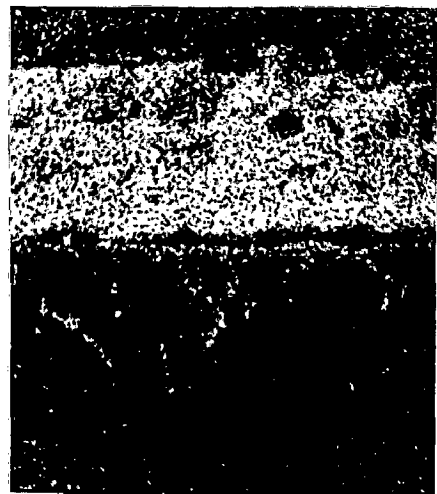
b



c



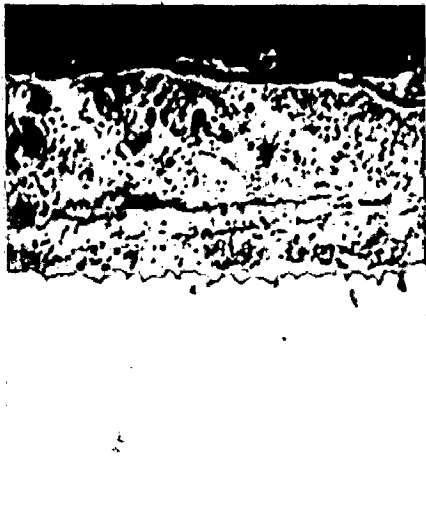
d



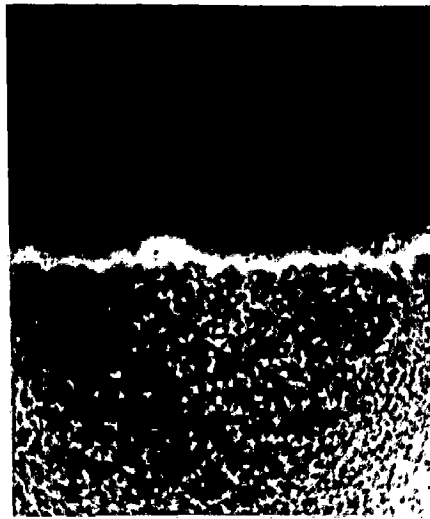
e

Fig. 5.100 BSEI and X-ray mappings of the cross-section of Alloy E (Superco 605) after cyclic hot corrosion at 1100°C in industrial atmosphere (X400).

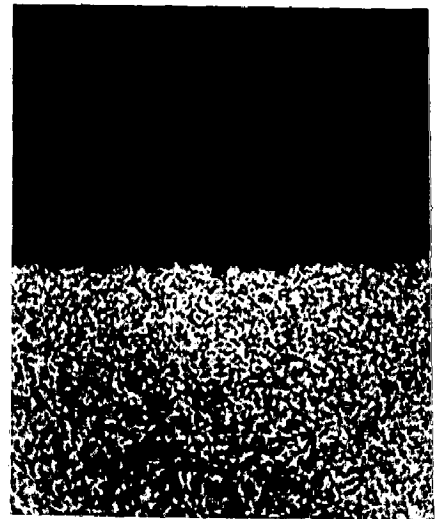
- (a) Composition image (BSEI)
- (b) Cr K_{α} x-ray image
- (c) Ni K_{α} x-ray image
- (d) Fe K_{α} x-ray image
- (e) Co K_{α} x-ray image
- (f) W K_{α} x-ray image
- (g) V K_{α} x-ray image
- (h) O K_{α} x-ray image



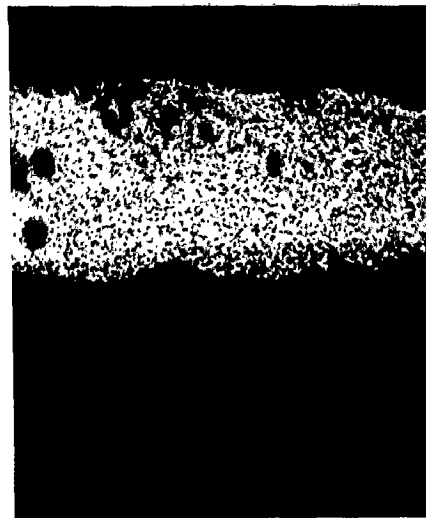
a



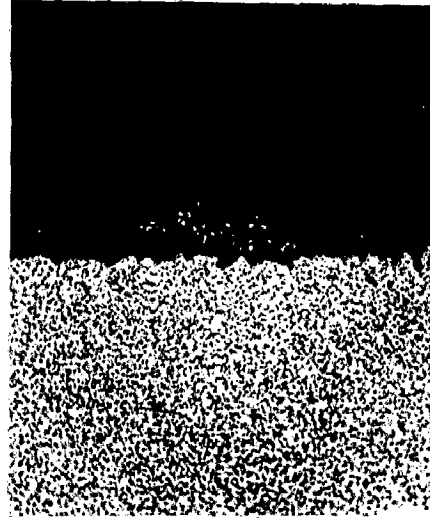
b



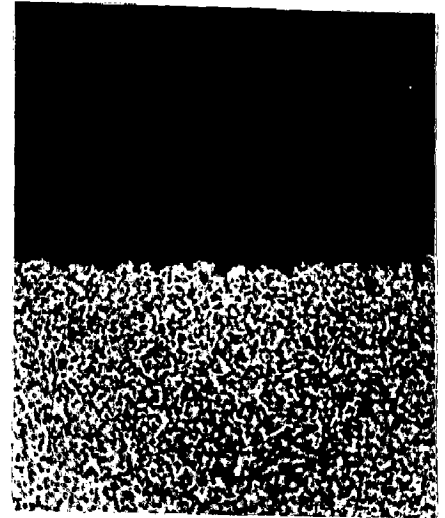
c



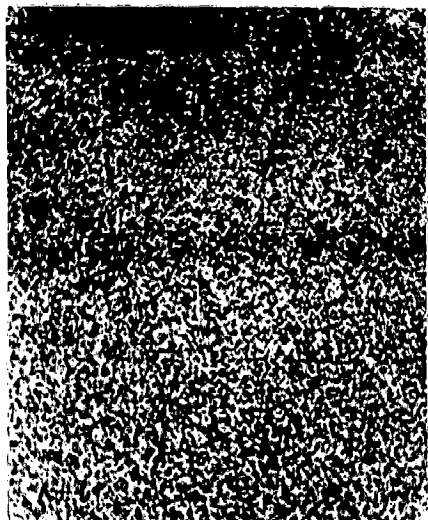
d



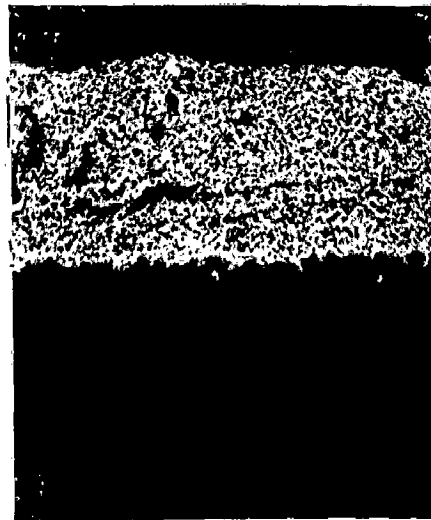
e



f



g



h

Fig. 5.101 BSEI and X-ray mappings of the cross-section of Alloy A (Superfer 800H) after cyclic hot corrosion at 900°C in Na₂SO₄-60%V₂O₅ + MgO (X600).

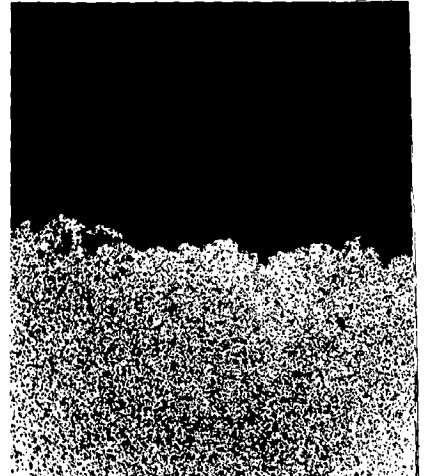
- (a) Composition image (BSEI)
- (b) Cr K_α x-ray image
- (c) Ni K_α x-ray image
- (d) Fe K_α x-ray image
- (e) V K_α x-ray image
- (f) Mg K_α x-ray image
- (g) S K_α x-ray image
- (h) O K_α x-ray image



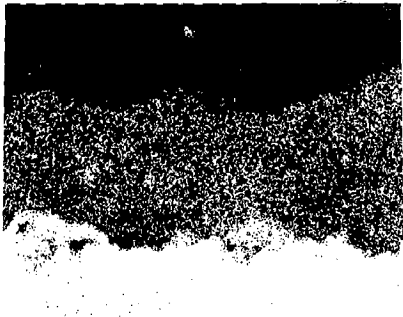
a



b



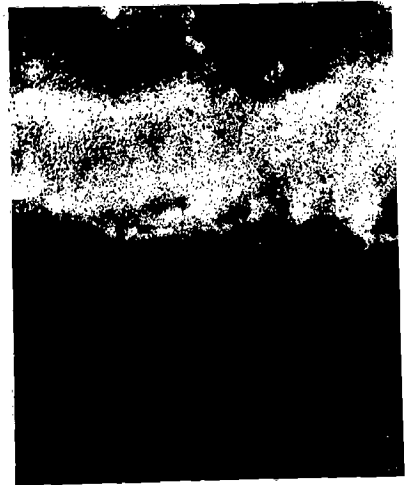
c



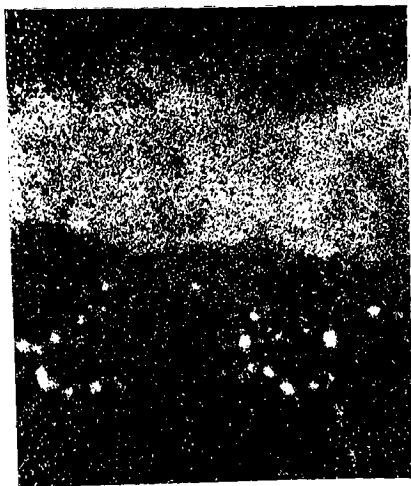
d



e



f



g

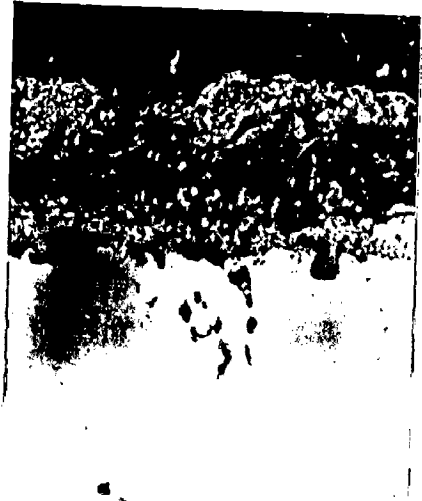


h

B33
5

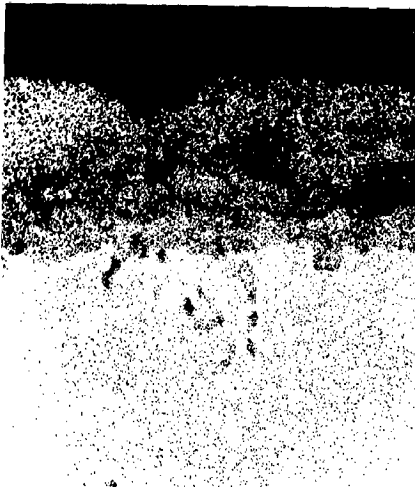
Fig. 5.102 BSEI and λ -EDS ¹⁶¹⁷ ss-section of Alloy B (Superni 75) after cyclic hot corrosion at 900°C in Na₂SO₄-60%V₂O₅ + MgO (X500).

- (a) Composition image (BSEI)
- (b) Cr K_α x-ray image
- (c) Ni K_α x-ray image
- (d) Fe K_α x-ray image
- (e) V K_α x-ray image
- (f) Mg K_α x-ray image
- (g) O K_α x-ray image

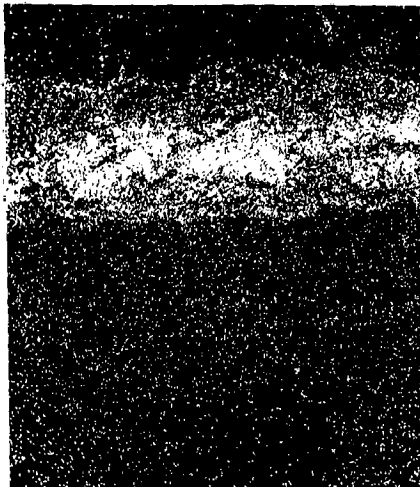


a

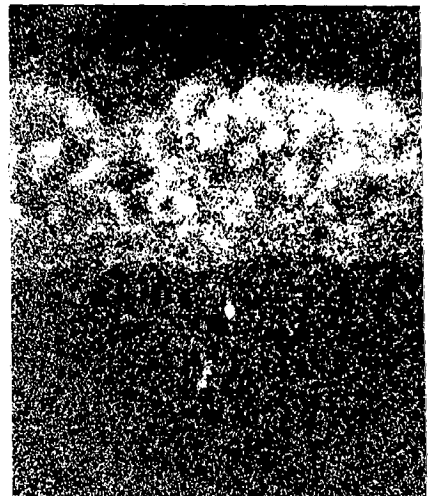
b



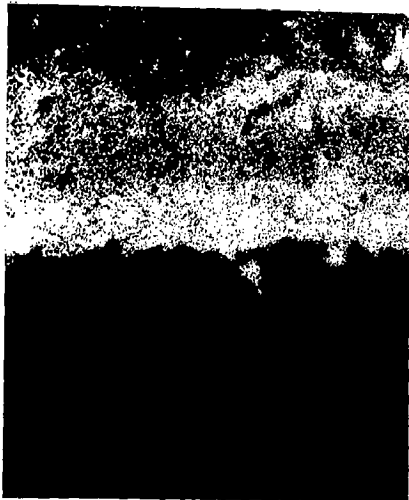
c



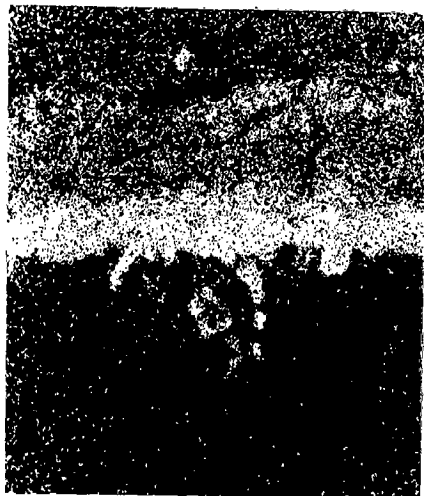
d



e



f



g

Fig. 5.103 BSEI and X-ray mappings of the cross-section of Alloy C (Superni 600) after cyclic hot corrosion at 900°C in Na₂SO₄-60%V₂O₅ + MgO (X600).

(a) Composition image (BSEI)

(b) Cr K_α x-ray image

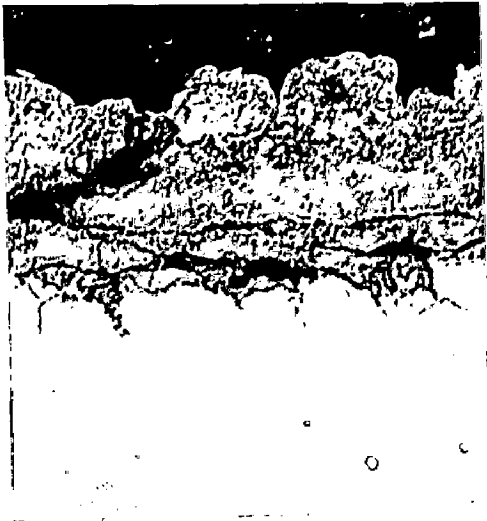
(c) Ni K_α x-ray image

(d) Fe K_α x-ray image

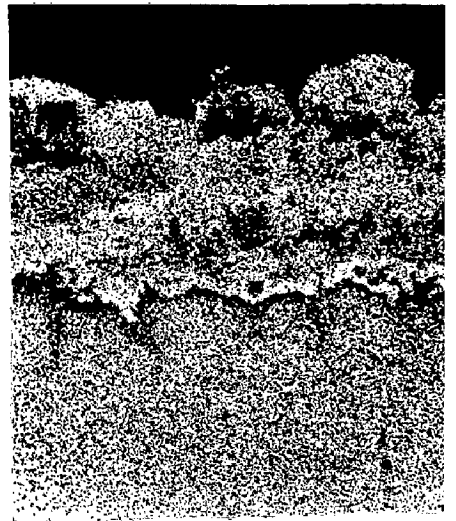
(e) V K_α x-ray image

(f) Mg K_α x-ray image

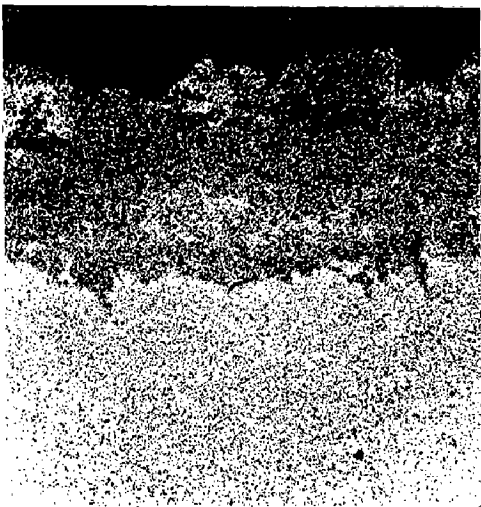
(g) O K_α x-ray image



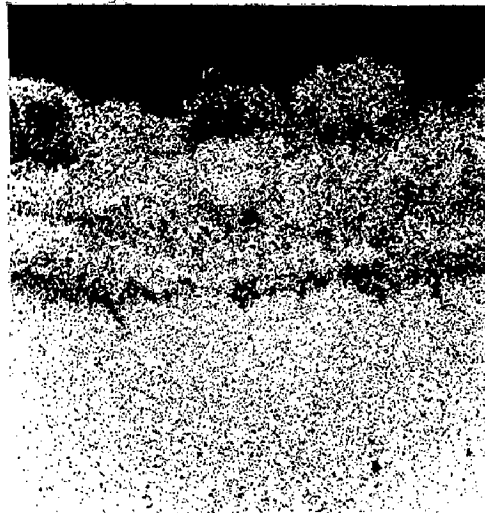
a



b



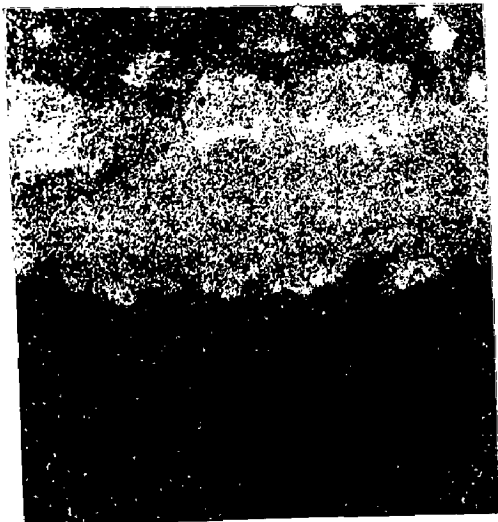
c



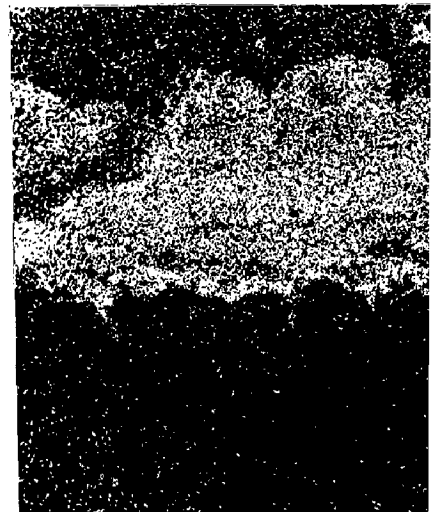
d



e



f



g

Fig. 5.104 BSEI and X-ray mappings of the cross-section of Alloy D (Superni 718) after cyclic hot corrosion at 900°C in Na₂SO₄-60%V₂O₅ + MgO (X300).

(a) Composition image (BSEI)

(b) Cr K_α x-ray image

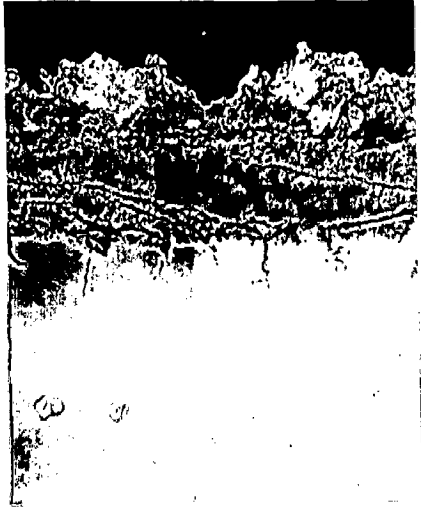
(c) Ni K_α x-ray image

(d) Fe K_α x-ray image

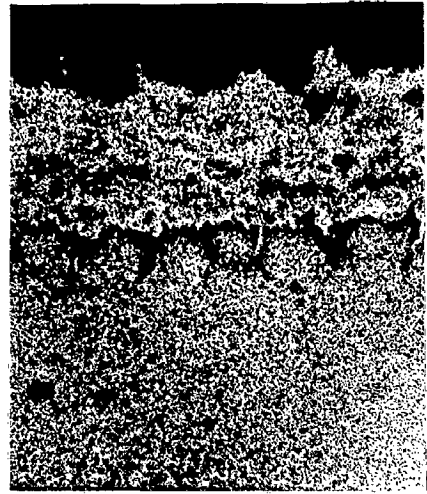
(e) V K_α x-ray image

(f) Mg K_α x-ray image

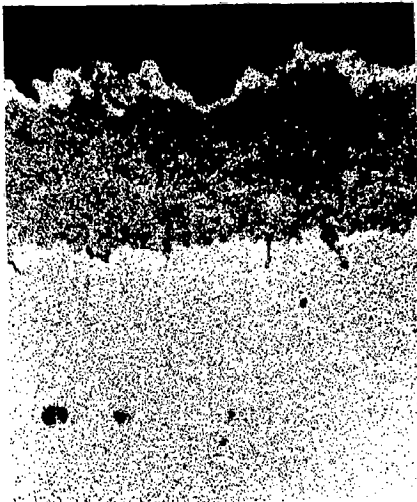
(g) O K_α x-ray image



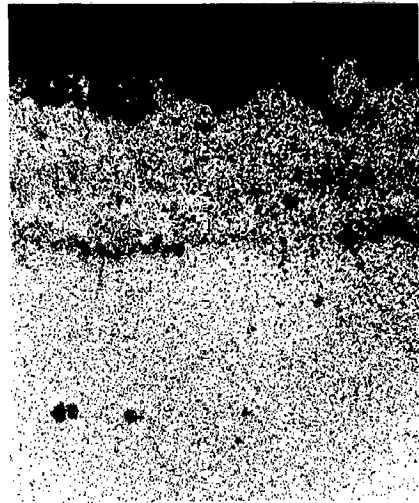
a



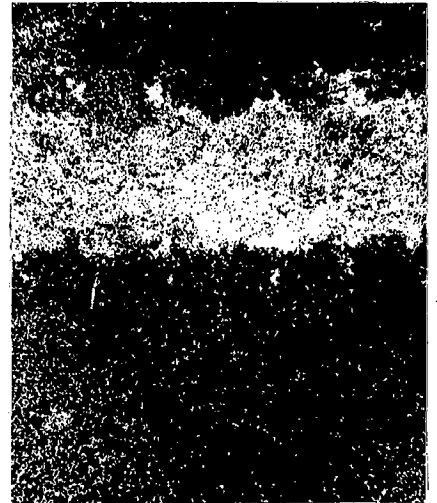
b



c



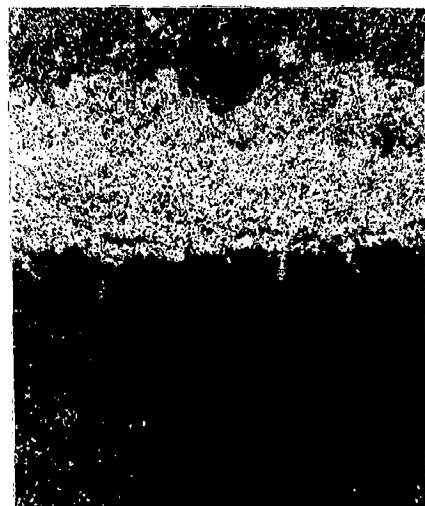
d



e



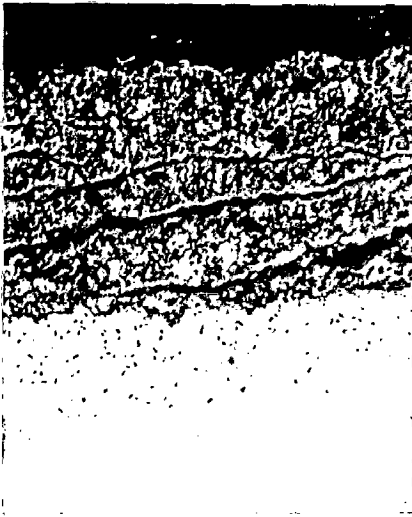
f



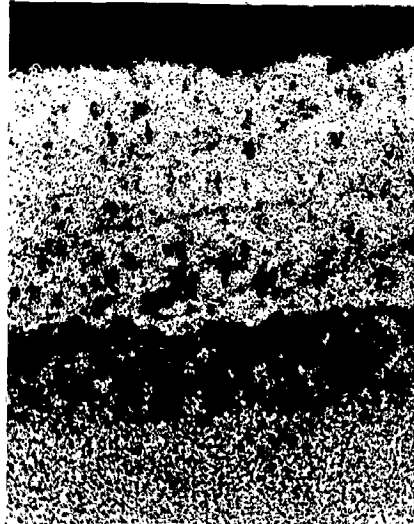
g

Fig. 5.105 BSEI and X-ray mappings of the cross-section of Alloy E (Superco 605) after cyclic hot corrosion at 900°C in Na₂SO₄-60%V₂O₅ + MgO (X400).

- (a) Composition image (BSEI)
- (b) Cr K_α x-ray image
- (c) Ni K_α x-ray image
- (d) Fe K_α x-ray image
- (e) Co K_α x-ray image
- (f) W K_α x-ray image
- (g) V K_α x-ray image
- (h) S K_α x-ray image
- (i) O K_α x-ray image



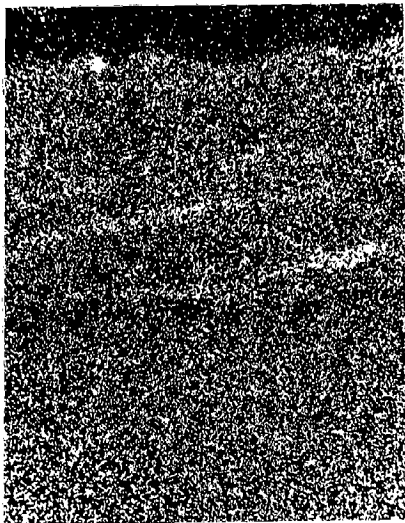
a



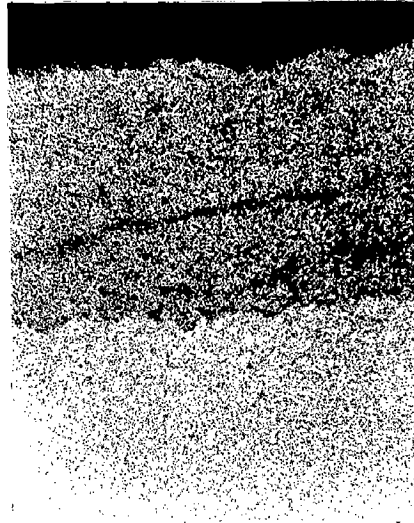
b



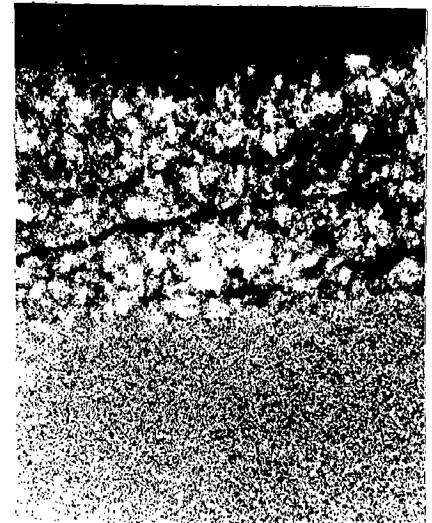
c



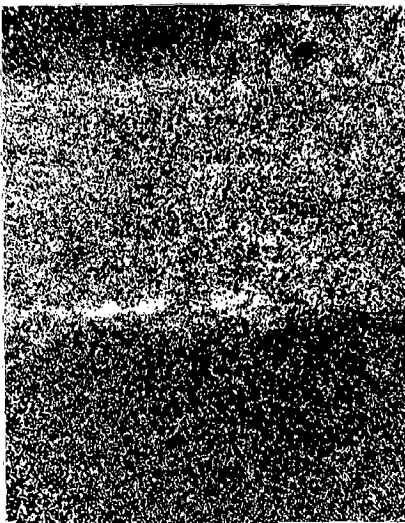
d



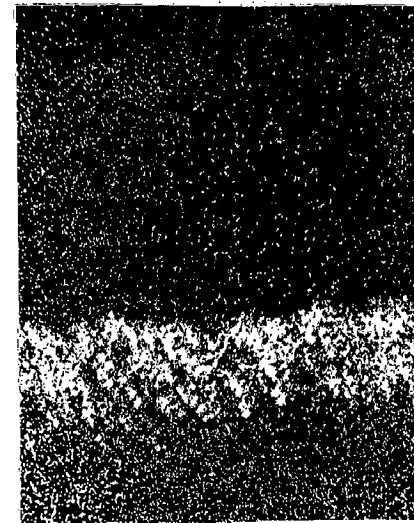
e



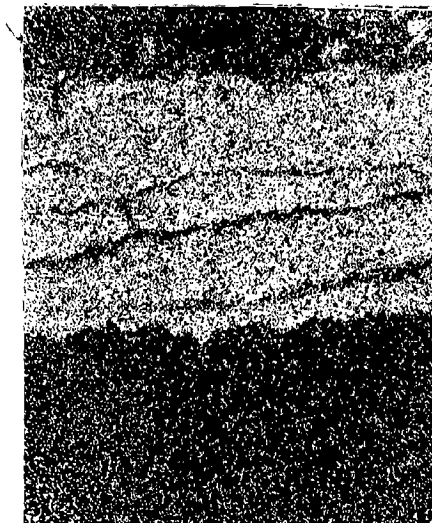
f



g



h



i

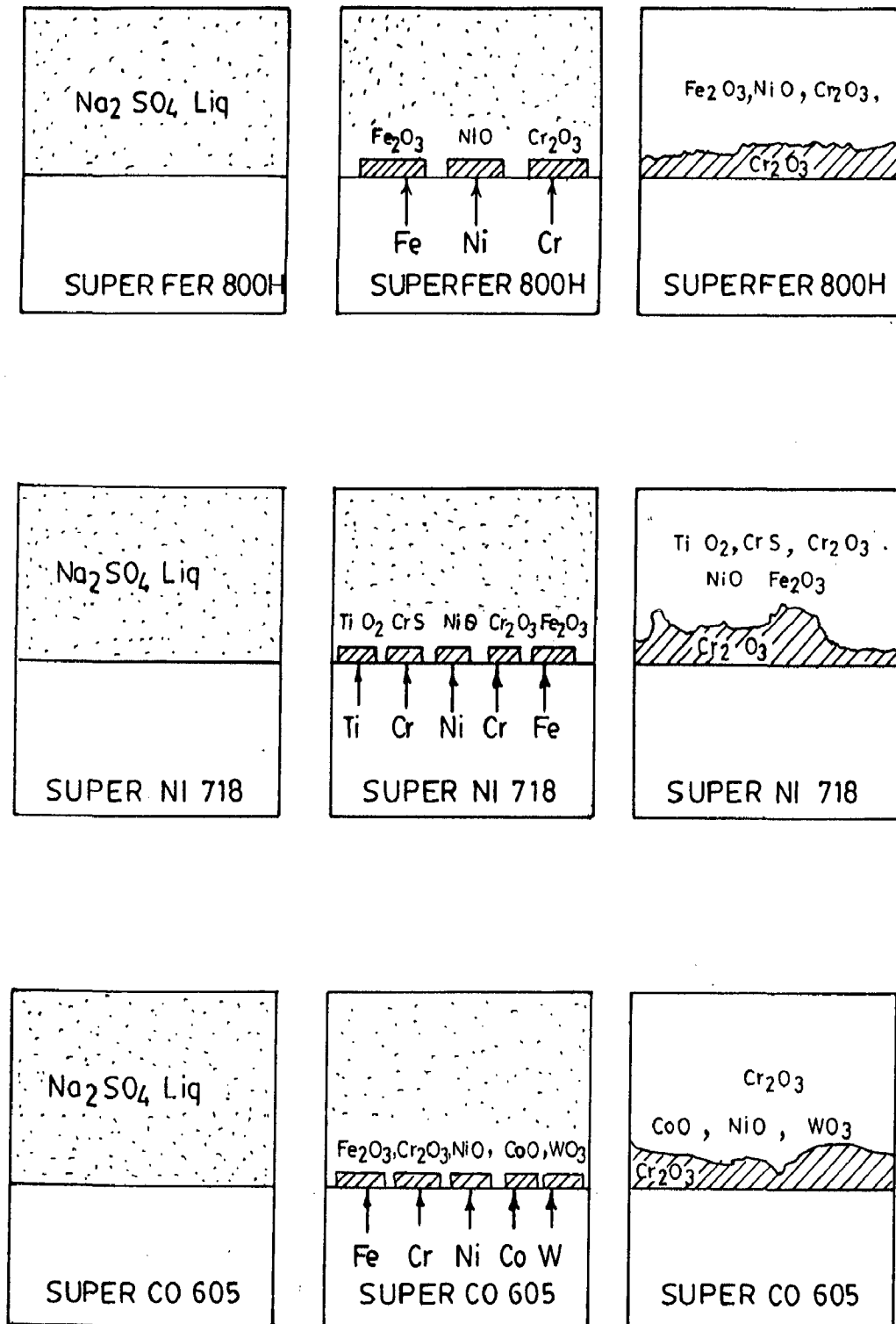


FIG. 61: SCHEMATIC DIAGRAM SHOWING PROBABLE MECHANISM OF HOT CORROSION OF ALLOY A (SUPER FER 800H) ALLOY D (SUPER NI 718) AND ALLOY E (SUPER CO 605) IN PURE Na_2SO_4 AT 900°C .
(SIMILAR TO REF. 48)

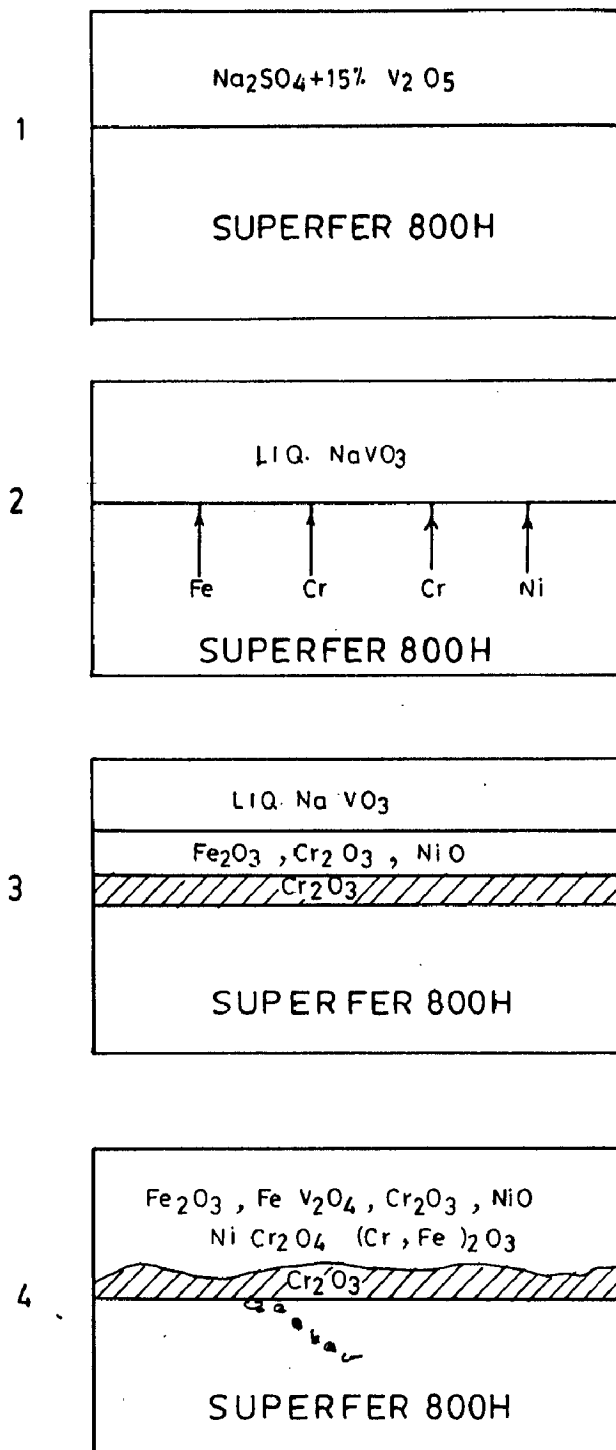


FIG. 6-2 SCHEMATIC DIAGRAM SHOWING PROBABLE HOT CORROSION MECHANISM OF ALLOY A (SUPERFER 800H) IN Na_2SO_4 -15% V_2O_5 AT 900°C (SIMILAR TO REF. 53)

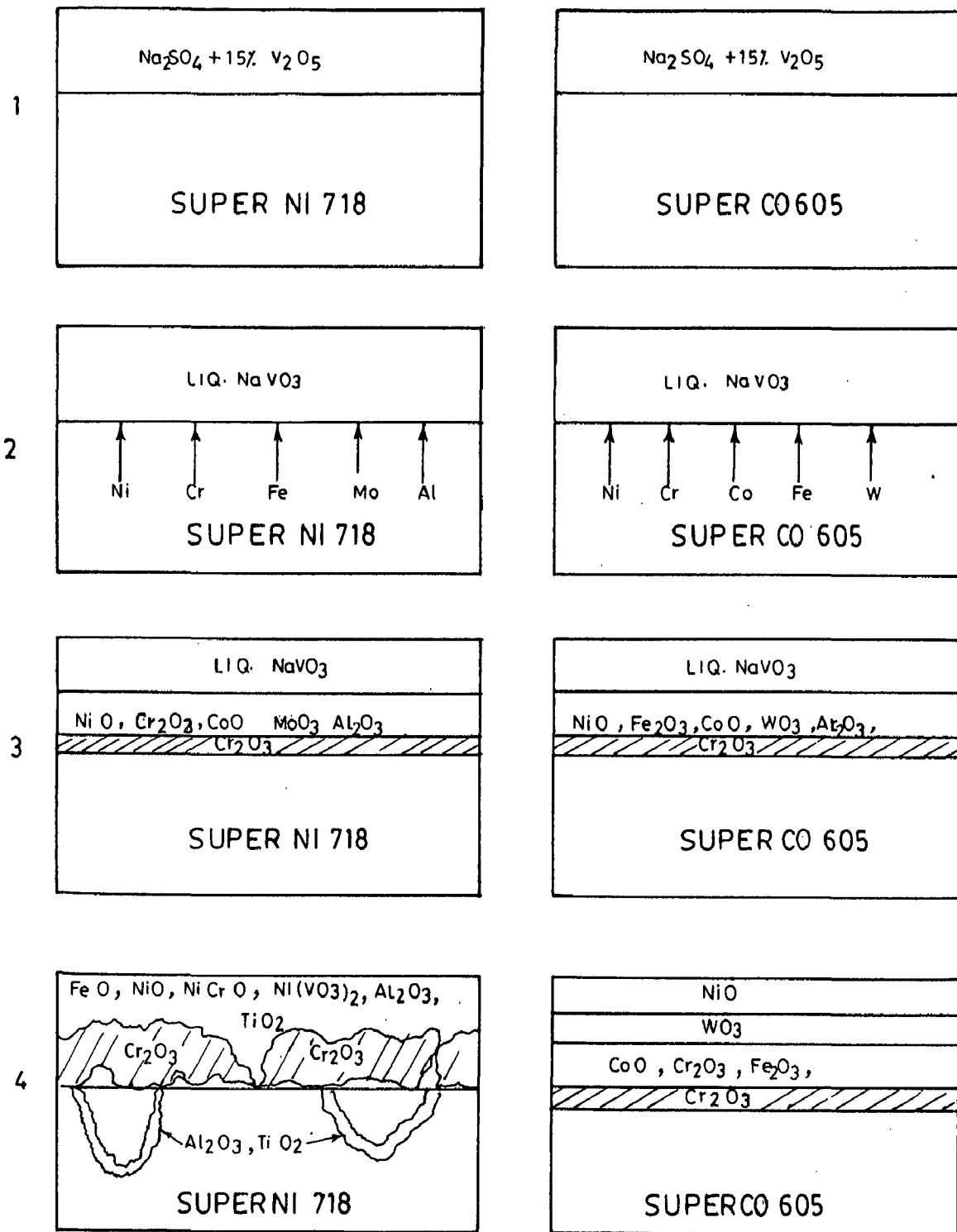
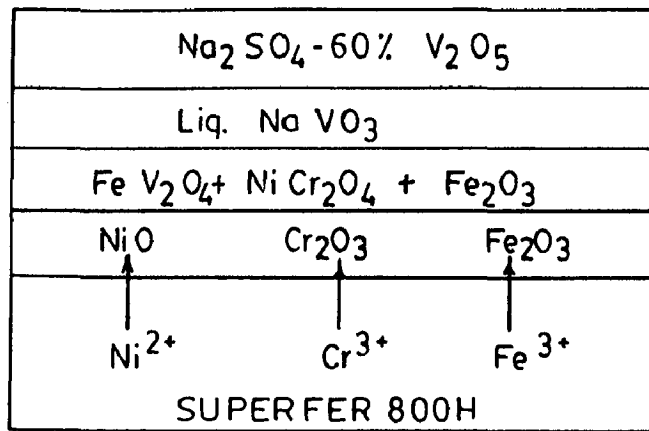
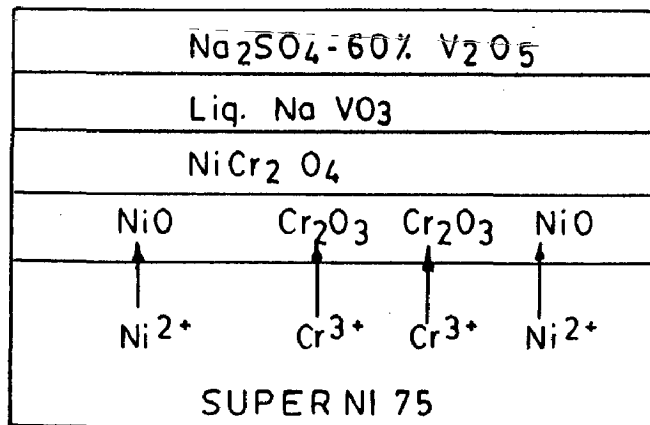


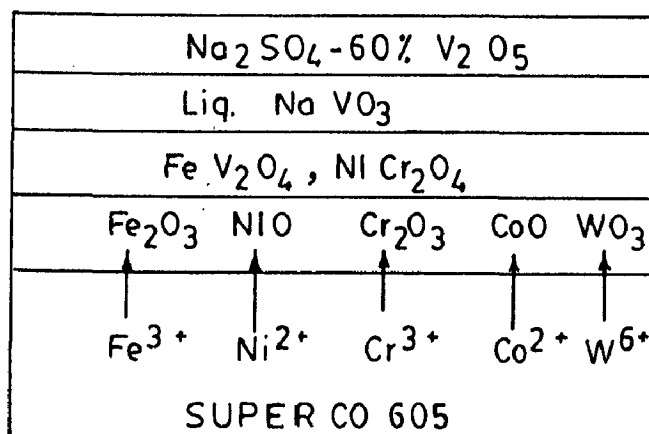
FIG.63:SCHEMATIC DIAGRAM SHOWING PROBABLE HOT CORROSION MECHANISM OF ALLOY D (SUPER NI 718) AND ALLOY E (SUPER CO 605) IN Na_2SO_4 -15% V_2O_5 AT 900°C (SIMILAR TO REF. 53)



a



b



c

FIG. 6.4 SCHEMATIC DIAGRAM SHOWING PROBABLE HOT CORROSION MECHANISM OF (a) ALLOY A (SUPERFER 800H) (b) ALLOY B (SUPER NI 75) AND (c) ALLOY E IN (SUPER CO 605) IN $\text{Na}_2\text{SO}_4\text{-60\% V}_2\text{O}_5$ AT 900°C (SIMILAR TO REF. 87)

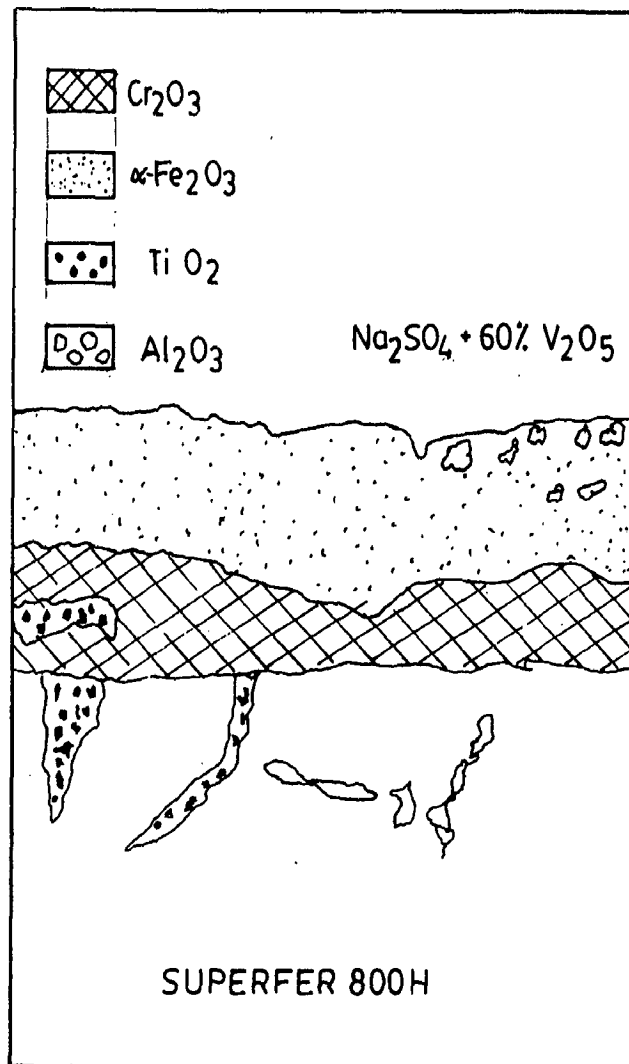
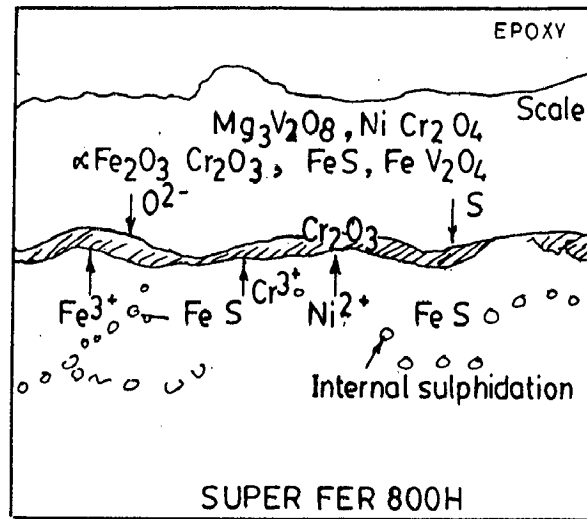
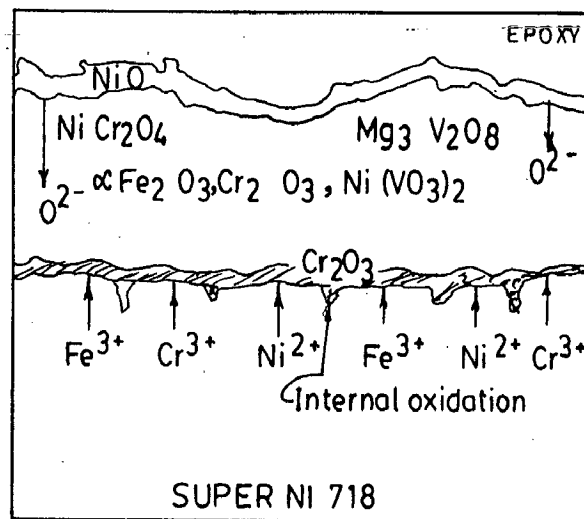


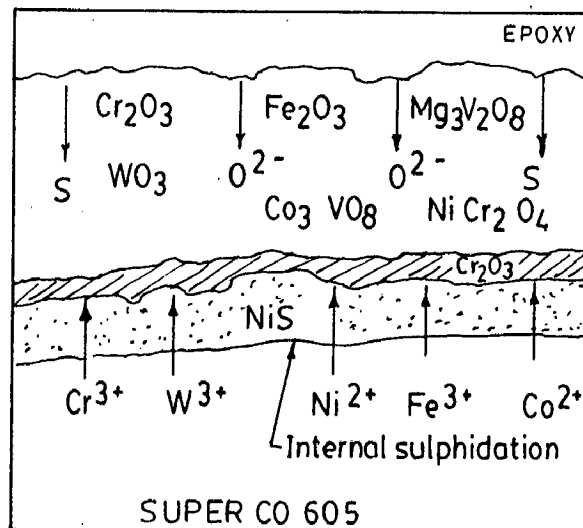
FIG. 6-5: SCHEMATIC DIAGRAM SHOWING PROBABLE HOT CORROSION MECHANISM OF ALLOY A (SUPERFER 800H) WITH $\text{Na}_2\text{SO}_4 + 60\% \text{V}_2\text{O}_5$ IN C.G. AT 1100°C (SIMILAR TO REF. 108)



a



b



c

FIG. 6-6: SCHEMATIC DIAGRAM SHOWING INTERNAL OXIDATION AND SULPHIDATION DURING HOT CORROSION OF (a) ALLOY A (b) ALLOY D and (c) ALLOY E IN Na_2SO_4 -60% V_2O_5 + MgO AT 900°C (Similar to Ref. 124)